

AN ABSTRACT OF THE THESIS OF

Chungu Lu for the degree of Master of Science in Atmospheric Sciences presented on August 5, 1988.

Title: A Study of Positive Cloud-to-Ground Lightning Flashes in Mesoscale Convective Systems

Abstract approved: Redacted for Privacy

This study is mainly concentrated on examining the positive cloud-to-ground lightning activity associated with Mesoscale Convective Systems. Six MCS events which occurred during the O.K. PRE-STORM program in 1985 are studied. Data indicating the location and polarity of the cloud-to-ground lightning flashes from a lightning location network are analyzed in conjunction with the low-level echo patterns as obtained from radar. Spatial and temporal characteristics of positive cloud-to-ground flashes are identified from the data analysis. For all cases examined, positive cloud-to-ground flashes were found most commonly in the stratiform regions of the MCSs examined, and their frequency tended to peak during the later stages of the storm lifecycle.

Two mechanisms responsible for the occurrence of positive cloud-to-ground lightning flashes with the above spatial and temporal characteristics are discussed. Based on the laboratory results, a 1-D charge generation model is developed. The

model results show that *in-situ* charging is unlikely to be the dominant mechanism for charge generation in the stratiform region under normal atmospheric conditions. Sensitivity studies show, however, that *in-situ* charging processes strongly depend upon the liquid water, graupel and snow contents in the cloud. Under favorable atmospheric conditions, *in-situ* charging may lead to a significant charge generation. Hence, we cannot completely dismiss *in-situ* charging mechanism. Analysis of wind fields from dual-Doppler radar in combination with vertical profile of electric fields indicates that charge advection from the convective region to the stratiform region of MCSs may be a potential mechanism responsible for the occurrence of positive cloud-to-ground lightning flashes in the stratiform region.

**A Study of Positive Cloud-to-Ground Lightning Flashes in
Mesoscale Convective Systems**

by

Chungu Lu

**A THESIS
submitted to
Oregon State University**

**in partial fulfillment of
the requirements for the
degree of**

Master of Science

**Completed August 5, 1988
Comemencement June 1989**

APPROVED:

Redacted for Privacy

Professor of Atmospheric Sciences in charge of major

Redacted for Privacy

Chairman of Department of Atmospheric Sciences

Redacted for Privacy

Dean of Graduate School

Date thesis is presented August 5, 1988

Presented by Chungu Lu

Acknowledgements

I would like to thank my Major Professor, Dr. Steven A. Rutledge, for his invaluable guidance and help during the course of this study. Also, I appreciate Drs. James H. Krueger, Larry Mahrt, and Murray Levine serving as my academic committee members.

Special thanks are extended to Dean A. Vickers for his expert assistance in programing, and to Phillip Barbour and Anthony Floyd for their help in checking my written English. I also would like to thank my friends Xingjian Jiang and Huel-I Huang for valuable discussions with them during this study.

I am deeply indebted to my best friend and wife Chuchu Yan, for her love, encouragement and understanding. She typed the manuscript and helped me in preparing some of the figures. Finally, I would like to thank the Government of the People's Republic of China for the financial support during my first year's study at Oregon State University.

This study was supported by the National Science Foundation under the contract ATM-8718861.

Table of Contents

	Page
1. Introduction	1
1.1 Cloud-to-ground lightning and the electric dipole model	1
1.2 Previous studies	6
1.3 Scientific background	11
1.4 Research objectives	14
1.5 Thesis organization	15
2. Data Sources	17
2.1 O.K. PRE-STORM program	17
2.2 Instrumentation used for this study	19
3. Characteristics of Positive Flashes in MCSs	22
3.1 Analysis of WSR-57 radar and lightning location data	22
1) Case of May 27	25
2) Case of May 28	28
3) Case of June 3	31
4) Case of June 4	33
5) Case of June 10	35
6) Case of June 24	36
3.2 Characteristics of Positive Flashes	38
1) Spatial characteristics	38
2) Temporal characteristics	44
4. Relationship of Positive Ground Flashes to Storm Structure	128
4.1 Discussions of in-situ charging mechanism	130
4.2 Discussions of charge advection mechanism	148
5. Conclusions	157
5.1 Conclusions	157

More
Space 2
to
visit

More 2
Space 1/14

5.2 Suggestions for further research	158
6. References	160

	Rutledge and Houze (1987) . a) cloud water content; b) temperature; c) graupel mixing ratio; d) snow mixing ratio.	137
Figure 4.4	Vertical distribution of charge generation rate produced by the 1-D model.	142
Figure 4.5	Results of sensitivity studies. a) Increase liquid water case. b) Increase in Q_s case. c) Increase in Q_g case. d) Increase in Q_s and Q_g . e) Increase in liquid water, Q_s and Q_g	145
Figure 4.6	Reflectivity and air motion fields for the 0202Z dual-doppler analysis on 10-11 June 1985. a) Reflectivity. b) Horizontal velocity field. c) Vertical velocity field.	150
Figure 4.7	Vertical profile of the electric field in the transition region of a squall-type MCS (from Marshall, 1988).	153
Figure 4.8	Vertical profile of charge density derived from electric field profile.	155

List of Figures

	Page
<u>Chapter 1</u>	
Figure 1.1 An upward electric dipole structure indicating the probable distribution of the thundercloud charge (from Uman, 1969).	2
Figure 1.2 Charge separation due to the collisions between hailstone and small ice crystal of differing surface temperatures.	4
Figure 1.3 Charge separation due to collisions between hailstone and freezing droplet.	4
Figure 1.4 Inductive charging process.	5
Figure 1.5 Tilted dipole model.	8
Figure 1.6 Conceptual model of a squall-type MCS (from Smull, 1986).	12
<u>Chapter 2</u>	
Figure 2.1 The O.K.PRE-STORM mesonet network (from Cunning, 1986).	18
Figure 2.2 Location of the various observational platforms used in this study (from Rutledge and MacGorman, 1988).	20
<u>Chapter 3</u>	
Statistic Figures: Frequency distributions of positive CG flashes with measured radar reflectivities. a) 27 May case; b) 28 May case; c) 3 June case; d) 4 June case; e) 10 June case; f) 11 June case; g) 24 June case; h) Composite statistics for all cases.	40
Figure 3.0 Areally integrated precipitation amounts for the convective and stratiform regions and cumulative lightning activity over the time period from 1008 to 1659 UTC.	48
Figure 3.1 Radar echo pattern and lightning map for 0336Z on 27 May	49
Figure 3.2 Radar echo pattern and lightning map for 0349Z on 27 May	50
Figure 3.3 Radar echo pattern and lightning map for 0431Z on 27 May	51
Figure 3.4 Radar echo pattern and lightning map for 0457Z on 27 May	52
Figure 3.5 Radar echo pattern and lightning map for 0534Z on 27 May	53
Figure 3.6 Radar echo pattern and lightning map for 0604Z on 27 May	54
Figure 3.7 Radar echo pattern and lightning map for 0624Z on 27 May	55
Figure 3.8 Radar echo pattern and lightning map for 0701Z on 27 May	56
Figure 3.9 Radar echo pattern and lightning map for 0733Z on 27 May	57

Figure 3.10	Radar echo pattern and lightning map for 0802Z on 27 May	58
Figure 3.11	Radar echo pattern and lightning map for 0833Z on 27 May	59
Figure 3.12	Radar echo pattern and lightning map for 0856Z on 27 May	60
Figure 3.13	Radar echo pattern and lightning map for 0926Z on 27 May	61
Figure 3.14	Radar echo pattern and lightning map for 0955Z on 27 May	62
Figure 3.15	Radar echo pattern and lightning map for 1024Z on 27 May	63
Figure 3.16	Radar echo pattern and lightning map for 1055Z on 27 May	64
Figure 3.17	Radar echo pattern and lightning map for 1124Z on 27 May	65
Figure 3.18	Radar echo pattern and lightning map for 1200Z on 27 May	66
Figure 3.19	Radar echo pattern and lightning map for 0858Z on 28 May	67
Figure 3.20	Radar echo pattern and lightning map for 0932Z on 28 May	68
Figure 3.21	Radar echo pattern and lightning map for 1008Z on 28 May	69
Figure 3.22	Radar echo pattern and lightning map for 1038Z on 28 May	70
Figure 3.23	Radar echo pattern and lightning map for 1106Z on 28 May	71
Figure 3.24	Radar echo pattern and lightning map for 1136Z on 28 May	72
Figure 3.25	Radar echo pattern and lightning map for 1201Z on 28 May	73
Figure 3.26	Radar echo pattern and lightning map for 1232Z on 28 May	74
Figure 3.27	Radar echo pattern and lightning map for 1356Z on 28 May	75
Figure 3.28	Radar echo pattern and lightning map for 1428Z on 28 May	76
Figure 3.29	Radar echo pattern and lightning map for 1456Z on 28 May	77
Figure 3.30	Radar echo pattern and lightning map for 1528Z on 28 May	78
Figure 3.31	Radar echo pattern and lightning map for 1554Z on 28 May	79
Figure 3.32	Radar echo pattern and lightning map for 1625Z on 28 May	80
Figure 3.33	Radar echo pattern and lightning map for 1659Z on 28 May	81
Figure 3.34	Radar echo pattern and lightning map for 1727Z on 28 May	82
Figure 3.35	Radar echo pattern and lightning map for 1752Z on 28 May	83
Figure 3.36	Radar echo pattern and lightning map for 2155Z on 3 June	84
Figure 3.37	Radar echo pattern and lightning map for 2234Z on 3 June	85
Figure 3.38	Radar echo pattern and lightning map for 2258Z on 3 June	86
Figure 3.39	Radar echo pattern and lightning map for 2327Z on 3 June	87
Figure 3.40	Radar echo pattern and lightning map for 2351Z on 3 June	88
Figure 3.41	Radar echo pattern and lightning map for 0017Z on 4 June	89
Figure 3.42	Radar echo pattern and lightning map for 0105Z on 4 June	90
Figure 3.43	Radar echo pattern and lightning map for 0140Z on 4 June	91
Figure 3.44	Radar echo pattern and lightning map for 0207Z on 4 June	92
Figure 3.45	Radar echo pattern and lightning map for 0227Z on 4 June	93
Figure 3.46	Radar echo pattern and lightning map for 0308Z on 4 June	94
Figure 3.47	Radar echo pattern and lightning map for 0337Z on 4 June	95
Figure 3.48	Radar echo pattern and lightning map for 0355Z on 4 June	96

Figure 3.49	Radar echo pattern and lightning map for 0417Z on 4 June	97
Figure 3.50	Radar echo pattern and lightning map for 0504Z on 4 June	98
Figure 3.51	Radar echo pattern and lightning map for 0755Z on 4 June	99
Figure 3.52	Radar echo pattern and lightning map for 0821Z on 4 June	100
Figure 3.53	Radar echo pattern and lightning map for 0856Z on 4 June	101
Figure 3.54	Radar echo pattern and lightning map for 0934Z on 4 June	102
Figure 3.55	Radar echo pattern and lightning map for 0952Z on 4 June	103
Figure 3.56	Radar echo pattern and lightning map for 1031Z on 4 June	104
Figure 3.57	Radar echo pattern and lightning map for 1102Z on 4 June	105
Figure 3.58	Radar echo pattern and lightning map for 1127Z on 4 June	106
Figure 3.59	Radar echo pattern and lightning map for 1154Z on 4 June	107
Figure 3.60	Radar echo pattern and lightning map for 1235Z on 4 June	108
Figure 3.61	Radar echo pattern and lightning map for 1258Z on 4 June	109
Figure 3.62	Radar echo pattern and lightning map for 1429Z on 10 June	110
Figure 3.63	Radar echo pattern and lightning map for 1505Z on 10 June	111
Figure 3.64	Radar echo pattern and lightning map for 1557Z on 10 June	112
Figure 3.65	Radar echo pattern and lightning map for 1629Z on 10 June	113
Figure 3.66	Radar echo pattern and lightning map for 1707Z on 10 June	114
Figure 3.67	Radar echo pattern and lightning map for 1734Z on 10 June	115
Figure 3.68	Radar echo pattern and lightning map for 1906Z on 10 June	116
Figure 3.69	Radar echo pattern and lightning map for 1933Z on 10 June	117
Figure 3.70	Radar echo pattern and lightning map for 0205Z on 24 June	118
Figure 3.71	Radar echo pattern and lightning map for 0236Z on 24 June	119
Figure 3.72	Radar echo pattern and lightning map for 0306Z on 24 June	120
Figure 3.73	Radar echo pattern and lightning map for 0339Z on 24 June	121
Figure 3.74	Radar echo pattern and lightning map for 0407Z on 24 June	122
Figure 3.75	Radar echo pattern and lightning map for 0437Z on 24 June	123
Figure 3.76	Radar echo pattern and lightning map for 0500Z on 24 June	124
Figure 3.77	Radar echo pattern and lightning map for 0529Z on 24 June	125
Figure 3.78	Radar echo pattern and lightning map for 0601Z on 24 June	126
Figure 3.79	Radar echo pattern and lightning map for 0746Z on 24 June	127

Chapter 4

Figure 4.1	The laboratory result of charge transfer per collision between graupel and small ice particles with temperature and liquid water content (from Saunders and Jayaratne, 1986).	132
Figure 4.2	Numerically derived function for Saunders and Jayaratne experimental data.	135
Figure 4.3	Vertical profile used in the 1-D model calculations, from	

	Rutledge and Houze (1987) . a) cloud water content; b) temperature; c) graupel mixing ratio; d) snow mixing ratio.	137
Figure 4.4	Vertical distribution of charge generation rate produced by the 1-D model.	142
Figure 4.5	Results of sensitivity studies. a) Increase liquid water case. b) Increase in Q_s case. c) Increase in Q_g case. d) Increase in Q_s and Q_g . e) Increase in liquid water, Q_s and Q_g	145
Figure 4.6	Reflectivity and air motion fields for the 0202Z dual-doppler analysis on 10-11 June 1985. a) Reflectivity. b) Horizontal velocity field. c) Vertical velocity field.	150
Figure 4.7	Vertical profile of the electric field in the transition region of a squall-type MCS (from Marshall, 1988).	153
Figure 4.8	Vertical profile of charge density derived from electric field profile.	155

List of Tables

	Page
<u>Chapter 3</u>	
Table 3.1 Overview of six cases for which radar and lightning data are analyzed.	24
Table 3.2 Summary of evolution of positive and negative cloud-to-ground lightning activity for seven cases.	45
<u>Chapter 4</u>	
Table 4.1 List of sensitivity studies and results.	144

A Study of Positive Cloud-to-Ground Lightning Flashes in Mesoscale Convective Systems

1. Introduction

1.1 Cloud-to-ground lightning and the electric dipole model

Cloud-to-ground lightning flashes usually lower negative charge to the earth's surface. This discharge process is conventionally referred to as a negative cloud-to-ground lightning flash. Associated with the cloud-to-ground flash is an upward electric dipole associated with the vertical separation of electric charge. The upper part of thundercloud ($T \approx -40$ °C) carries a preponderance of positive charge while the lower part of the cloud ($T \approx -20$ °C) carries a net negative charge. In addition to this main charge separation, a small pocket of positive charge is normally located at the base of the thundercloud (Uman, 1969). This model is shown schematically in Fig. 1.1.

The theoretical efforts to explain the above charge distribution generally can be divided into two categories: (1) those which emphasize the microphysical processes in which charge is generated by the interactions of hydrometeors within the cloud, followed by separation in the vertical associated with vertical air motion

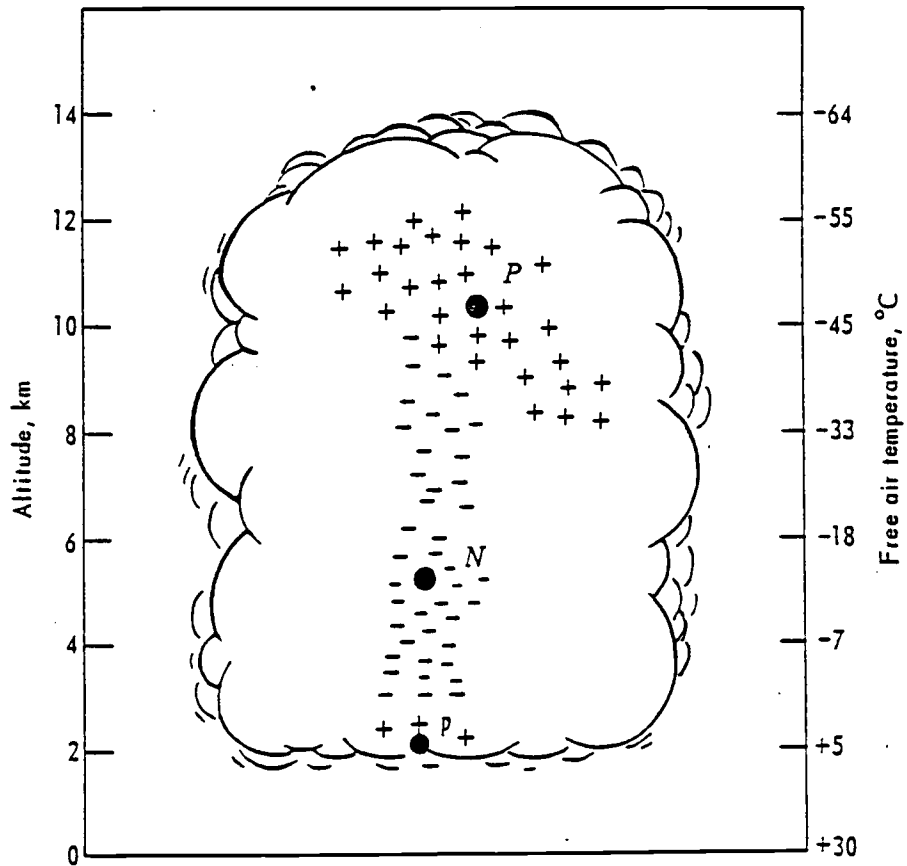


Fig. 1.1 An upward electric dipole structure indicating the probable distribution of the thundercloud charge (Adapted from Uman, 1969).

and hydrometeor fallspeeds; (2) those which emphasize the dynamical processes which redistribute and organize already existing charge. In general, there are two microphysical mechanisms considered to be important in the charge separation process. One is the non-inductive mechanism based on the thermoelectric effect, which leads to charge separation when the ice particles of different surface temperature contact. Large ice particles such as graupel and hail, whose surfaces are warmer relative to small ice particles in their vicinity due to the release of latent heat of fusion, collide with the colder ice crystals, thereby separating charge by the thermoelectric effect. The larger graupel particles acquire a negative charge and fall to the lower portion of the cloud due to their large fallspeed. The small ice crystals acquire a net positive charge and are carried upward in the strong updraft due to their small sizes (Fig. 1.2.). The thermoelectric effect also applies when a large graupel is in contact with a freezing droplet whose exterior surface is much colder than its interior surface, and fractures it into several fragments (Fig. 1.3.).

In the inductive mechanism, the existing in-cloud electric field leads to the polarization of hydrometeors within the cloud as shown in Fig. 1.4. When the polarized particles collide and rebound from one another, the lower particle (being small in mass) retains a net positive charge and moves upward, whereas the upper particle (graupel and hail) retains a net negative charge and settles to lower portions of the cloud.

One of the challenges to this dipole model is the occurrence of positive cloud-to-ground lightning flashes, which lower positive charge to earth's surface. The study of positive cloud-to-ground flashes in Mesoscale Convective System is the focus of this thesis.

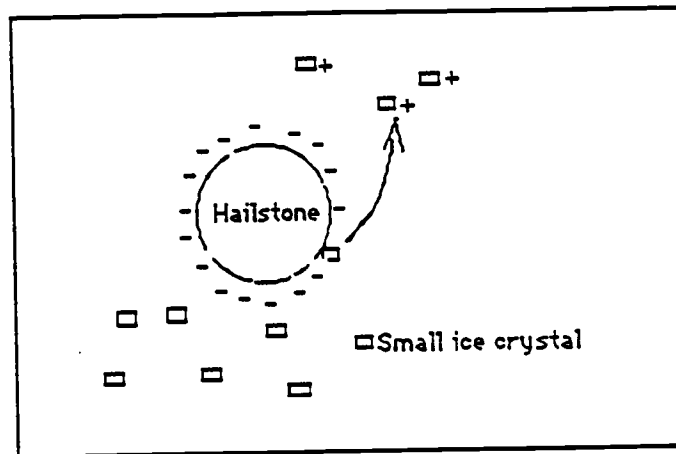


Fig. 1.2 Charge separation due to the collisions between hailstone and small ice crystal of differing surface temperatures.

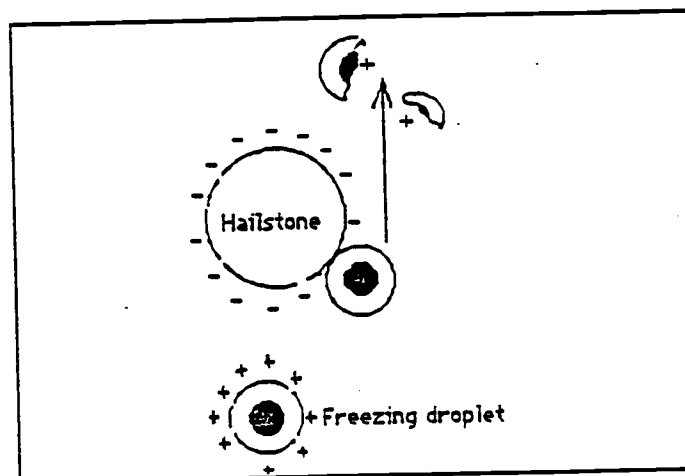


Fig. 1.3 Charge separation due to collisions between hailstone and freezing droplet.

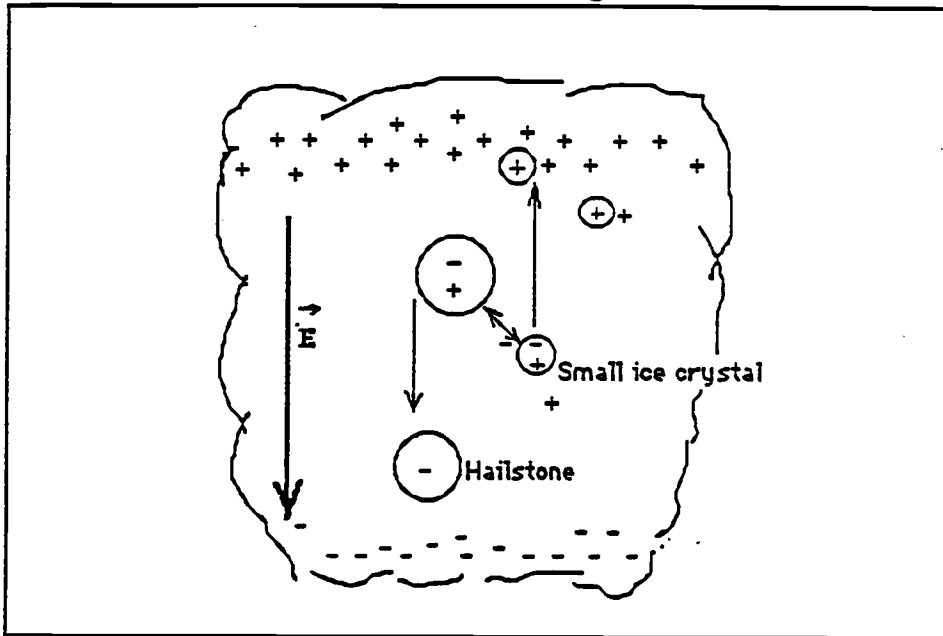


Fig. 1.4 Inductive charging process.

1.2 Previous studies

Positive cloud-to-ground lightning has been reported and studied for more than 70 years. The earliest study was conducted by Wilson (1914) in Britain by using the field change to infer the existence of positive ground flashes, while the earliest observations of positive cloud-to-ground lightning flashes through current experiments were carried out by Berger (1935) in Switzerland, Rokkaku and Katch (1936) in Japan and Stekolnikov and Lamdon (1937) in the Soviet Union. However, studies of positive cloud-to-ground lightning were slowly paced in the early days due to the limitation of the technology. A general review and evaluation of those studies can be found in Beasley (1985).

Beginning in the 1970's, with the rapid development of instrumentation to provide more precise observations of positive cloud-to-ground lightning activities with higher spatial and temporal resolution, more attention was given to ground flashes that lowered positive charge to the earth's surface. Rakeuti et al. (1973) reported interesting observations of positive ground discharges in winter storms in Japan. Brook et al. (1982) studied lightning activity that lowered the positive charge to earth, and they found those discharges often exhibited large continuing currents (exceeded 10^4 A) for periods up to 10 ms. They also found a strong correlation between the occurrence of positive cloud-to-ground lightning flashes and vertical wind shear, and hence suggested that the occurrence of positive cloud-to-ground lightning was a consequence of the vertical shear in the horizontal wind field. Following this conjecture, they proposed a tilted electric dipole hypothesis. A

threshold shear value of $1.5 \text{ m s}^{-1} \text{ km}^{-1}$ was found to be necessary for the occurrence of positive cloud-to-ground lightning flashes. In the tilted dipole model (shown in Fig. 1.5) the vertical wind shear facilitates the transport of positive charge at upper levels in the thundercloud away from the convective tower, thus allowing the positive charge center to move from a position directly above the negative charge center to a position downshear. In response to the horizontal transport of positive charge, negative charge were induced at the earth's surface, thus possibly leading to cloud-to-ground flashes that lower positive charge. Idone et al. (1984) presented an observation of positive cloud-to-ground lightning that was accompanied by a vertical wind shear of $3 \text{ m s}^{-1} \text{ km}^{-1}$, in agreement with the work of Brook et al. (1982).

Rust et al. (1981) studied positive cloud-to-ground lightning in severe storms and found prominent temporal and spatial features of the positive cloud-to-ground lightning flashes. Positive cloud-to-ground flashes usually appeared in the mature stage of severe storms, and nearly all of the flashes to ground from the downshear anvil and well away from storm tower were positive. In view of these observations, they contemplated whether positive cloud-to-ground lightning flashes are a function of internal dynamics in severe storms or of the general environmental shear in which severe storms normally.

Fuquay (1982) used electric field change data to have made positive cloud-to-ground lightning records from 48 thunderstorm days over three consecutive summer seasons in the northern Rocky Mountain region. In his study, the general electrical characteristics of positive cloud-to-ground lightning were discussed such as the single return stroke, continuing current, and typical duration time. Furthermore he concluded that positive CG flashes usually occurred within the final 30 min. of storm lifetime.

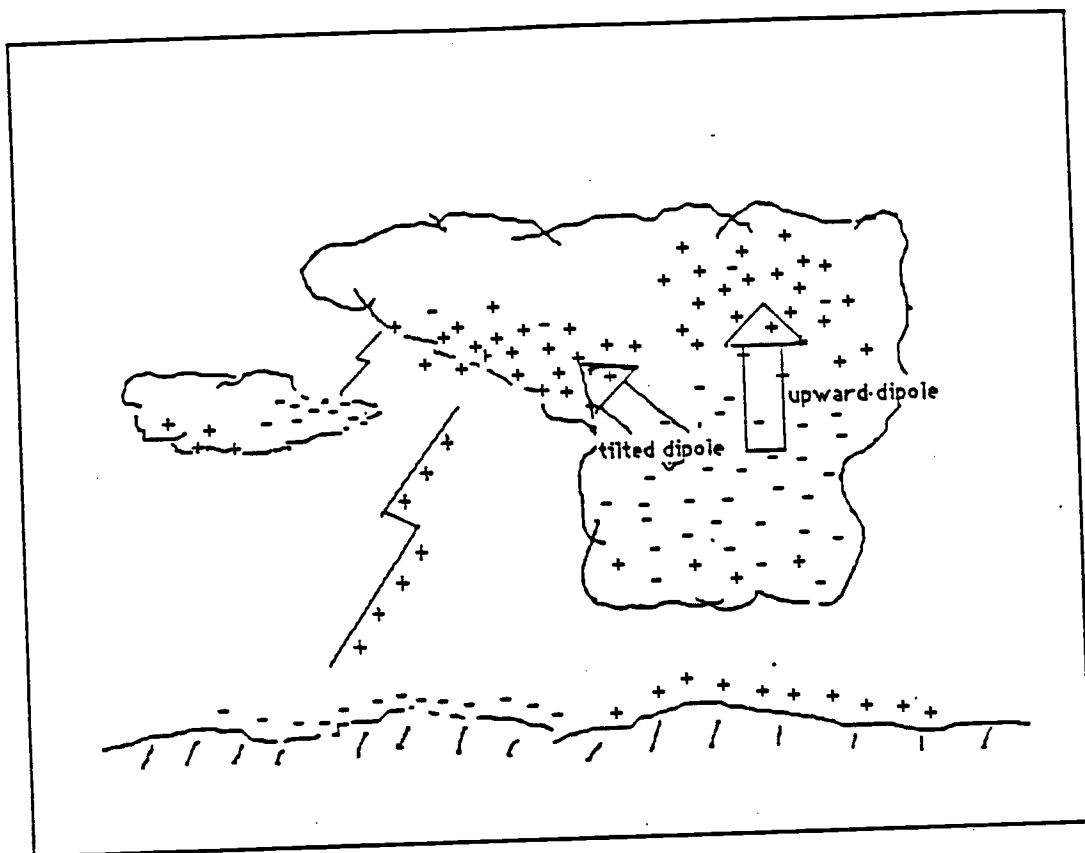


Fig. 1.5 Tilted dipole model.

The most extensive study of cloud-to-ground lightning activity associated with mesoscale convective systems to date was done by Goodman and MacGorman (1986), who analyzed cloud-to-ground lightning locations in conjunction with satellite data for 10 MCSs. Their analysis showed that the CG lightning locations tended to occur most frequently beneath the coldest cloud tops as determined by satellite IR imagery. Lightning flash rates typically exceeded 1000/hr over a several hour period from an individual MCS. They concluded that MCSs are one of the most prolific lightning producing weather systems that occur in the United States. In their study, however, they were not able to specify the polarity of the flashes, nor did they characterize the lightning flash rate and location by storm organization.

Following Goodman and MacGorman's work, Holle et al. (1988) made a statistical study on the lightning activity in mesoscale convective systems based on the data acquired during the PRE-STORM program in 1985 (this is also the data base which is to be used by our study). Their study analyzed both positive and negative CG flash rates with storm structure, e.g. the convective and stratiform radar echoes, and the relation to the areal rainfall in convective and stratiform regions. They found that negative flashes in convective core areas are the dominant category of flashes (about 62% of negative flashes were in convective echoes and 38% in stratiform echoes). Positive flashes were more frequently in stratiform (59%) than in convective echoes (41%). Negative flashes tended to peak about an hour earlier in convective areas than in stratiform areas. Ratios of negatives to positives in convective regions were usually higher than in stratiform regions, especially earlier in the storm life.

The most recent work on MCS lightning activity was done by Rutledge and

MacGorman (1988). They examined the lightning activity in a squall line storm accompanied by a trailing region of stratiform rain during the Oklahoma-Kansas PRE-STORM PROJECT in May-June 1985 (the 10-11 June case). Their results showed that the majority of the negative cloud-to-ground lightning flashes were located in the convective precipitation region, in agreement with Holle et al. (1988). The frequency of negative CG lightning flashes was highest around the period of most intense convective rainfall, while the positive CG flashes were mainly confined to the trailing stratiform region. A correlation between the areally integrated stratiform precipitation and the frequency of positive CG flashes was also found. The observed lag time between the maximum convective rainfall (and the maximum frequency of negative flashes), and the maximum stratiform rainfall (and the maximum frequency of positive flashes) was on the order of two hours. Trajectory calculations revealed that the time required for the downward transit of ice particles from convective cells to the stratiform region was on the order of 1-2 hours, consistent with the observed lag time between maximum negative and positive CG frequencies. Based on these findings, they hypothesized that the occurrence of positive cloud-to-ground flashes in the trailing stratiform region is a result of the rearward advection of positive charge on small ice particles from the upper levels of the convective cells by the storm relative wind. However, they pointed out that the generation of positive charge in the stratiform region i.e. *in-situ* charging, may also occur through mesoscale updraft motion. Therefore, *in-situ* charging may also be as an important candidate mechanism responsible for the occurrence of positive cloud-to-ground lightning in the stratiform region. The evaluation of this *in-situ* charging process will be developed in this thesis.

1.3 Scientific background

This study is based primarily on the hypotheses raised by Rutledge and MacGorman (1988) that the occurrence of positive cloud-to-ground lightning is due to the rearward advection of positive charge from the convective cells into the stratiform region by the storm relative front-to-rear flow, or the charging process can alternatively be realized through microphysical processes generated by the mesoscale updraft, embedded in wide spread region of stratiform precipitation, characteristic of Mesoscale Convective System (MCS).

A MCS is broadly defined as a precipitation system that has a horizontal scale of 10-500 km and contains significant convection during some part of its lifetime. Our present understanding of this system can be summarized by the conceptual model shown in Fig. 1.6 of Smull and Houze (1985). The dynamical features of this model indicate a front-to-rear relative flow at mid-levels extending from the convective cell region rearward into the stratiform region. Below this front-to-rear flow is a low-level rear inflow jet that enters the system from the rear at mid-levels and descends into the region of the convective cells. Mesoscale upward motion in the stratiform cloud and mesoscale subsidence between the base of the stratiform cloud and the surface are also present. Smull and Houze (1987) suggested that the front-to-rear flow was responsible for spreading ice particles, which were produced in the convective cells, rearward into the stratiform region. Rutledge and Houze (1987) confirmed this hypothesis by using a two-dimensional, diagnostic cloud model. They showed that the location of the most intense stratiform rainfall is

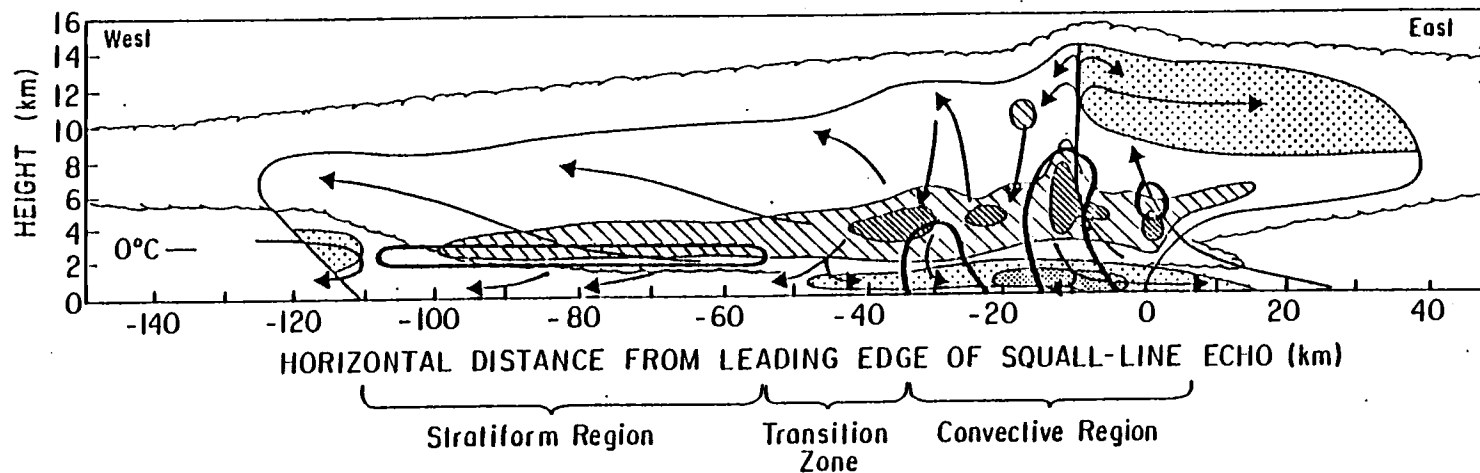


Fig. 1.6 Conceptual model of the mature 22 May 1976 Oklahoma squall-type MCS viewed in a vertical cross section oriented normal to the convective line, based in part on dual-Doppler radar observations. Outermost, scalloped line marks extent of cloud. Outermost solid contour marks boundary of detectable precipitation echo, while heavy solid lines enclose more intense echo features. Stippling indicates regions of system-relative horizontal wind directed from rear to front (left to right); darker stippling represents stronger flow. Elsewhere within echo, relative flow is from front to rear (right to left). Maximum front-to-rear flow at middle and upper levels is show by hatching (from Smull, 1986).

explained by the rearward movement of ice particles initiated in the convective cells. The Rutledge and MacGorman (1988) hypothesis for positive cloud-to-ground lightning flashes follows from this hydrometeor transport argument.

The microphysical charging process involving the interactions between small ice crystals and rimed ice particles in the presence of supercooled water were discussed by Jayaratne et al. (1983) and Saunders and Jayaratne (1986). Their laboratory results indicated that the electrical charge separation was made when the ice crystals and supercooled water droplets collided with a soft-hailstone target. The charge transfer due to the impact was a function of temperature, liquid water content, relative velocity and crystal sizes. In general, there existed a charge transfer reversal temperature; at warmer temperatures the ice target charge positively and at colder temperatures, negatively. This mechanism requires only small liquid water contents, such as those that may be present in stratiform regions of MCSs. For example, the experimental data showed that when liquid water content was only 0.06 g m^{-3} , with temperature -4° C , the charge transfer due to separating ice particle collisions was about 0.2 fC. With a liquid water content of 0.11 g m^{-3} and inverse temperature of -20° C , when given a temperature of -12° C , the charge transfer increased to 1.0 fC. To extrapolate the laboratory results above to atmospheric conditions, Gardiner et al. (1985) parameterized the charge transfer per graupel-ice separation as:

$$\delta q = k D_I^m \Delta V^n (LWC - LWC_c) f(\tau)$$

where k is a proportionality constant, D_I the diameter of small separating ice crystals, $\Delta V = V_G - V_I \propto D_G^{0.77}$ the relative impact speed with graupel size of D_G , LWC_c

is a critical value of liquid water content (LWC), and $\tau \equiv T - T_0$ with $T_0 = 273\text{K}$. Gardiner et al. used a cubic expansion for $f(\tau) = a\tau^3 + b\tau^2 + c\tau + d$.

With assumptions of $\text{LWC} = 1 \text{ g m}^{-3}$, $\text{LWC}_c = 0.1 \text{ g m}^{-3}$ and $T = -10^\circ \text{C}$, they obtained a relation of charge transfer δq versus differential fall speed ΔV , graupel size D_G and ice crystal size D_i . The results for δq are quite significant. For example, given a fallspeed $\Delta V = 100 \text{ cms}^{-1}$ for graupel size $D_G = 1000 \mu\text{m}$, charge transfer was up to 100 fC. This value is substantially larger than laboratory measurements presented by Saunders and Jayaratne (1986).

From these background studies, two hypotheses for positive cloud-to-ground flashes in stratiform region associated with MCS are identified; the rear movement of ice particles from the convective cells carrying positive charge (the tilted dipole model), or *in-situ* charging in the mesoscale updraft through the Jayaratne et al. (1983) mechanism. More generally, both front-to-rear flow and mesoscale updraft charging could be important in the generation of positive ground flashes. If this is the case, which candidate mechanism dominates? And is this predominance a function of time or different from storm to storm? All these questions will be addressed in the later chapters.

1.4 Research objectives

The past studies have demonstrated some of the characteristics of positive CG lightning activity associated with isolated severe thunderstorms, winter cyclonic storms, and squall lines. However, the most active and intense cloud-to-ground lightning flashes often occur in the mesoscale convective system. A single MCS can

produce one-fourth of the mean annual lightning strikes to the ground at any site it passes over during its life cycle (Goodman and MacGorman 1986). The high frequency of lightning activity in MCSs is one of the most interesting features of mesoscale convective systems. Hence, the study of positive CG lightning in this type of system is of particular significance. The main focus of this thesis is then to determine the characteristics of positive CG lightning activities associated with mesoscale convective system.

Knowing where the positive CG lightning flashes occur in a storm and the dependence of its frequency on storm life cycle is essential to gain insight into the relation between lightning and storm structure. This study, therefore, will specifically address:

- 1) the location of positive CG flashes within storms;
- 2) the behavior of positive CG flashes with storm evolution;
- 3) the quantification of charge advection versus *in-situ* charging.

Combining 1), 2) and 3) forms the general objective of this study, namely, to examine the relationship between positive CG lightning characteristics and storm structure and evolution.

1.5 Thesis organization

This study will mainly concentrate on the data analysis of cloud-to-ground lightning flashes in association with the precipitation structure of mesoscale convective systems and quantification of the *in-situ* charging mechanism. The data used for this study was obtained from the PRE-STORM program. Hence, in Chapter 2, we will briefly introduce some aspects of the PRE-STORM program.

Three components of the observational network are relevant for our study, conventional weather radar, Doppler radar and a surface lightning location network. In Chapter 3, the lightning location and radar echo data will be analyzed in six different MCS events. Comparisons will be made with 10-11 June case as analyzed by Rutledge and MacGorman (1988). Therefore, the characteristics of positive CG flashes in MCS will be revealed through these analyses. The evaluation of two different charging mechanisms, i.e., *in-situ* charging process and the ice particle advection process (tilted dipole model) will be given in Chapter 4. Finally, summarization and conclusions will be presented in Chapter 5.

2. Data sources

2.1 O. K. PRE-STORM Program

During May and June of 1985, the Oklahoma-Kansas Preliminary Regional Experiment for STORM-Central (the Oklahoma-Kansas PRE-STORM program) was conducted. This program was a cooperative research effort between the National Oceanic and Atmospheric Administration (NOAA), the National Center for Atmospheric Research (NCAR), and a number of university groups including the Department of Atmospheric Sciences at Oregon State University (OSU). This program was designed to investigate the structure and dynamics of mesoscale convective systems. It had two major goals (Cunning, 1986):

- 1) to achieve a reliable and coordinated observing system for investigating MCSs, while incorporating many new sensing systems and sensing strategies;

- 2) to collect the data necessary to conduct investigations of the origin, development, dissipation, and structure of MCSs.

A number of sensing systems, including Doppler radars, digitized conventional radars, surface mesonetwork stations, supplemental and National Weather Service (NWS) radiosondes, wind profilers, a lightning location system, satellite products, and research aircraft were brought together to collect the data necessary to begin the investigations. This network covered a broad area, mainly centering over the states of Kansas and Oklahoma. Figure 2.1 gives an overview of

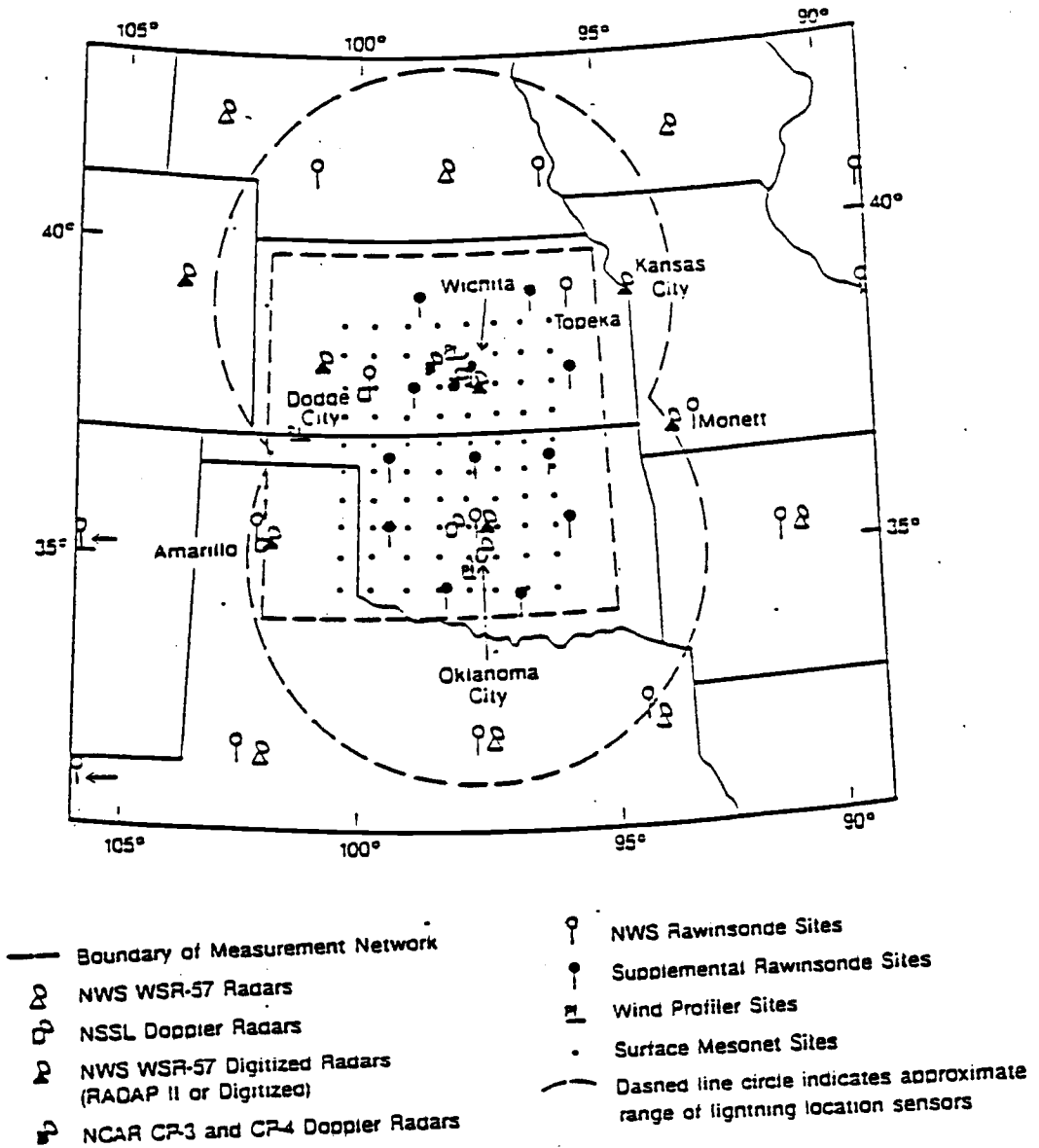


Fig. 2.1 The Oklahoma-Kansas PRE-STORM mesonetwork (Adapted from Cuning, 1986).

the entire surface observational network.

During each MCS event studied, an array of data-collecting instruments on the ground and aboard specially-equipped aircraft amassed various meteorological data, which would be analyzed following the field program.

2.2 Instrumentation used for this study

As part of the field program for the Oklahoma-Kansas PRE-STORM project, a network of electromagnetic direction-finders (DF) were used to locate and detect characteristics of the cloud-to-ground lightning flashes associated with Mesoscale Convective Systems. Besides this lightning location network deployed by NSSL (National Severe Storm Laboratory), the Wichita WSR-57 10 cm weather radar, and the NCAR CP-3 and CP-4 dual-Doppler radar network located west of Wichita will also serve as primary data sources for our study. The locations of these various components are shown in Fig. 2.2.

The lightning system consisted of seven electromagnetic direction finding stations which were located in Norman, Ft. Sill, Cordell, and Watonga, Oklahoma, and in Salina, Smith Center, and Marysville, Kansas. A central position analyzer was located at NSSL. The individual stations were equipped to identify ground flashes that lowered either polarity of charge and to process concurrent flashes that had return strokes interlaced in time, thus allowing for their positions to be determined. The cloud-to-ground lightning strokes were extracted out from background noise by characterizing their distinguished wave-form signals, thus filtering out the intra-cloud lightning flashes. Each DF station measured the

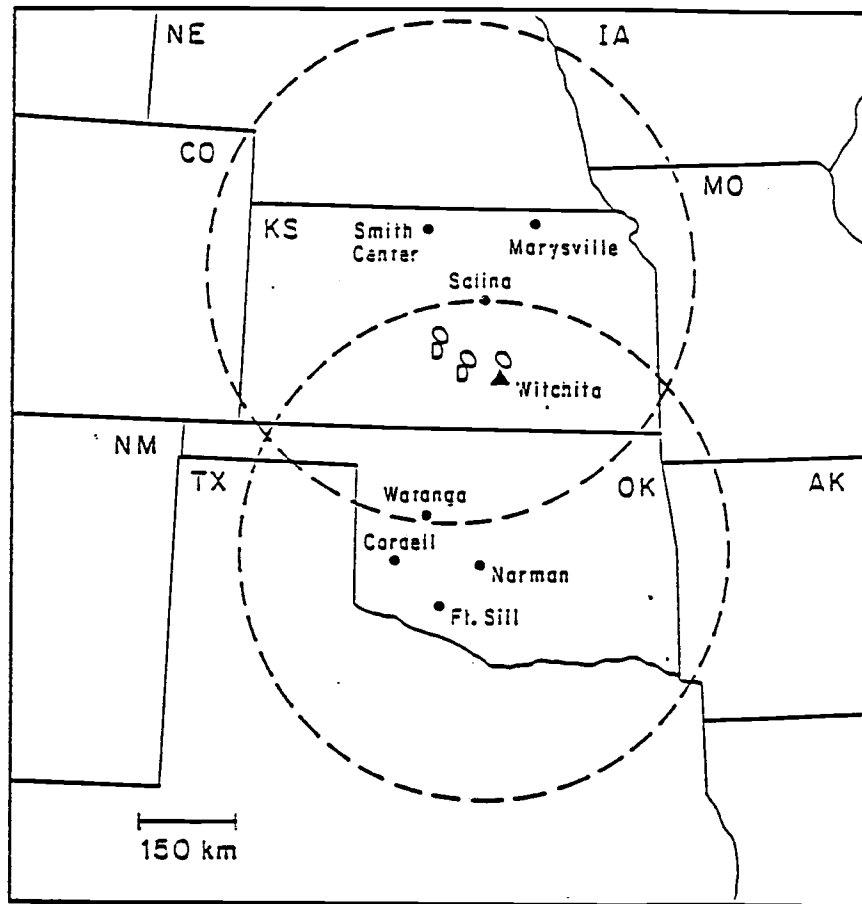


Fig. 2.2 Location of the various observational platforms used in this study (Adapted from Rutledge and MacGorman, 1988).

direction to a lightning strike and transmitted this data along with the time of the strike to a central position analyzer at NSSL. Whenever the position analyzer received coincident data from two or more stations, it triangulated from the two stations closest to a strike to calculate the strike location in real time. More detailed descriptions of this system as well as the systematic error treatment can be found in Hiscox et al. (1984) and Mach et al. (1986).

The lightning data collected included the following information: the strike time, which was specified as year, month, day, hour, min., and sec.; the strike location, which was denoted as the relative distance and direction from Wichita; the flash polarity, negative or positive; the amplitude and the average amplitude of positive flashes. In this study, however, we will only use the first three quantities.

The Wichita WSR-57 weather radar was employed to reveal storm structure as the MCSs migrated over the observational area. In this field program, a volume scan method was adopted at this radar. However, we have chosen the volume-scan data with a fixed elevation angle of 1.0° as our input. In doing so, we obtain a PPI (Plan-Position Indicator) display of the low level precipitation structure. The radar reflectivity data was quantified at each grid point with a resolution of 1 km in range and 1° of azimuth by using a digitizer from the NOAA Hurricane Research Division attached to the Wichita radar.

The NCAR CP-3 and CP-4 Doppler radars operated in a dual-Doppler mode during PRE-STORM. The horizontal as well as the vertical wind field within the mesoscale convective systems were provided by the analysis of data from this network. The NCAR CP-4 Doppler radar was located at Cheney State Park 30 km west of Wichita, and the NCAR CP-3 Doppler radar was located near Nickerson, about 60 km to the northwest of CP-4.

3. Characteristics of positive flashes in MCSs

3.1 Analysis of WSR-57 radar and lightning location data

In this chapter we investigate the characteristics of cloud-to-ground lightning activity through analysis of LLP data and storm echo patterns as revealed by the Wichita WSR-57 radar. We are most interested in the spatial distribution and temporal variation of positive CG flashes.

Lightning data indicating the position and polarity of cloud-to-ground flashes, and low-level radar echo patterns (1° elevation angle) from the Wichita WSR-57 weather radar are analyzed over a domain of $600\text{km} \times 600\text{km}$, which represents the maximum range of the WSR-57 radar. This domain size allows coverage of a large portion of individual storms, often from the developing to decaying stages. In most cases, the radar echo patterns are analyzed every half hour, with a contour interval of 10 dBZ. In this study, we define the convective region as that region enclosed by the 30 dBZ reflectivity contour, while the stratiform region will be defined as all echoes below 30 dBZ (following definitions used by Gamache and Houze, 1982). The cloud-to-ground lightning data indicated on each plot represent the accumulated number of positive and negative CG flashes respectively (over a thirty minute period), centered on the time of the radar echo pattern.

Six mesoscale convective systems experienced during May and June of 1985 in

the PRE-STORM program are analyzed in this study. Brief descriptions of these six MCSs are shown in Table 3.1. From this table we see that MCSs in the six cases are different from one another in storm structure. The case of May 28 represents a well defined squall line with a small trailing stratiform precipitation region, confined to the northern portion of the convective line. This pattern is somewhat similar to the case of June 11 (Rutledge and MacGorman 1988). The June 24 case formed as an linear system that later separated into two smaller line segments, each trailed by a small stratiform region. The case of 27 May commenced with two isolated storms merging to form a squall line accompanied by a small trailing stratiform region. The cases of 3 and 4 June represent non-linear squall lines with irregular convective patterns and surrounding stratiform regions. In the 10 June case, a group of convective cells (which remained relatively stationary) led to the formation of a small stratiform region downshear of the convective region. In general, we can loosely divide these storms into linearly organized mesoscale convective systems (Bluestein and Jain, 1985), such as storms in the cases of May 28, May 27 and June 24, and nonlinearly organized mesoscale convective systems, such as storms in the cases of June 3, June 4 and June 10. We will see in the case studies following that positive cloud-to-ground lightning activity in association with these MCSs, although of considerably different storm structure, present similar spatial and temporal characteristics, with respect to flash location and flash frequency.

Table 3.1 Overview of six cases for which radar and lightning data are analyzed.

Storm	Case description
1) 5/27/85 0300Z-1400Z	System was formed by several isolated weak convective cells around Wichita, later organized into a squall line with small trailing stratiform region. This squall line moved southeast accompanied by a surface cold front, finally dissipating in the southeastern portion of the observational area.
2) 5/28/85 0800Z-1800Z	Well defined squall line with a trailing stratiform precipitation region formed in the early morning of May 28 in Kansas. System approached radar from the northwest. A stationary front extended along the Oklahoma-Kansas border.
3) 6/3/85-2000Z 6/4/85-0600Z	A cluster of convective cells was surrounded by an extensive stratiform region. These convective cells began to organize in a linear fashion in the mature stage. A large area of stratiform precipitation resulted.
4) 6/4/85 0800Z-1300Z	MCS developed from former decaying system. Extensive convective motion embedded in large area of stratiform precipitation. This slowly moving system was associated with a relatively stationary front across central Oklahoma.
5) 6/10/85 1400Z-2300Z	MCS began to form early on June 9. A cluster of convective cells with a small leading stratiform precipitation region persisted over the radar.
6) 6/24/85 0200Z-0900Z	Monitored MCS that developed as a line type system, and approached the radar from the northwest. This MCS broke up into two squall line systems, each with trailing stratiform regions.

1) Case of May 27

Two storm systems were studied on 27 May. The first storm formed at 2300Z on 26 May, within range of the WSR-57 radar. From Fig. 3.1 (mature storm phase, 0336Z), we can see that this system was comprised mainly of two isolated storms. They were located southeast and northeast of Wichita, respectively. Each storm consisted of several convective cells surrounded by relatively small stratiform regions. Some additional weak echoes appeared at the upper left of the analysis domain (the approach of the second storm on 27 May). The cloud-to-ground lightning activity was very intense at this time. Both negative and positive flashes were nearly at their maximum frequency values with the 1057 negative and 107 positive flashes over a thirty minute period. The behavior of the cloud-to-ground lightning flashes relative to reflectivity structure was quite different in these two isolated storms. In the southeastern storm, the positive and negative flashes were intertwined, with most of the flashes contained within the two convective cells. In the storm northeast of Wichita, on the contrary, cloud-to-ground lightning flashes tended to be situated outside the cell locations, especially for positive flashes. It is interesting to note that positive CG flashes were associated with the weak radar echoes associated with the approaching squall line at the upper left of our domain; more than 12% of total positive CG flashes at this time were found in this region. The data for 0349Z (Fig 3.2) showed this system was fully developed 13 minutes after the situation discussed above, with the CG lightning frequencies reaching their maximum values of 1062 negative flashes and 114 positive flashes.

The echo patterns and lightning maps for 0431Z and 0457Z are shown in Figs 3.3 and 3.4. The basic radar reflectivity pattern remained the same as that in the

previous figures except that the intensity of each convective cell in both storms had weakened. After these times the lightning frequency of both positive and negative flashes decreased associated with the decaying convective activity. Meanwhile, the echoes at the upper left of the domain continued to develop. At 0534Z and 0604Z (Figs. 3.5 and 3.6), the system continued to decay, with the convective cells in the two isolated storms diminishing in both area and strength. A considerable number of positive ground flashes were found in the stratiform region of the decaying storms. The negative lightning frequency was reduced quite sharply at these time, while the number of positive flashes decreased more slowly.

At 0624Z (Fig. 3.7), the two formerly isolated storms had now merged together, bridged by a newly developed convective cell just east of the Wichita radar. Considerable positive cloud-to-ground lightning activity was located in the stratiform region (at upper and lower right portions of our domain). The approaching squall line northwest of Wichita continued to develop and move towards the southeast, accompanied by modest amounts of cloud-to-ground flashes. The bulk of these ground strikes were negative. At 0701Z (Fig. 3.8), an arc-shaped squall line had emerged from the approaching storm. Positive CG flashes were found along the squall line, with a cluster of positive CG flashes located just north of Wichita, or rearward of an intense convective cell (marked by the ground cluster of the Wichita radar). At 0733Z (Fig. 3.9), the approaching arc-shaped squall line was nearly merged with the eastern storm, which was entirely stratiform at this time. Associated with the development of the arc-shaped squall line, negative cloud-to-ground lightning activity began to increase again, with most of the negative CG flashes located in the vicinity of the developing convection region.

Most of positive CG flashes were found in the stratiform region left by the old system, although a small amount of positive CG activity was situated in the convective portion of the arc-shaped squall line. It is interesting to note that positive CG activity continued to be present in the eastern storm, despite the absence of convection for several hours.

The bow-like squall line accompanied by a small trailing stratiform region entered its mature stage at 0833Z (Fig. 3.11). The negative CG flashes peaked again at this time, and most of them occurred along the convective line. The positive CG flashes, compared to a half hour ago (0802Z, Fig. 3.10), continued to decrease in number. The overall cloud-to-ground lightning activity for this newly organized squall line was less intense than that for the old system of two isolated storms in the earlier periods. Almost the same situation was found at 0856Z in Fig. 3.12.

Shown in Fig. 3.13 is the radar echo pattern and lightning map at 0926Z. At this time the arc-shaped squall line was in its collapsing stage, with only weak convective activity present. The bulk of the positive lightning activity (25 out of 27) occurred in the remaining stratiform region. Most of the negative CG flashes at this time were found around the only existing convective cell located at the south leading edge.

As shown in Figs. 3.14 and 3.15, this system continued to decay as it slowly moved to the southeast. At 1055Z (Fig. 3.16), the intensity of the convective cell at the south leading edge had declined. The remaining portion of the convective line had largely decayed into stratiform rain at this time. The distribution of cloud-to-ground lightning flashes was very similar to that at 0926Z. Most of negative CG flashes appeared near the convective region, while virtually all of positive CG

flashes (18 out of 19) were situated in the stratiform region. The echo patterns and lightning maps for the later stages of this system are shown in Figs. 3.17 to 3.18, covering the period of time from 1124Z to 1200Z. This system gradually dissipated during this time period, accompanied by declining lightning activity.

2) Case of May 28

On 28 May 1985, a squall line with a trailing stratiform precipitation passed over the PRE-STORM study area. At maturity, this system was accompanied by a relatively small stratiform region, that contained a well-defined mesovortex circulation at mid-levels. This system began to form at 0700Z northwest of Wichita, and moved southeast toward the Wichita WSR-57 radar.

At 0858Z (Fig. 3.19), this system was still in its developing stage. An elongated convective region (> 30 dBZ) was embedded in a stratiform region. The negative cloud-to-ground lightning flashes were also distributed along the convective line. There were 347 negative and 8 positive CG flashes over the half hour period. The positive CG flashes, although very small in number, were distributed primarily behind the convective line in the stratiform region. A similar situation was seen at 0932Z (Fig. 3.20).

The radar echo pattern and cloud-to-ground lightning map at 1008Z is shown in Fig. 3.21. The frequency of negative CG flashes steadily increased as the convective cell intensified. The positive CG flashes exhibited no response to this intensification of the convection, as only 8 positive flashes occurred at this time period, which was identical to the previous 30 min. period. Most of the positive CG

flashes were again however found in the stratiform region. From 1038Z to 1106Z the squall line intensified further and a strong convective region (> 40 dBZ) could easily be identified (Figs. 3.22 - 3.23). During this time period the stratiform region continued to expand, accompanied by a slight increase in positive CG activity.

The radar echo patterns and lightning maps for the period from 1136Z to 1232Z are shown in Figs. 3.24 - 26. At this time, the squall line continued to intensify as it passed over the Wichita radar site. The number of both positive and negative CG lightning flashes steadily increased during this period. Most of the negative CG flashes were confined to the convective region along the leading edge of the convective line, while the positive CG flashes were more prominent in the stratiform region.

Between 1356Z and 1428Z, shown in (Figs. 3.27 - 28), the squall line system reached its most intense stage. From these figures we can see that the strong convective cells (> 40 dBZ) extended over a large area and the cloud-to-ground lightning activity was most intense at this time. For example, at 1428Z, both the negative and positive CG flashes reached their peak frequencies, with 1084 negative flashes and 45 positive flashes during this 30 min. period (from 1413Z to 1443Z). The negative ground flashes were located in or around the vicinity of the convective cells, while most positive CG flashes were either located right behind the convective line, or in the stratiform precipitation region. Evidently the positive flashes immediately behind the convective line originated in the upper-level trailing anvil cloud, but in a region devoid of surface rainfall. This pattern and behavior of cloud-to-ground lightning activity is similar to the pattern found in the 10 - 11 June case studied by Rutledge and MacGorman (1988). Their case was similar to the 28 May storm, with both systems consisting of a line of convective cells accompanied by a

trailing stratiform region. The main difference between the two cases is that the 10 - 11 June case had a much more extensive stratiform region. This led to a significant difference in temporal characteristics between the two systems, as will be discussed in more detail in the next section. Although the stratiform region for the 28 May case was less areally extensive in comparison to the 10 - 11 June case, peak positive CG frequencies were similar (45 for 28 May, 55 for 10 - 11 June). This result suggests that the positive CG frequency in stratiform region associated with MCSs may not be areally dependent, i.e., correlated to the area covered by stratiform precipitation.

Fig. 3.29 and 3.30 show the radar echo patterns and lightning maps at 1456Z and 1528Z. Around this time the squall line had entered its collapsing stage, as both the strength and areal coverage of the convective region had diminished. The stratiform precipitation did not show much change during this period. Accompanying the dissipation of the system, the number of both positive and negative cloud-to-ground lightning flashes decreased. Unlike the pattern in the 10 - 11 June case presented by Rutledge and MacGorman (1988), there was no distinctive time lag between the maximum value of positive and negative CG flashes in this case. In the 10 - 11 June case, Rutledge and MacGorman found that the peak flash frequencies for negative and positive flashes were separated in time by two hours. They suggested that ice particle advection from the convective region to the stratiform region led to this time lag, thus implying that positive charge was carried rearward into the stratiform region by this flow. This relationship is not seen in the 28 May case.

Further dissipation of the storm echo pattern and the lightning activity is

indicated in Figs. 3.31 - 35, spanning the period from 1554Z to 1752Z. In this period the convective cells died out and weakened. Part of the "dissipation" of this storm is associated with movement beyond the range of the radar.

3) Case of June 3

This storm formed in the late afternoon, west of Wichita. Significant new convective activity rapidly developed from the remains of a dissipated storm system. At 2155Z (Fig. 3.36), newly developed convective cells began to organize linearly to the west of Wichita. The weak echoes to the east of Wichita were associated with a weakening storm. As the new system developed, cloud-to-ground lightning activity was triggered. At this time however, the positive and negative CG flashes were located together, randomly distributed in both convective cells and surrounding stratiform regions.

The echo patterns and lightning maps for the 2234Z and 2258Z periods are shown in Figs. 3.37 - 38. The strength and areal coverage of both convective and stratiform precipitation regions had considerably increased at this time, marked by intense lightning activity. Both positive and negative CG flashes reached their maximum values (773 negatives flashes and 88 positive flashes) at 2258Z (Fig. 3.38). It should be noted that a few lightning flashes were contributed to this maximum value by the dissipated weak echoes to the east of Wichita, associated with reflectivities below the contour threshold. The positive and negative CG flashes were located together and no organized pattern could be recognized, although many of the positive CG flashes could be found in the stratiform region (northern half of

the echo pattern). A significant number of positive flashes were located in or in the near vicinity of the convective cell at the south end of the storm. This situation also occurred in the May 27 case. Overall the 3 June case did not show much distinctive spatial or temporal behavior of cloud-to-ground lightning activity relative to storm structure as compared to the June 10 - 11 case (Rutledge and MacGorman, 1988). One reason may be that the storm structure in the two cases are quite different, this case forming in a low shear environment promoting only weak organization, whereas the 10 - 11 June case formed in moderate shear, leading to squall line organization.

For the period from 2327Z of June 3 to 0017Z of June 4 (Figs. 3.39 - 41), intensification of convective cells along a north-south line directly west of Wichita took place. The northern portion of the storm was weakly convective to stratiform. Considerable number of positive flashes occurred during this time period. The positive flashes were situated in two regions; in the new convective area, and within the expanding stratiform region. The location of positive flashes in the stratiform region, and their increase in number as the system matured, is similar to the behavior seen in the 10 - 11 June case (Rutledge and MacGorman 1988). A similar pattern was observed at 0105Z (Fig. 3.42).

For the period from 0140Z to 0337Z (Fig. 3.43-47), a rather similar pattern prevailed. However during the latter portion of this period, the convective activity east of Wichita weakened considerably. The area of stratiform precipitation to the north and east continued to be associated with positive ground flashes. The number of negative and positive CG flashes decreased rather slowly during this time period, associated with the general weakening of the storm echo pattern.

Further storm dissipation and decreased lightning rates (probably partly due

to movement off the grid) were observed during the period from 0355Z to 0504Z (Figs. 3.48 - 50).

4) Case of June 4

Within a few hours after the previous storm dissipated, numerous convective elements began to develop in the vicinity of Wichita. This storm was the third in a sequence of three Mesoscale Convective Complexes that developed within a 24-hour period in central Kansas. The synoptic pattern was dominated by weak upper level flow (low shear) and abundant low-level moisture. Significant convective activity was present at 0755Z (Fig. 3.51), accompanied by considerable amounts of lightning CG flashes. The convective cells were randomly distributed and embedded in larger stratiform regions, similar to the previous case (characteristic of weak shear storm). Although the lightning activity appeared less organized, the positive cloud-to-ground lightning flashes occurred more frequently in stratiform regions than in convective cells (Figs. 3.51 - 52).

At 0856Z (Fig. 3.53) the system had intensified. Associated with the strengthened convective regions, the number of negative cloud-to-ground lightning flashes steadily increased. Most of the negative CG flashes were located in the regions where the convective cells were most intense. Positive cloud-to-ground lightning flashes, on the other hand, slightly decreased in number from the previous period, and were situated away from the convective regions. The same situation was found at 0934Z and 0952Z (Figs. 3.54 - 55), although the convection appeared to have intensified somewhat. Over 1000 negative CG flashes occurred during the 30 minute period centered on 0934Z. The relatively small number of

positive CG flashes were again situated around the periphery of the stratiform region.

By 1031Z (Fig. 3.56), the strength of the convective cells had diminished, accompanied by a decrease in the number of negative CG flashes. Meanwhile, the number of positive CG flashes continued to increase slightly, and were situated in the stratiform precipitation area to the rear of the storm.

At 1102Z (Fig. 3.57), the number of positive cloud-to-ground lightning flashes increased sharply to a maximum value of 55 over the thirty minute period centered on 1102Z. In this storm a rather distinct time lag between the times associated with maximum negative and positive CG activity is evident (approximately 1.5 hours). This is similar to the 10-11 June case discussed by Rutledge and MacGorman (1988), where a time lag of about two hours was observed. It is worthy of mention that similar time lags were observed for these two cases, despite considerably different radar echo patterns. Furthermore, the separation in the location of positive and negative CG flashes were very pronounced for both cases. Most of the positive ground flashes occurred in the stratiform regions associated with these storms, while most of the negative ground flashes occurred in the vicinity of the convective cells. This observed separation is clearly indicated at 1127Z (Fig. 3.58).

The dissipating stage of this storm, for the period from 1154Z to 1258Z, is shown by Figs. 3.59 - 61. For these times the echo patterns and lightning maps still revealed distinctive spatial distribution, although the number of negative and positive CG flashes both decreased.

5) Case of June 10

Our analysis on this storm starts at 1429Z of June 10 (Fig. 3.62). This storm, at early stages, consisted of an area of weak convection precipitation southeast of Wichita. A region of stratiform precipitation was located west of the convection. This stratiform region was associated with an earlier storm that dissipated in this region. The cloud-to-ground lightning activity associated with this echo pattern was quite distinct (Fig. 3.62). Most of the negative CG flashes were located in the region of developing convection. The positive CG flashes were mainly situated in the stratiform region, although a few positive flashes were interspersed among the convective cells. As was the case for the 27 May storm, we again see numerous positive CG flashes situated in stratiform precipitation, devoid of convective activity for several hours.

The echo pattern and lightning map for 1505Z is shown in Fig. 3.63. At this time, the CG frequency for both negative and positive flashes had decreased. Most interesting is the two-fold decrease in positive CG flashes in the decaying stratiform region.

At 1557Z (Fig. 3.64), new convection developed leading to an expansion of the system in a northward direction. It is interesting to note that downshear of the convection zones both positive and negative CG flashes were present. A similar pattern occurred at 1629Z (Fig. 3.65). The distinct line of positive CG flashes seen at 1629Z (Fig. 3.65) formed about two hours after the convection initiated, which is again like the "lag times" seen in other cases (4 June, 10-11 June).

The dissipation stage of this storm, along with a decrease in CG flash rate, is

shown by the series of maps in Figs. 3.66 - 69. Early in this time period we see the collapse of the distinct line of positive flashes, followed by a general weakening of the storm echo patterns and decrease in total lightning rates. It is also interesting that the small stratiform region situated to the north and east of Wichita (e.g. Fig. 3.68) was not characterized by positive CG activity with any appreciable frequency.

6) Case of June 24

Late on 23 June a squall line approached the Wichita radar from the northwest. At 0205Z of 24 June (Fig. 3.70), the reflectivity pattern indicated this system consisted of two rather short squall line segments, each accompanied by a small trailing stratiform region. The cloud-to-ground lightning pattern was complicated with no pronounced distribution features. The number of negative CG flashes totalled 362, with 31 positive flashes at this time. The CG lightning activity for both negative and positive flashes reached their maximum values thirty minutes later at 0236Z (Fig. 3.71) with the number of negative ground flashes reaching 584 and the positive 47.

The system split into two short squall segments near 0306Z (Fig. 3.72). Each of these storms was accompanied by stratiform precipitation. The echo pattern for one of the storms, located west of Wichita, consisted of a major and a minor convective cell trailed by a stratiform region. Associated with the major cell, whose radar reflectivity exceeded 40 dBZ, was a significant number of negative CG flashes. Relatively few negative CG flashes were located near and within the minor cell. The positive CG flashes were located in the stratiform region immediately behind the two convective cells, again exhibiting a line-like pattern parallel to the convective

line. The echo pattern for the second storm, located northeast of Wichita, appeared as a relatively weak convective line trailed by a stratiform region. In this storm, the distribution of lightning flashes revealed a less distinctive feature as in the other storm. Almost the same situation was found at 0339Z (see Fig. 3.73). The total CG lightning flashes began to decline in number at this time.

At 0407Z and 0437Z, shown in Figs. 3.74 and 3.75, both storms had diminished in intensity, as indicated by radar reflectivity returns. The storm to the west of Wichita had only one weak convective element at this time. Most of the negative CG flashes were found in this convective region, while most positive CG flashes occurred in the stratiform region. In the storm located northeast of Wichita, some negative CG flashes occurred in the two convective cells, which the stratiform region contained both negative and positive ground flashes. The lightning frequency decreased sharply at this time.

The system continued to decay as indicated in Fig. 3.76 for 0500Z. The total number of cloud-to-ground lightning flashes decreased further although the positive CG flashes slightly increased in number. At this time, both storms showed the same distribution pattern of lightning activity. The positive and negative CG flashes were separated in locations in association with the dissipating convective and stratiform regions respectively.

Fig. 3.77 shows radar echo pattern and lightning map for time 0529Z. The positive cloud-to-ground lightning flashes peaked again at this time, totaling 39, in association with the dissipation of the western system. Problems with the radar prevented reflectivity data from being obtained in the eastern storm.

The collapsing stage for both storms from 0601Z-0746Z is shown in Fig. 3.78 -

79. During this period the number of lightning flashes steadily decreased, and the distribution pattern for both positive and negative CG flashes became less distinct due to the small sample of lightning flashes.

3.2 Characteristics of positive flashes

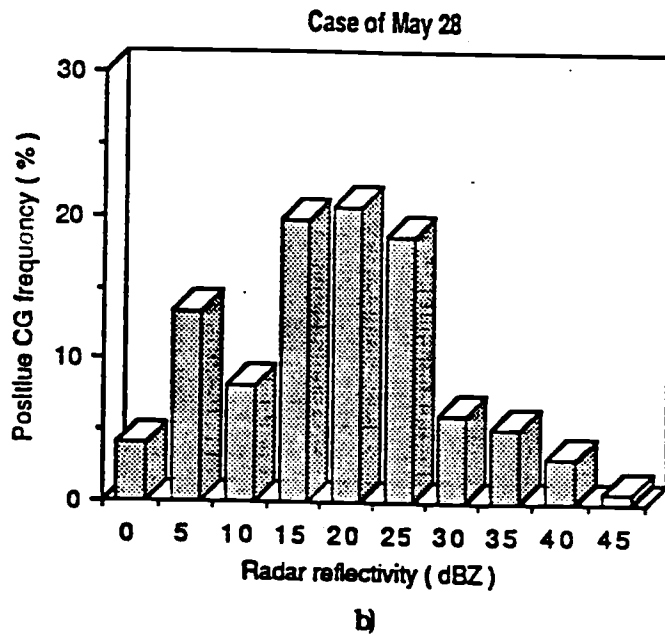
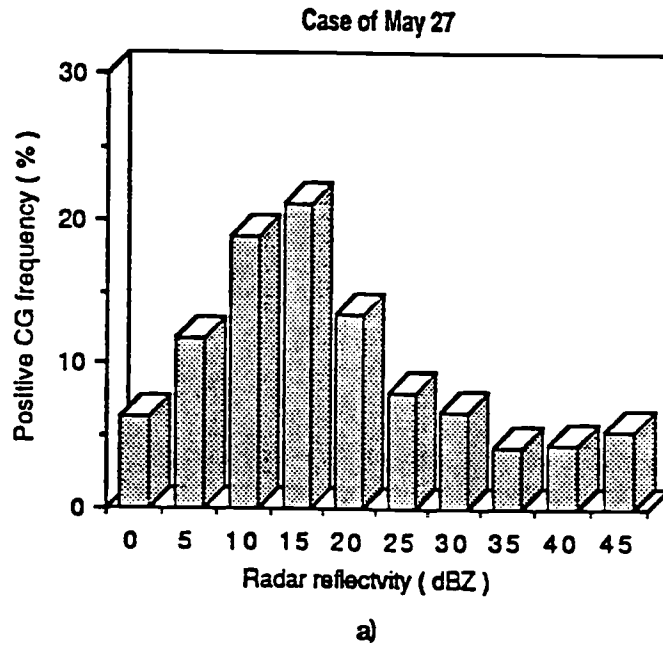
1) Spatial characteristics

In the previous section we analyzed the cloud-to-ground lightning data in conjunction with storm structure for six different MCS events. From these case studies, a general picture of the nature of the positive cloud-to-ground flashes is presented. One pattern that emerges is the high percentage of positive cloud-to-ground lightning flashes that occur in stratiform precipitation. Evidence for this characteristic exists in all seven MCS events in various degrees (including the case of June 11 studied by Rutledge and MacGorman, 1988) despite considerably different storm echo patterns (storm structure). To gain better insight, we examined the location and frequency of positive cloud-to-ground lightning flashes as a function of radar reflectivity (Fig. 3.80). From these figures we can see that the distributions of positive CG flashes among these seven cases have a rather similar Gaussian distribution. This indicates that there exists a preferential reflectivity area where positive cloud-to-ground lightning flashes are most likely to occur in MCSs.

The June 11 case consisted of a well defined line of convection and a large area of trailing stratiform precipitation. In this case, the largest number of positive CG flashes occurred in a narrow band of reflectivity centered around 15 to 20 dBZ (Fig.

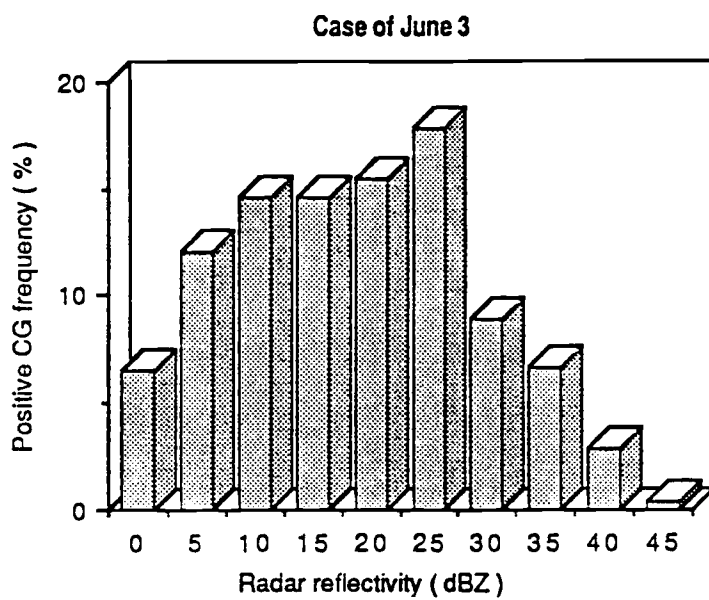
3.80 f). Ten reflectivity categories were used ranging from 0 to 45 dBZ, with intervals of 5 dBZ. A similar distribution of positive CG flashes relative to radar reflectivity is shown in the June 24 case (Fig. 3.80 g). Both the June 11 and June 24 cases are linearly organized systems. In the June 24 case, the original convective system split into two storms, each consisting of a convective line at the leading edge and a stratiform region to the rear. In the May 28 case, as we described in the previous section, there was a well defined convective line, but only a small trailing stratiform region formed. Therefore, a large percentage of positive flashes occurred immediately behind the convective line, which leads to broadening of the flash percentage-reflectivity distribution. Positive cloud-to-ground lightning flashes occupied an even broader reflectivity range in the cases of 3 and 4 June (Figs. 3.80 c, d). For these cases, positive CG flashes in the range from 5 to 25 dBZ contributed significantly to the total amount of positive cloud-to-ground lightning activity. This may be attributable to the storm organization in these cases, which were highly nonlinear MCSs. These results suggest that in linear systems, positive CG flashes tend to be arranged in a rather linear manner. In non-linear storms, the positive flashes do not show a preferred tendency towards organization, with the exception that the bulk of them are situated in regions of modest reflectivities (< 30 dBZ).

Our calculations show that 87% of the total positive cloud-to-ground flashes in the cases of the June 3 and June 4 occurred in the stratiform region, while 13% occurred in regions of convection. These results are consistent with those found by Holle et al. (1988). Their results showed that the positive CG flashes occurred more frequently in stratiform regions (59%) than in convective regions (41%). The

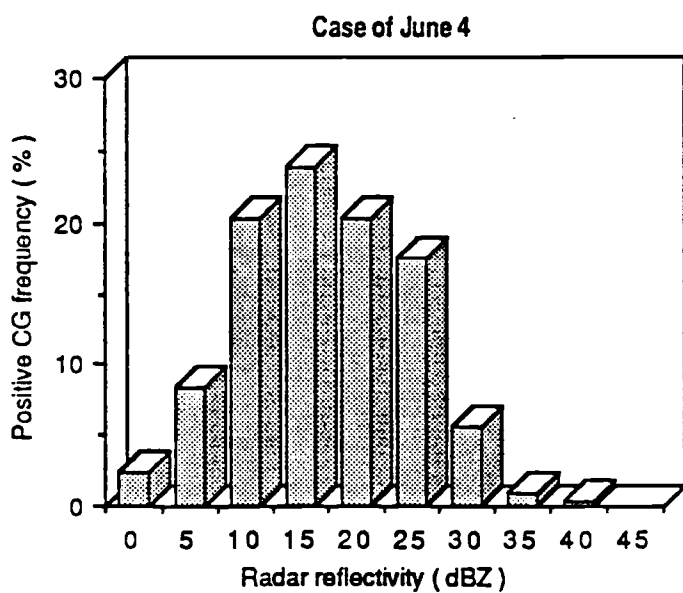


Statistic Fig. Frequency distributions of positive CG flashes with measured radar reflectivities.

a) 27 May 1985 case; b) 28 May 1985 case;



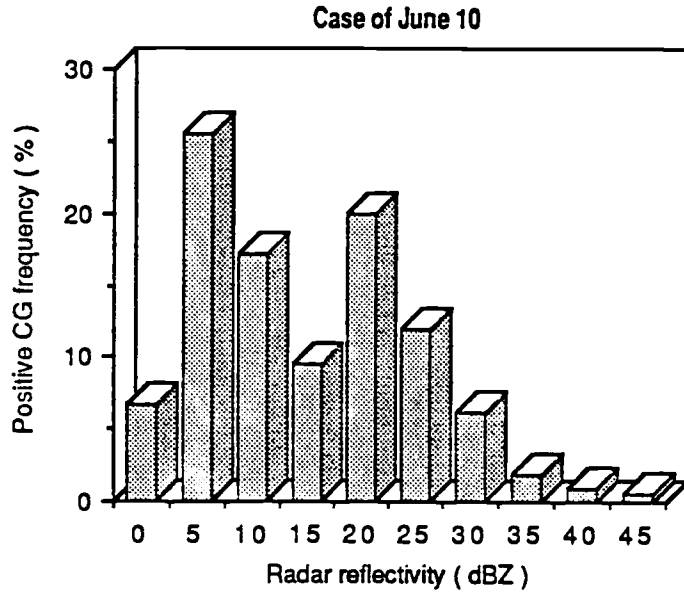
c)



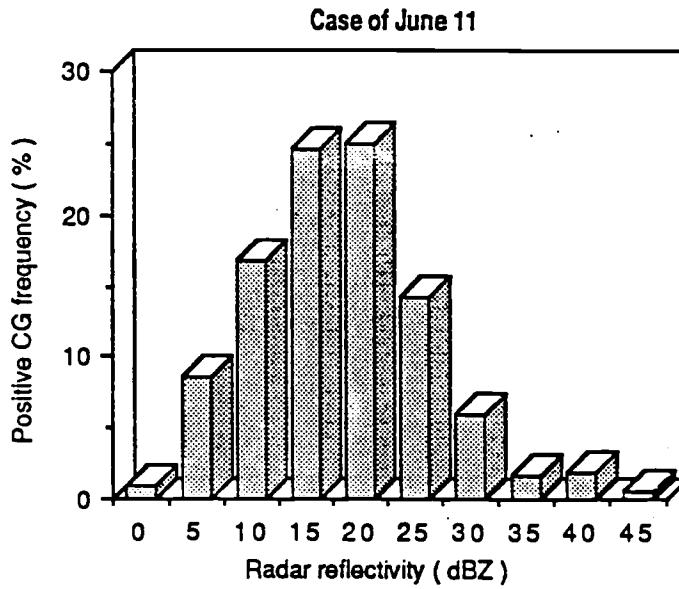
d)

Statistic Fig. continued

c) 3 June 1985 case; d) 4 June 1985 case;



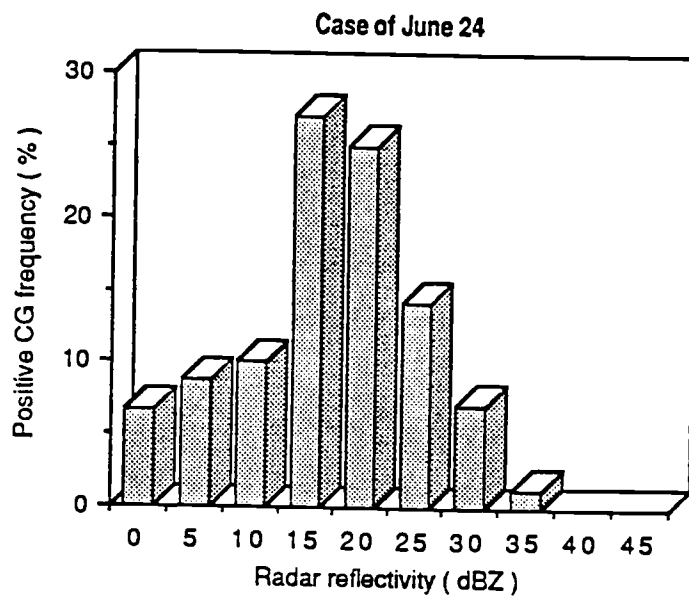
e



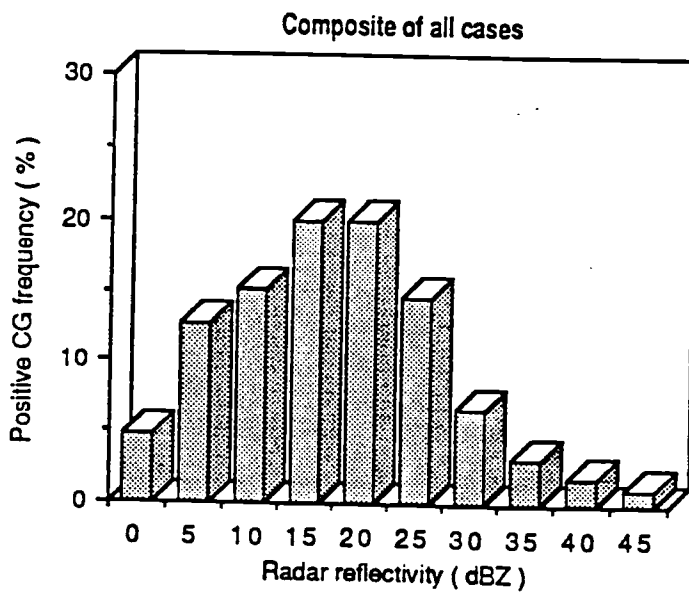
f

Statistic Fig. continued

e) 10 June 1985 case; f) 11 June 1985 case;



g)



h)

Statistic Fig. continued

g) 24 June 1985 case; h) Composite statistics for all cases.

June 11, the positive cloud-to-ground lightning flashes tended to peak during the storm dissipating stage. In the case of June 24, like the May 27 case, positive flash frequency peaked twice. From Fig. 3.72 and Fig. 3.78, we see that maximum positive flash frequency occurred at storm mature stage (0236Z) and dissipating stage (0529Z) respectively.

To examine the evolution of positive CG flashes in association with storm development in more detail we adapted the method used by Rutledge and MacGorman (1988) to plot the time sequence for cloud-to-ground lightning flashes both for positive and negative flashes, along with the time sequence for areally integrated precipitation amounts both for convective and stratiform components of the storm for the case of May 28. The analysis covers the time period of 1008Z-1659Z. Empirical relations between the radar reflectivity (dBZ) and precipitation rate (mmh^{-1}) were used in this calculation. For the convective region, we used the relation,

$$\text{dBZ} = 24.77 + 13.5 \log_{10} R \quad (3.1)$$

where R is rainfall in mmh^{-1} (Sekhon and Srivastara, 1971).

For the stratiform region, we used the relation given by Marshall and Palmer (1948),

$$\text{dBZ} = 23.01 + 16 \log_{10} R \quad (3.2)$$

Again, we define the convective region as the region where the radar

reflectivity is greater than 30 dBZ, while stratiform region is defined as all echoes whose reflectivity is less than 30 dBZ.

The results are shown in Fig. 3.81. Curves A and B represent convective and stratiform areal rainfall rate respectively and curves C and D represent the counts of negative and positive cloud-to-ground lightning flashes respectively.

From this figure we can see that the convective precipitation amount peaked at 1356Z, while the stratiform precipitation amount peaked at 1528Z. Hence about a 1.5 hr time lag occurred between the maximum convective and rainfall rate and stratiform rainfall amounts. This lag time is similar to the time lag for the June 11 case discussed by Rutledge and MacGorman (1988). Negative CG flashes reached their maximum values near in time to the occurrence of maximum convective rainfall, as Rutledge and MacGorman (1988) found for the 11 June case. The maximum in positive CG flash frequency occurred near 1430Z, coincident with the maximum rate of increase of stratiform rainfall amounts. A secondary peak in positive CG flash rates was found near the time when the stratiform precipitation was at a maximum. It is interesting that both the 28 May and 11 June cases showed that the maximum CG flash frequency occurred coincident in time with the rate of greatest stratiform rainfall intensification, not necessarily with the maximum stratiform rainfall rates.

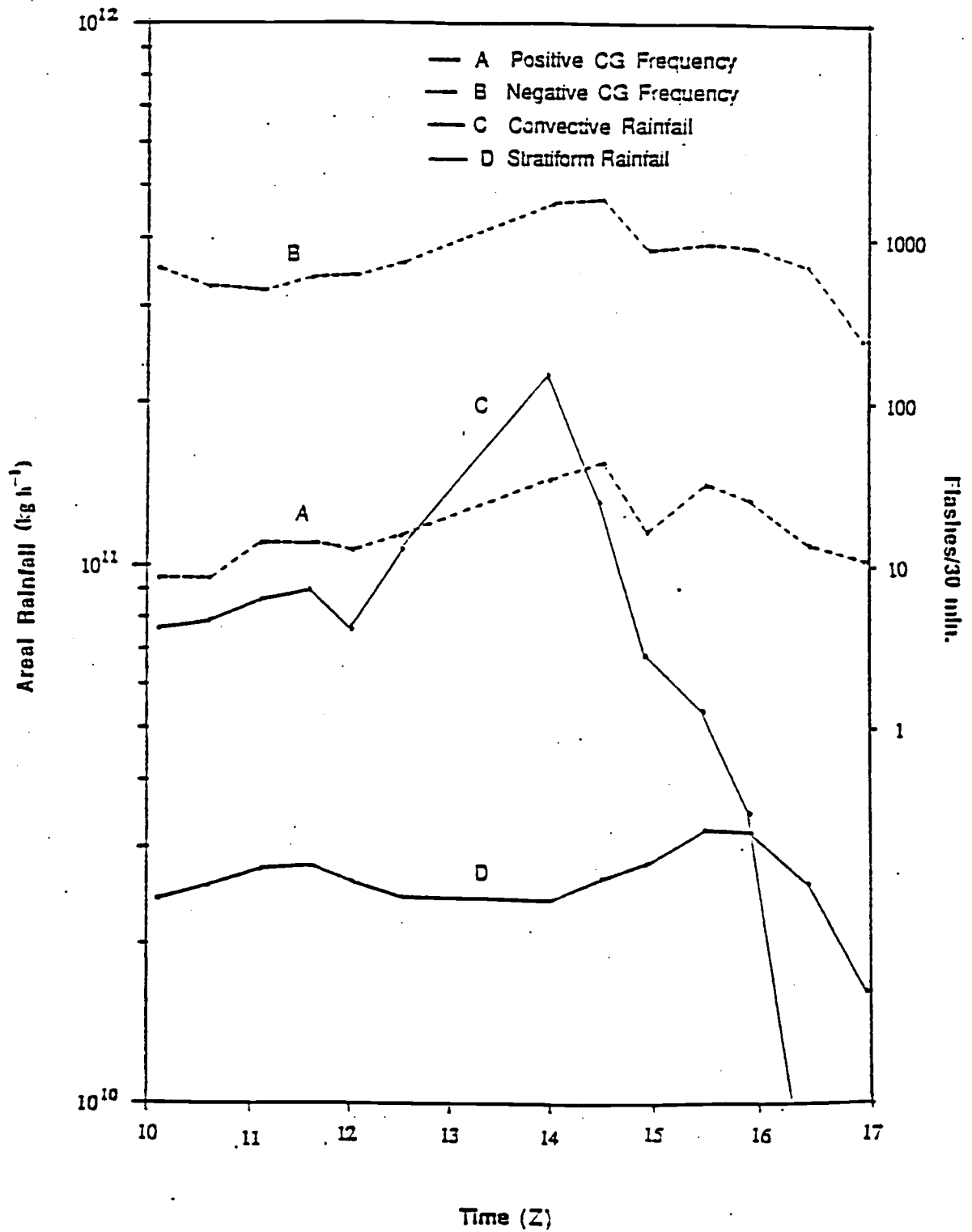


Fig. 3.0 Areal integrated precipitation amounts for the convective and stratiform regions and cumulative lightning activity (- and +) over the time period from 1008 to 1659 UTC.

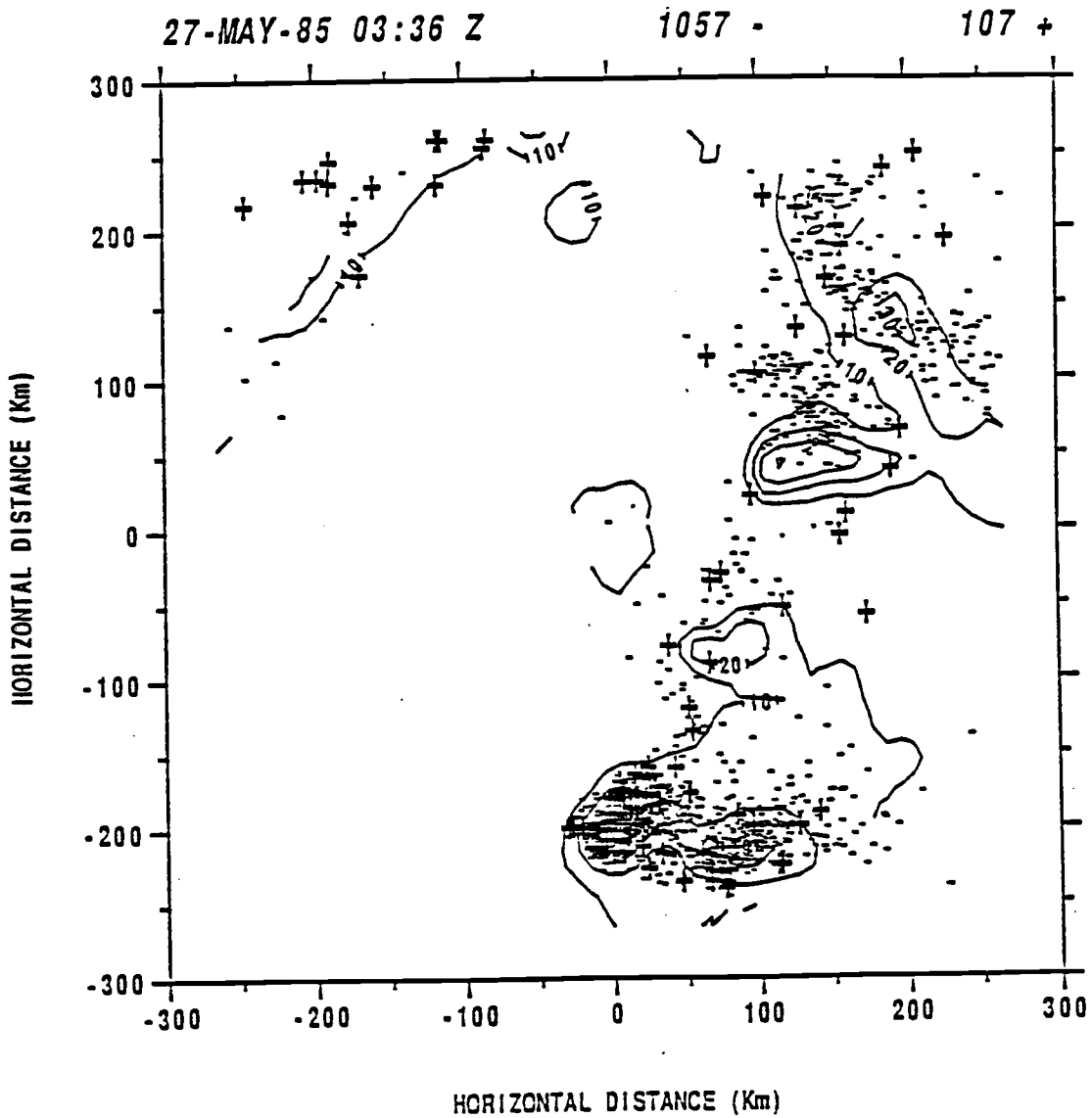


Fig. 3.1 Radar echo pattern and lightning map for 0336Z on 27 May 1958. Radar echo contours are for 10, 20, 30, 40 and 50 dBZ. Locations of negative cloud-to-ground flashes are denoted by (-). locations of positive flashes are denoted by (+). Flash statistics represent cumulative flash amounts for a 30 min. period centered on the radar echo time.

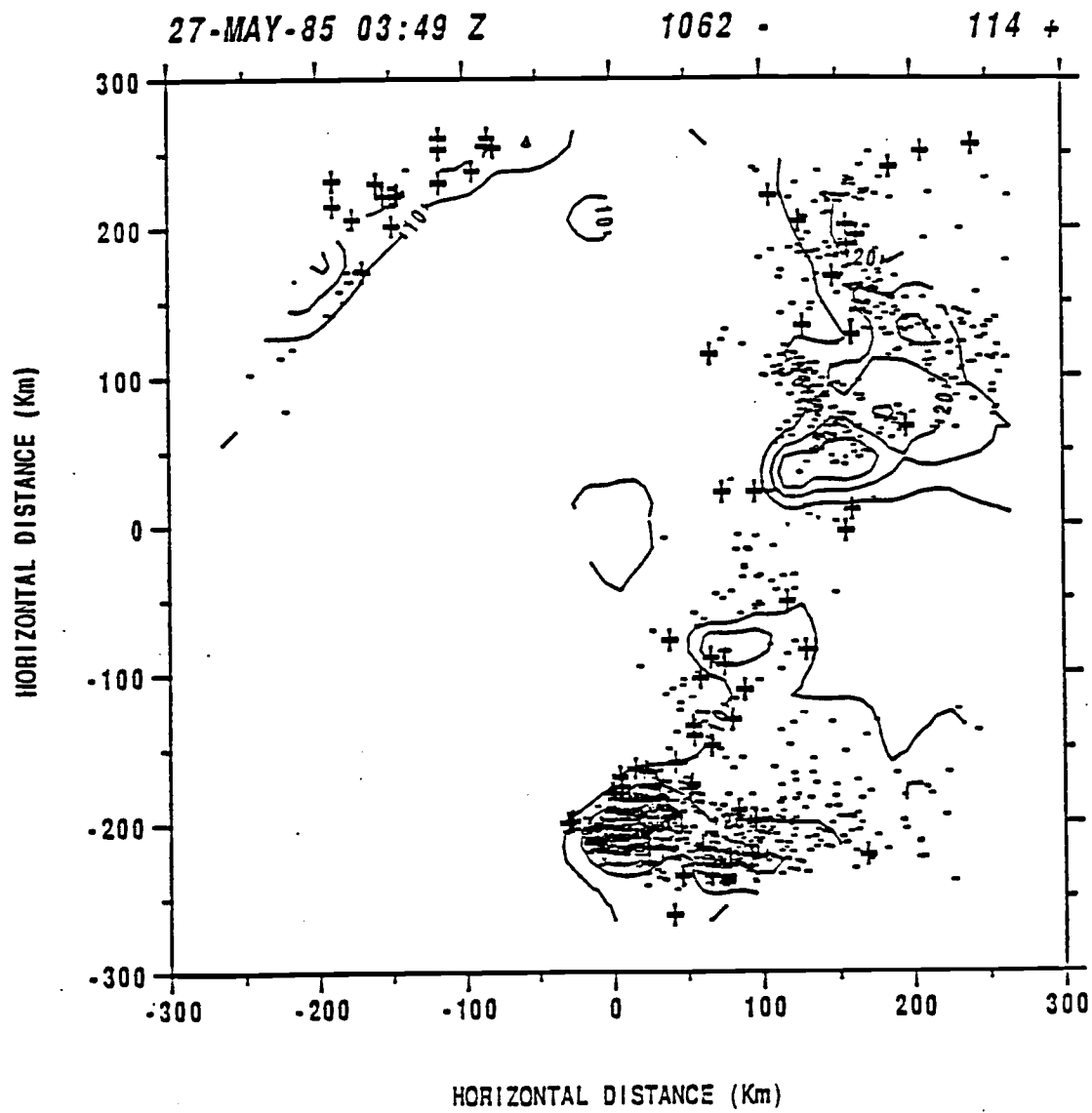


Fig. 3.2 Radar echo pattern and lightning map for 0349Z on 27 May.

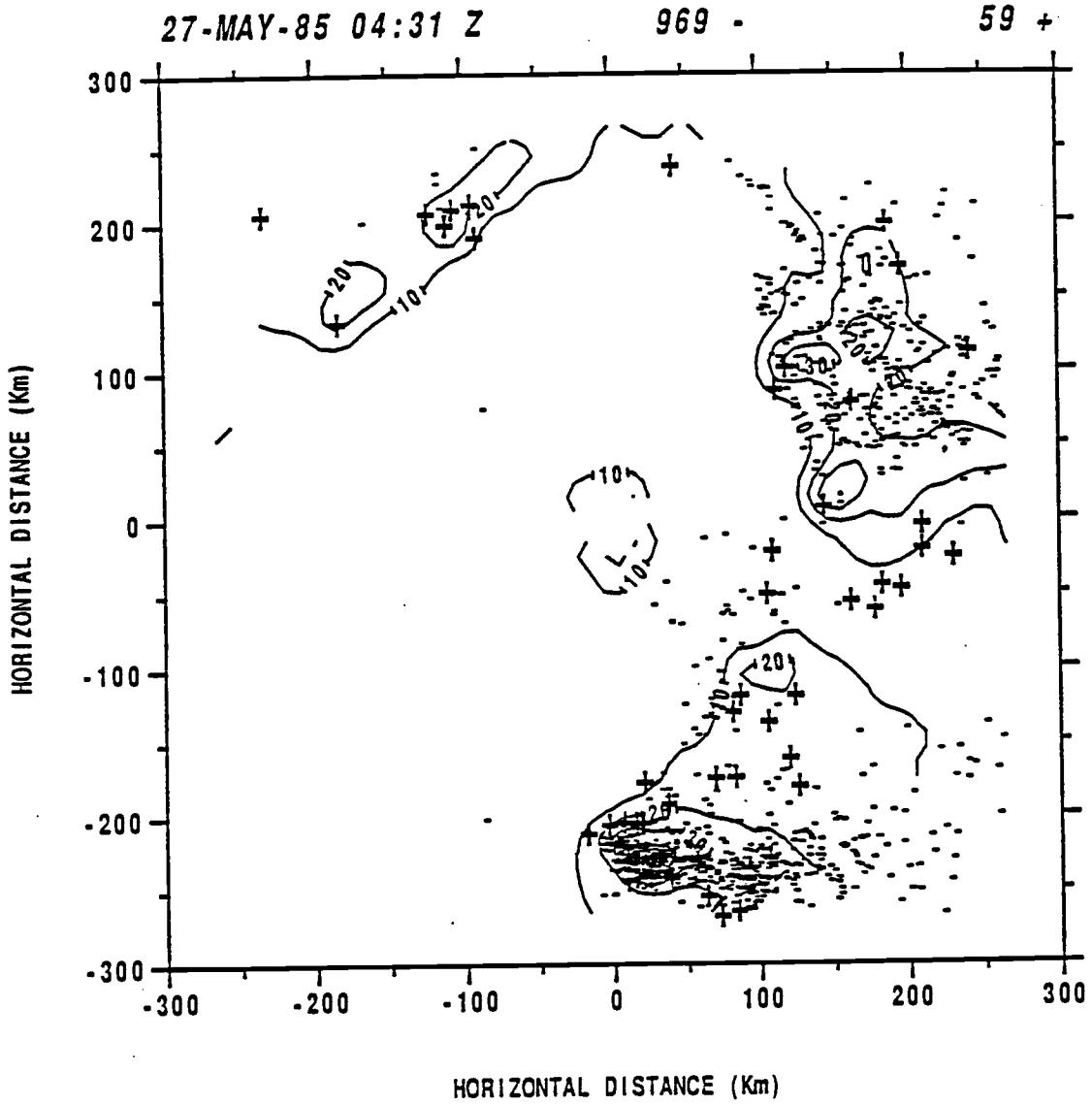


Fig. 3.3 Radar echo pattern and lightning map for 0431Z on 27 May.

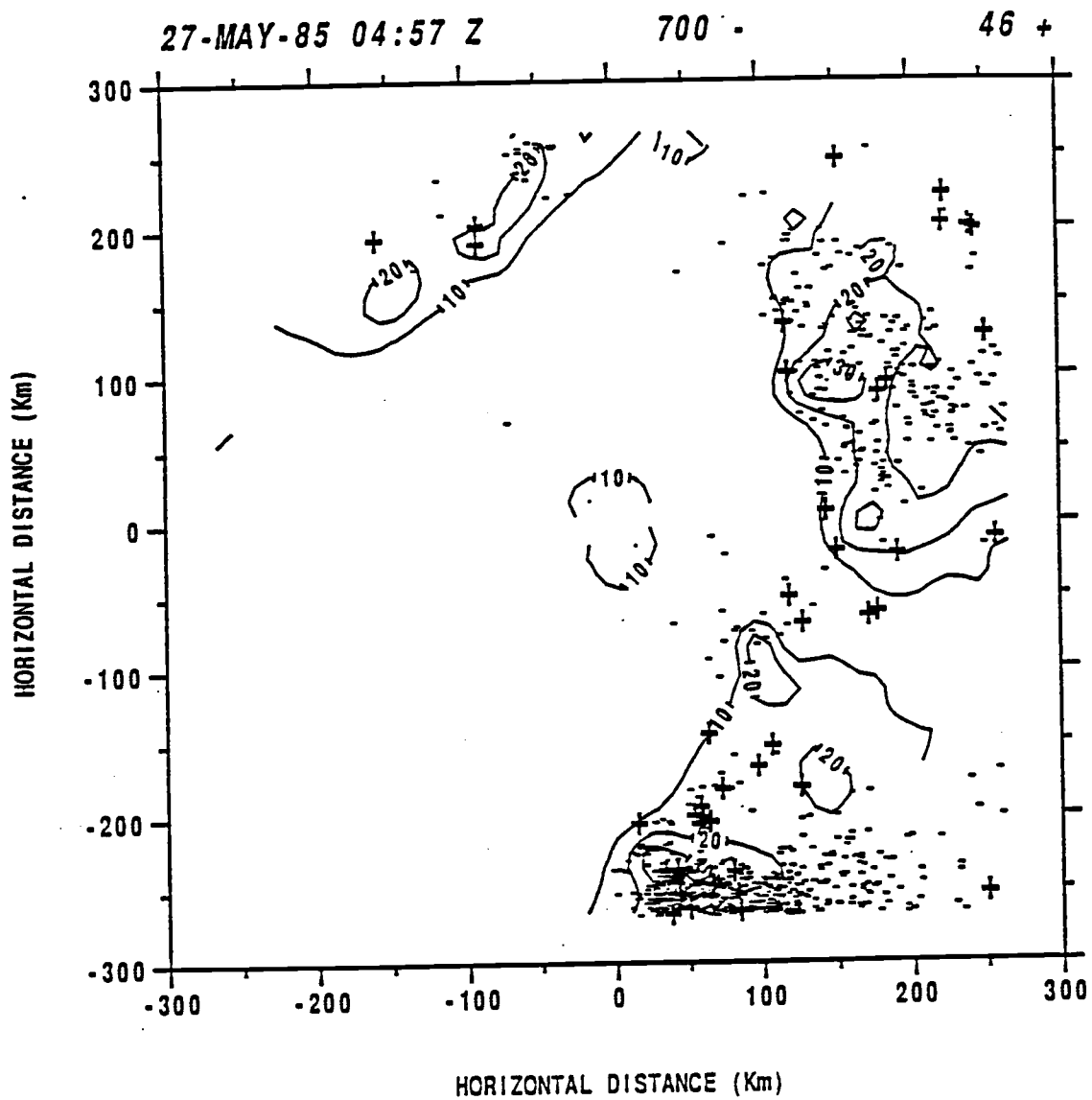


Fig. 3.4 Radar echo pattern and lightning map for 0457Z on 27 May.

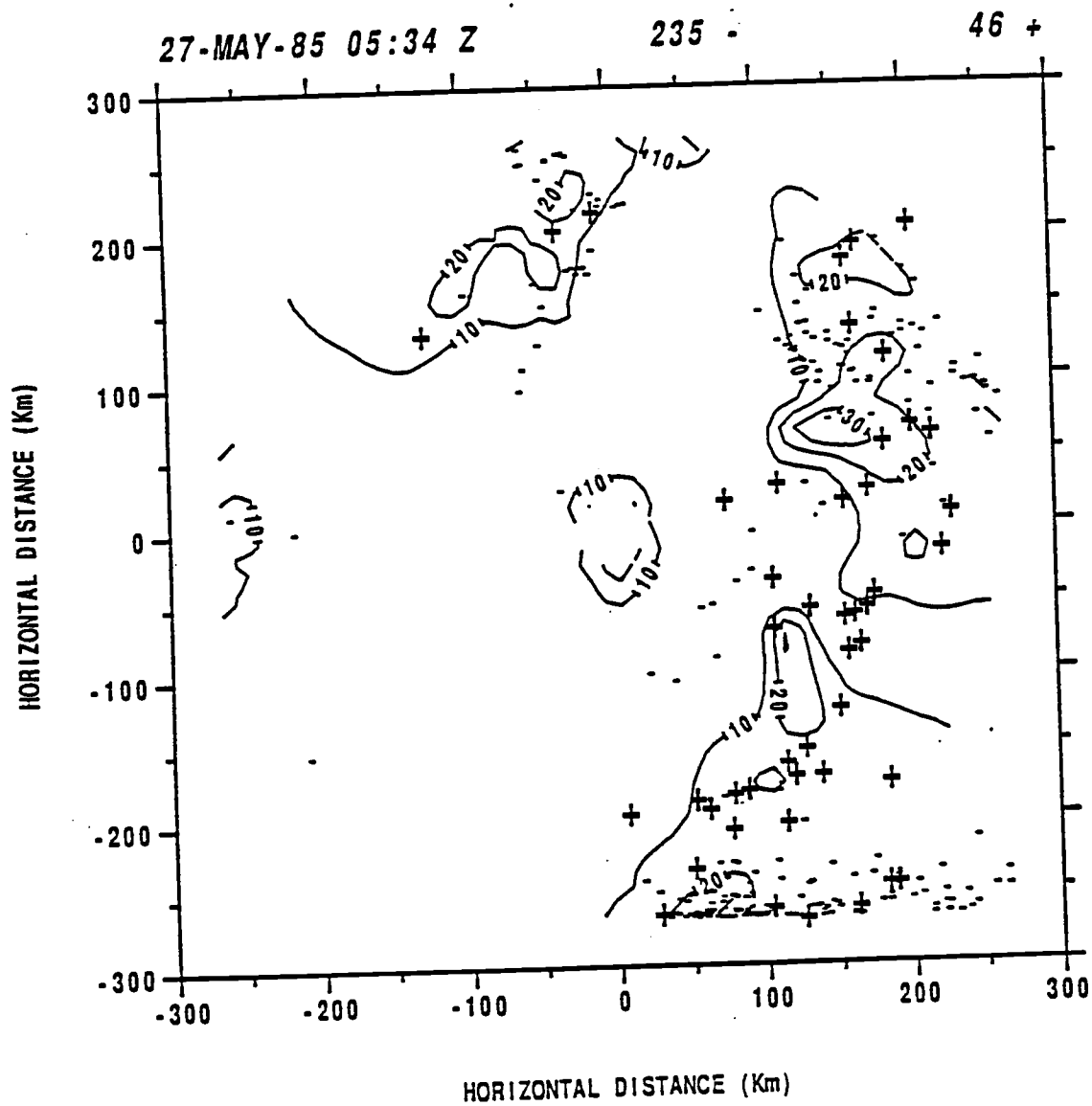


Fig. 3.5 Radar echo pattern and lightning map for 0534Z on 27 May.

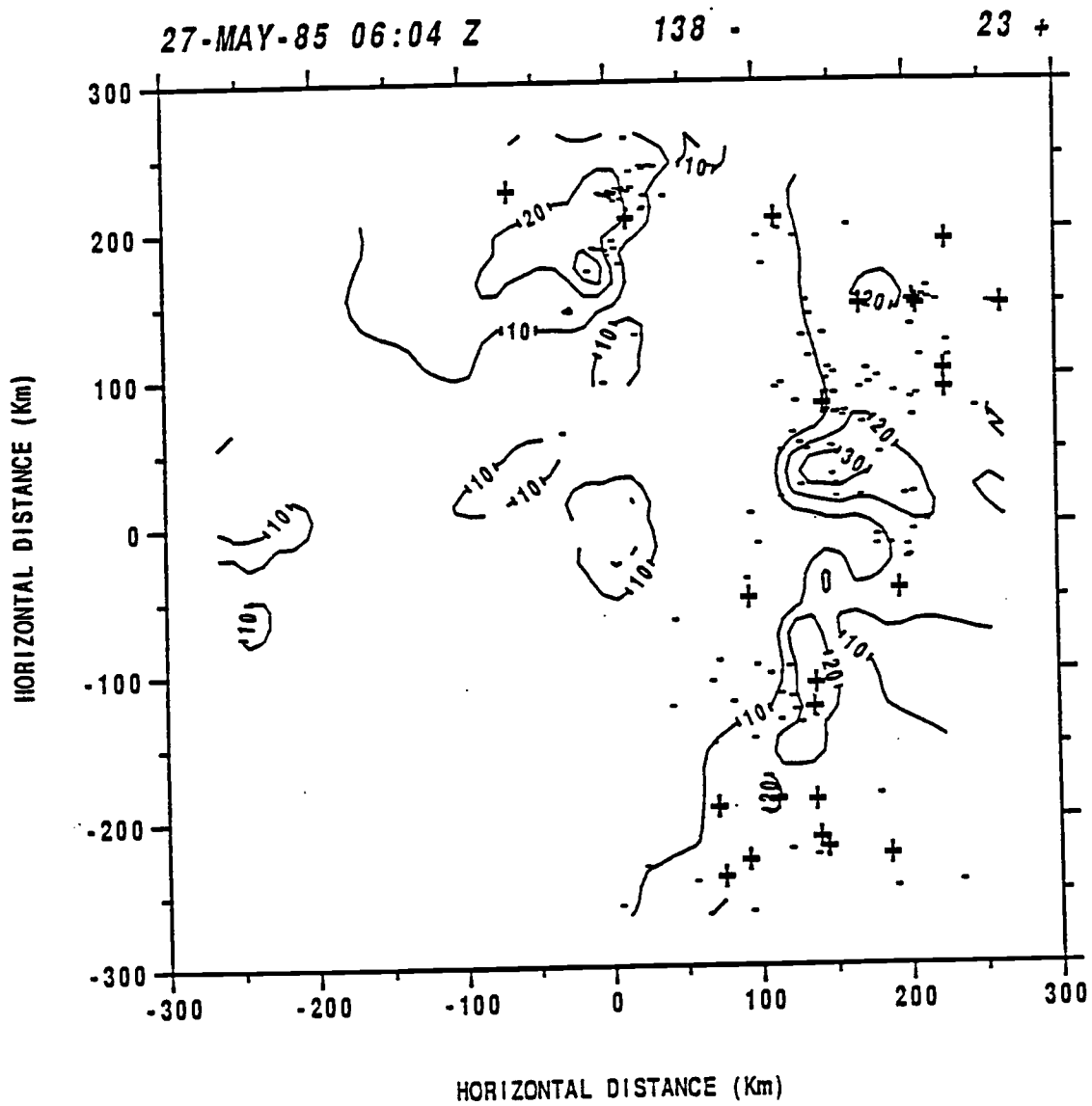


Fig. 3.6 Radar echo pattern and lightning map for 0604Z on 27 May.

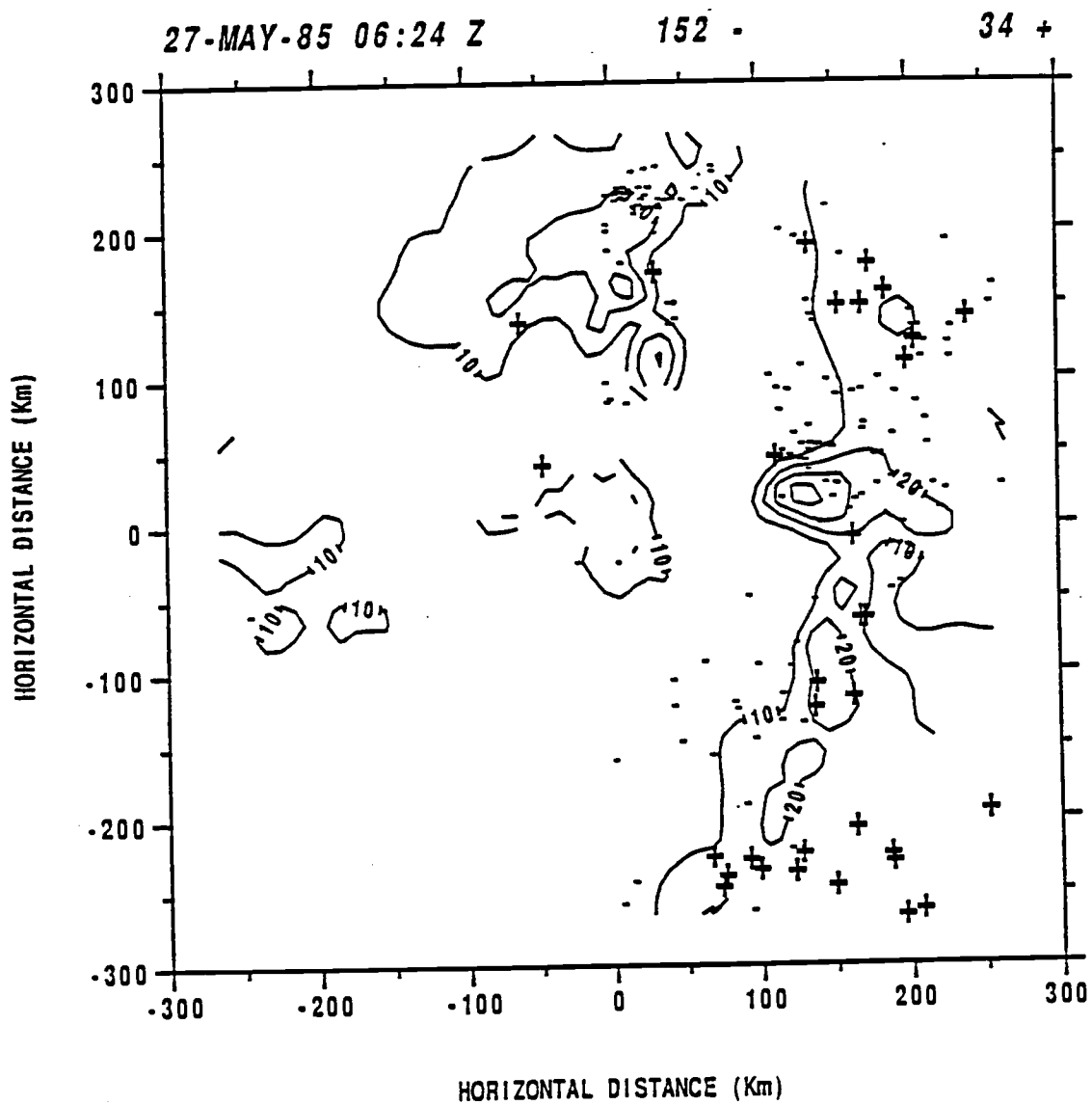


Fig. 3.7 Radar echo pattern and lightning map for 0624Z on 27 May.

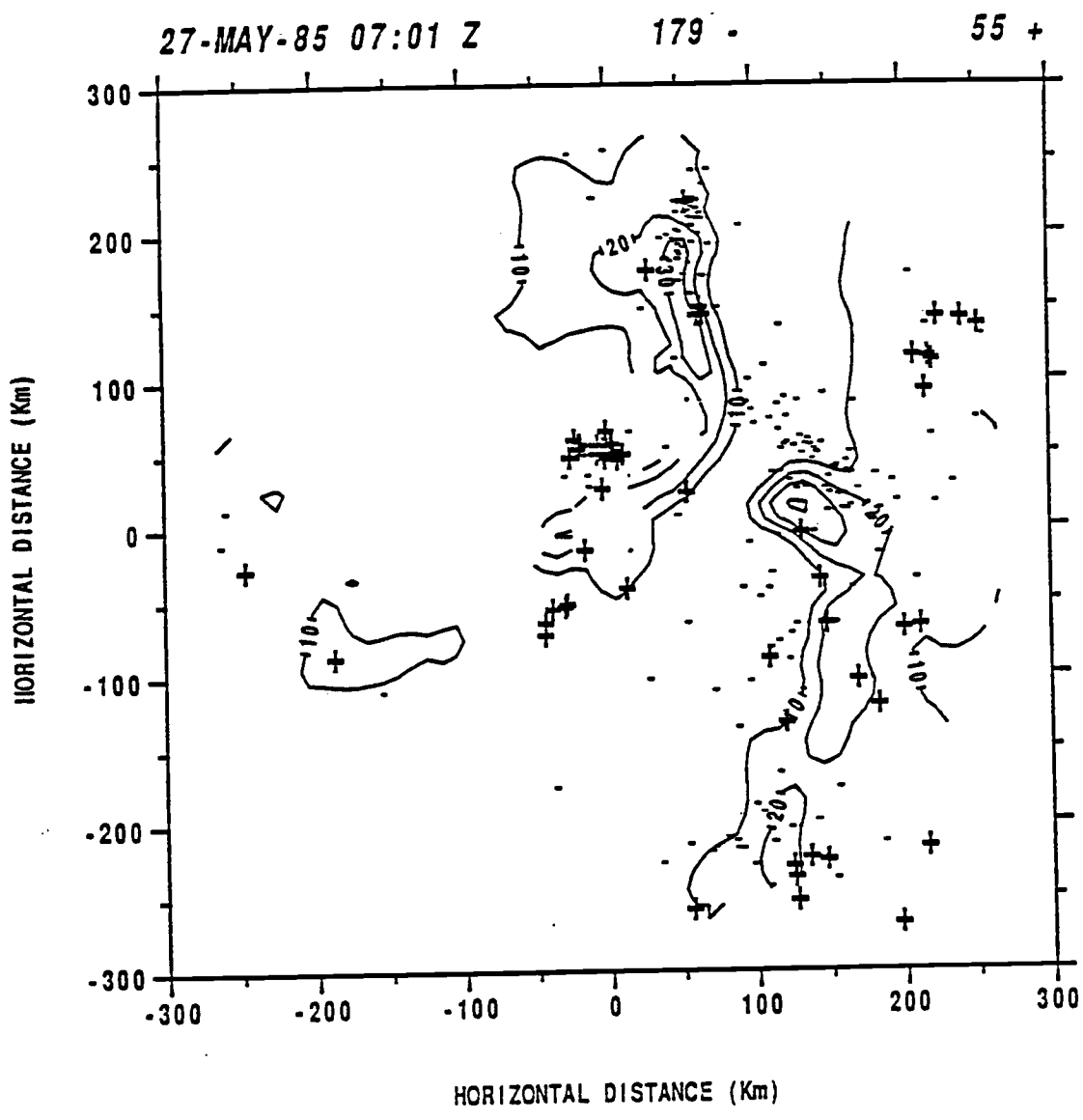


Fig. 3.8 Radar echo pattern and lightning map for 0701Z on 27 May.

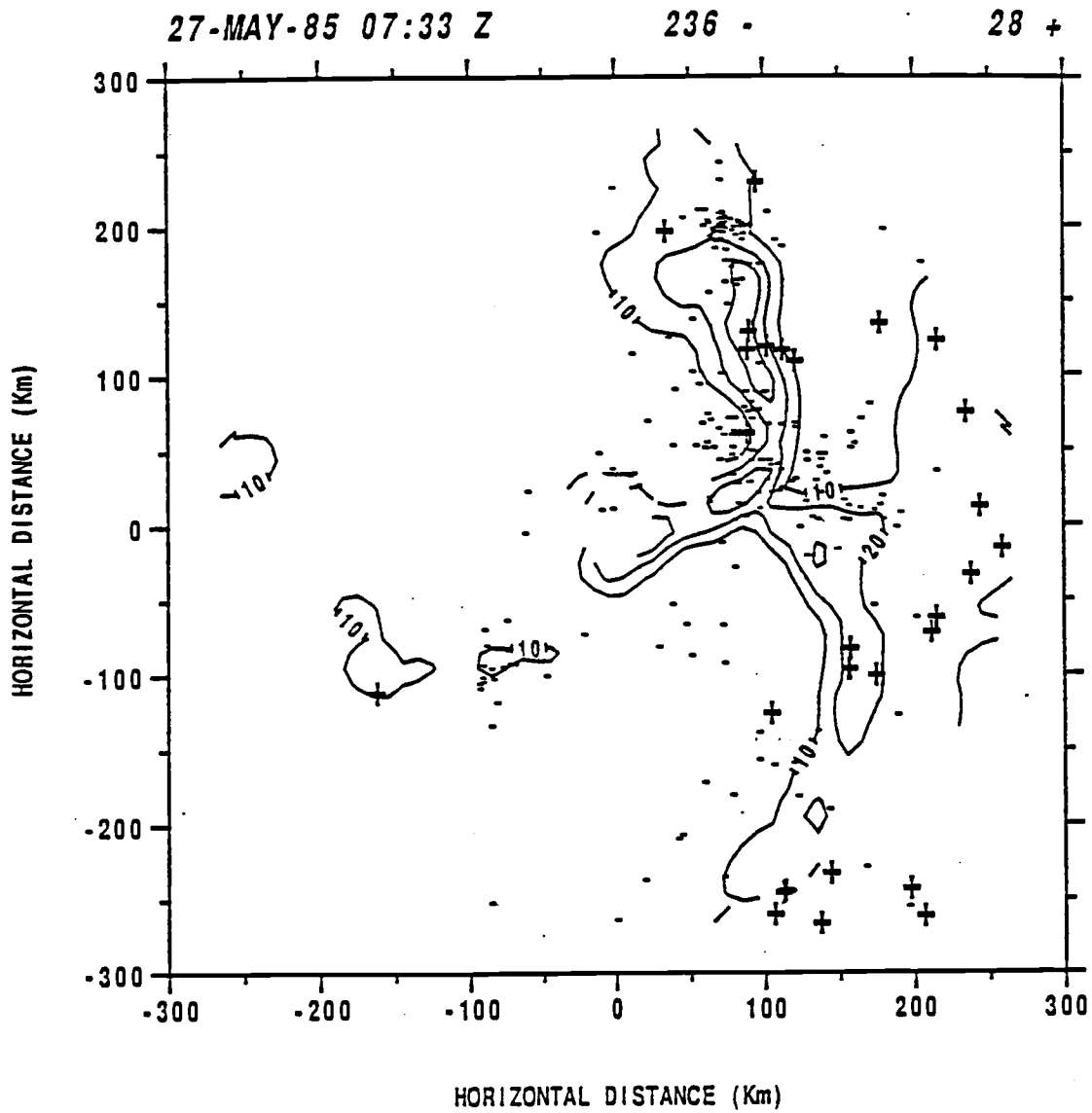


Fig. 3.9 Radar echo pattern and lightning map for 0733Z on 27 May.

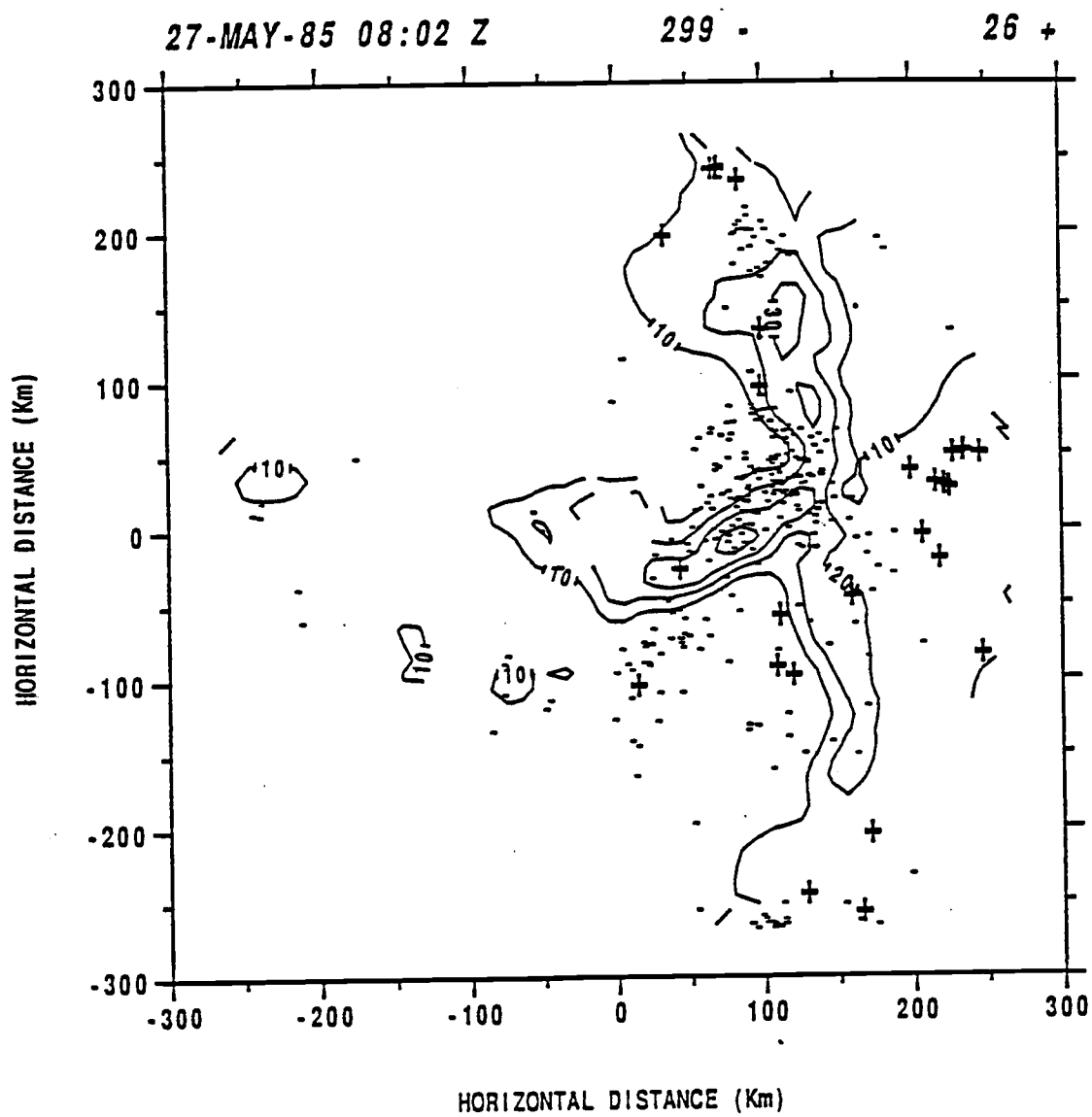


Fig. 3.10 Radar echo pattern and lightning map for 0802Z on 27 May.

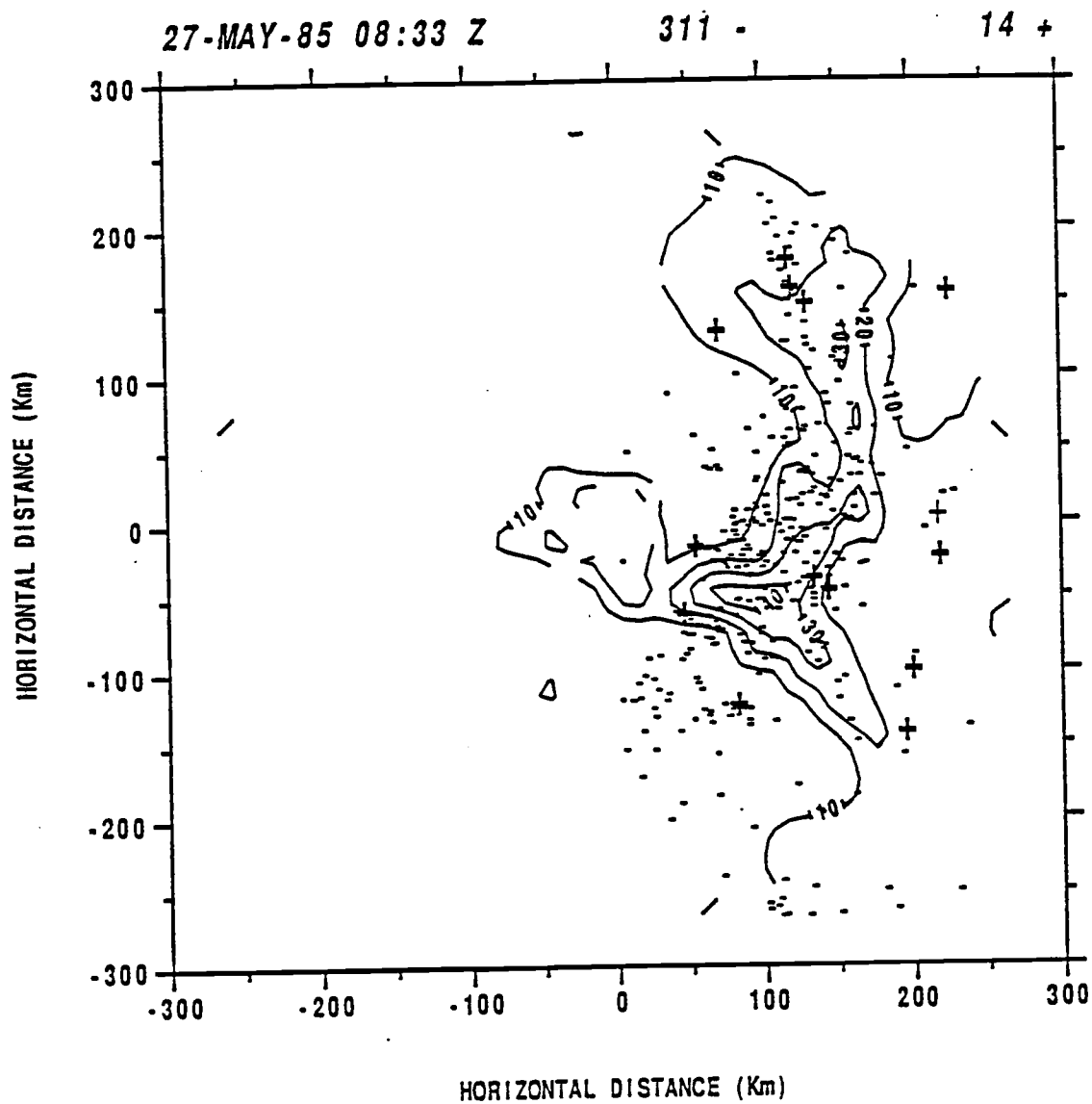


Fig. 3.11 Radar echo pattern and lightning map for 0833Z on 27 May.

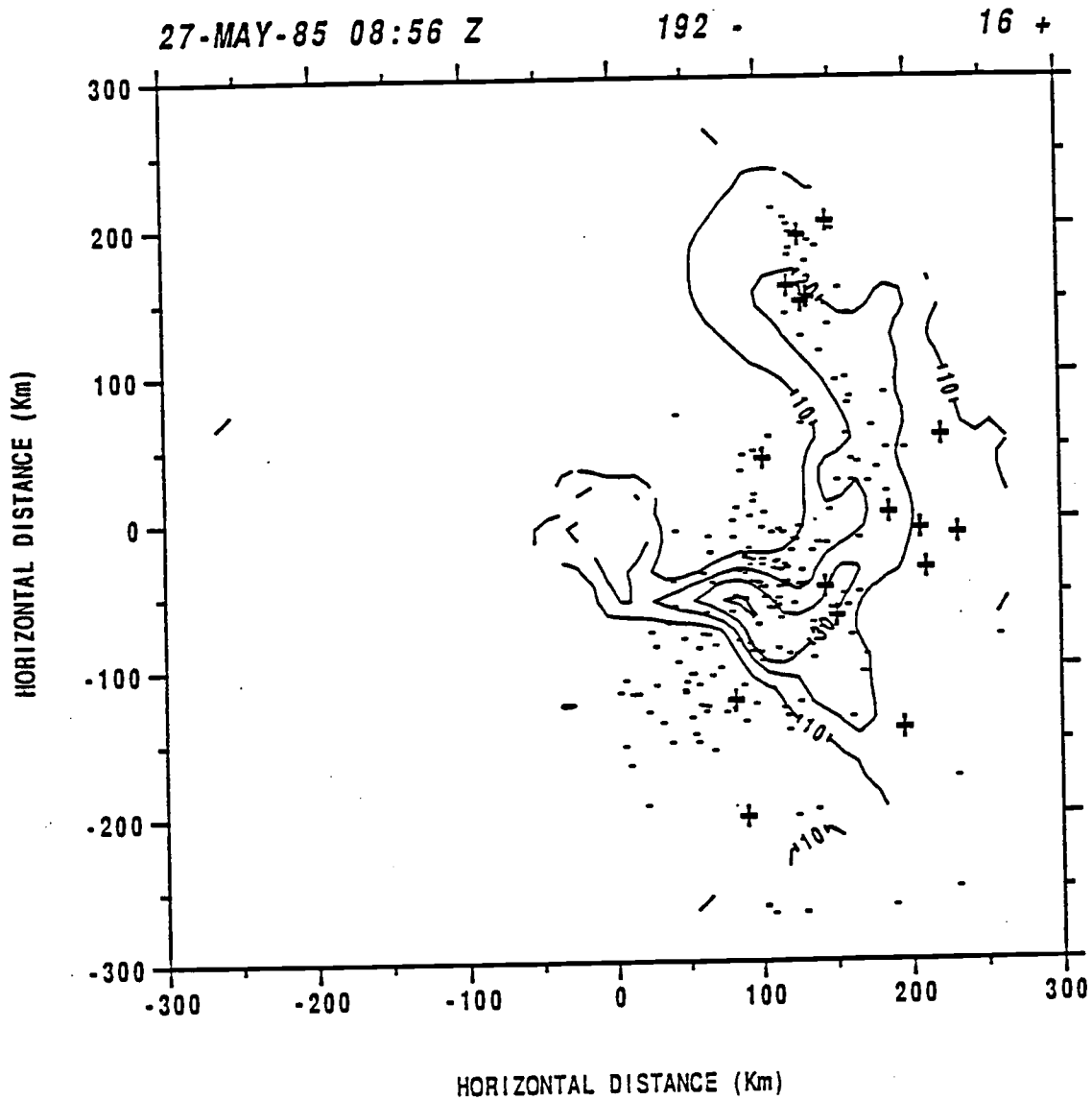


Fig. 3.12 Radar echo pattern and lightning map for 0856Z on 27 May.

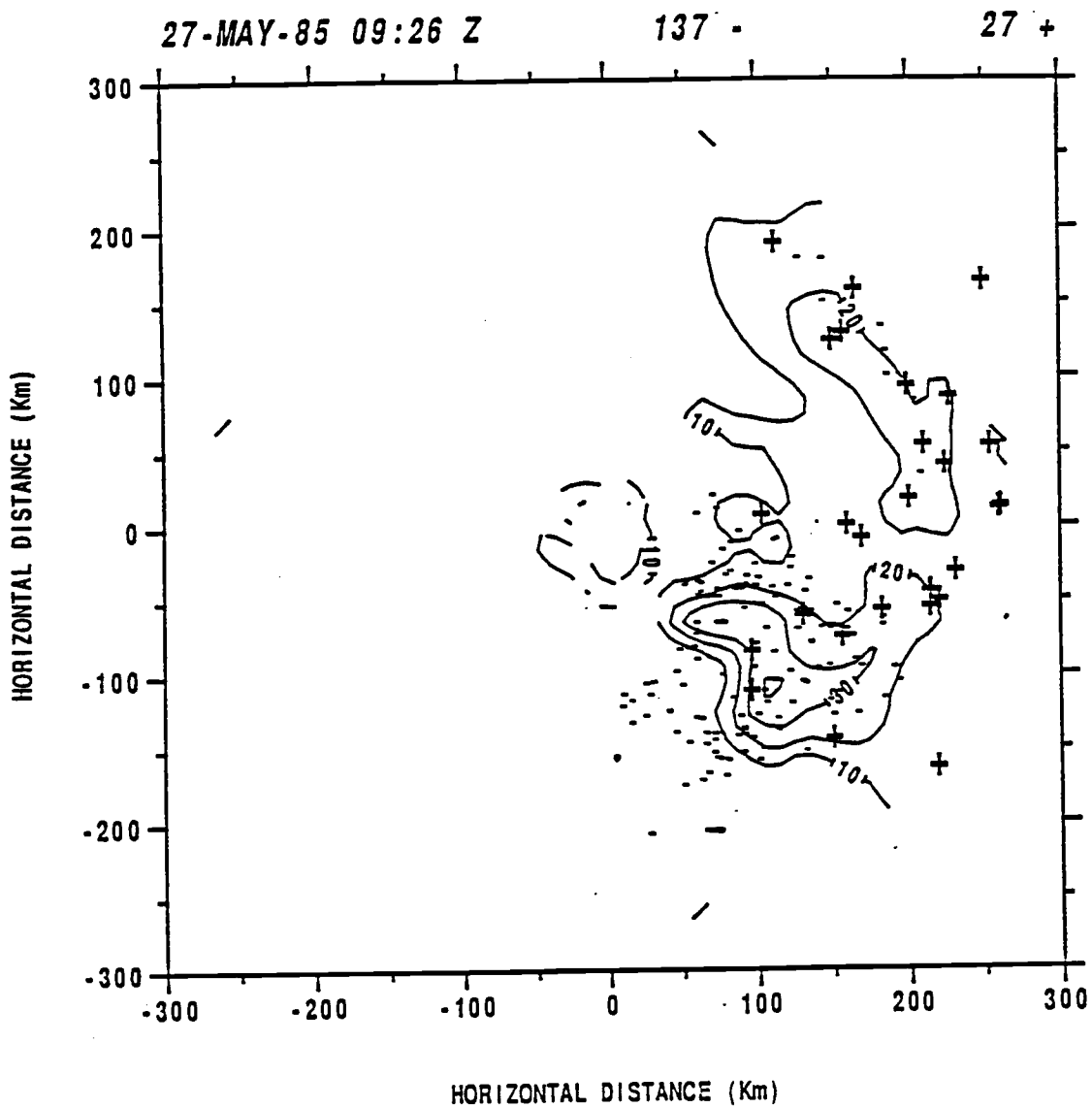


Fig. 3.13 Radar echo pattern and lightning map for 0926Z on 27 May.

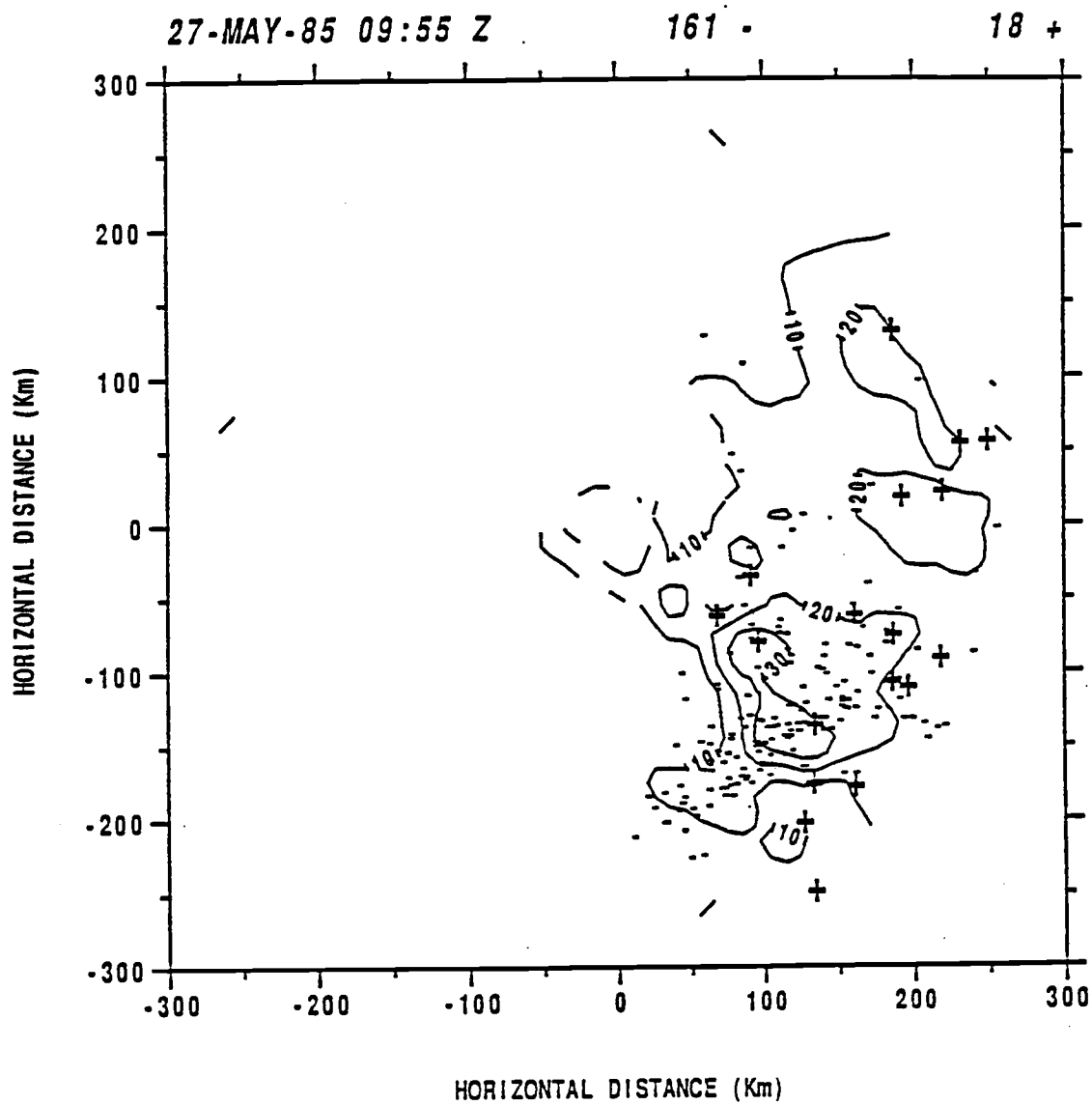


Fig. 3.14 Radar echo pattern and lightning map for 0955Z on 27 May.

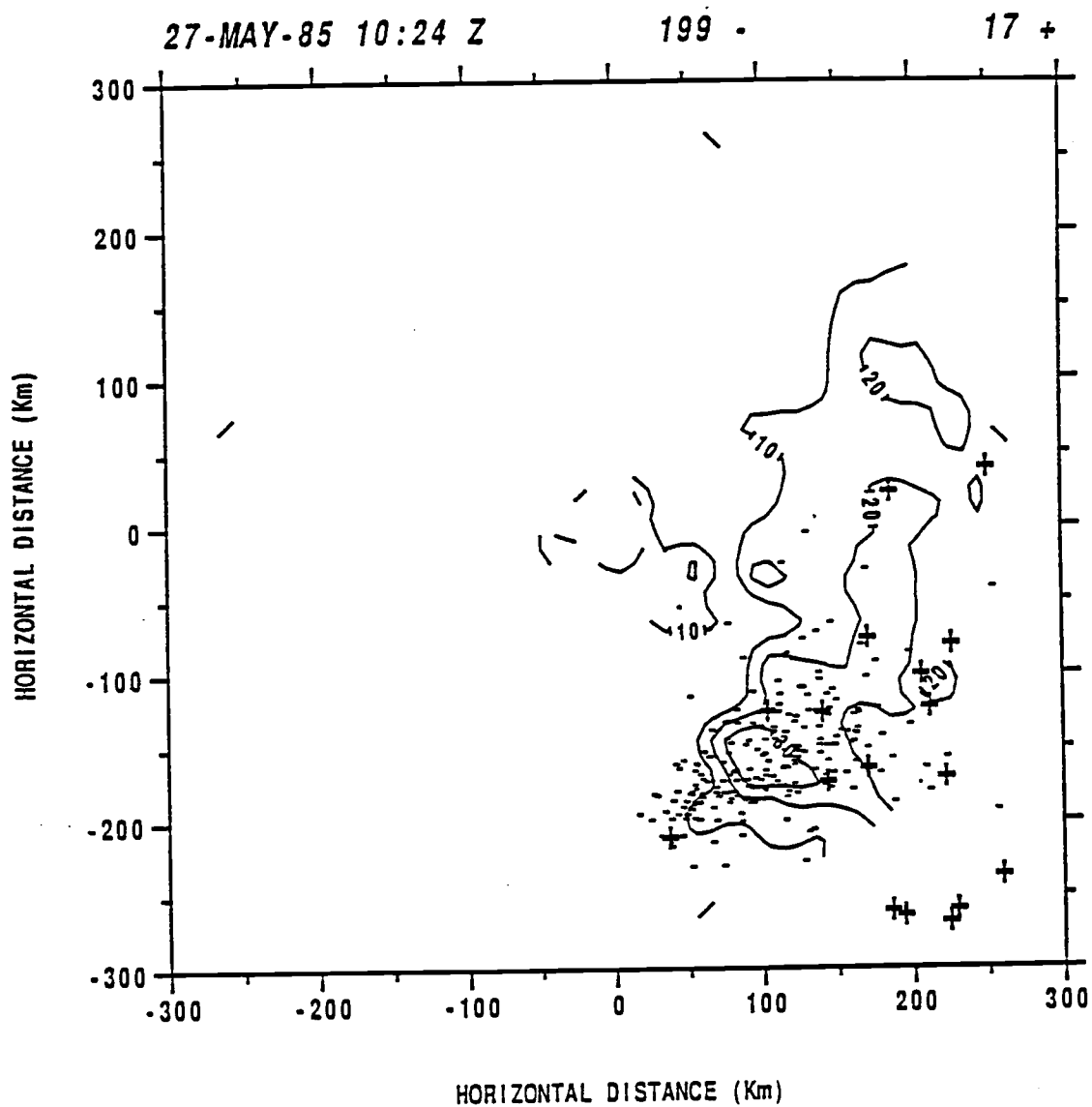


Fig. 3.15 Radar echo pattern and lightning map for 1024Z on 27 May.

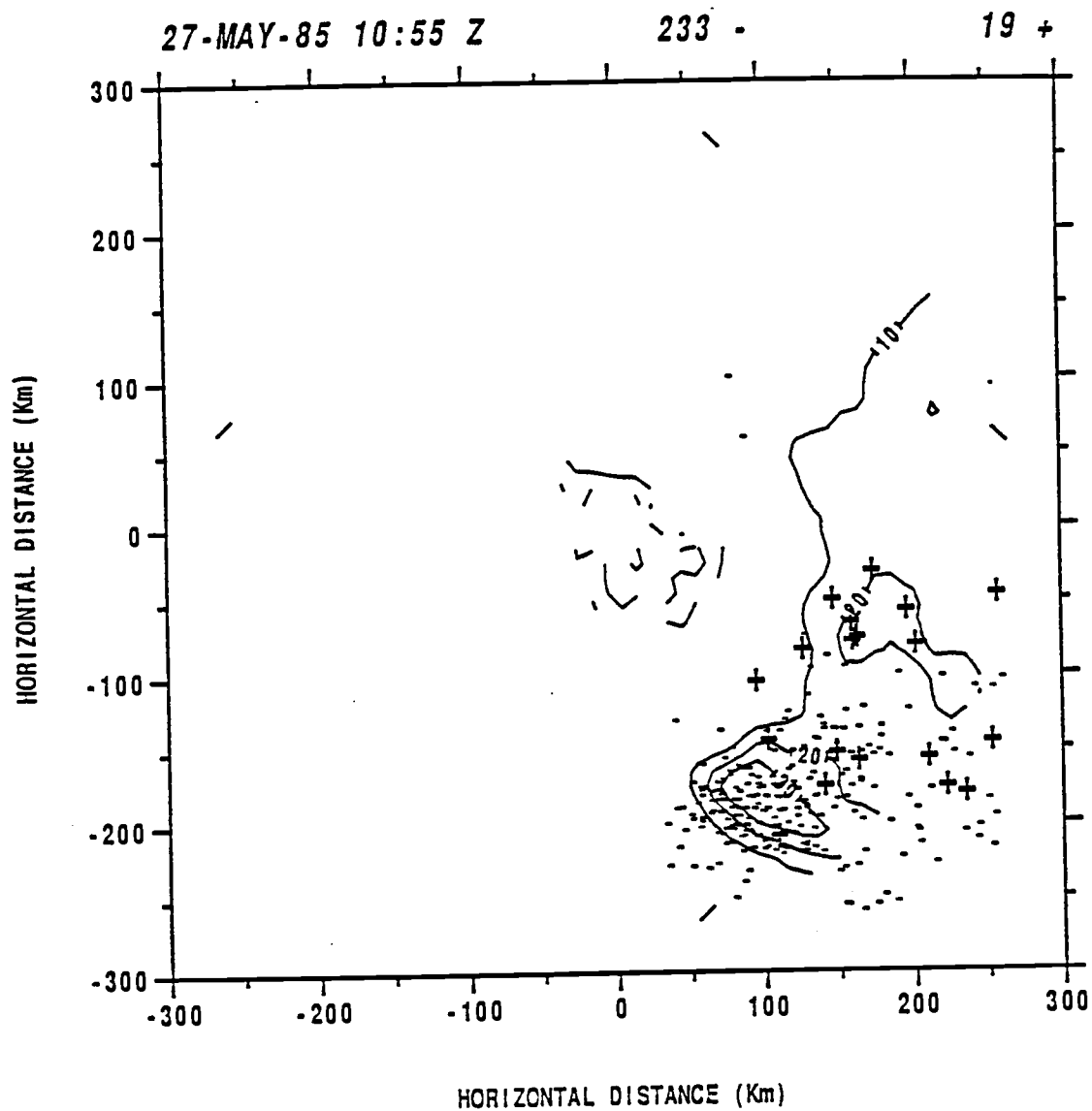


Fig. 3.16 Radar echo pattern and lightning map for 1055Z on 27 May.

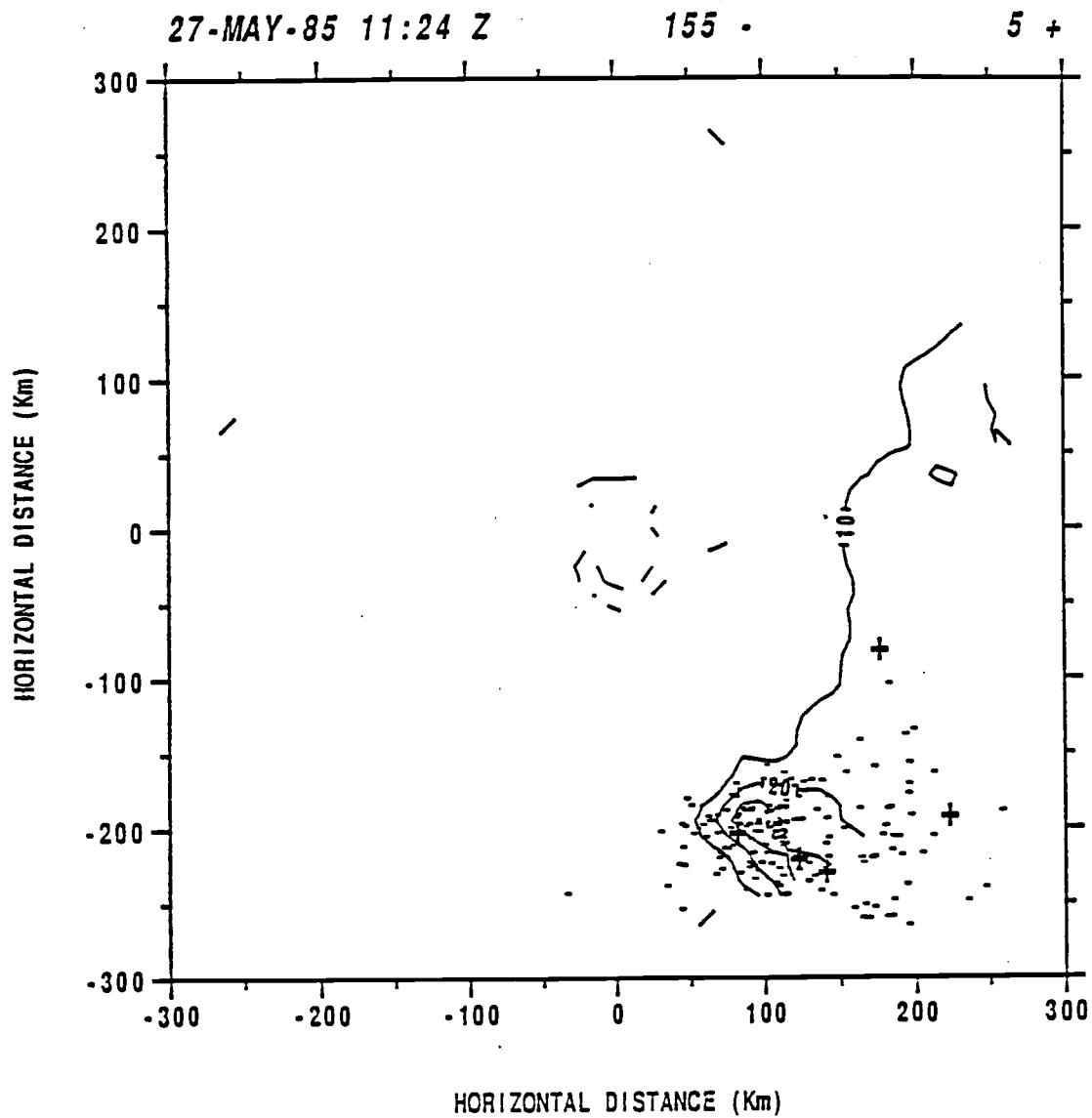


Fig. 3.17 Radar echo pattern and lightning map for 1124Z on 27 May.

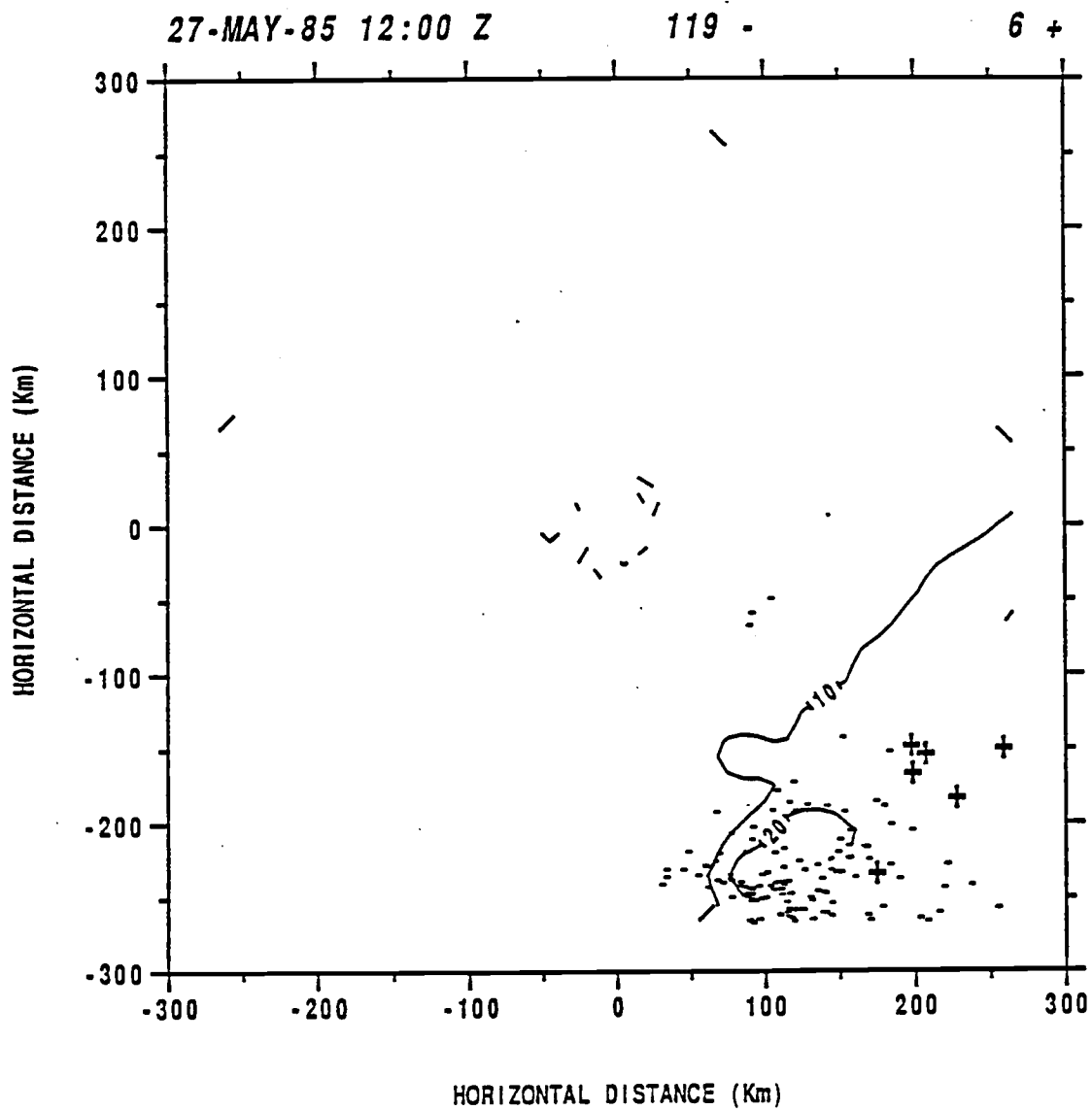


Fig. 3.18 Radar echo pattern and lightning map for 1200Z on 27 May.

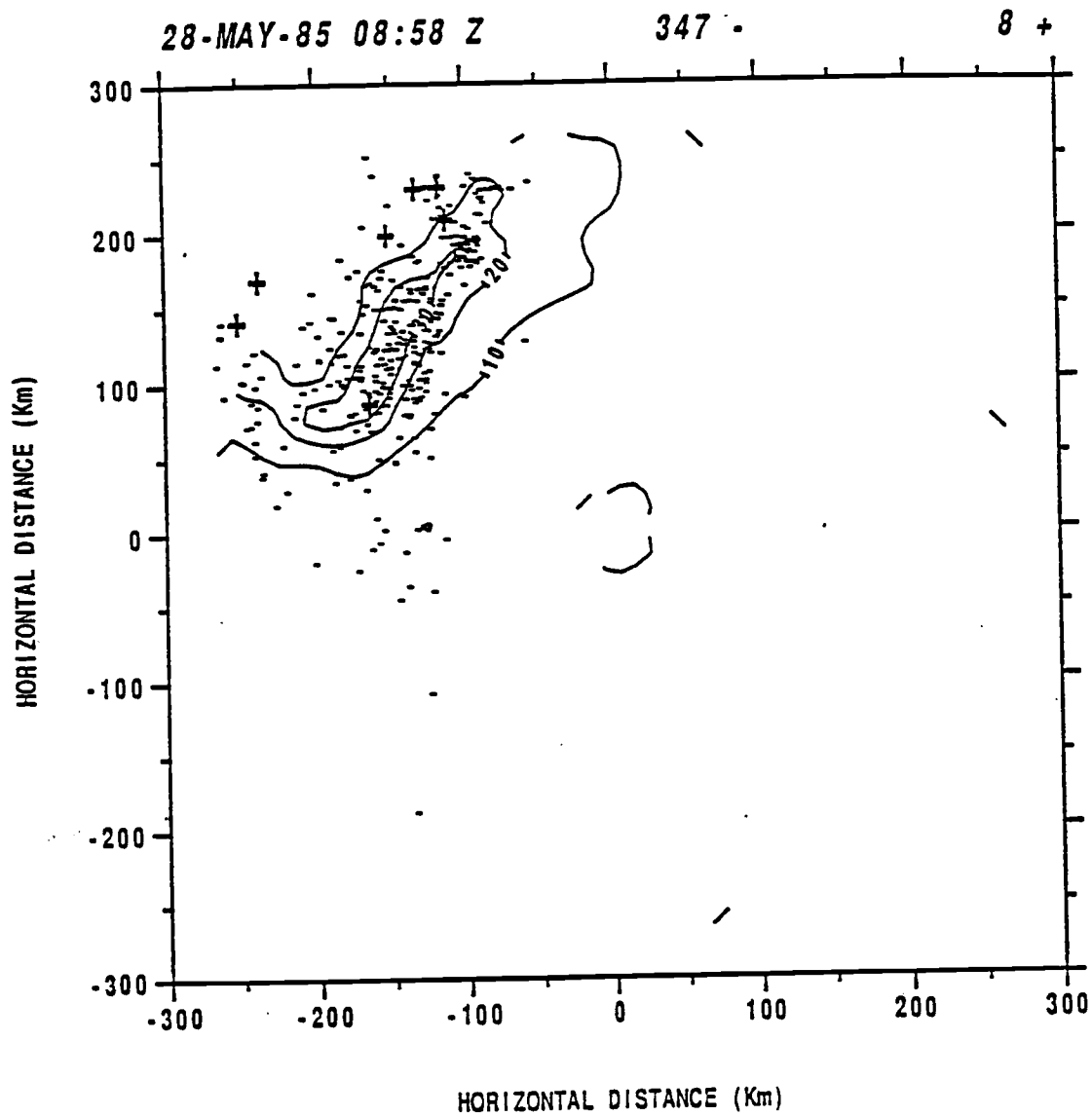


Fig. 3.19 Radar echo pattern and lightning map for 0858Z on 28 May.

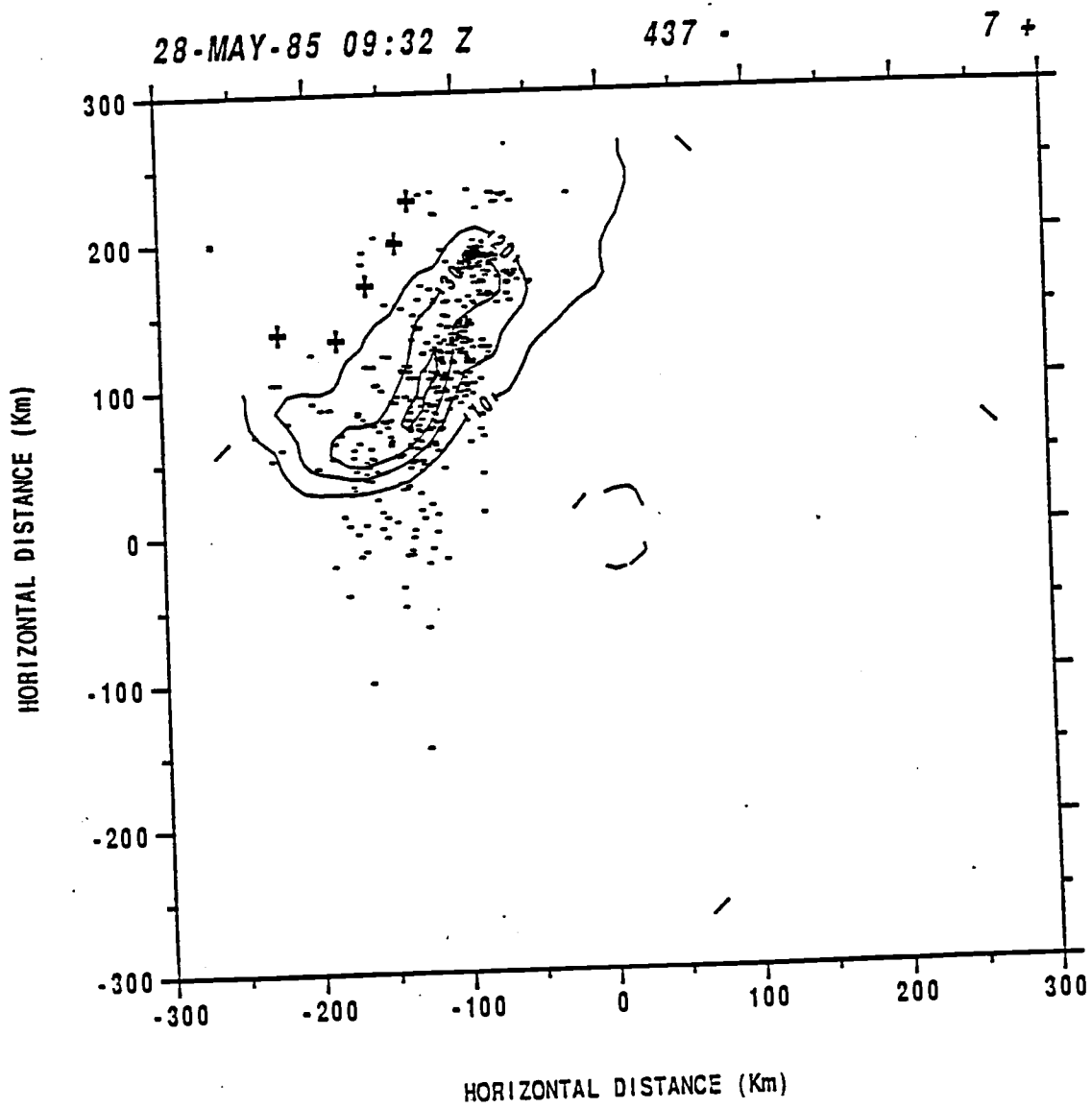


Fig. 3.20 Radar echo pattern and lightning map for 0932Z on 28 May.

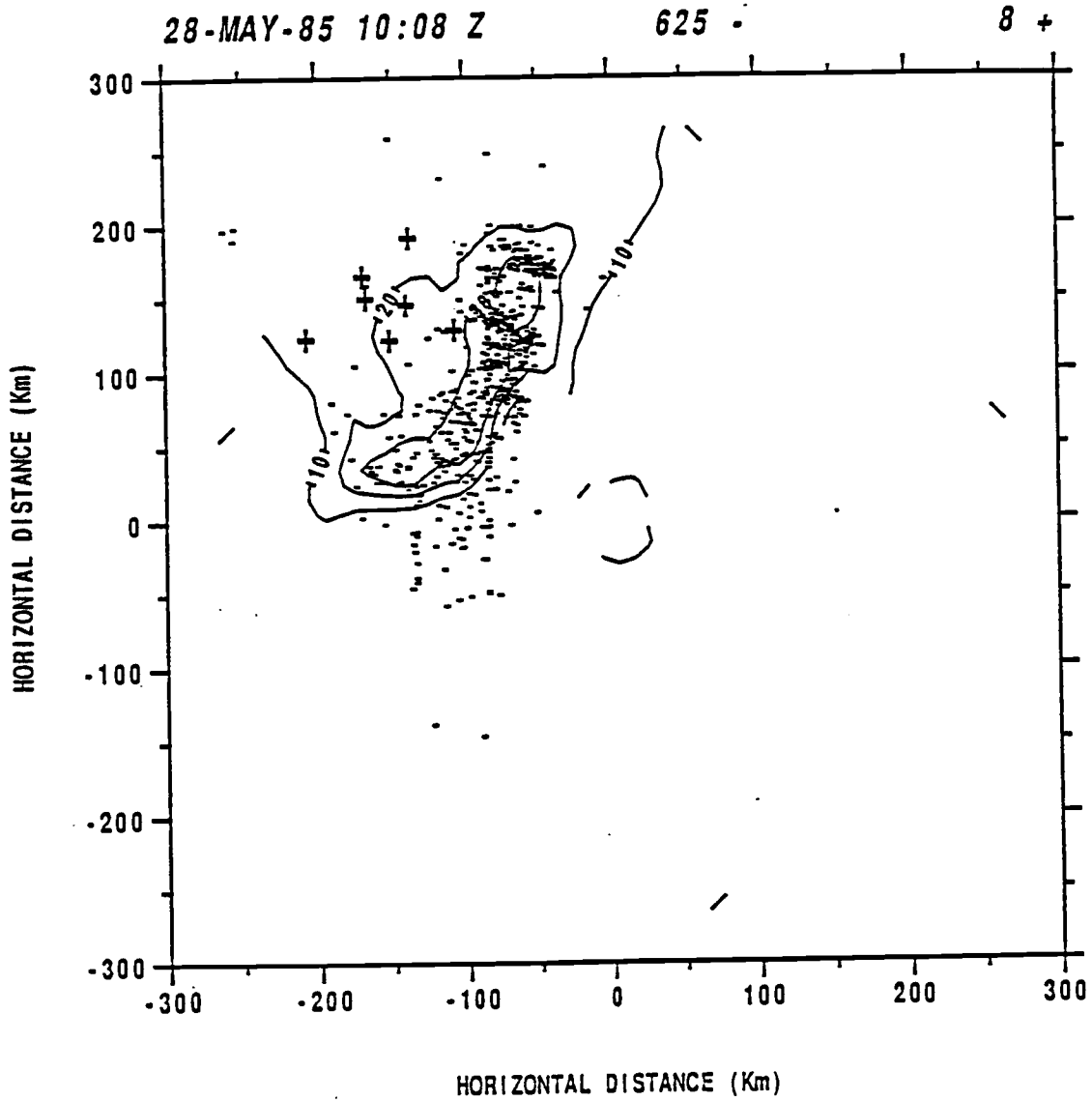


Fig. 3.21 Radar echo pattern and lightning map for 1008Z on 28 May.

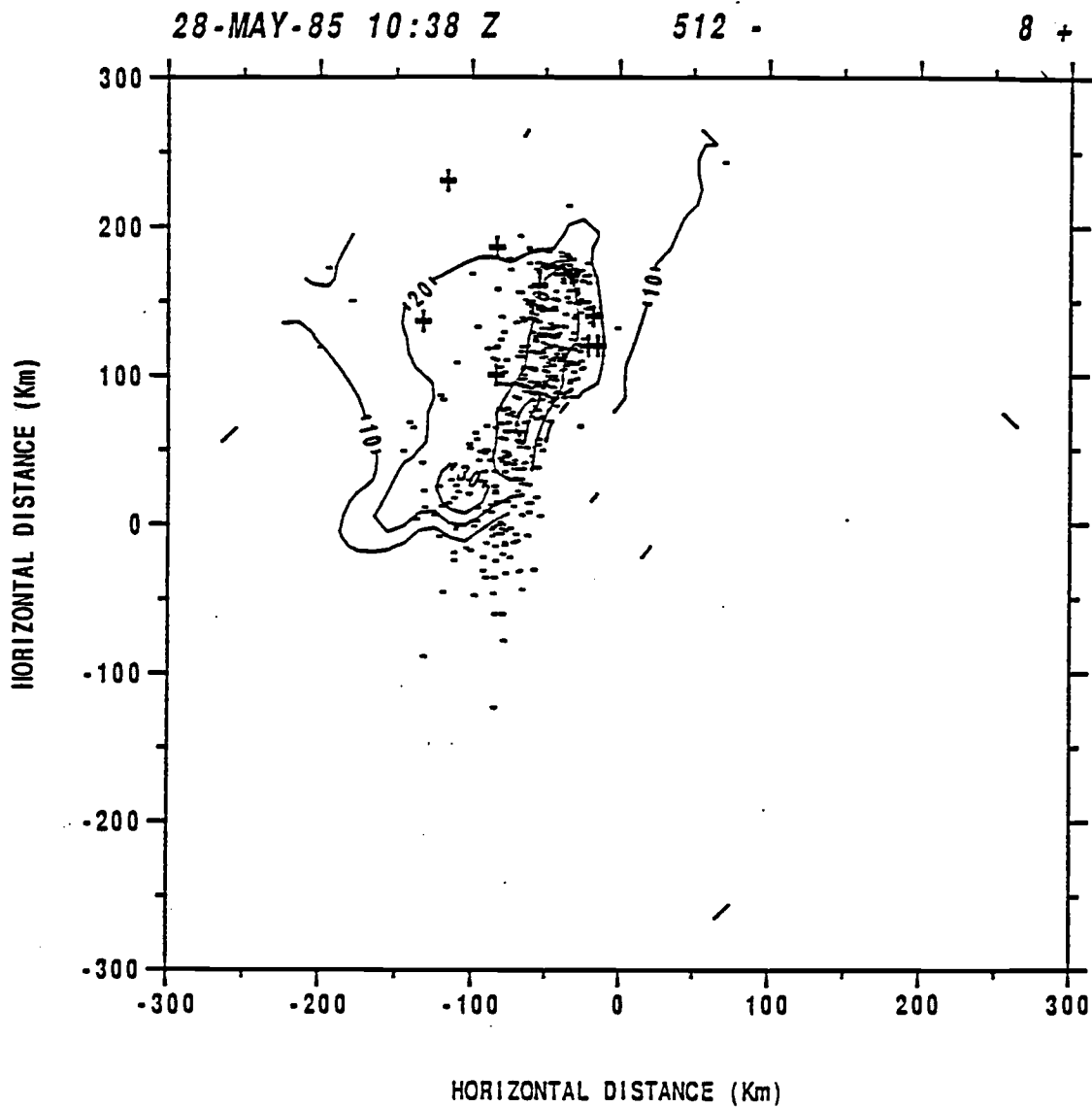


Fig. 3.22 Radar echo pattern and lightning map for 1038Z on 28 May.

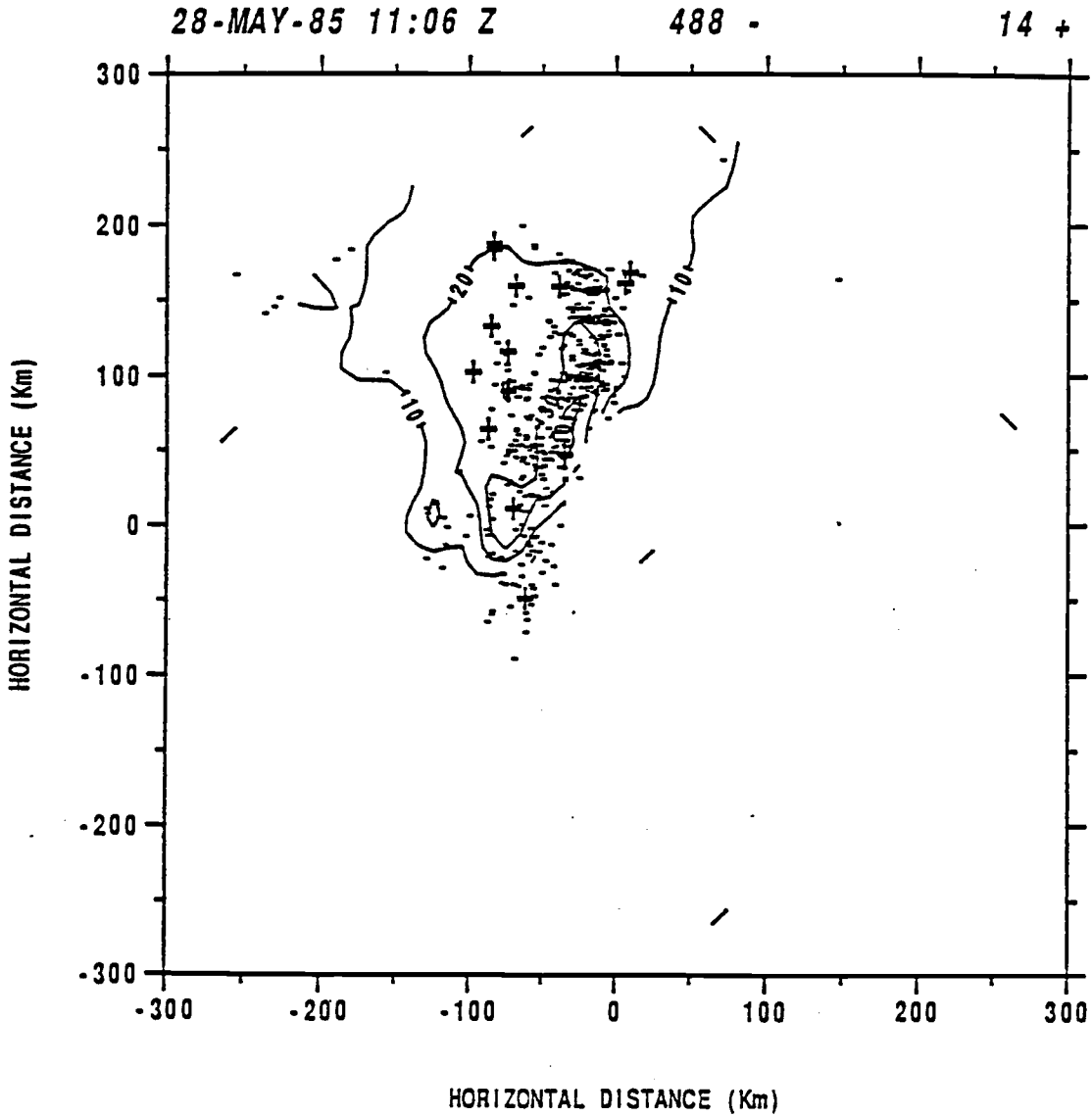


Fig. 3.23 Radar echo pattern and lightning map for 1106Z on 28 May.

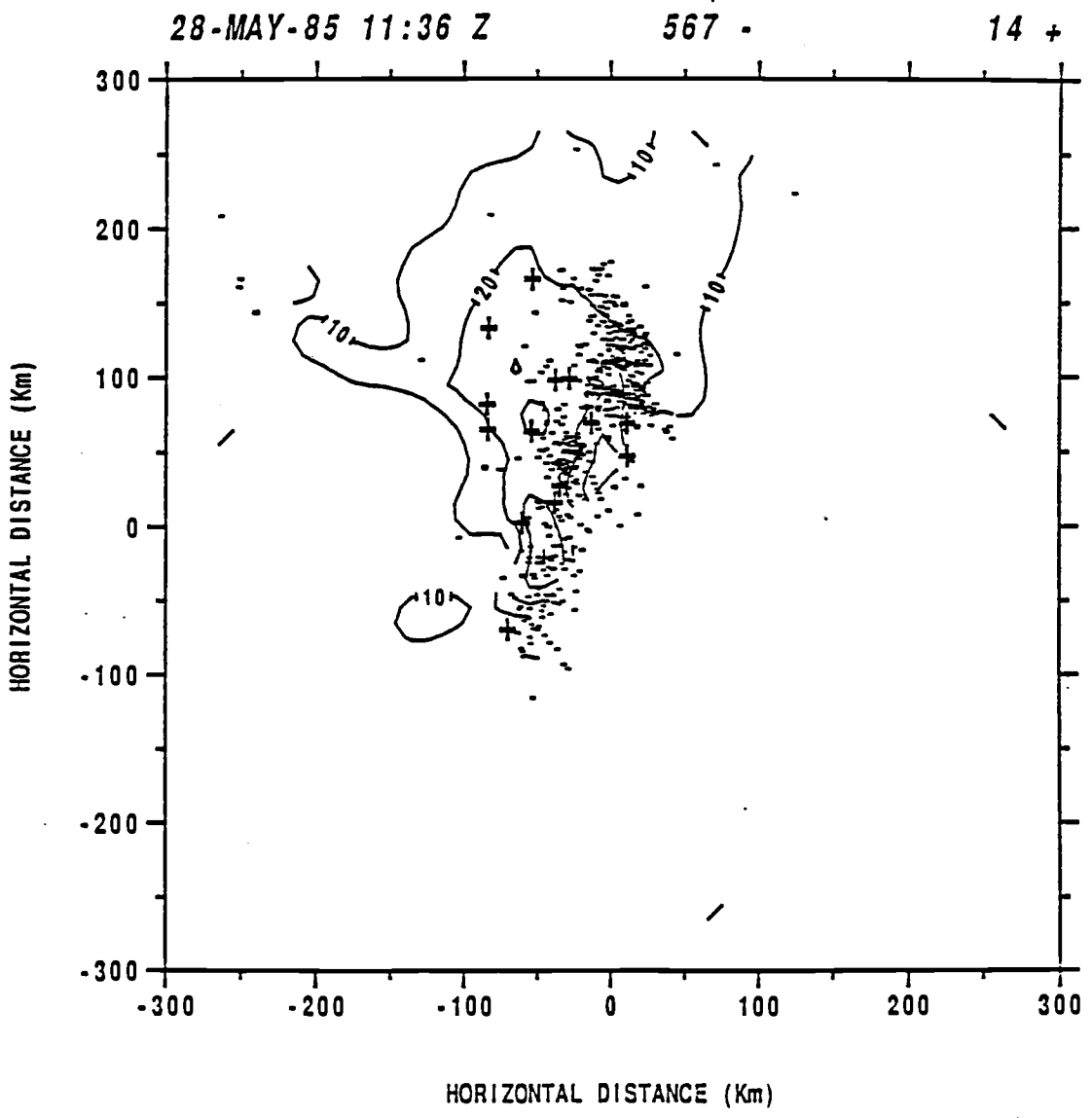


Fig. 3.24 Radar echo pattern and lightning map for 1136Z on 28 May.

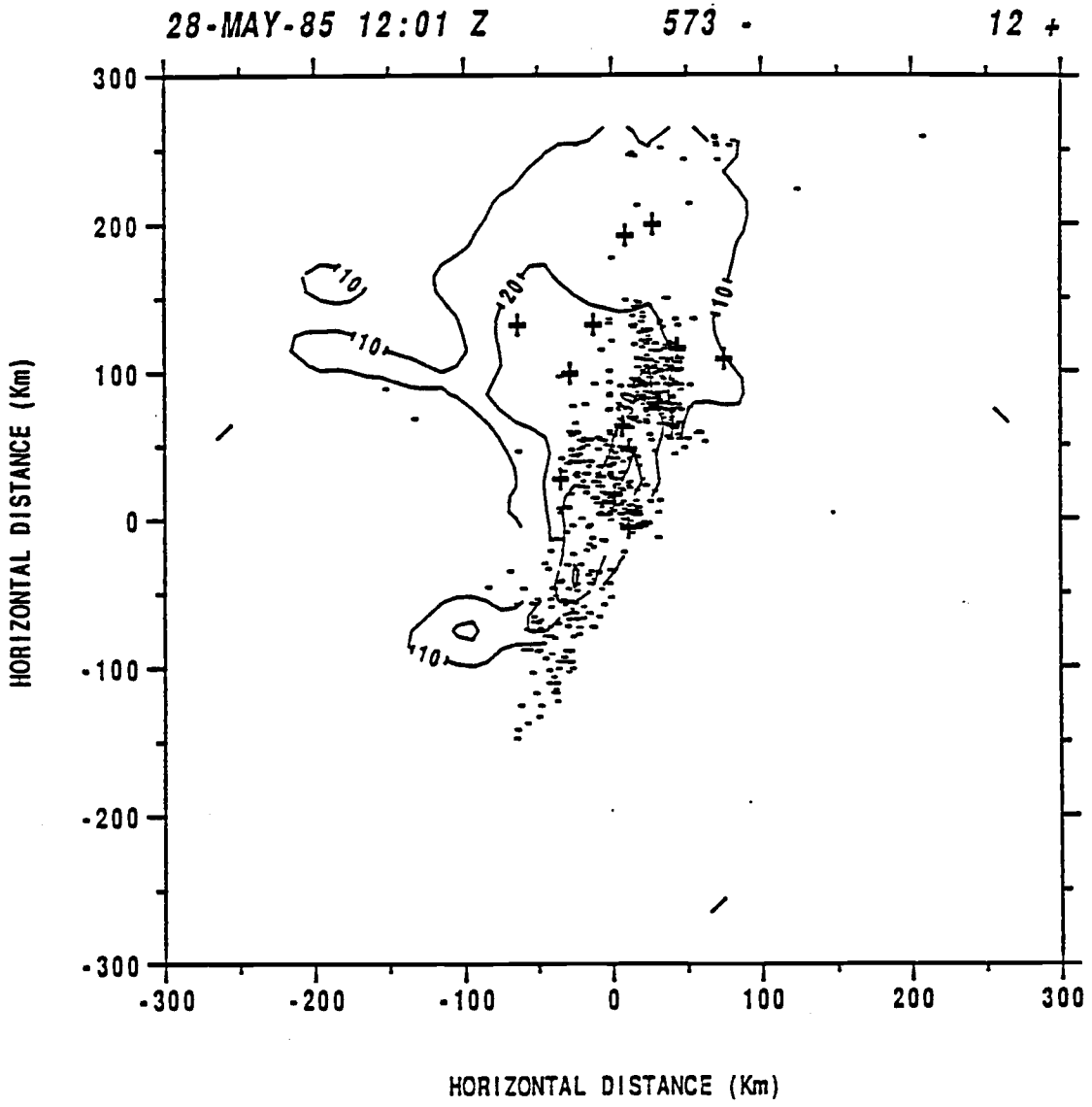


Fig. 3.25 Radar echo pattern and lightning map for 1201Z on 28 May.

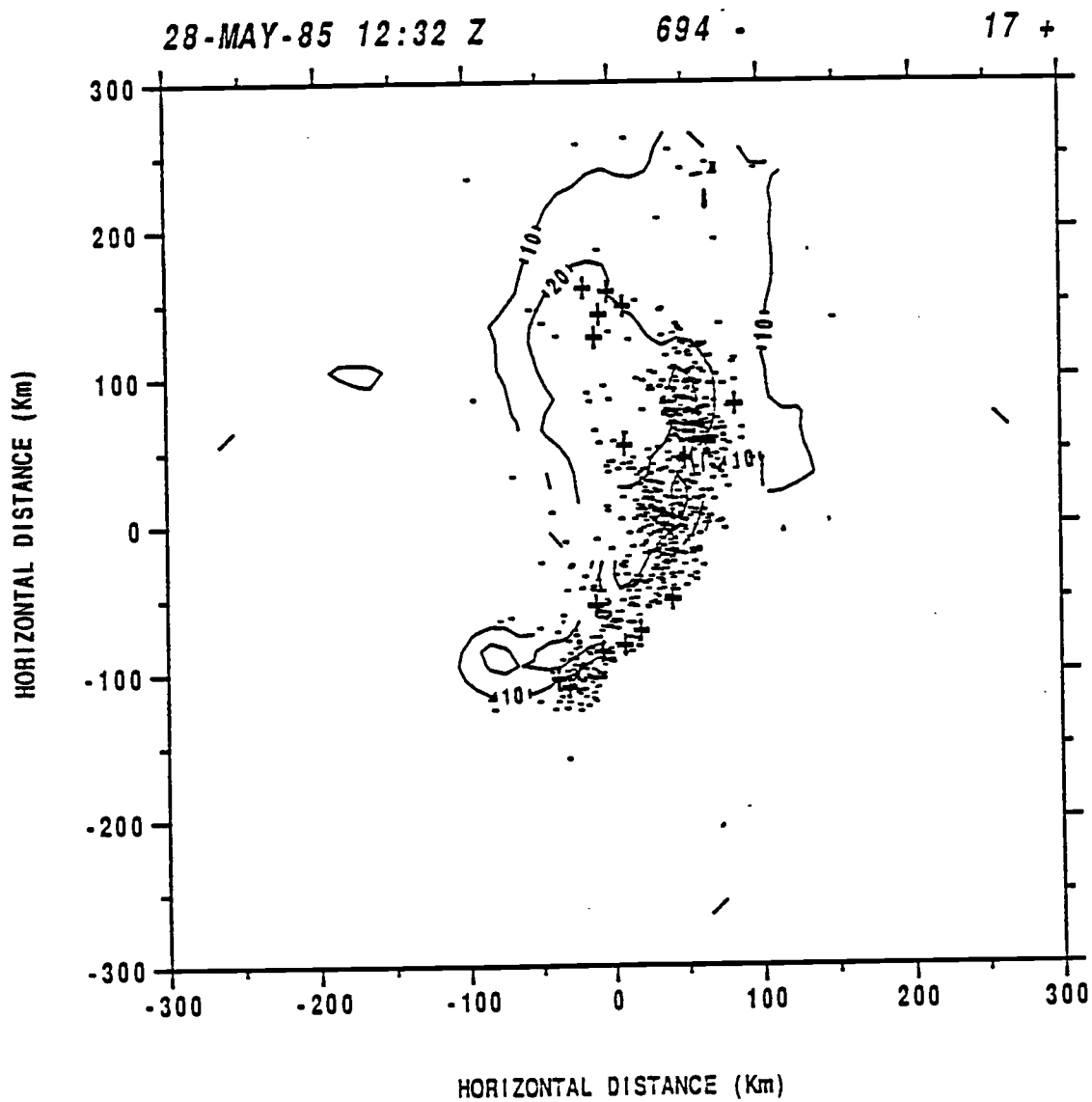


Fig. 3.26 Radar echo pattern and lightning map for 1232Z on 28 May.

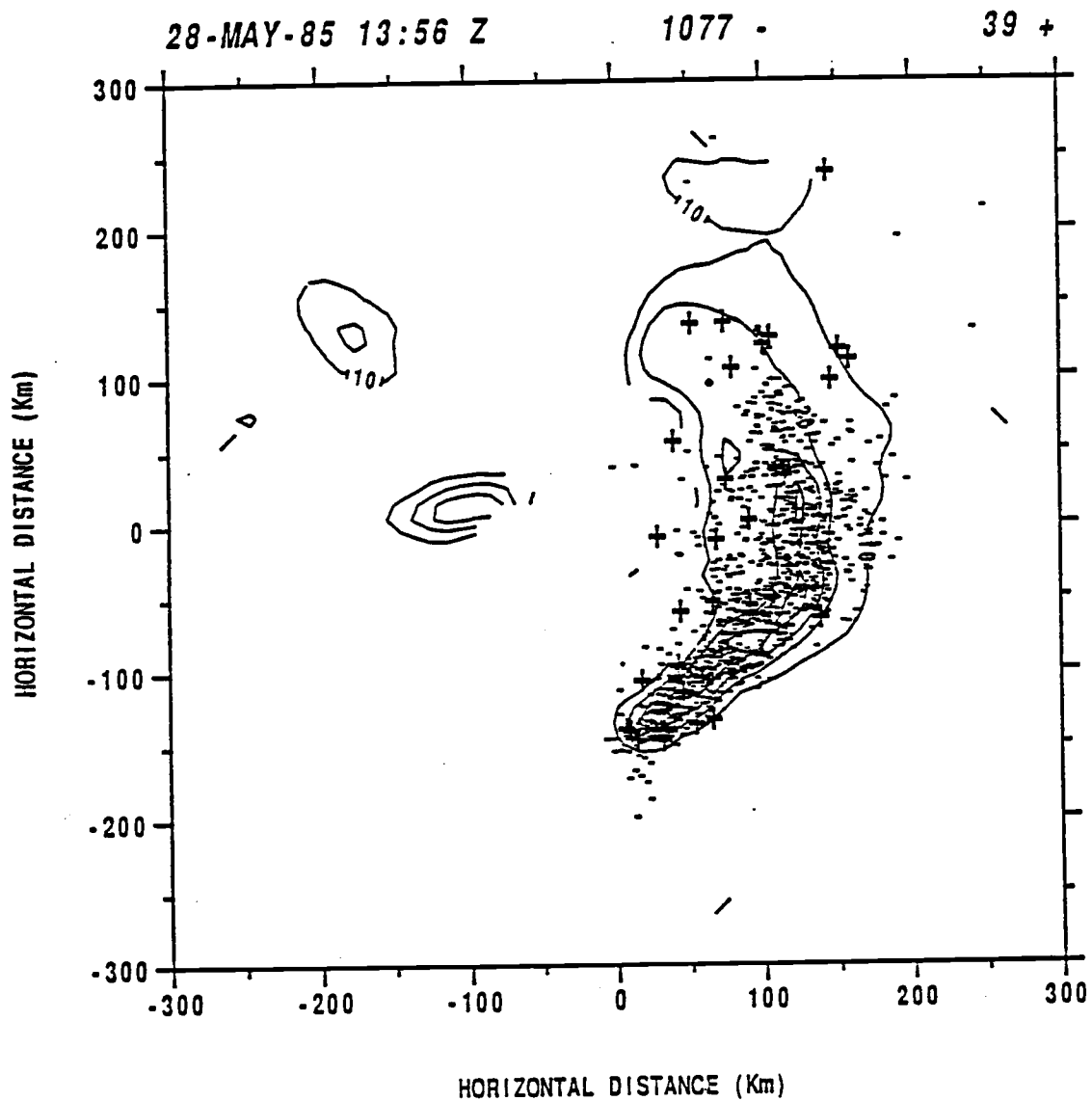


Fig. 3.27 Radar echo pattern and lightning map for 1356Z on 28 May.

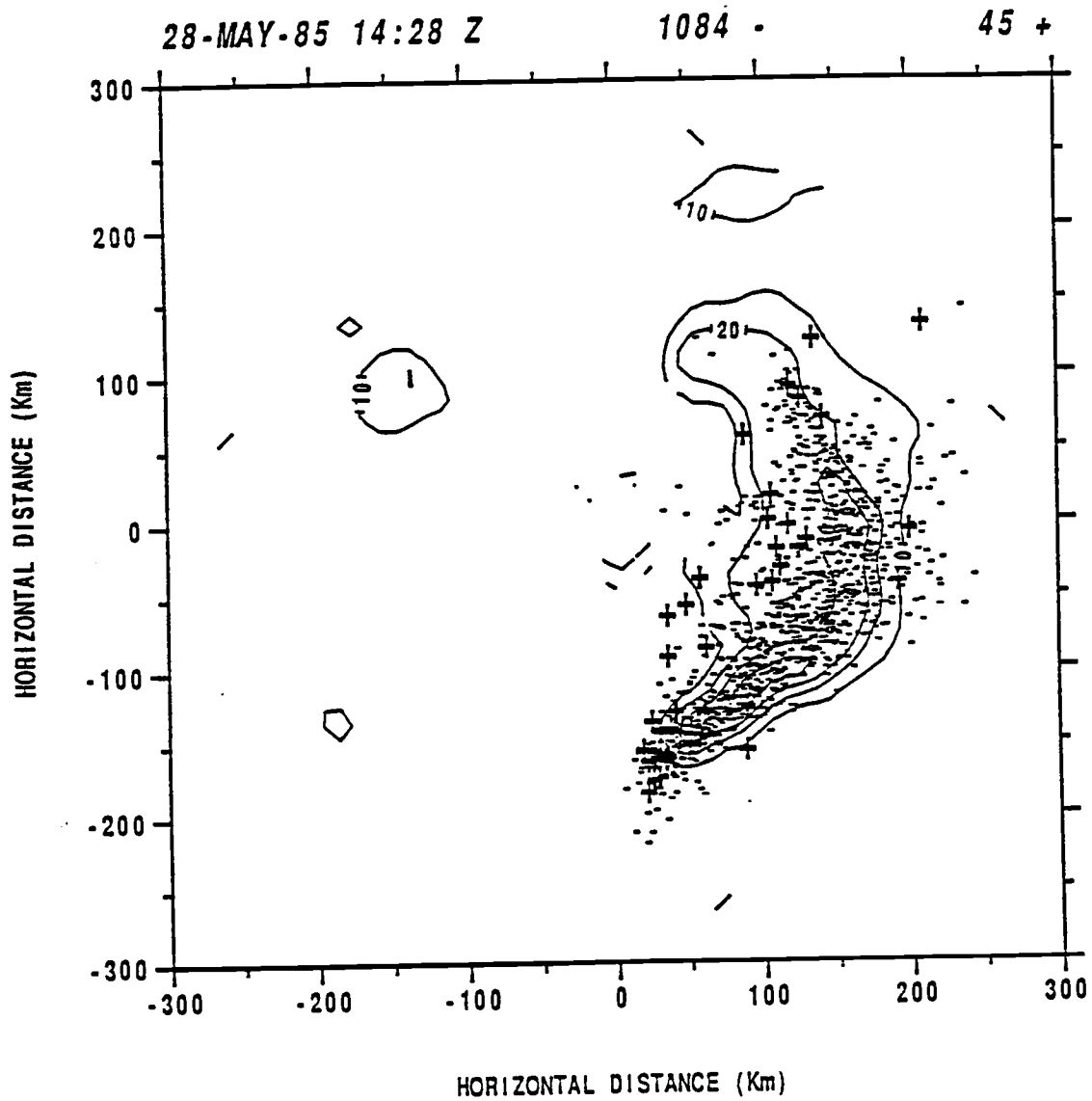


Fig. 3.28 Radar echo pattern and lightning map for 1428Z on 28 May.

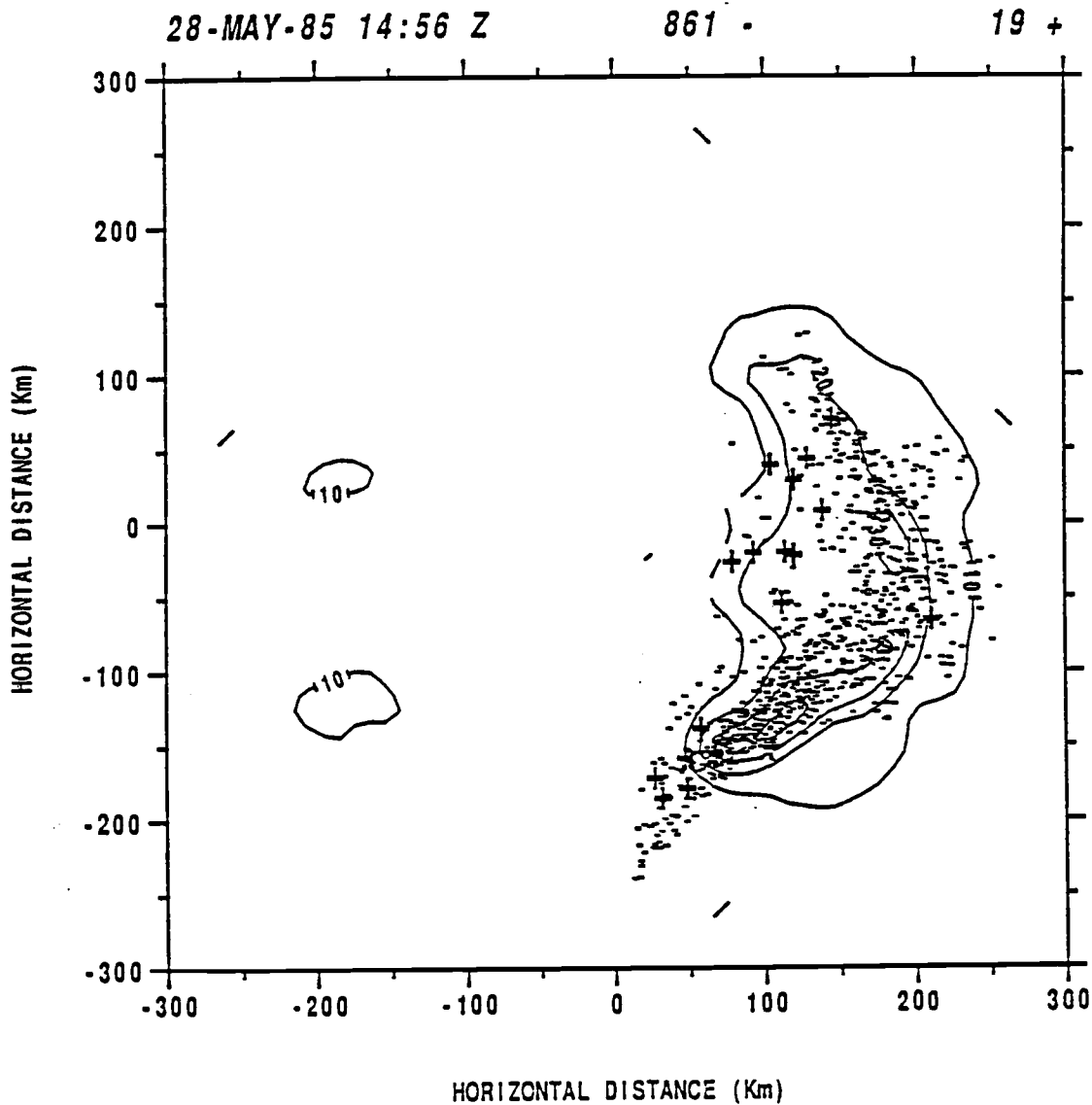


Fig. 3.29 Radar echo pattern and lightning map for 1456Z on 28 May.

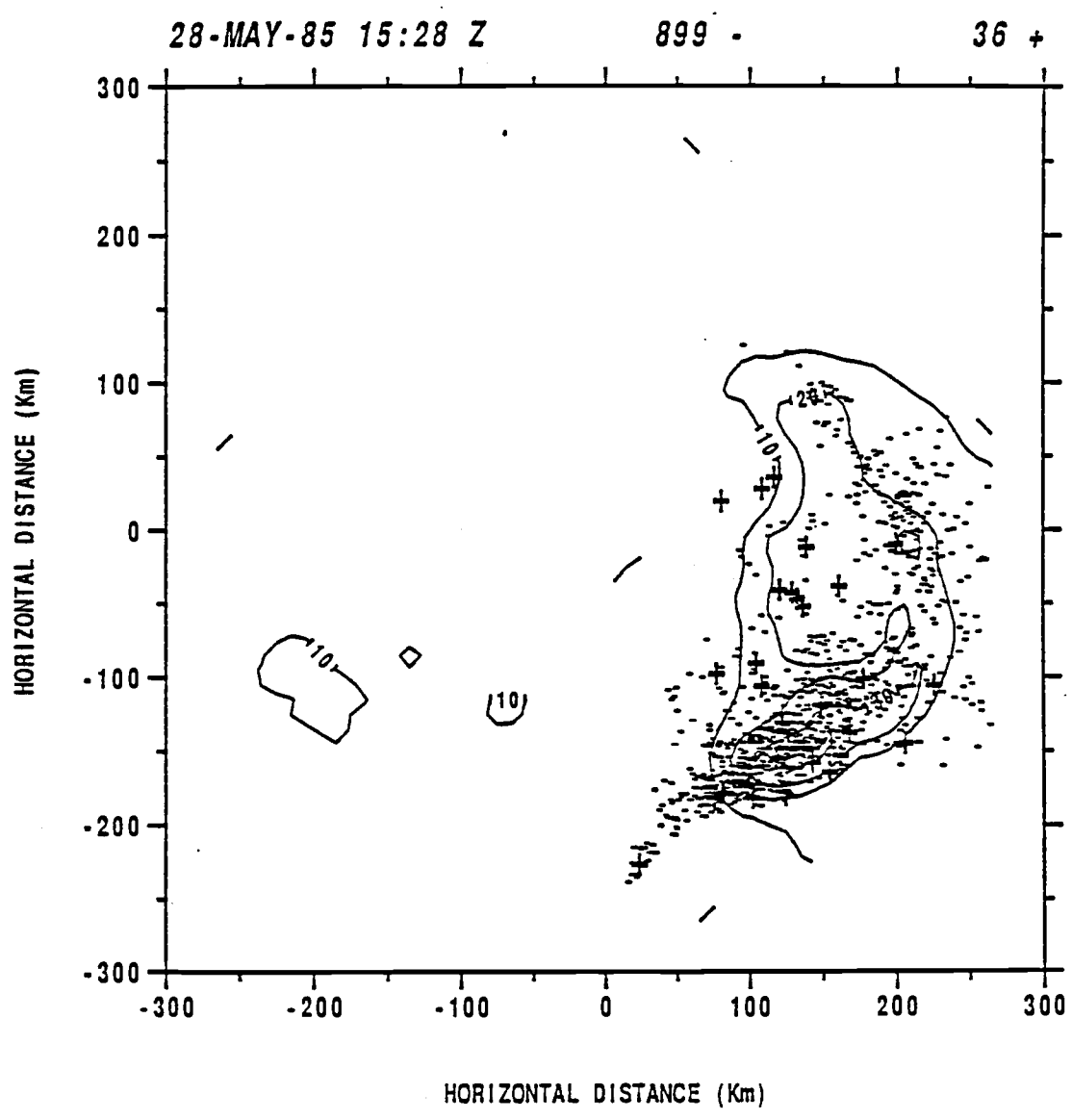


Fig. 3.30 Radar echo pattern and lightning map for 1528Z on 28 May.

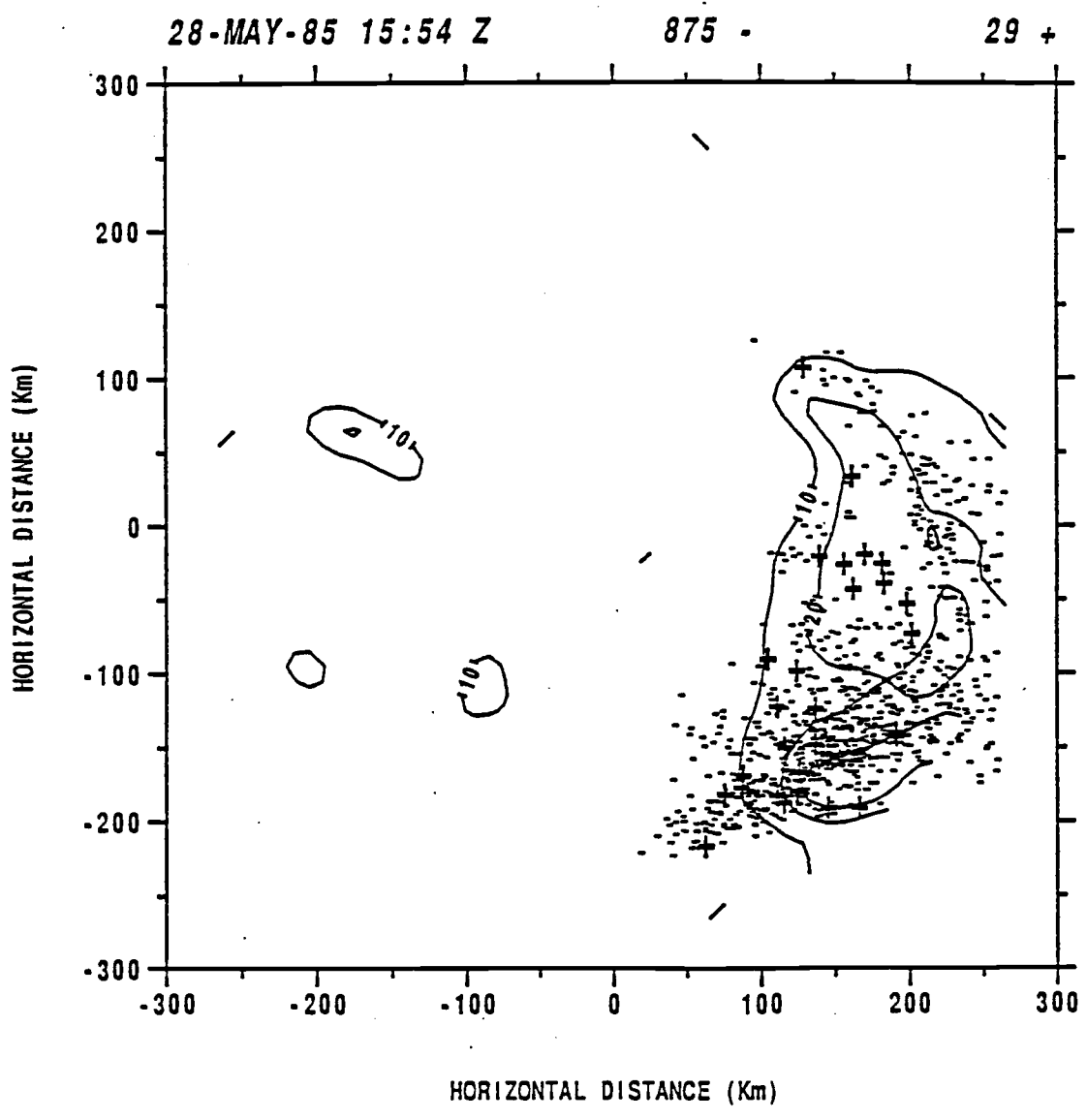


Fig. 3.31 Radar echo pattern and lightning map for 1554Z on 28 May.

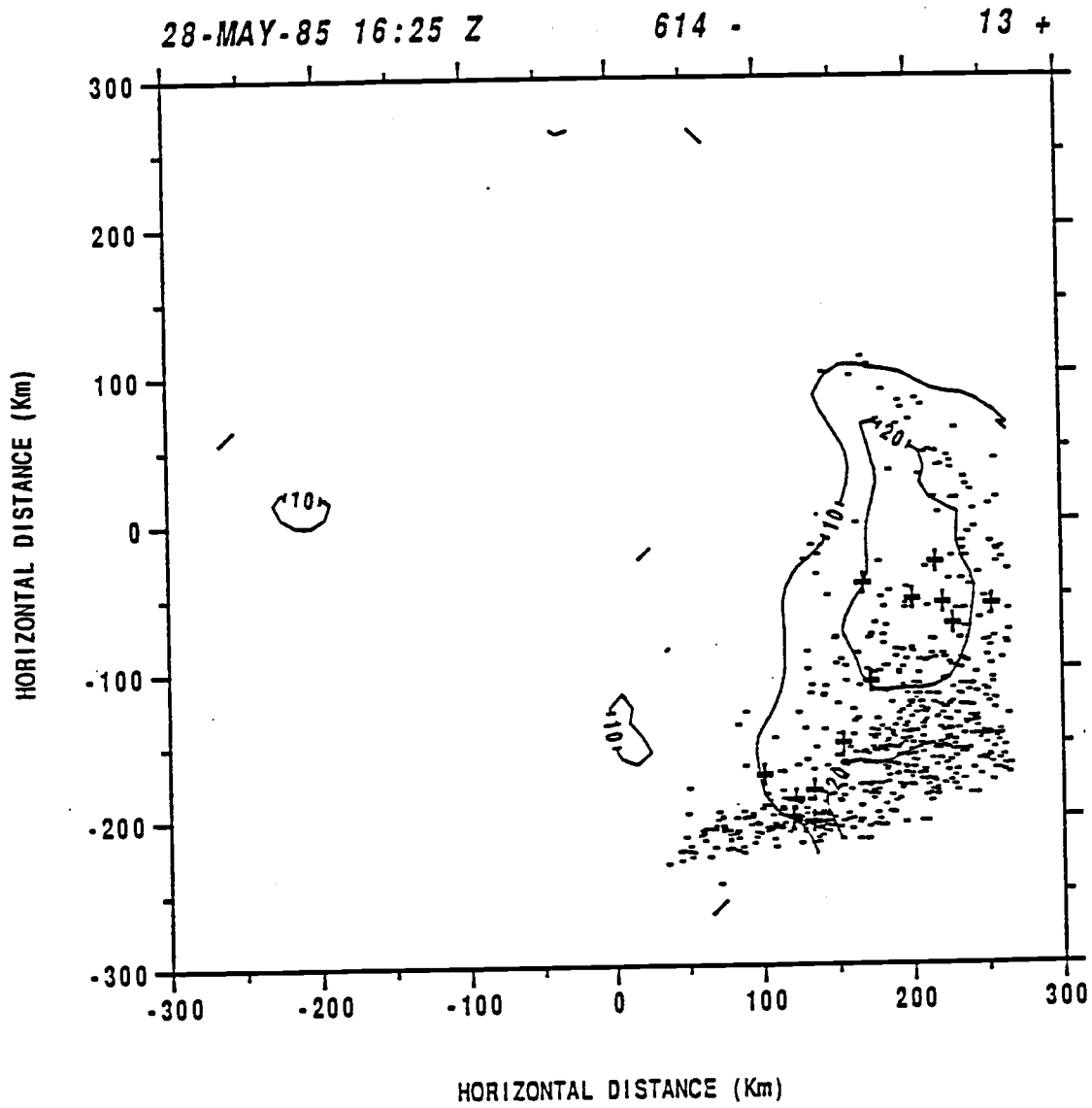


Fig. 3.32 Radar echo pattern and lightning map for 1625Z on 28 May.

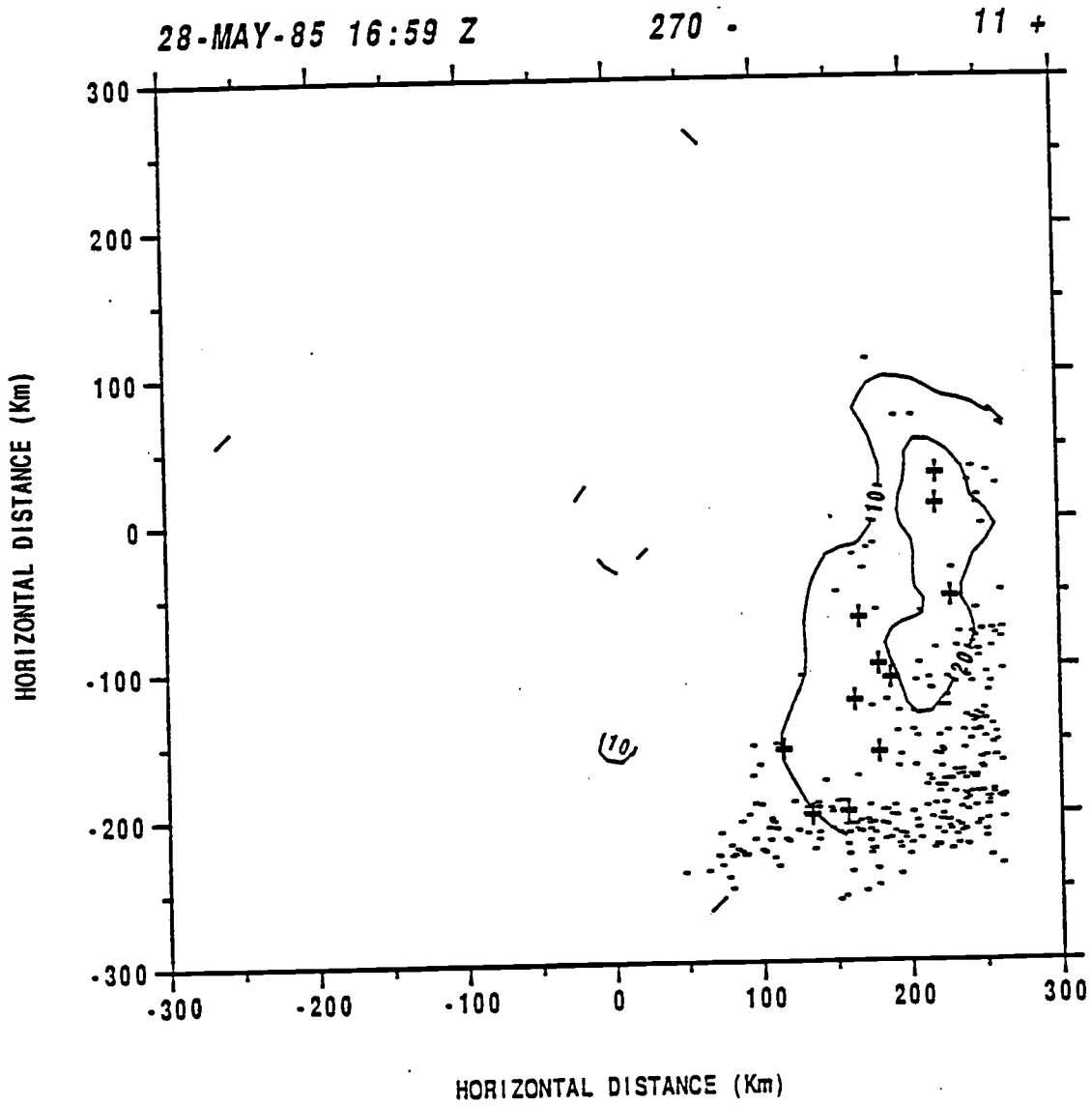


Fig. 3.33 Radar echo pattern and lightning map for 1659Z on 28 May.

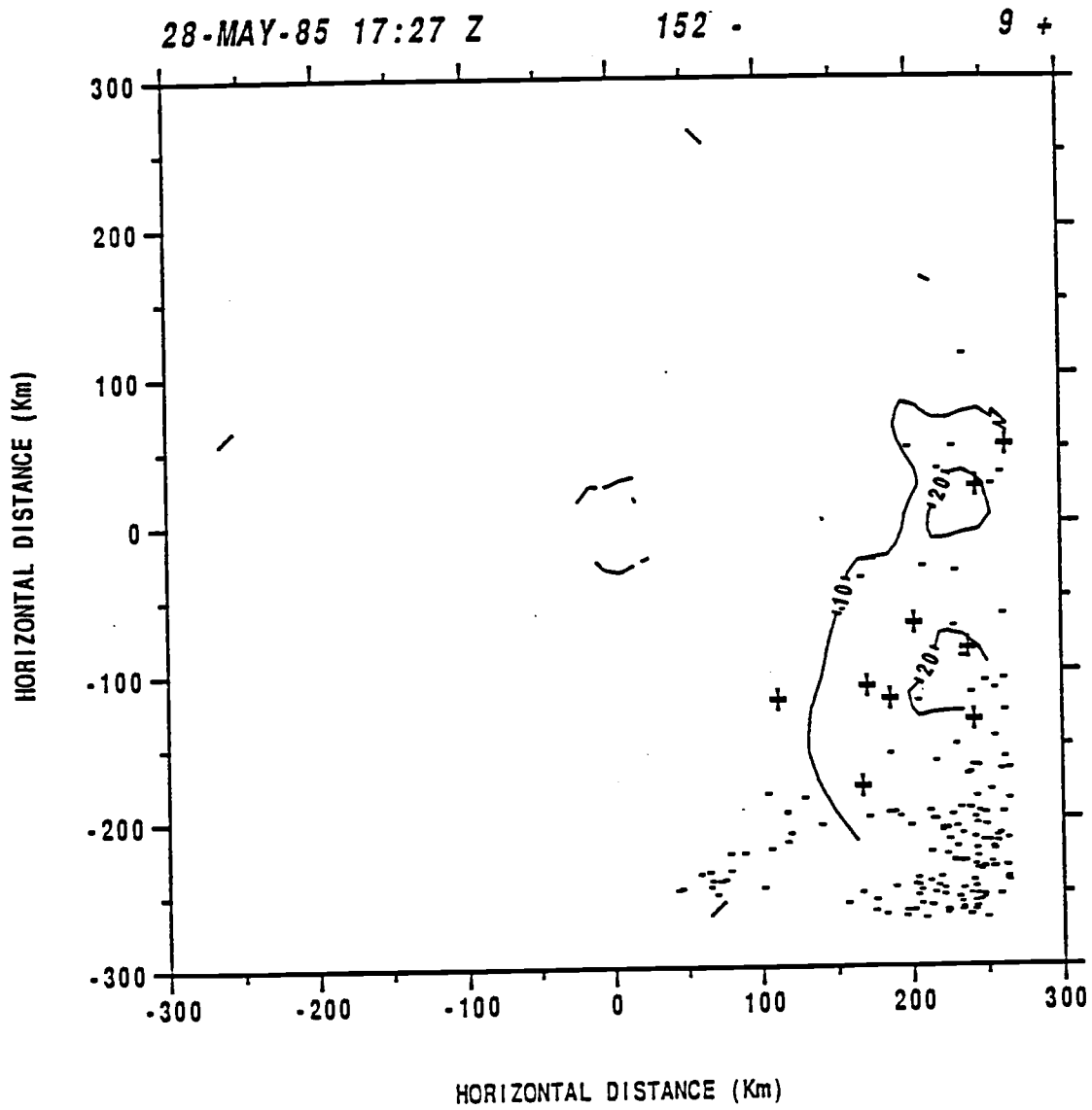


Fig. 3.34 Radar echo pattern and lightning map for 1727Z on 28 May.

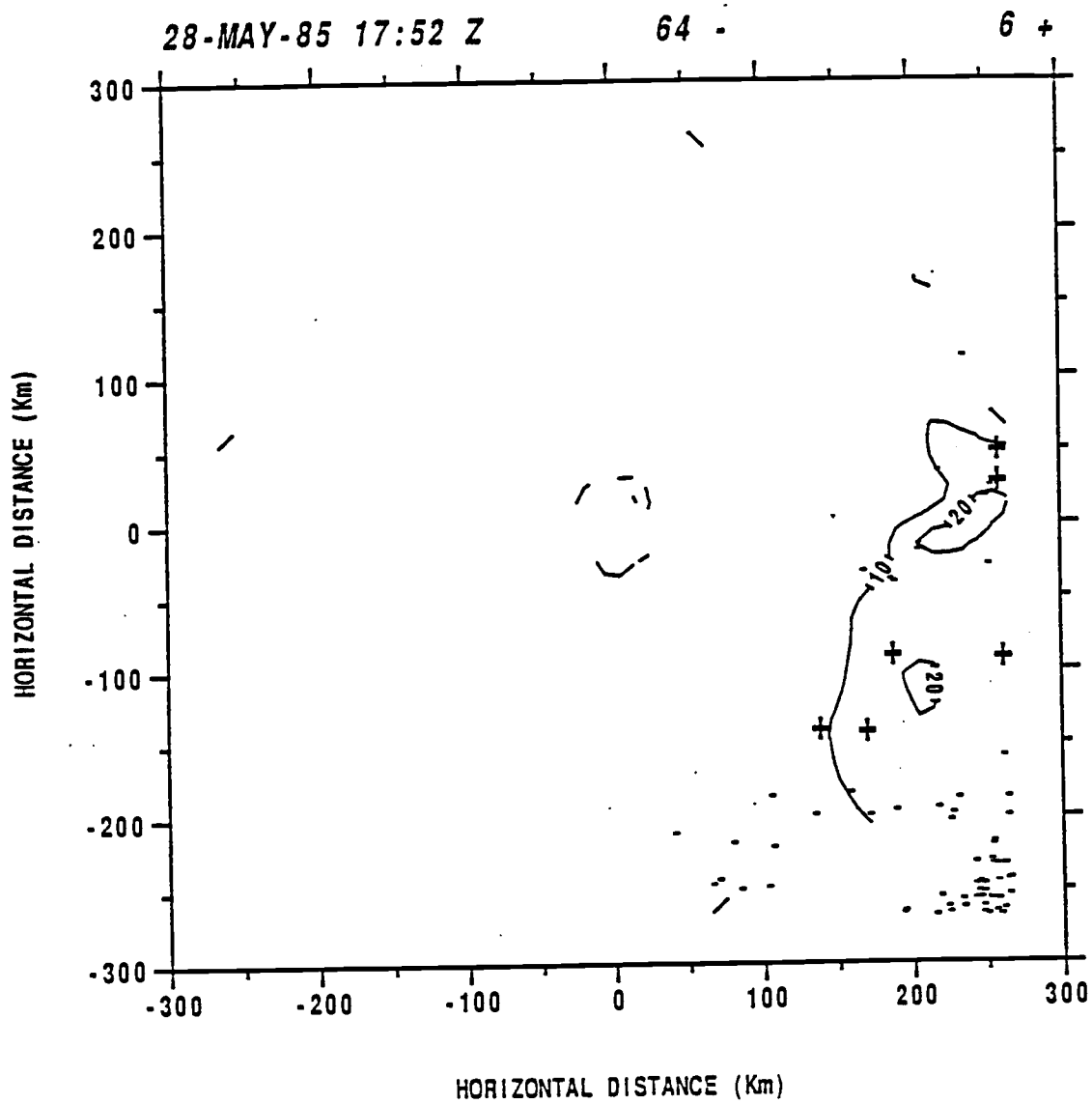


Fig. 3.35 Radar echo pattern and lightning map for 1752Z on 28 May.

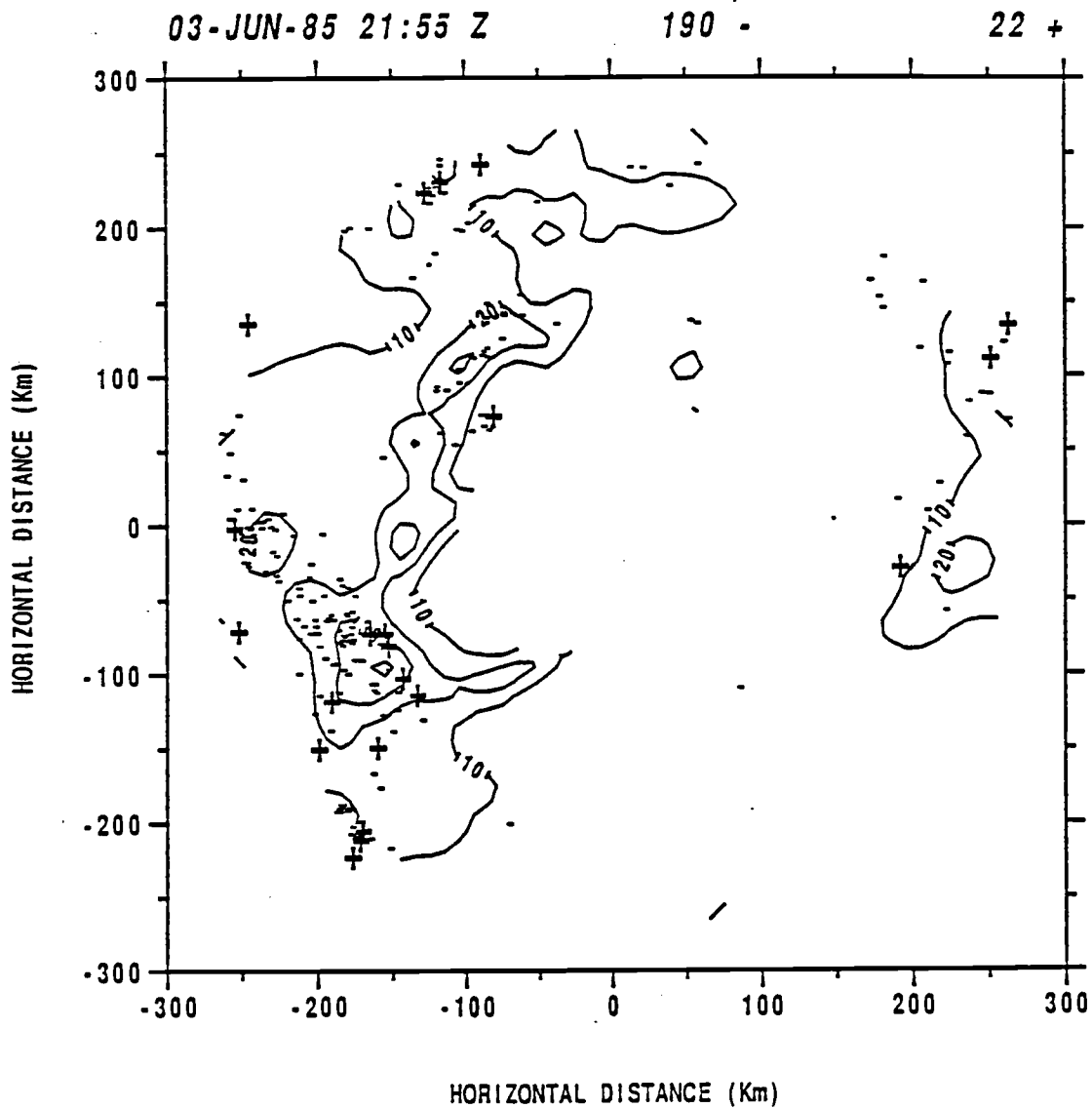


Fig. 3.36 Radar echo pattern and lightning map for 2155Z on 03 June.

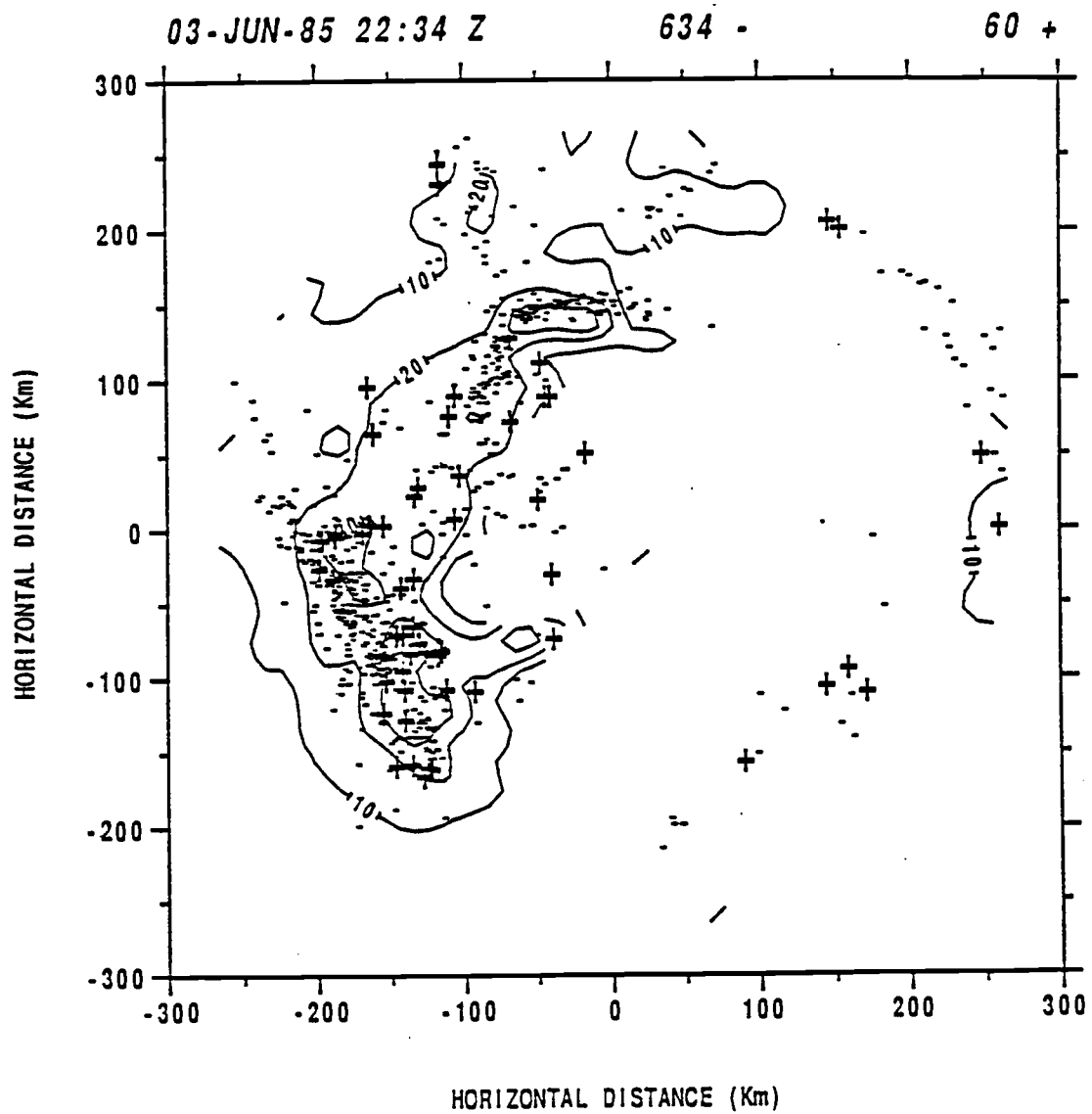


Fig. 3.37 Radar echo pattern and lightning map for 2234Z on 03 June.

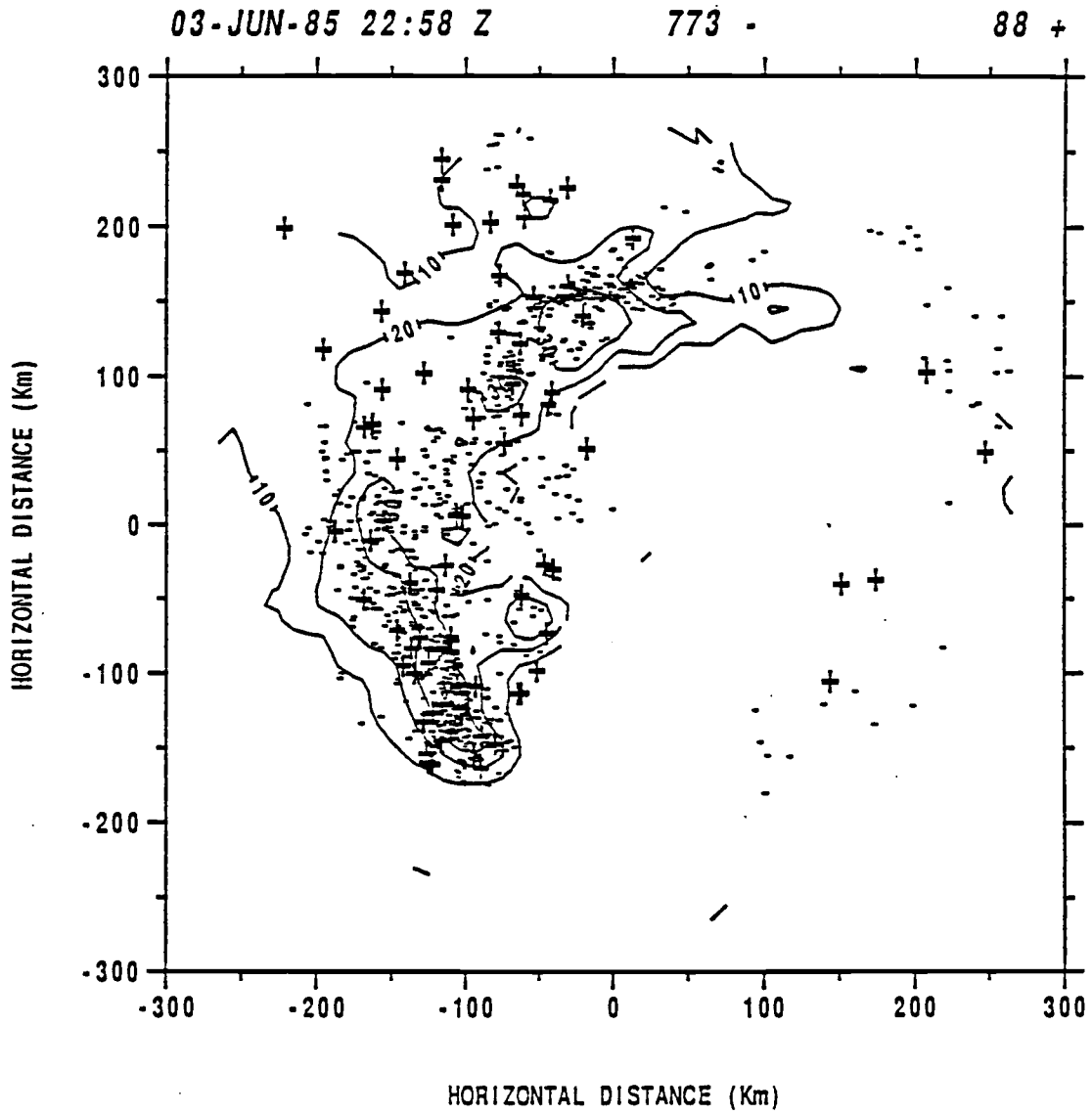


Fig. 3.38 Radar echo pattern and lightning map for 2258Z on 03 June.

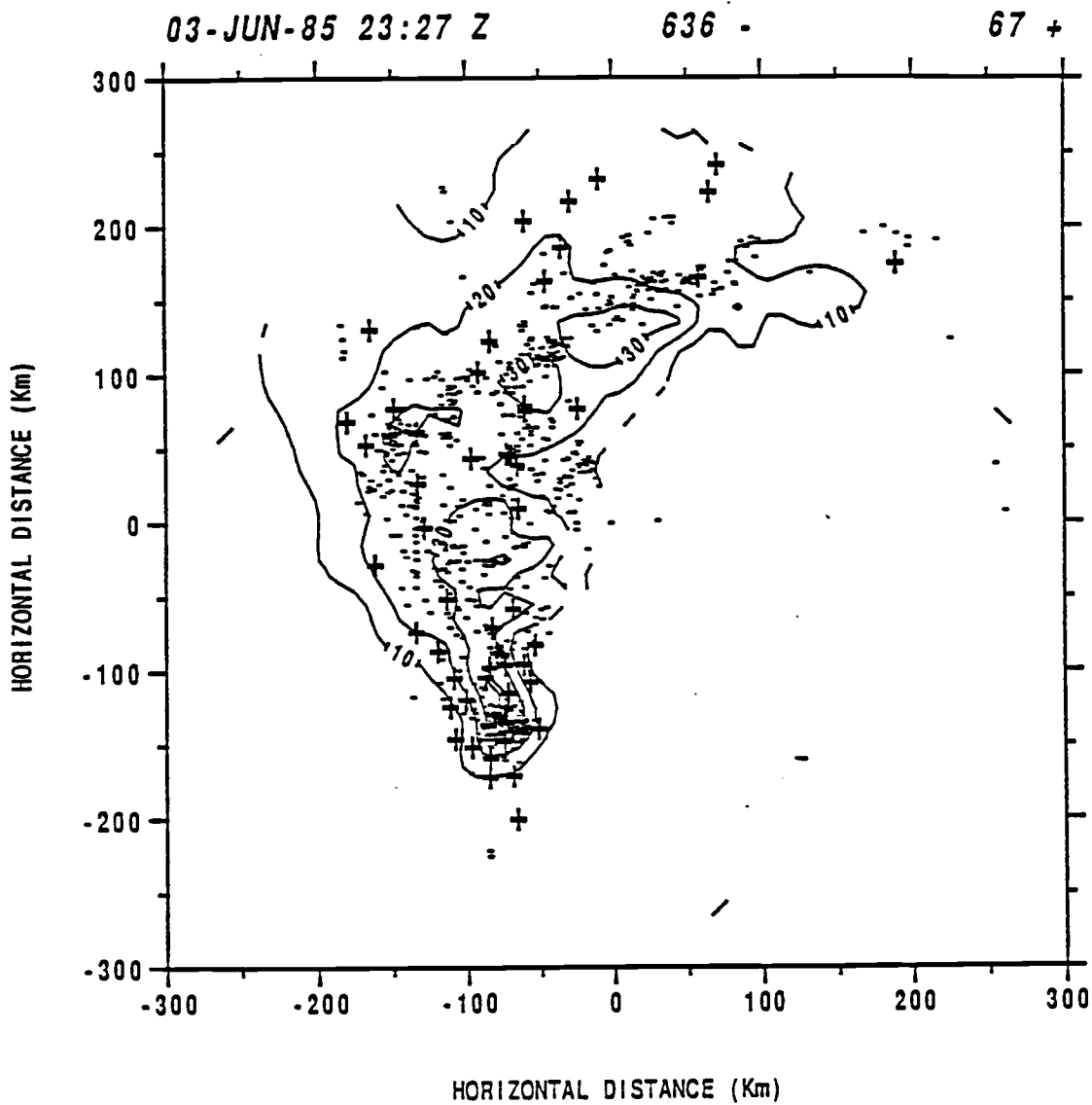


Fig. 3.39 Radar echo pattern and lightning map for 2327Z on 03 June.

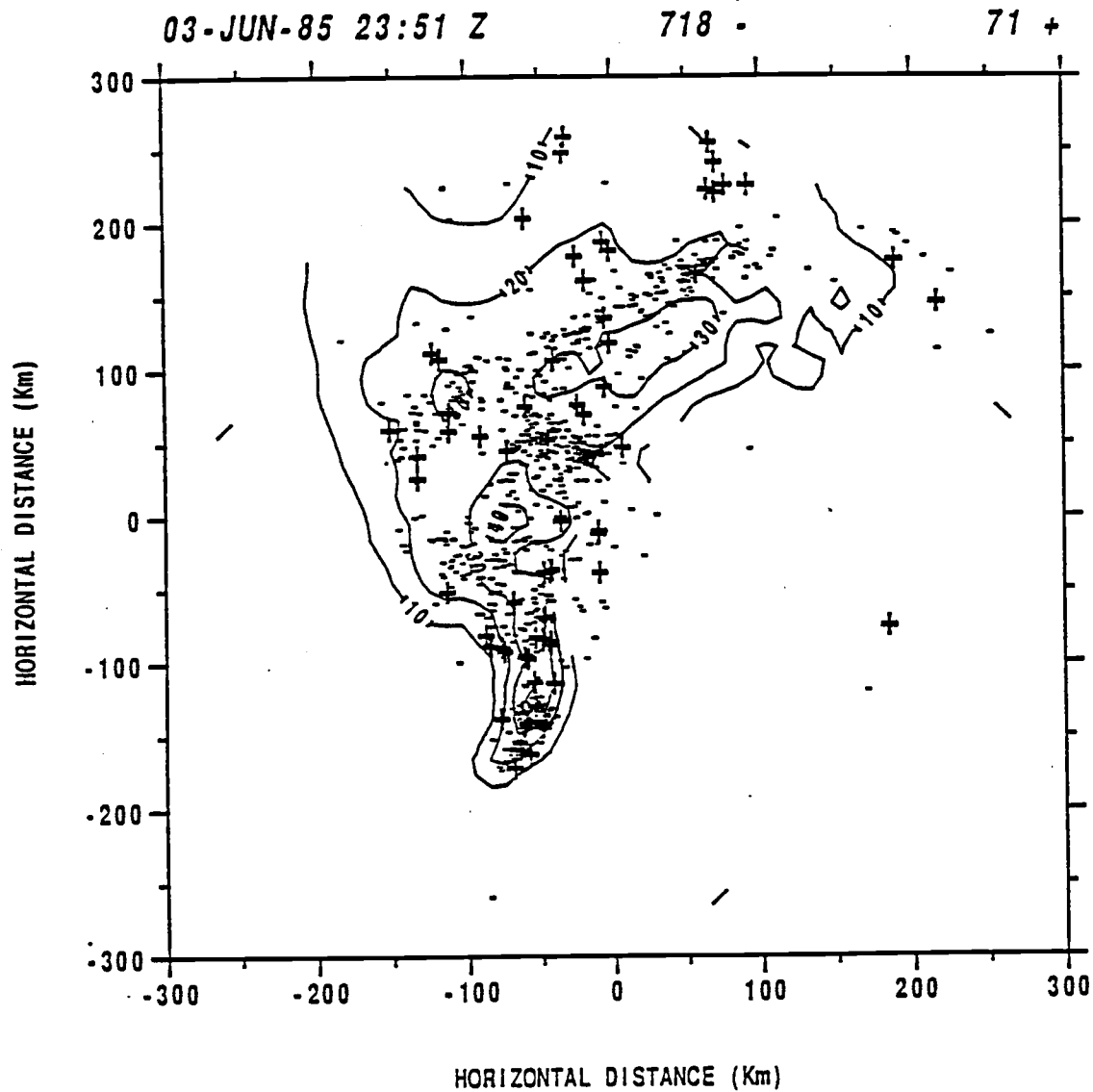


Fig. 3.40 Radar echo pattern and lightning map for 2351Z on 03 June.

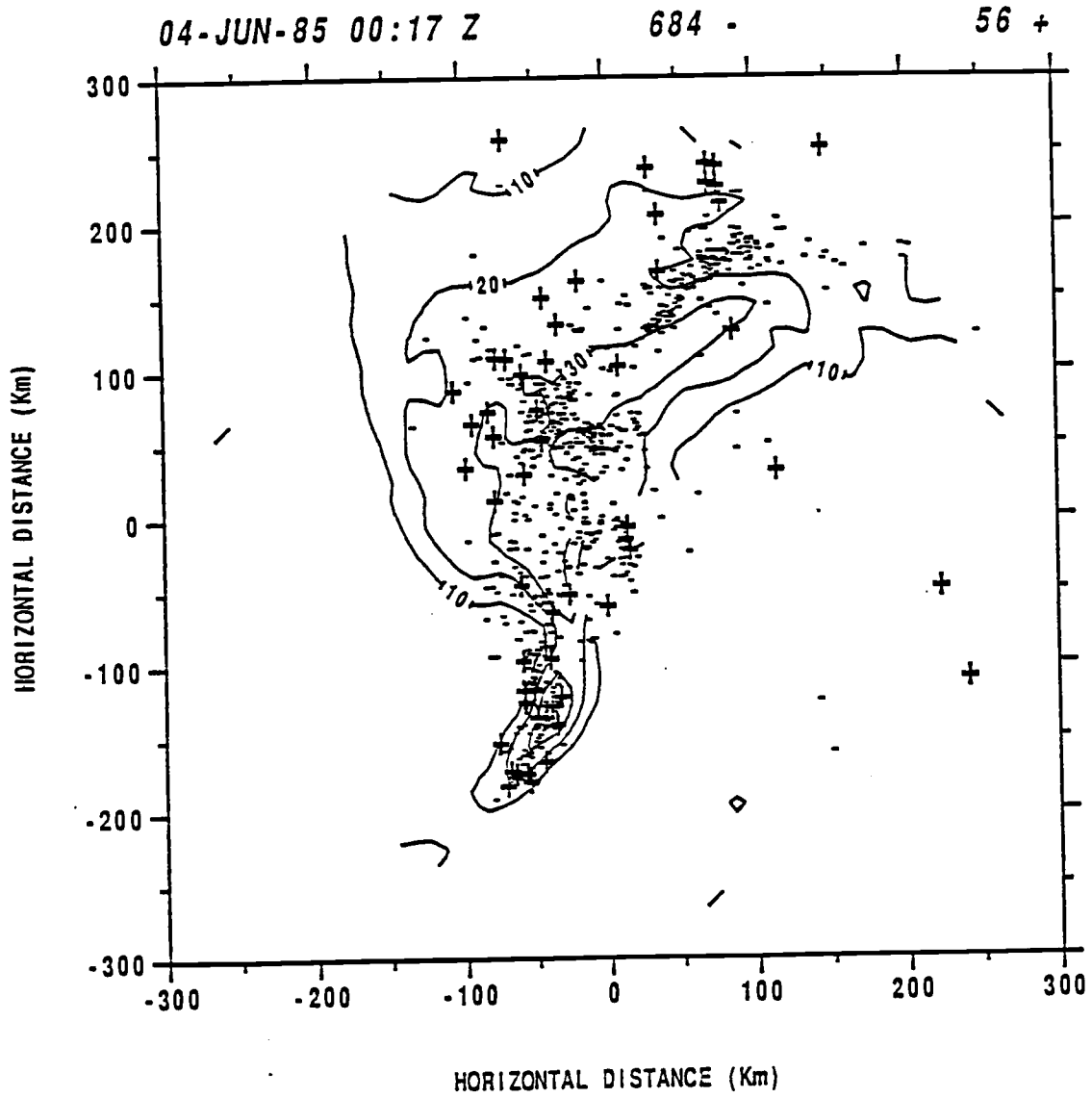


Fig. 3.41 Radar echo pattern and lightning map for 0017Z on 04 June.

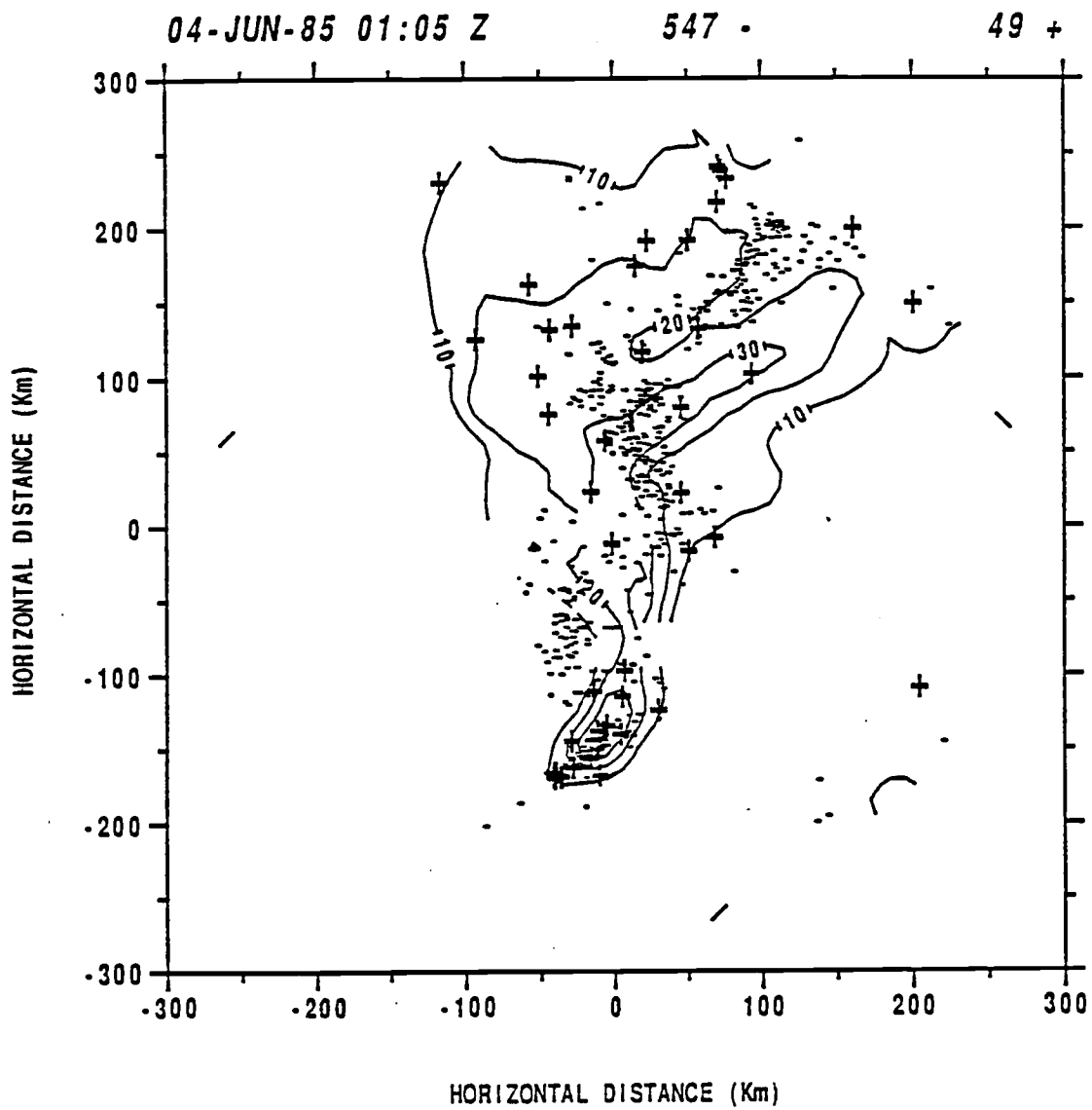


Fig. 3.42 Radar echo pattern and lightning map for 0105Z on 04 June.

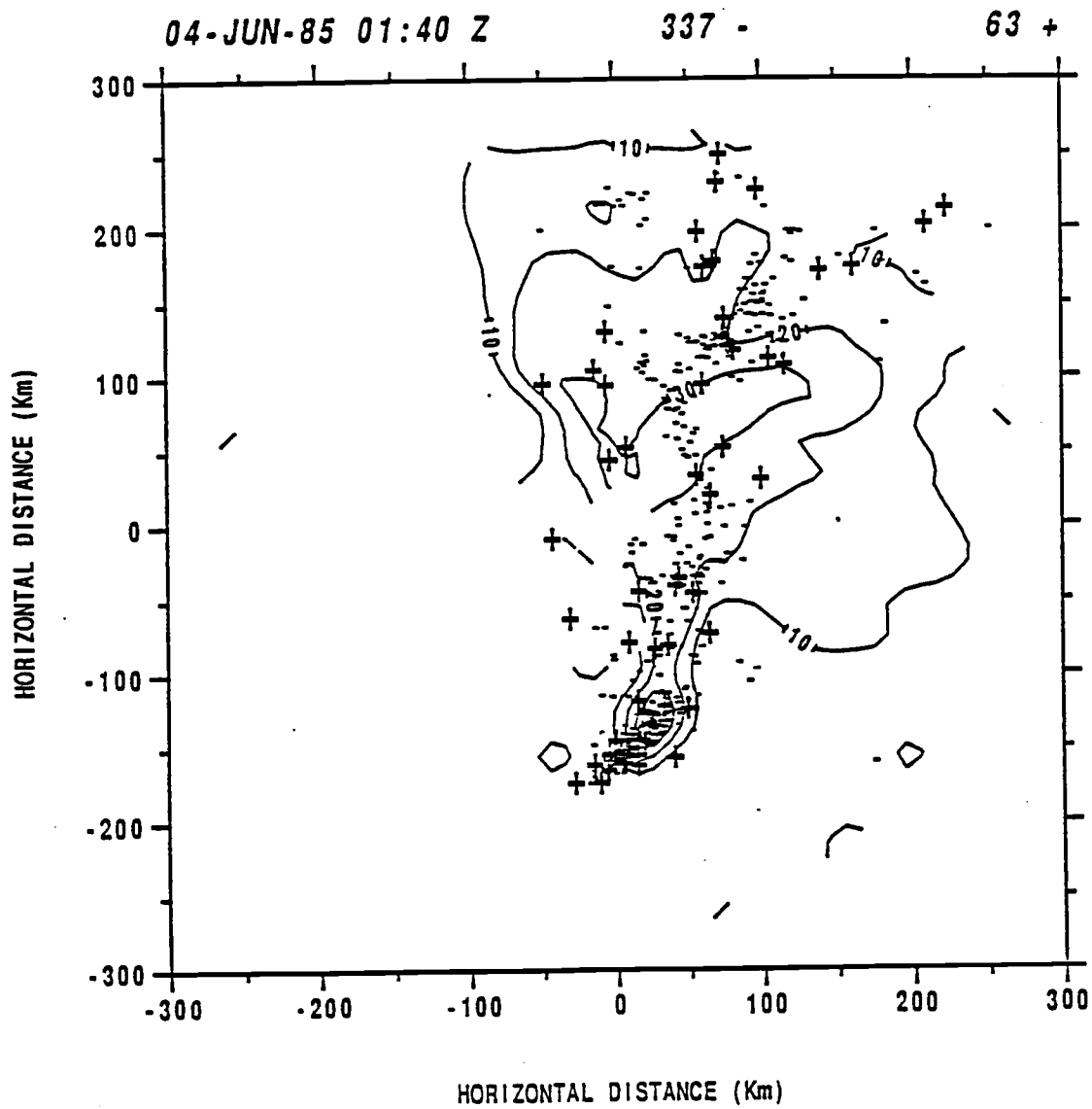


Fig. 3.43 Radar echo pattern and lightning map for 0140Z on 04 June.

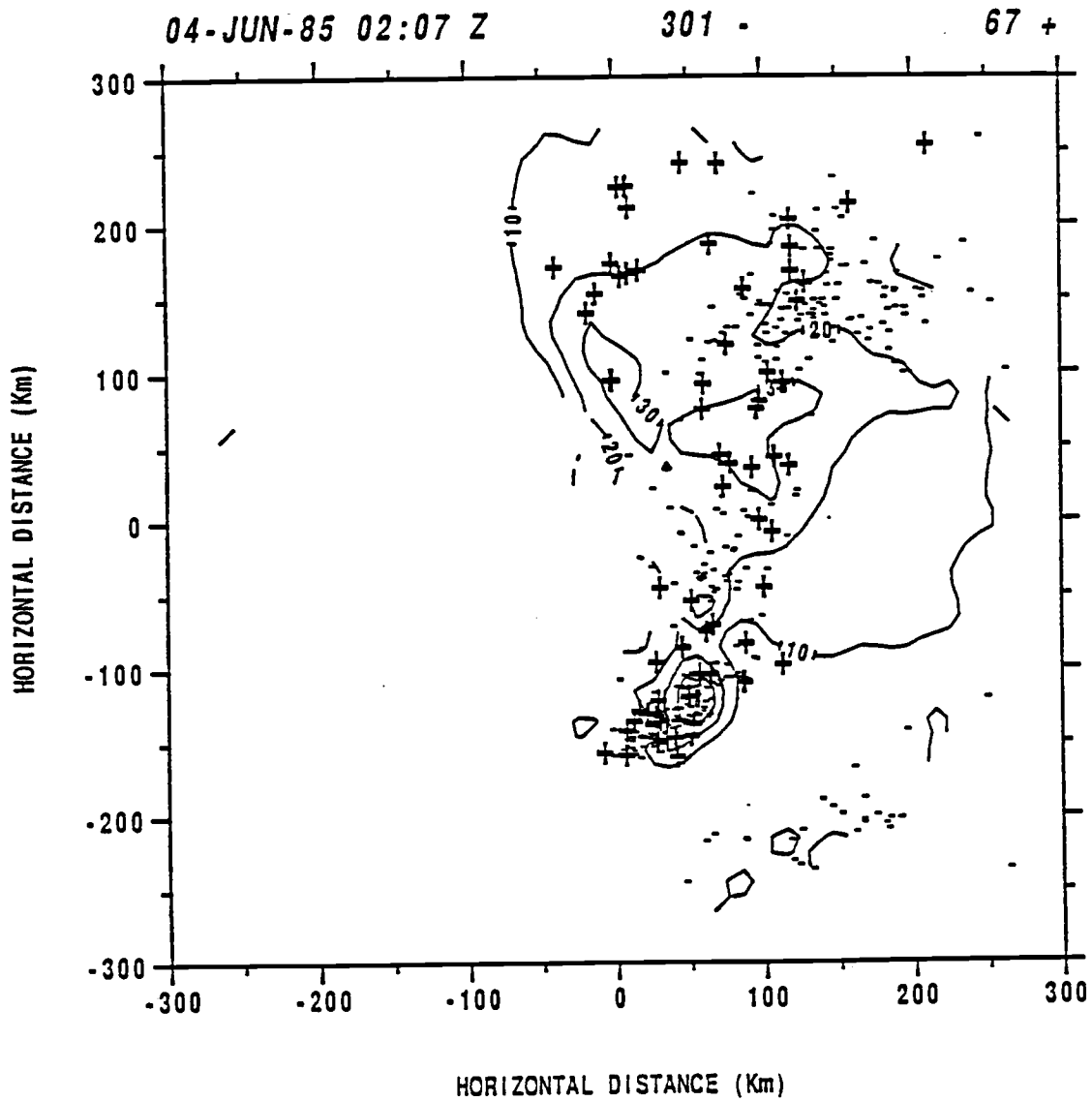


Fig. 3.44 Radar echo pattern and lightning map for 0207Z on 04 June.

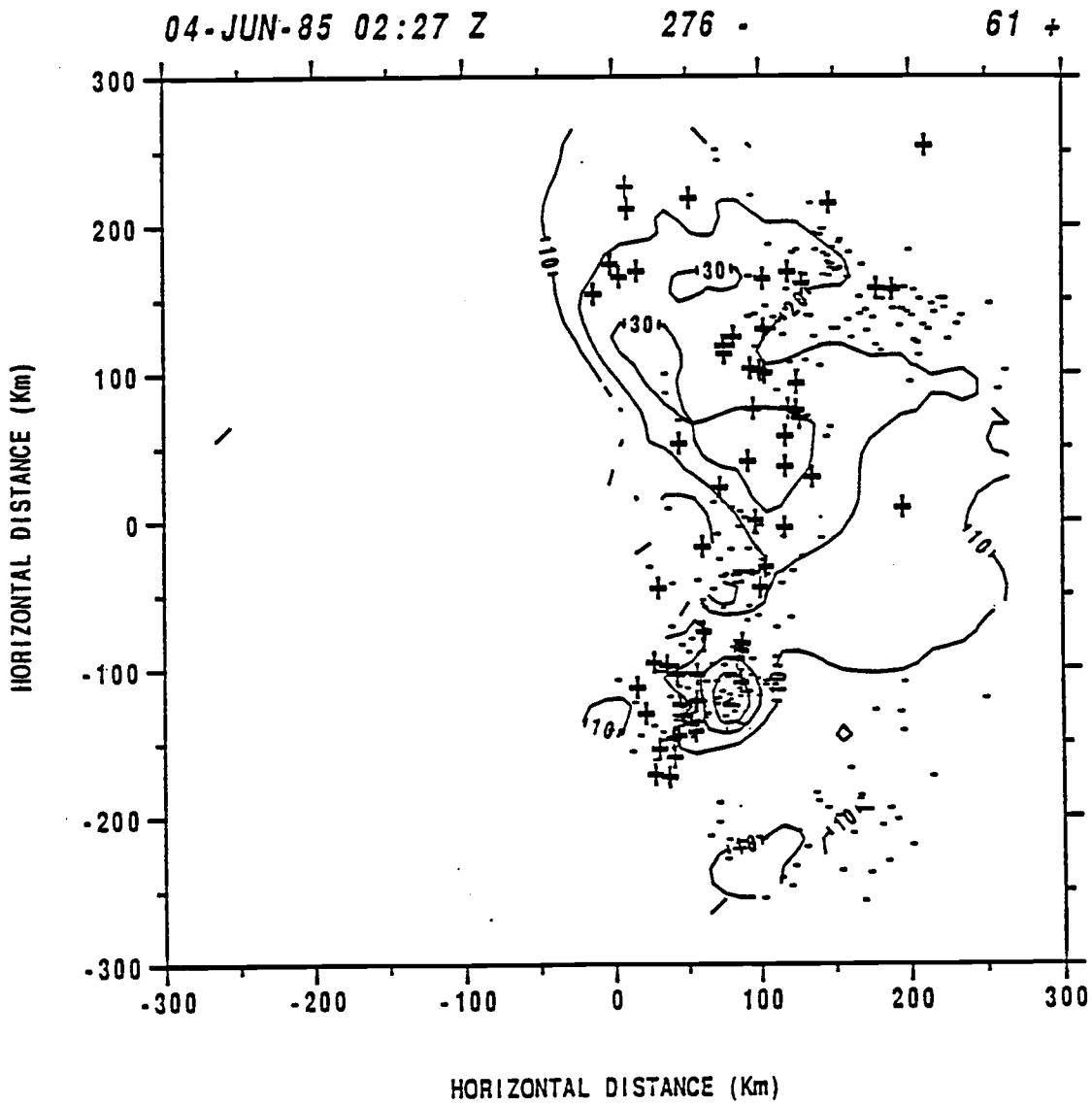


Fig. 3.45 Radar echo pattern and lightning map for 0227Z on 04 June.

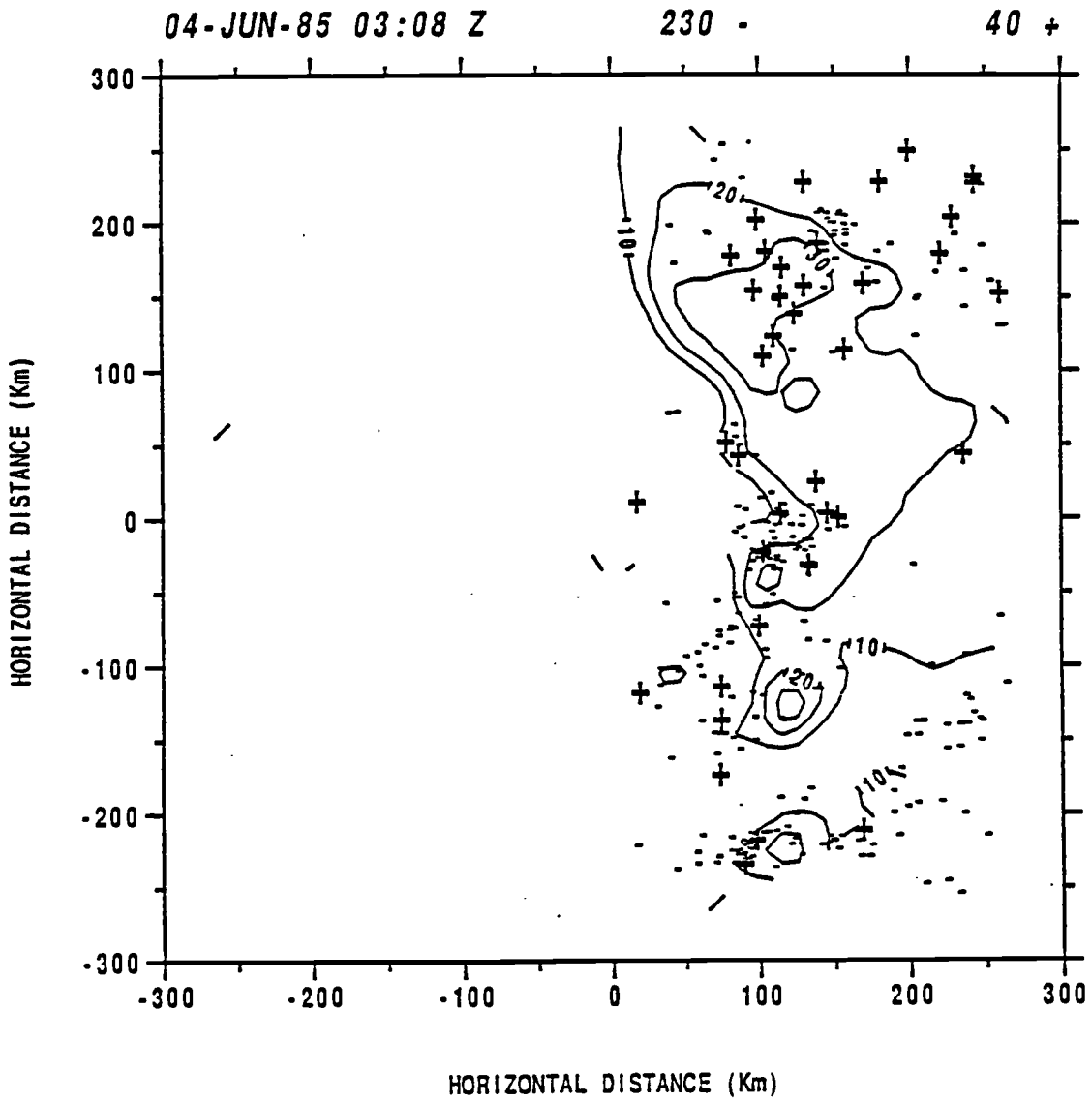


Fig. 3.46 Radar echo pattern and lightning map for 0308Z on 04 June.

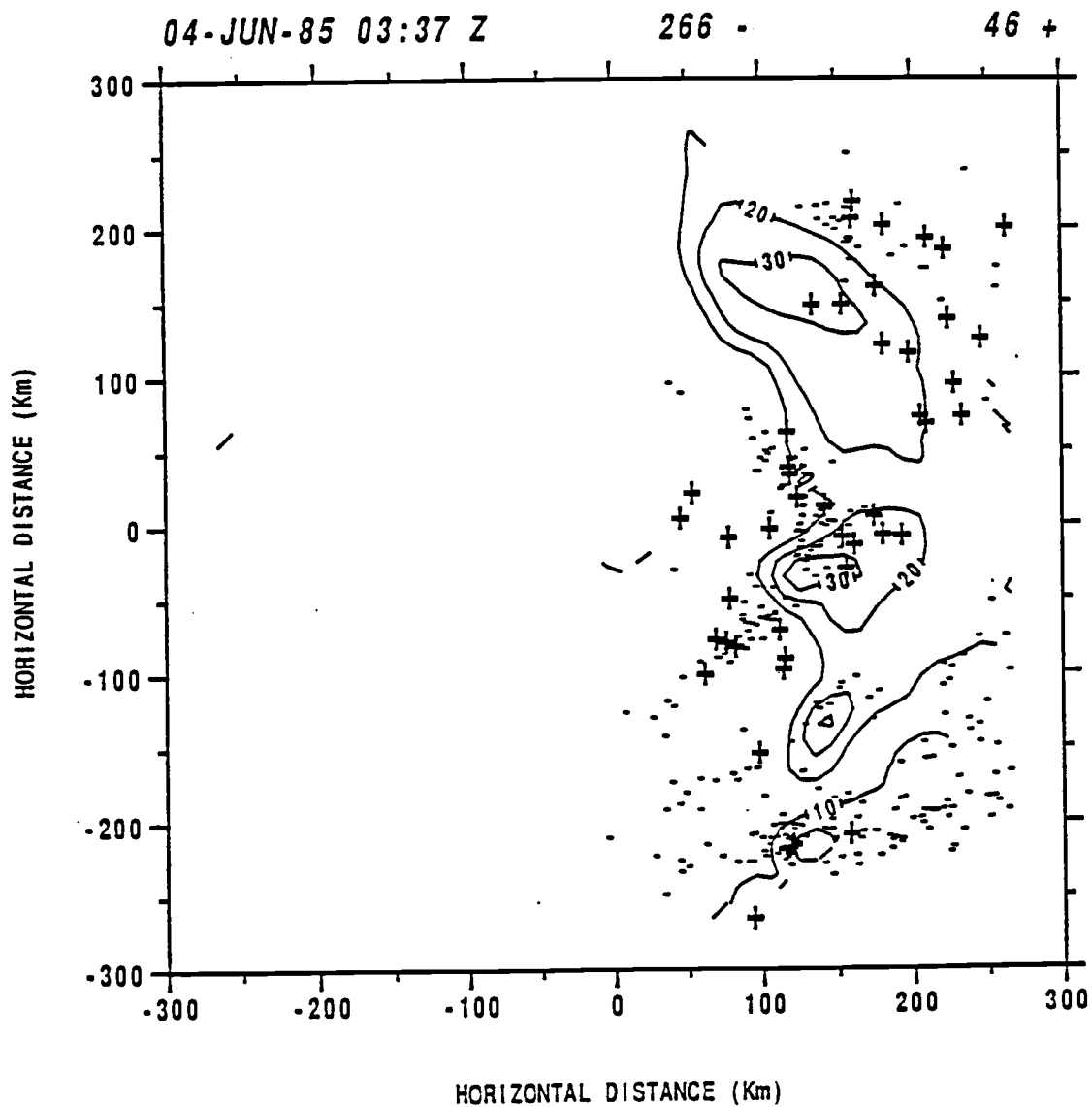


Fig. 3.47 Radar echo pattern and lightning map for 0337Z on 04 June.

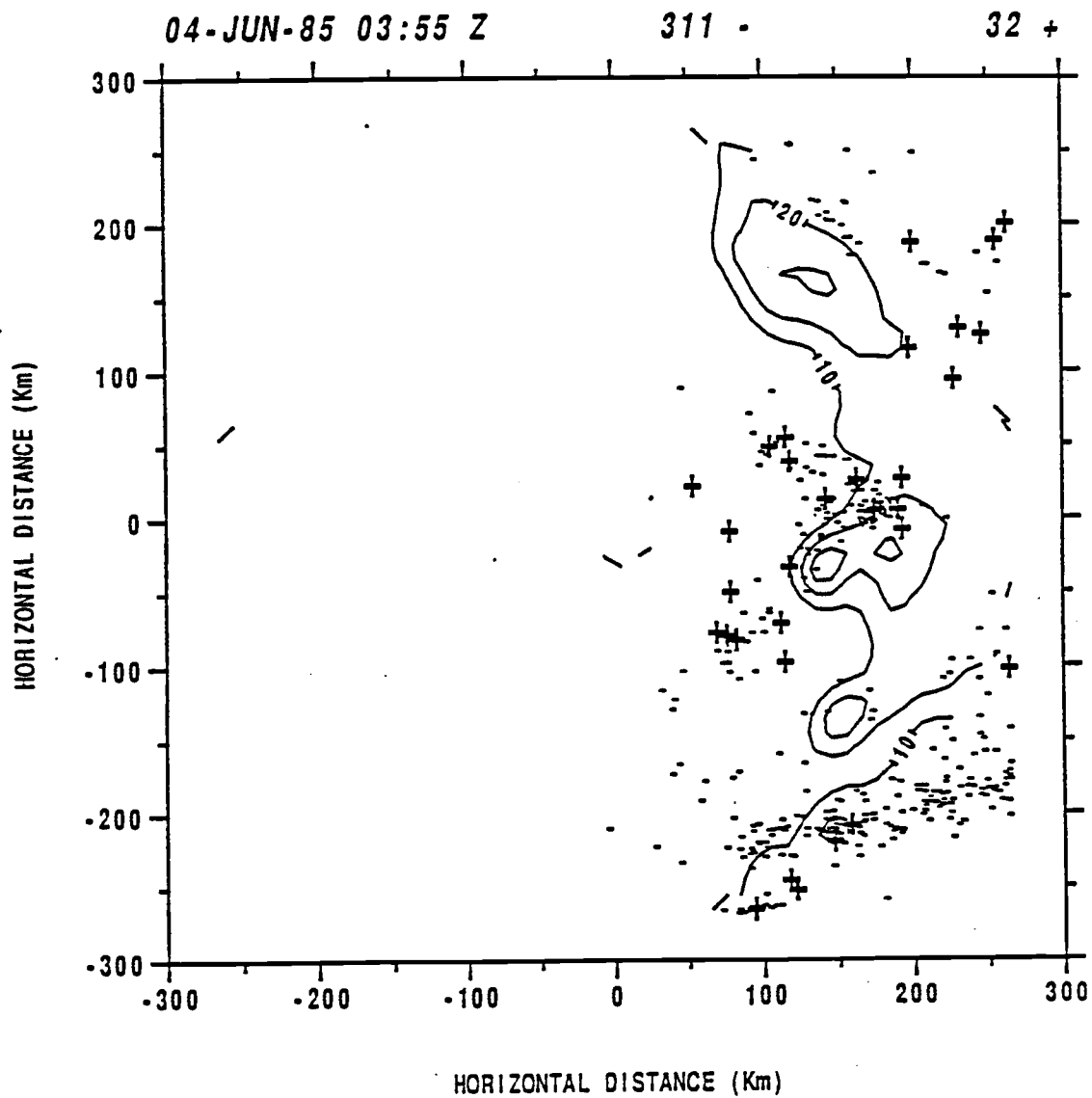


Fig. 3.48 Radar echo pattern and lightning map for 0355Z on 04 June.

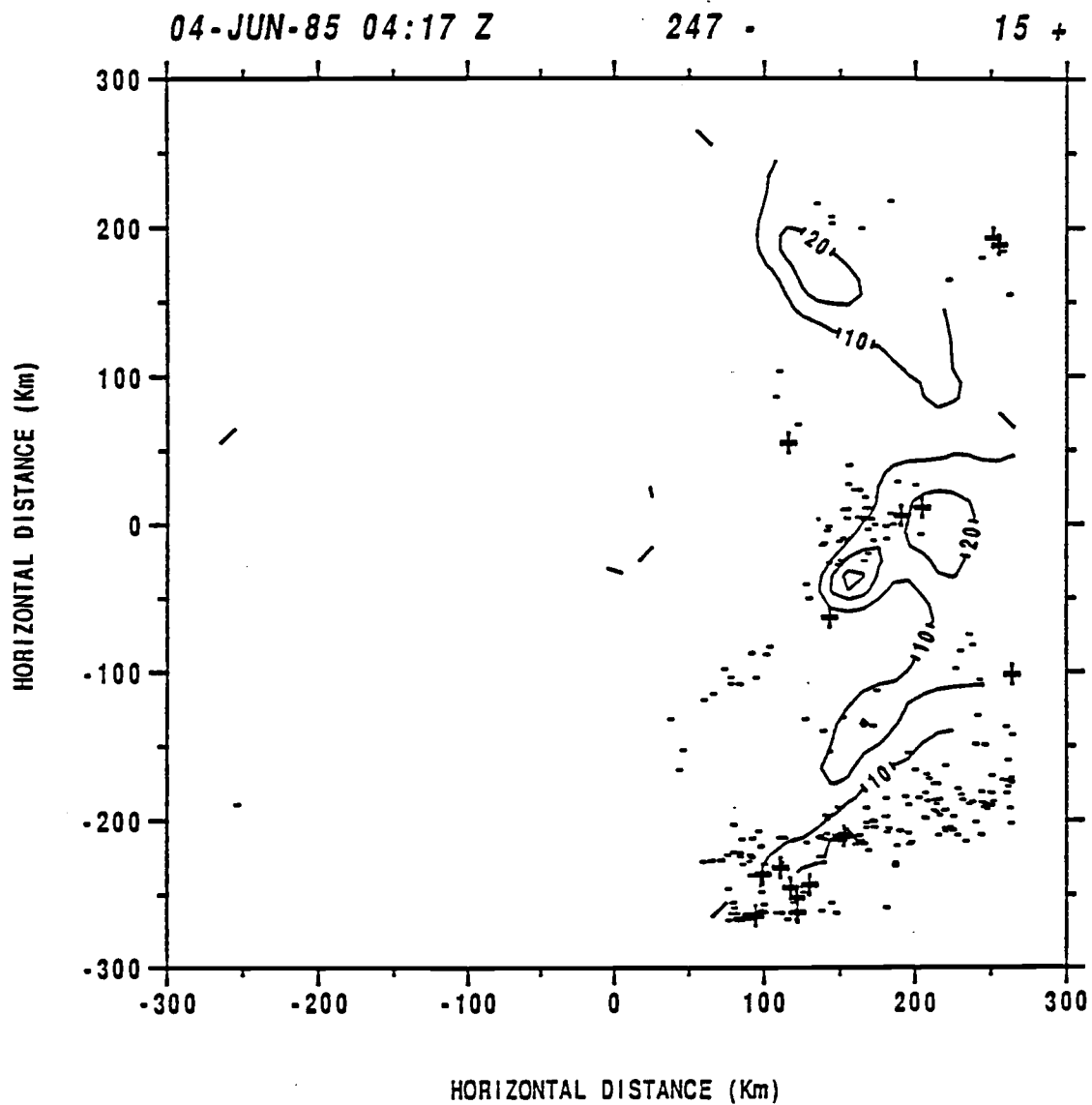


Fig. 3.49 Radar echo pattern and lightning map for 0417Z on 04 June.

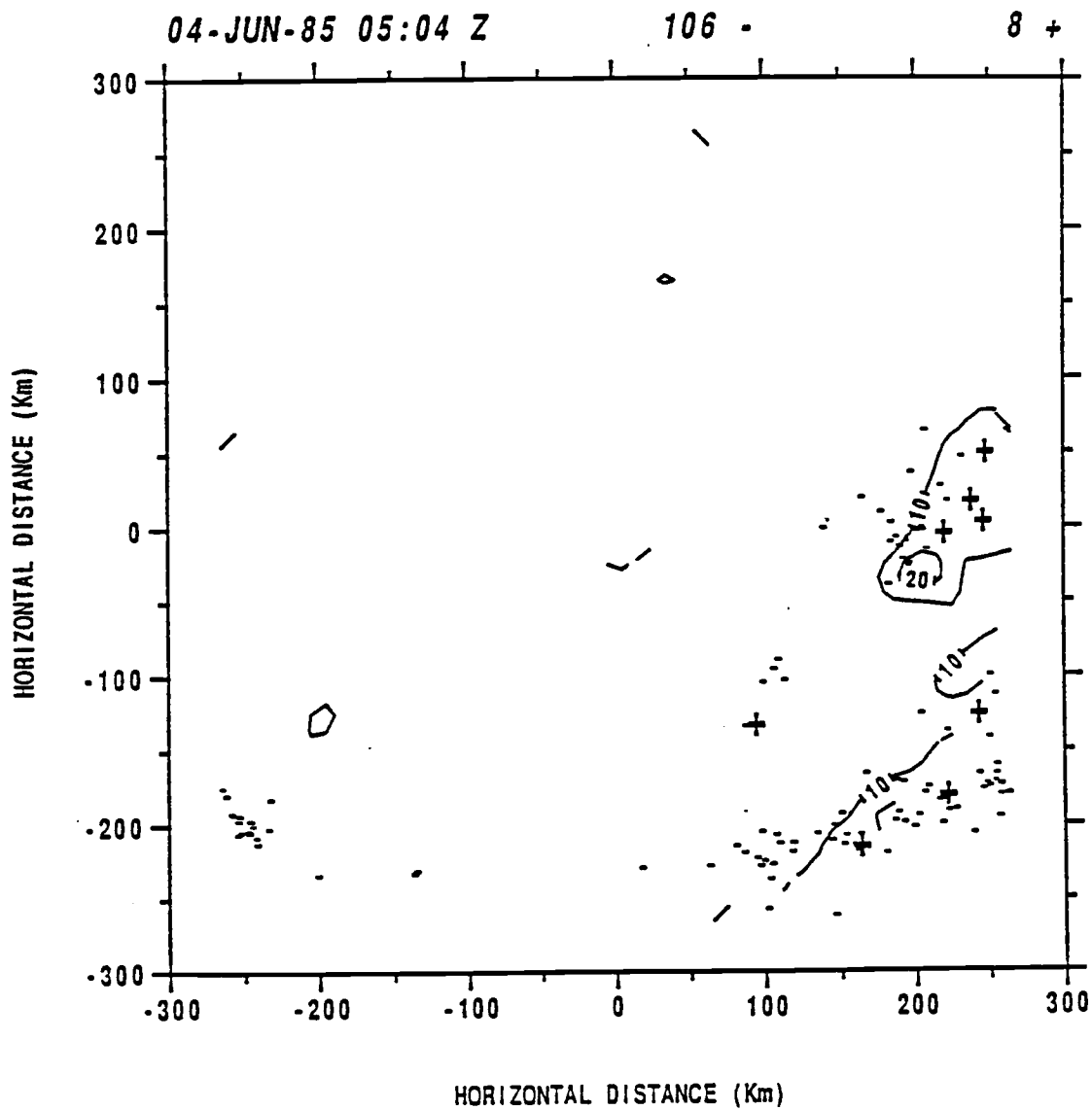


Fig. 3.50 Radar echo pattern and lightning map for 0504Z on 04 June.

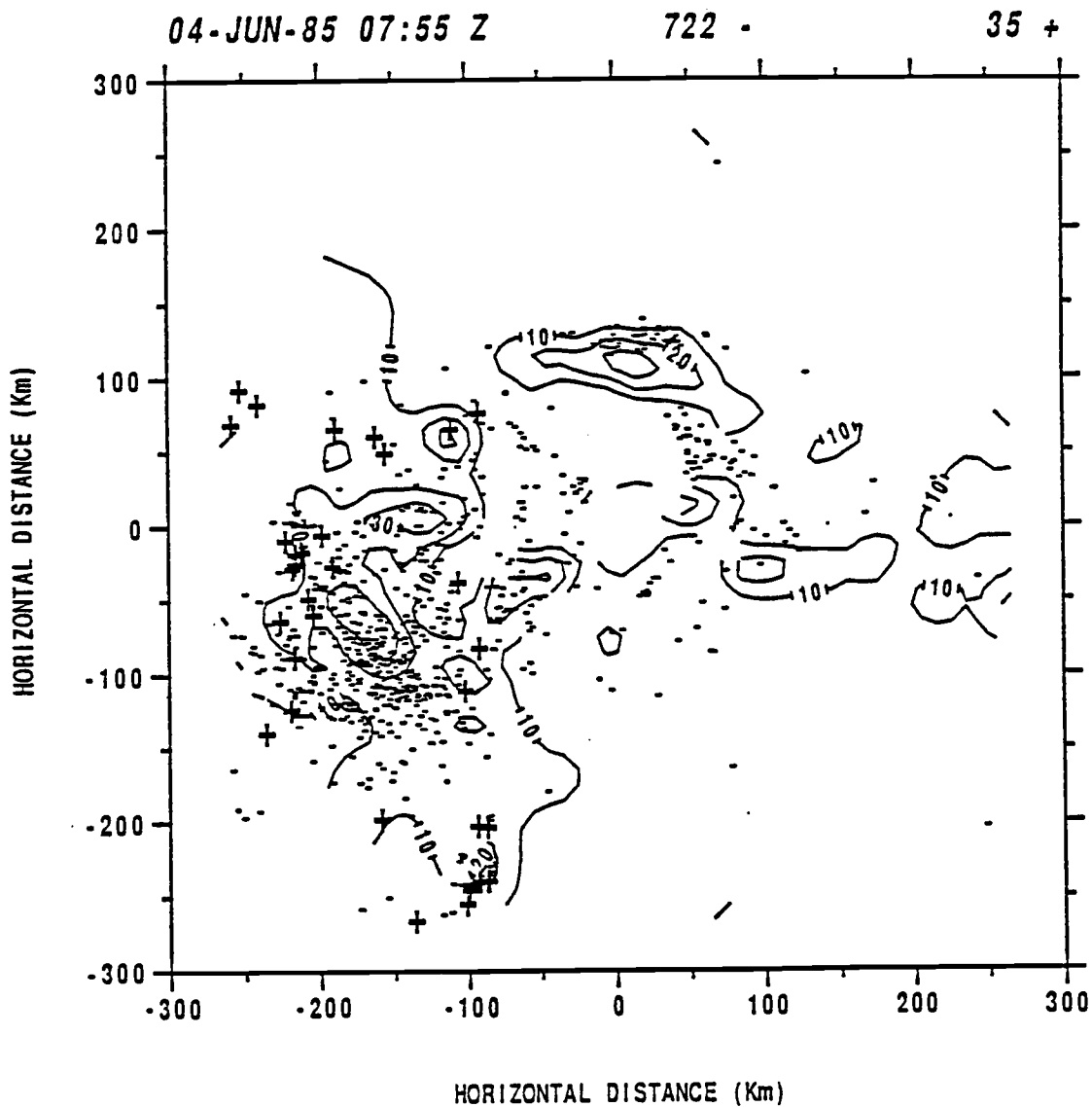


Fig. 3.51 Radar echo pattern and lightning map for 0755Z on 04 June.

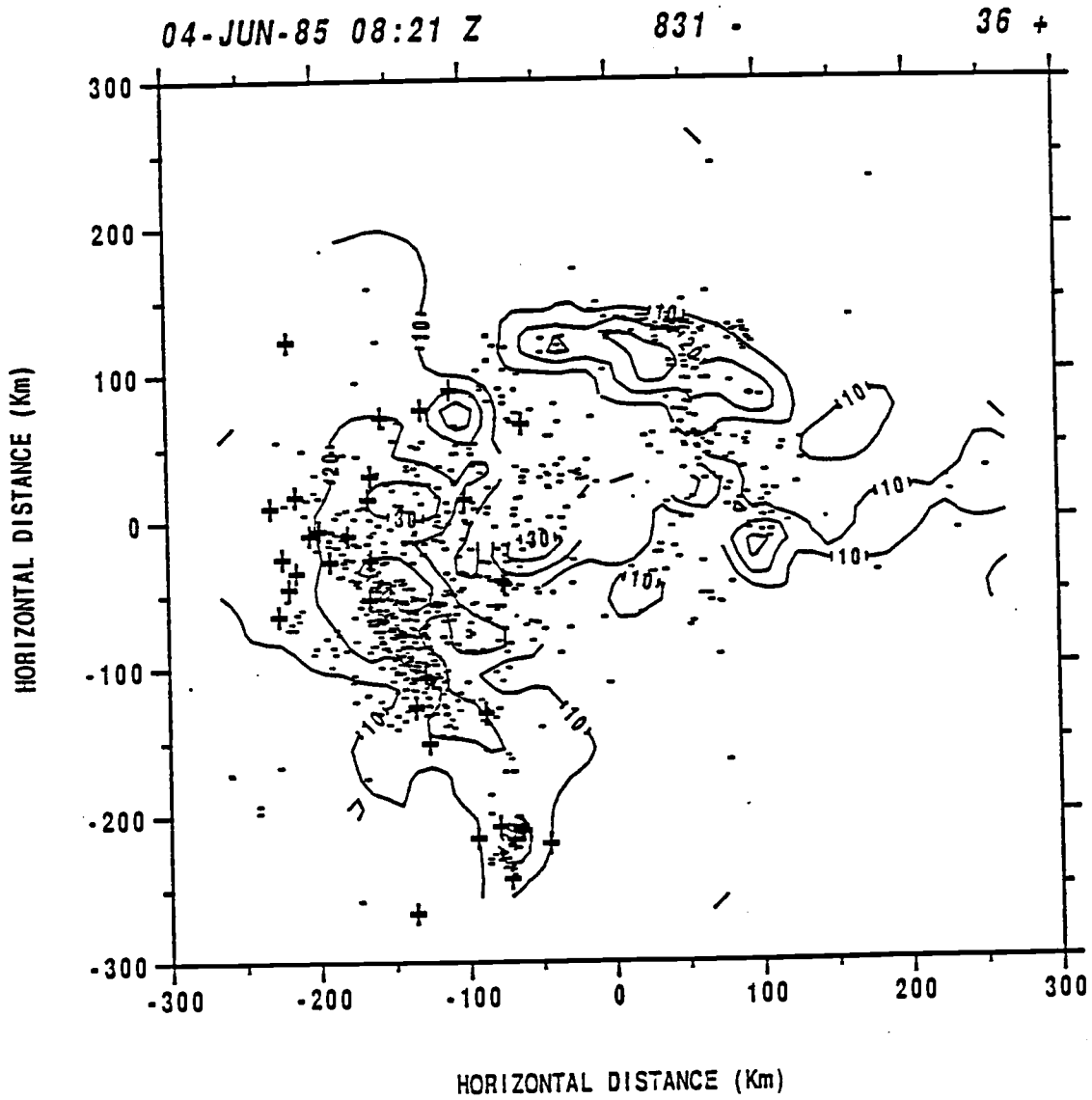


Fig. 3.52 Radar echo pattern and lightning map for 0821Z on 04 June.

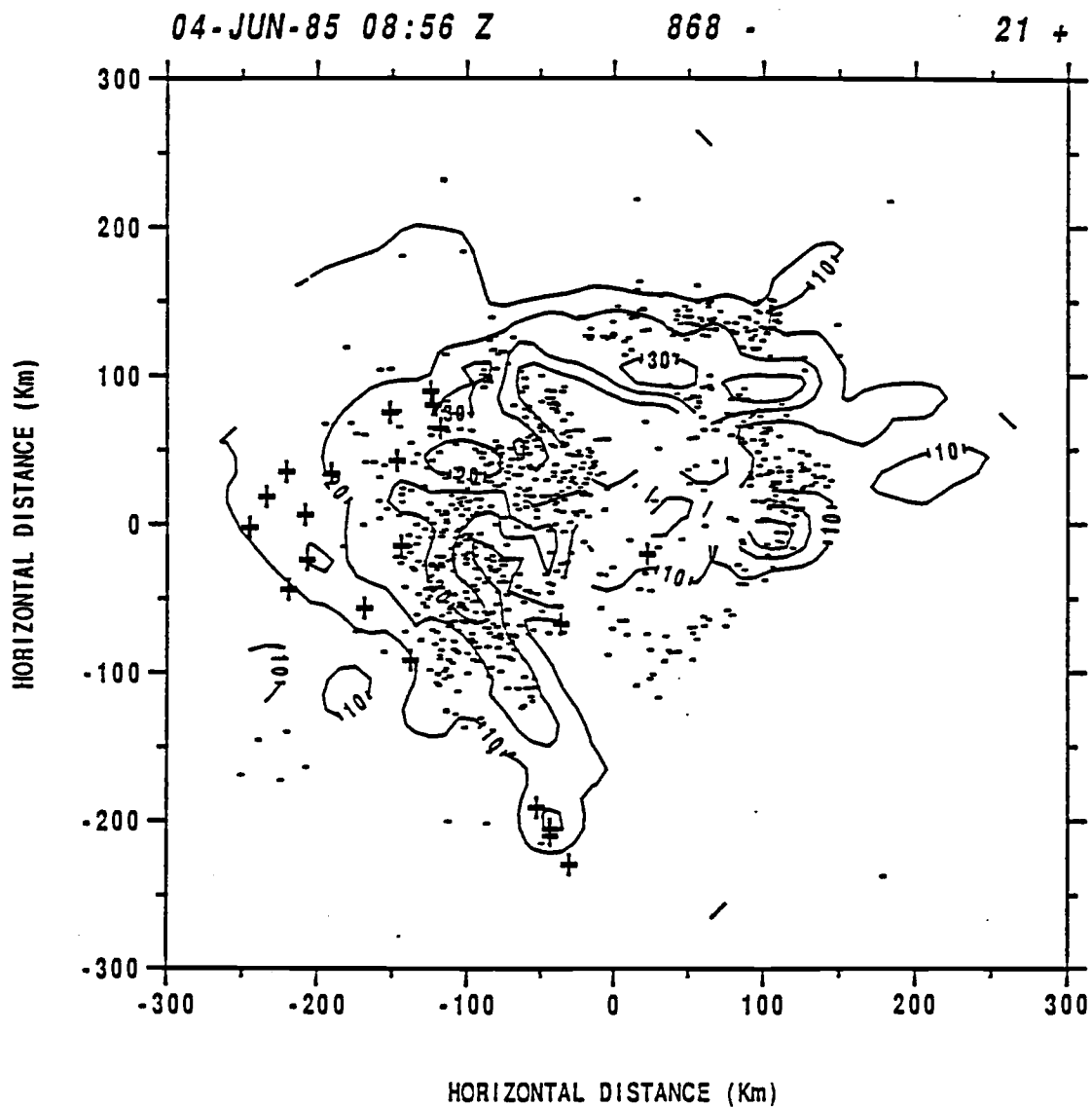


Fig. 3.53 Radar echo pattern and lightning map for 0856Z on 04 June.

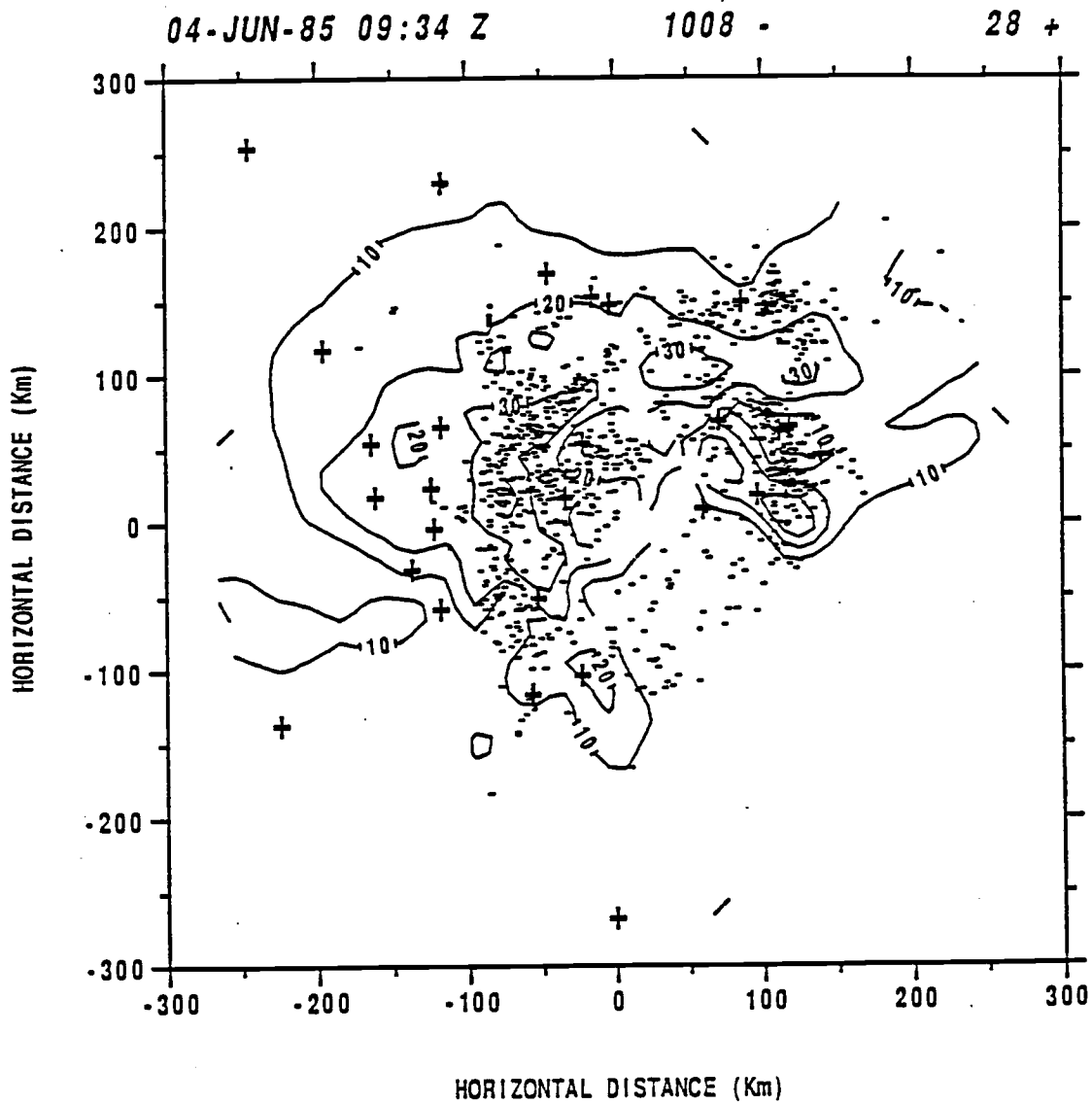


Fig. 3.54 Radar echo pattern and lightning map for 0934Z on 04 June.

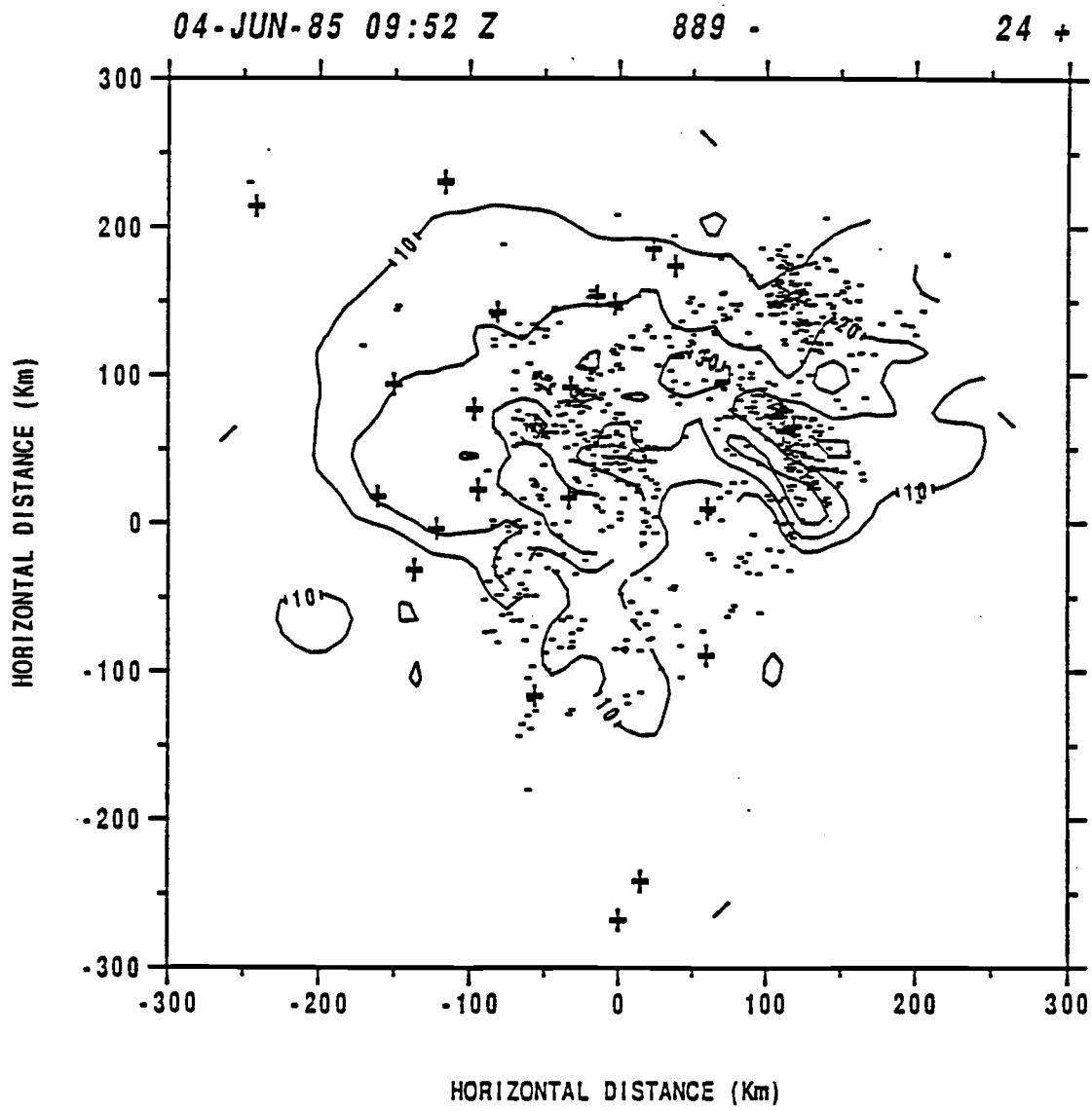


Fig. 3.55 Radar echo pattern and lightning map for 0952Z on 04 June.

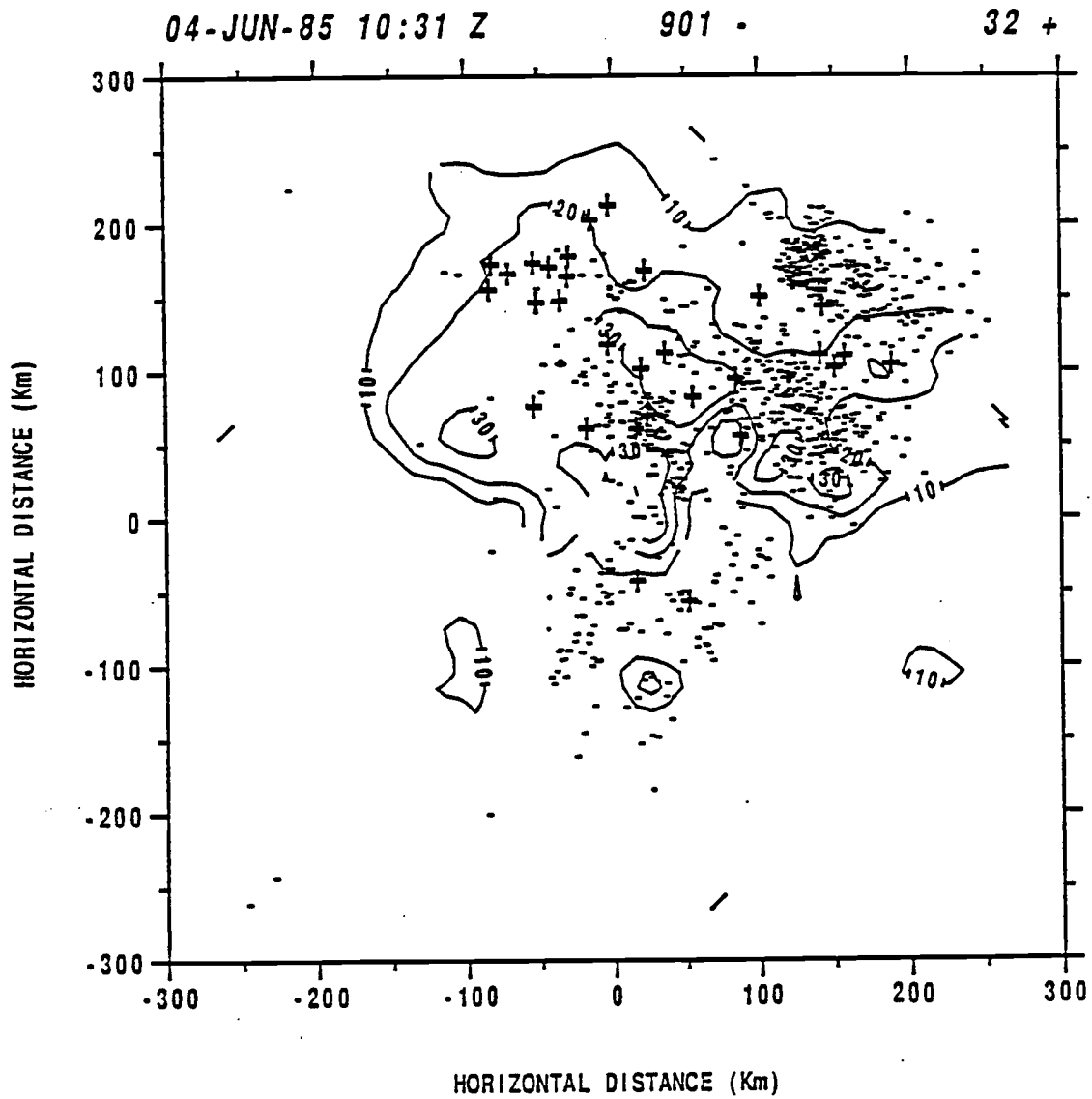


Fig. 3.56 Radar echo pattern and lightning map for 1031Z on 04 June.

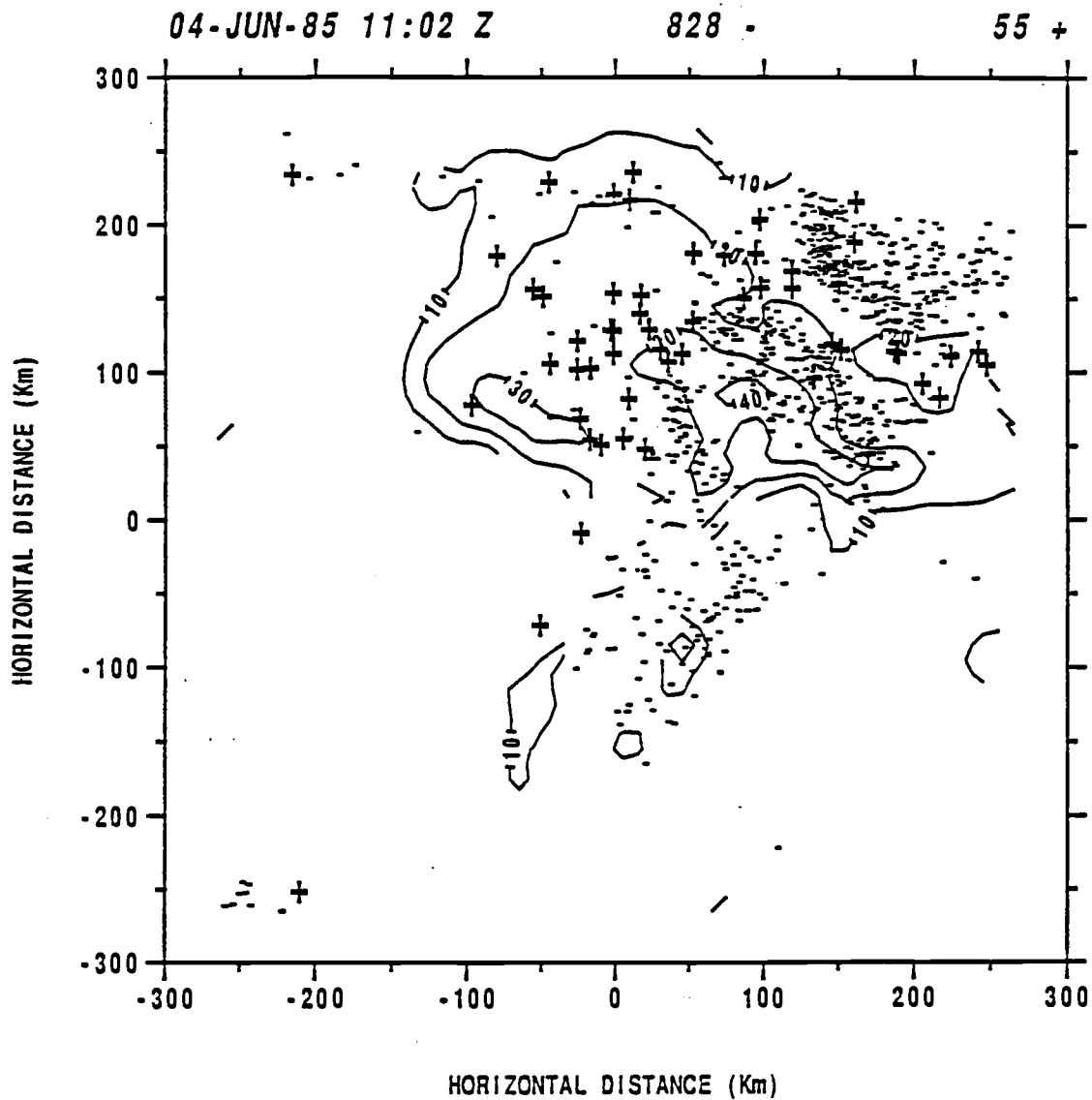


Fig. 3.57 Radar echo pattern and lightning map for 1102Z on 04 June.

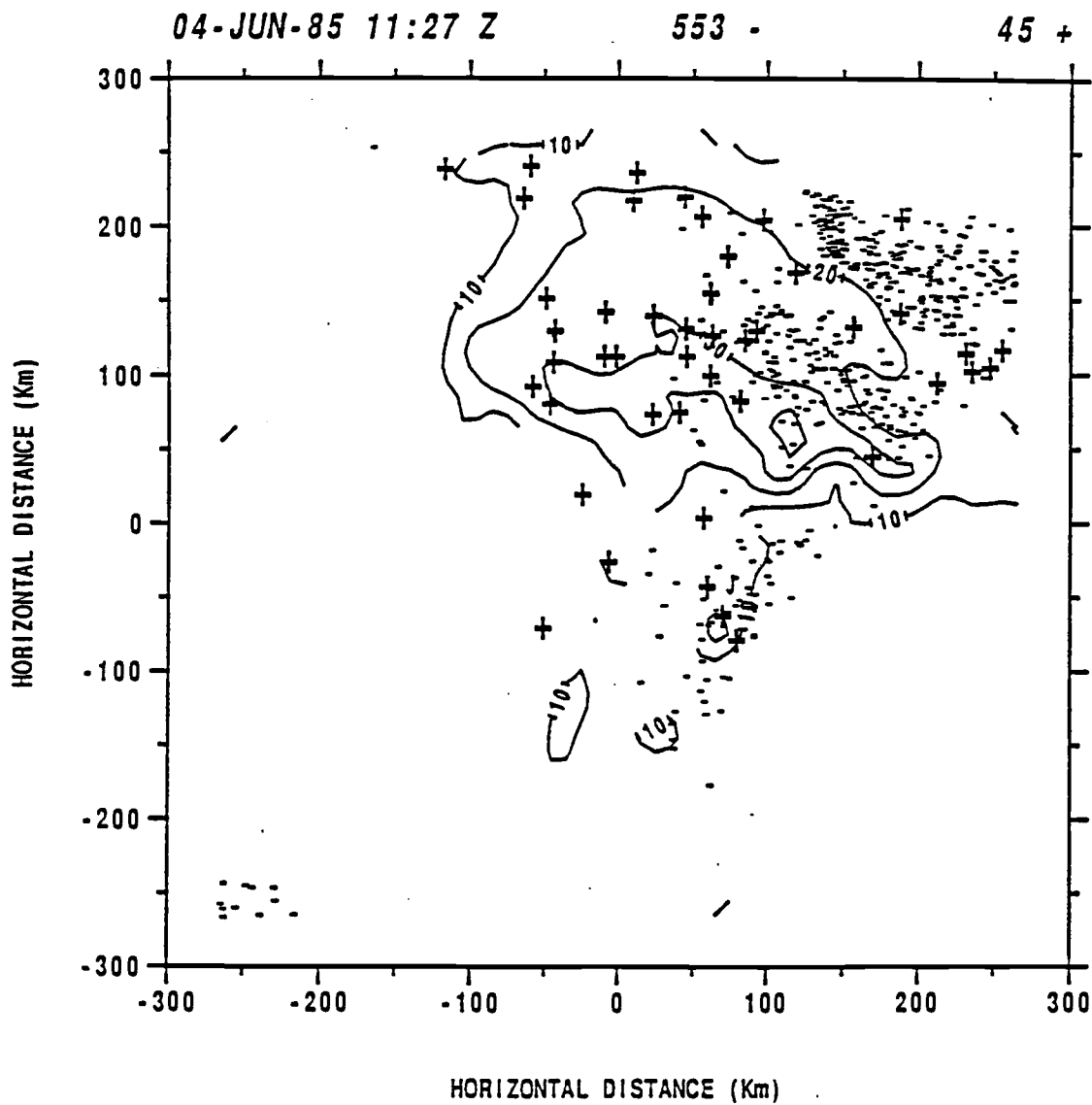


Fig. 3.58 Radar echo pattern and lightning map for 1127Z on 04 June.

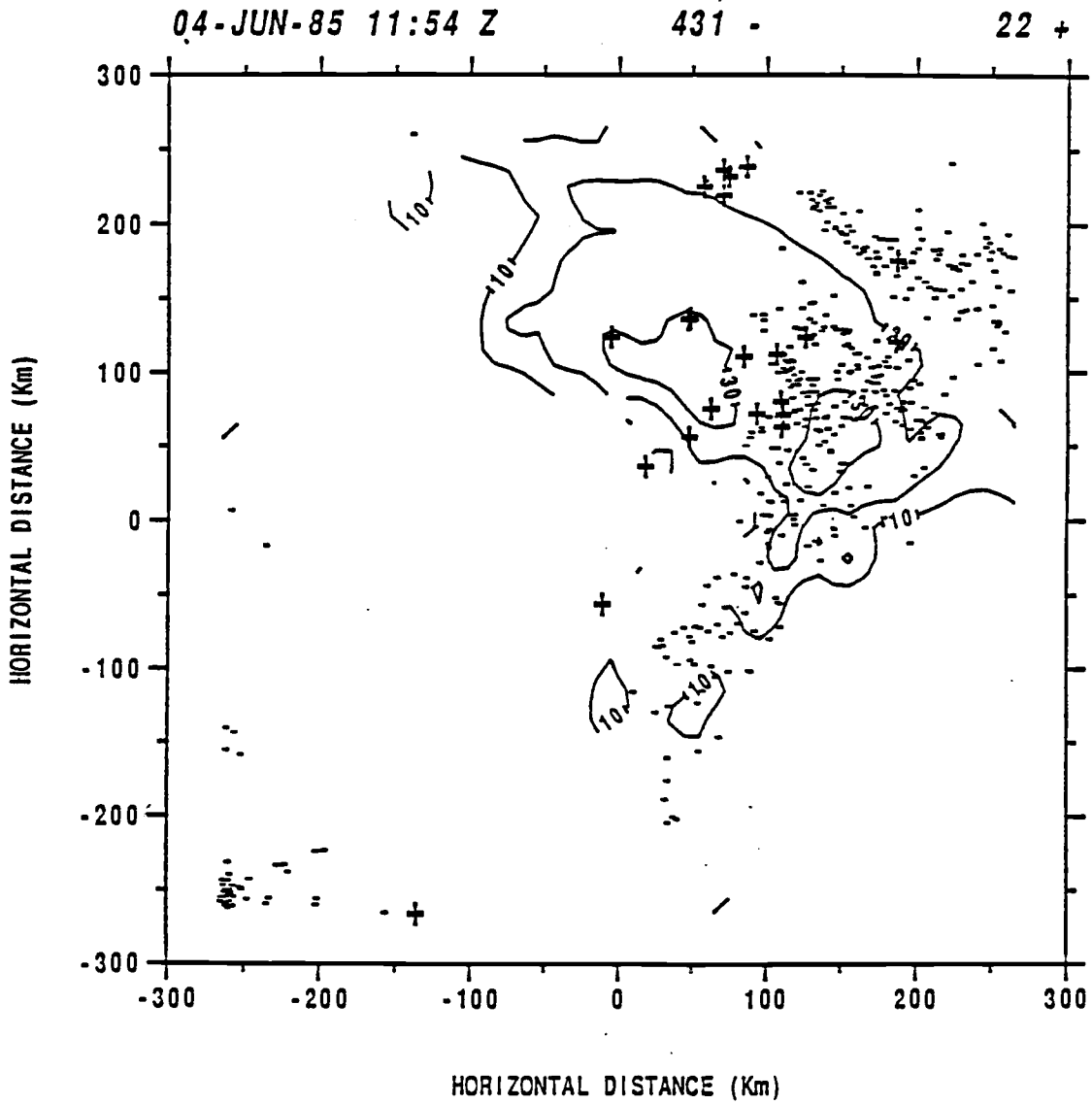


Fig. 3.59 Radar echo pattern and lightning map for 1154Z on 04 June.

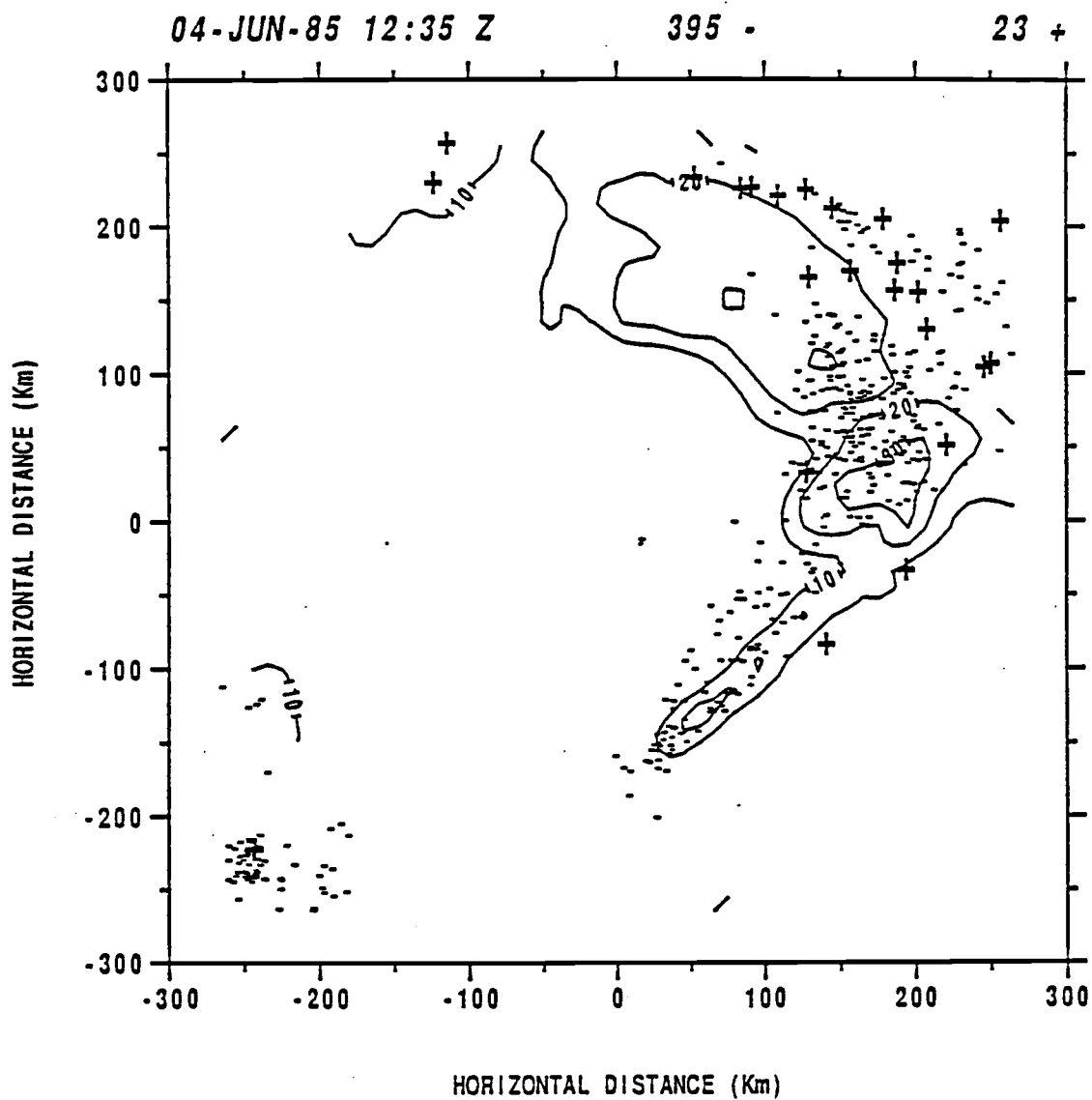


Fig. 3.60 Radar echo pattern and lightning map for 1235Z on 04 June.

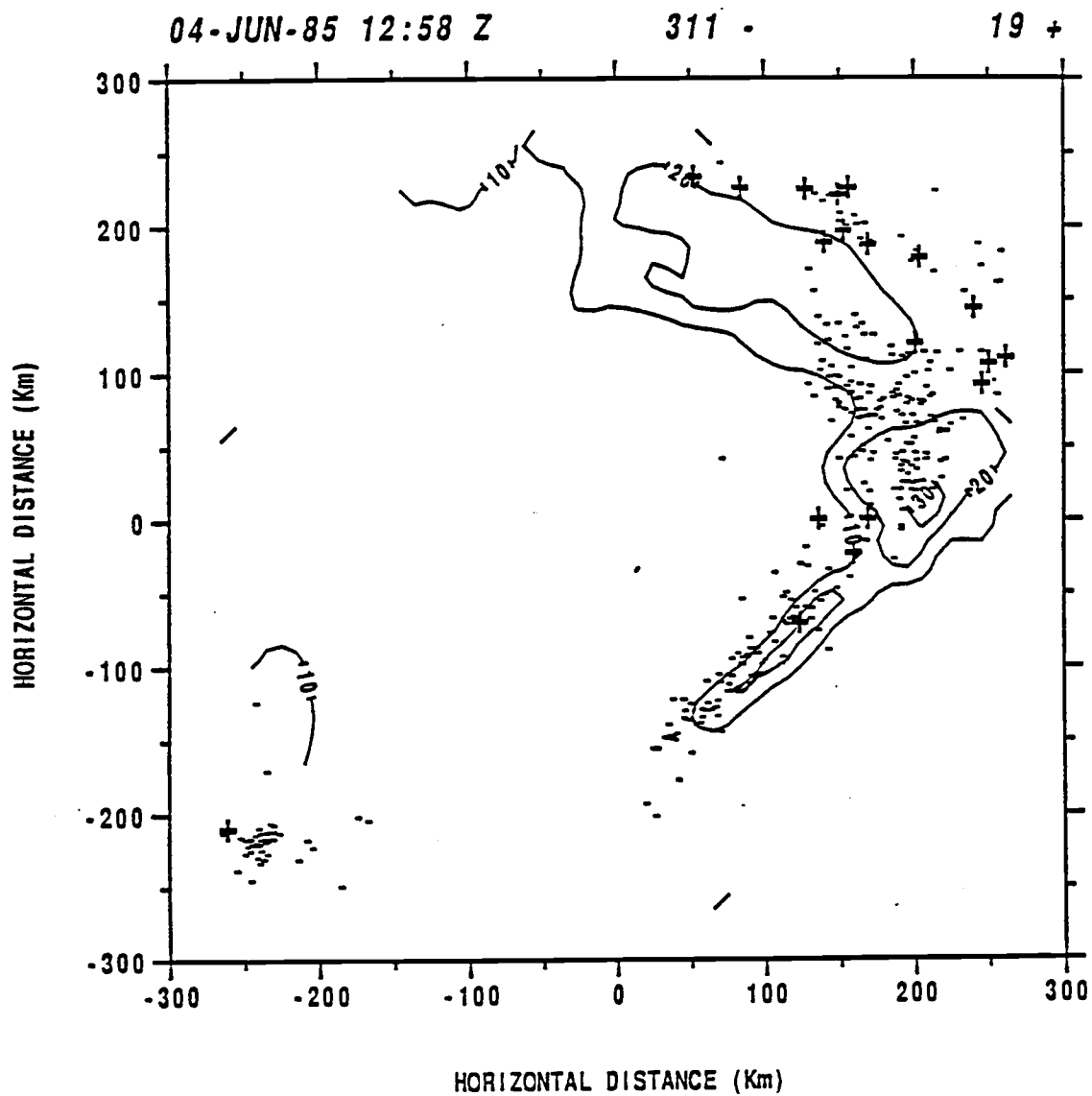


Fig. 3.61 Radar echo pattern and lightning map for 1258Z on 04 June.

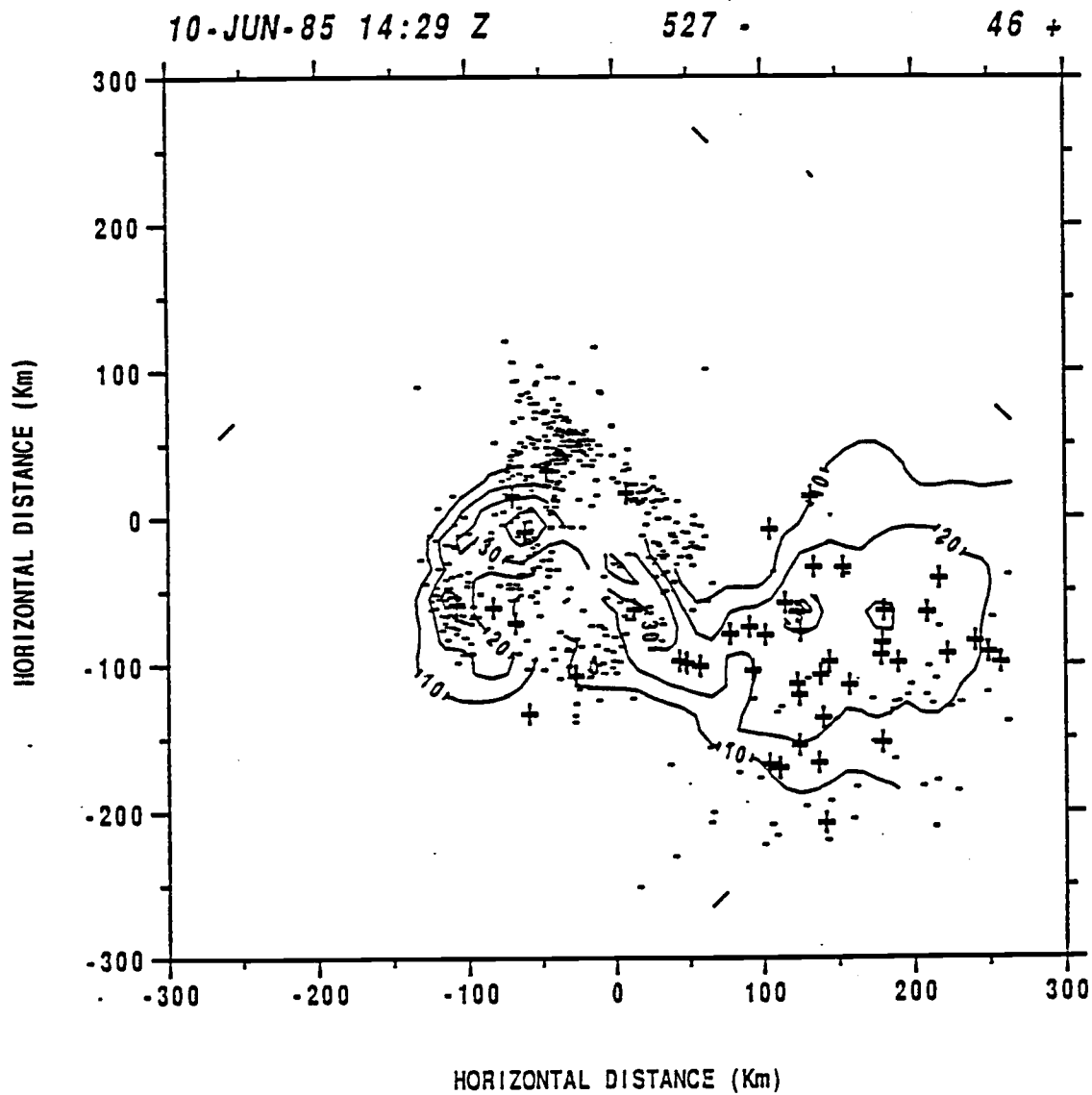


Fig. 3.62 Radar echo pattern and lightning map for 1429Z on 10 June.

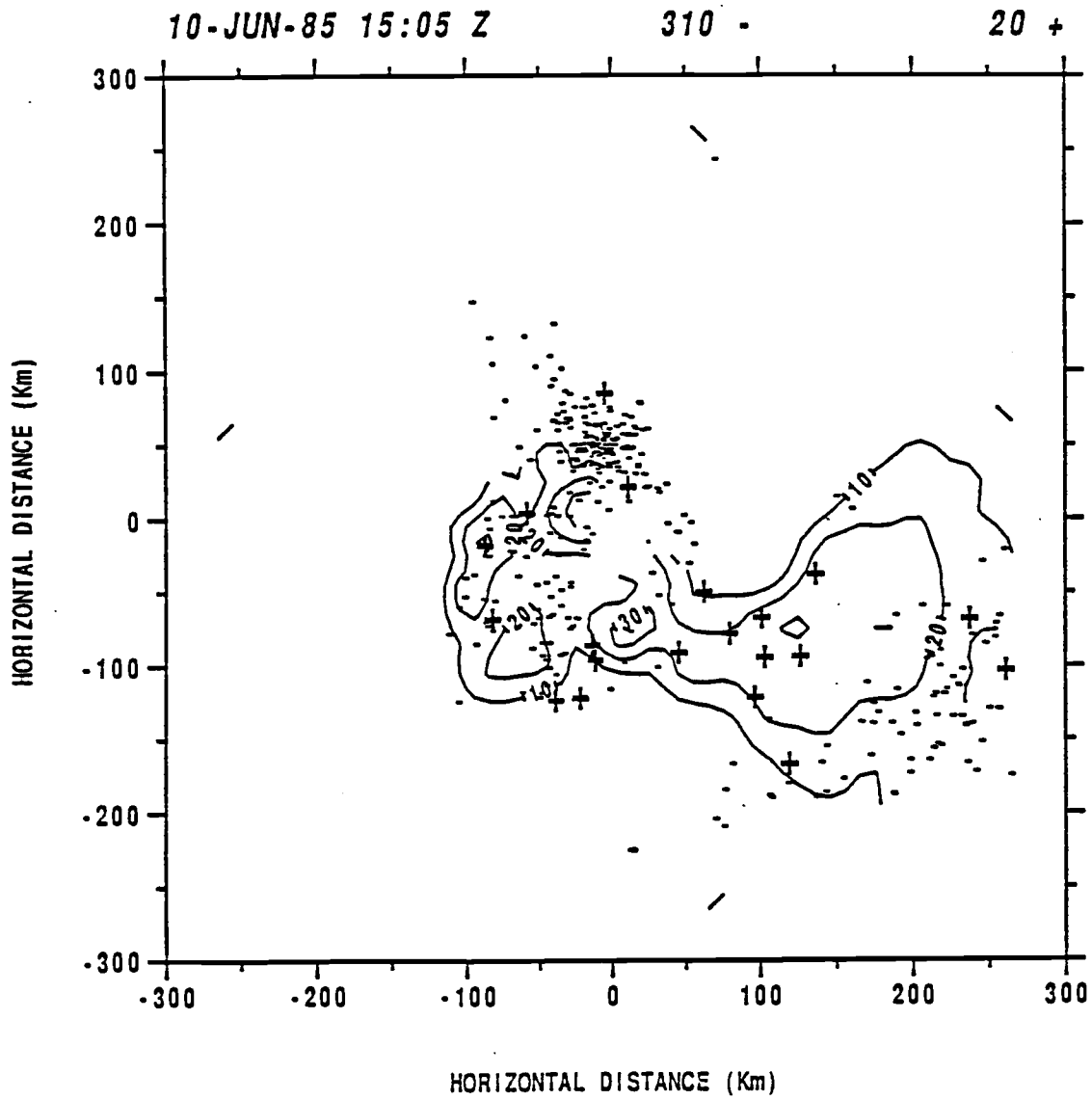


Fig. 3.63 Radar echo pattern and lightning map for 1505Z on 10 June.

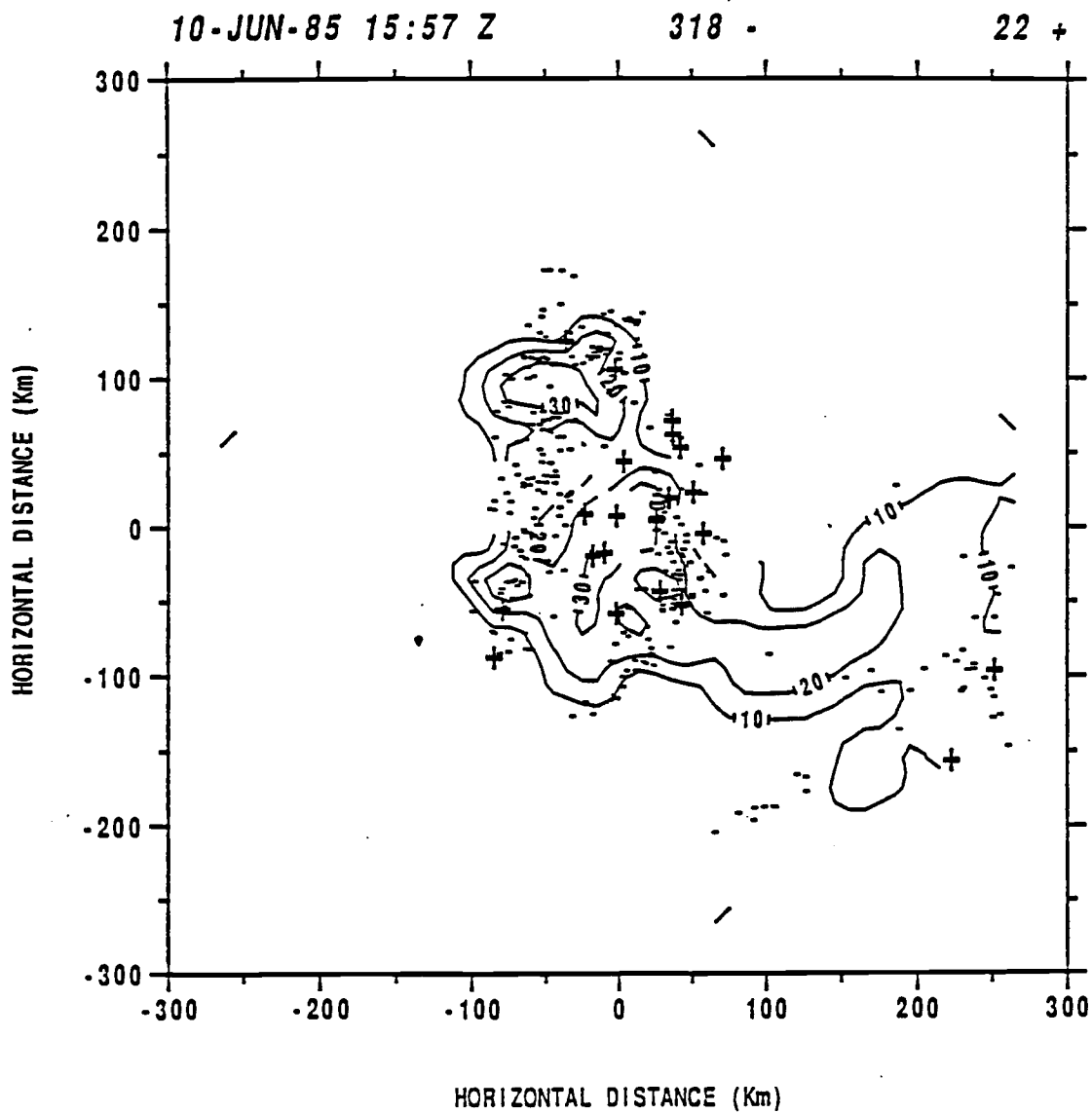


Fig. 3.64 Radar echo pattern and lightning map for 1557Z on 10 June.

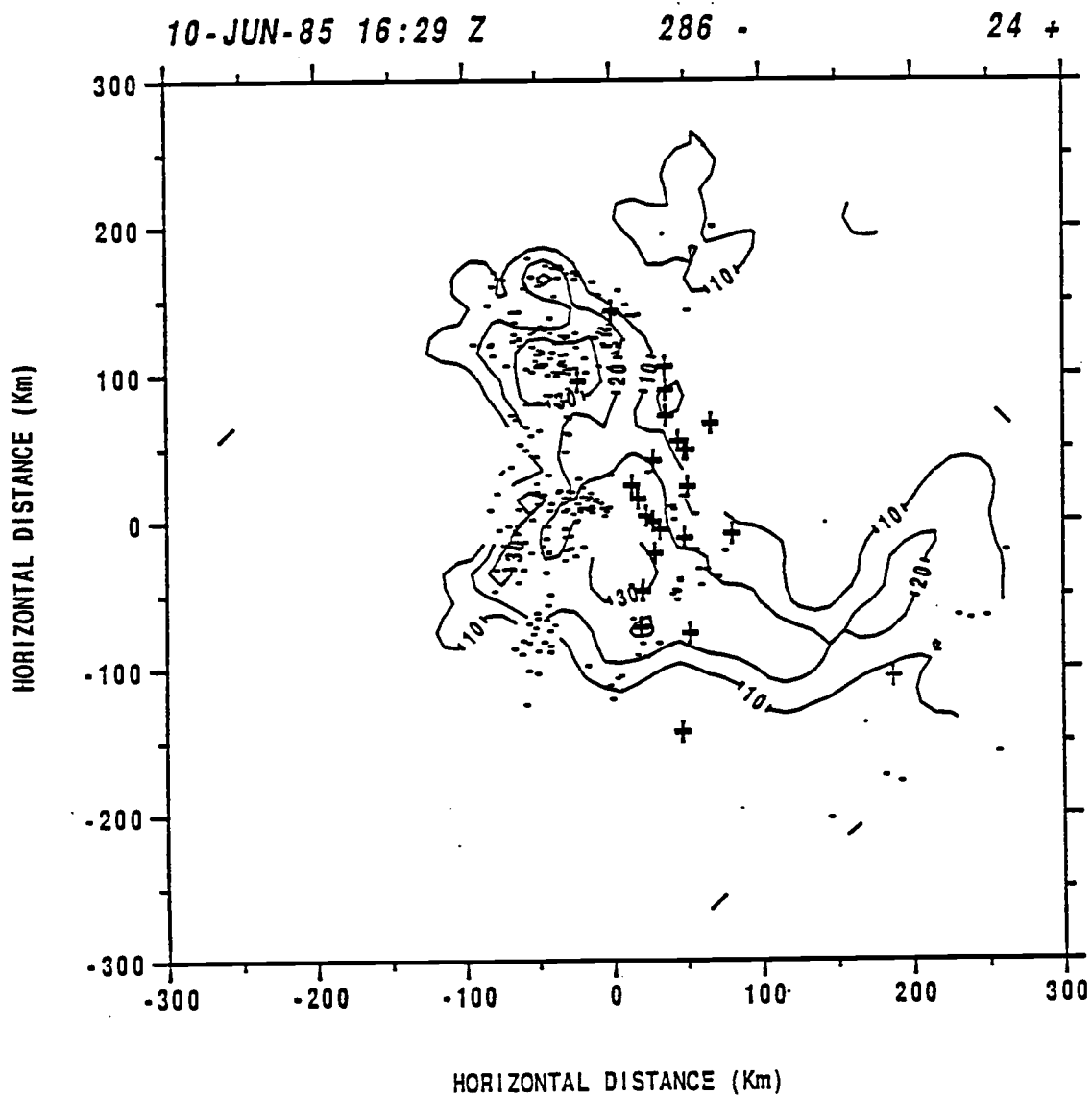


Fig. 3.65 Radar echo pattern and lightning map for 1629Z on 10 June.

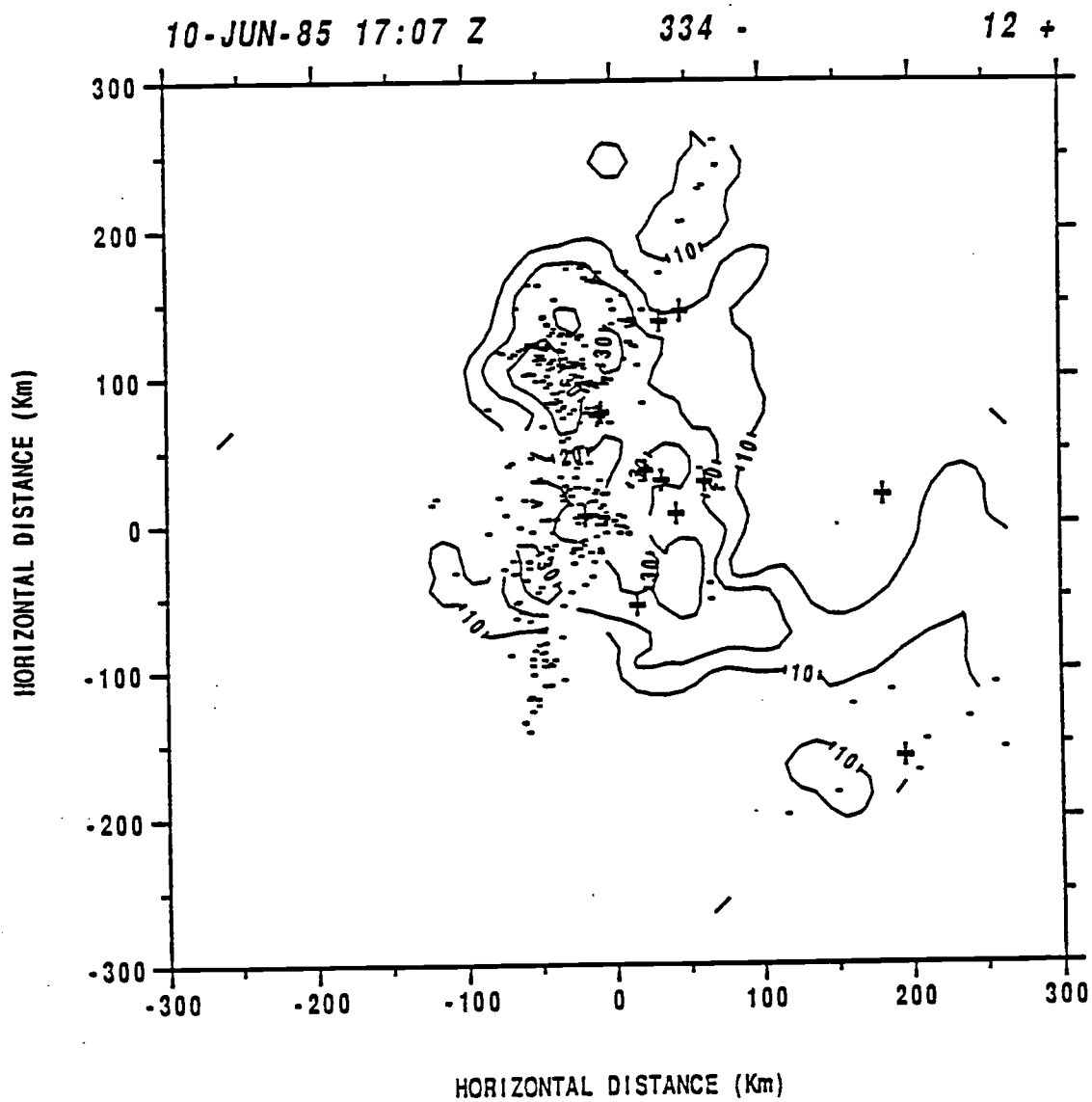


Fig. 3.66 Radar echo pattern and lightning map for 1707Z on 10 June.

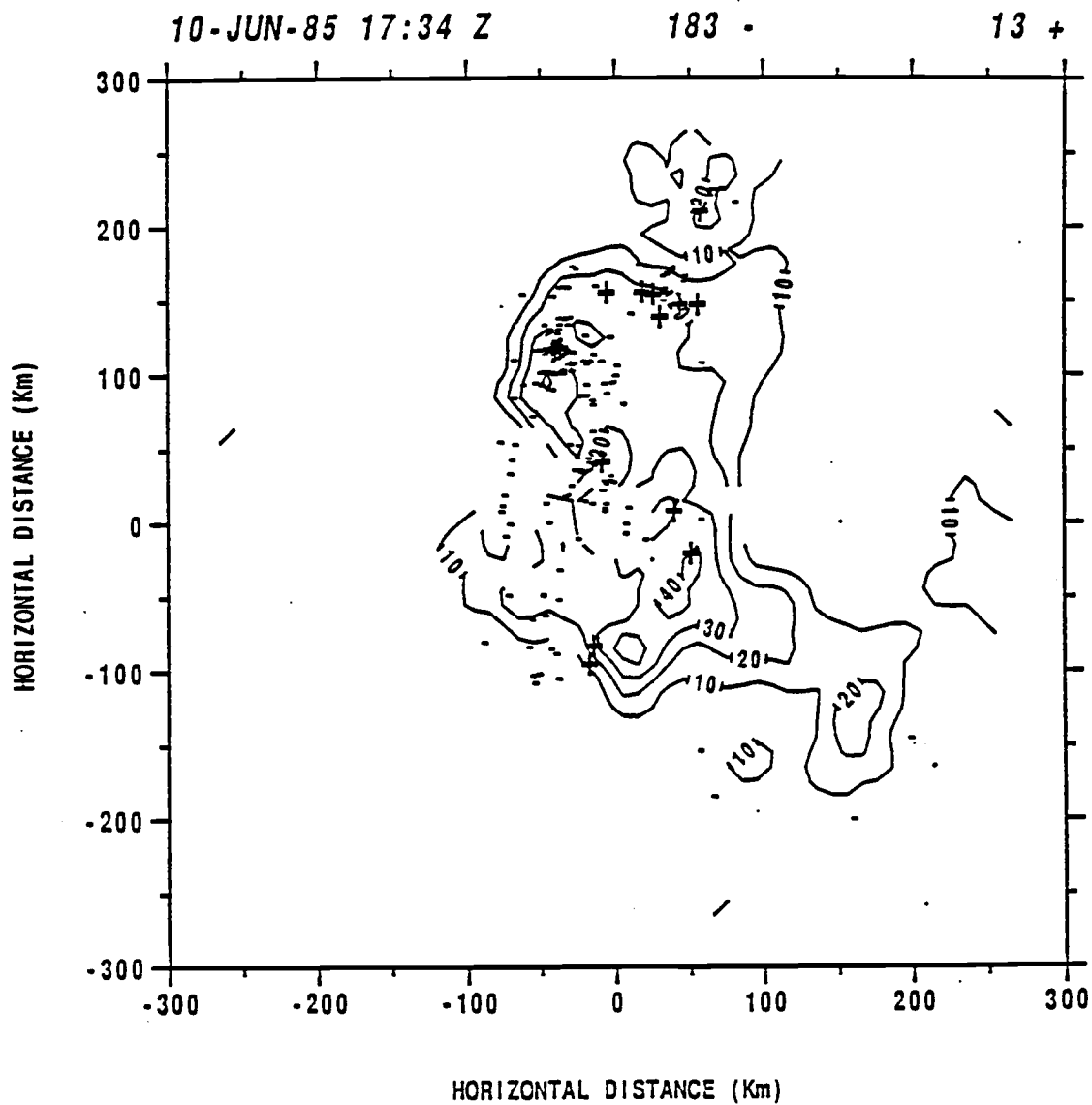


Fig. 3.67 Radar echo pattern and lightning map for 11734Z on 10 June.

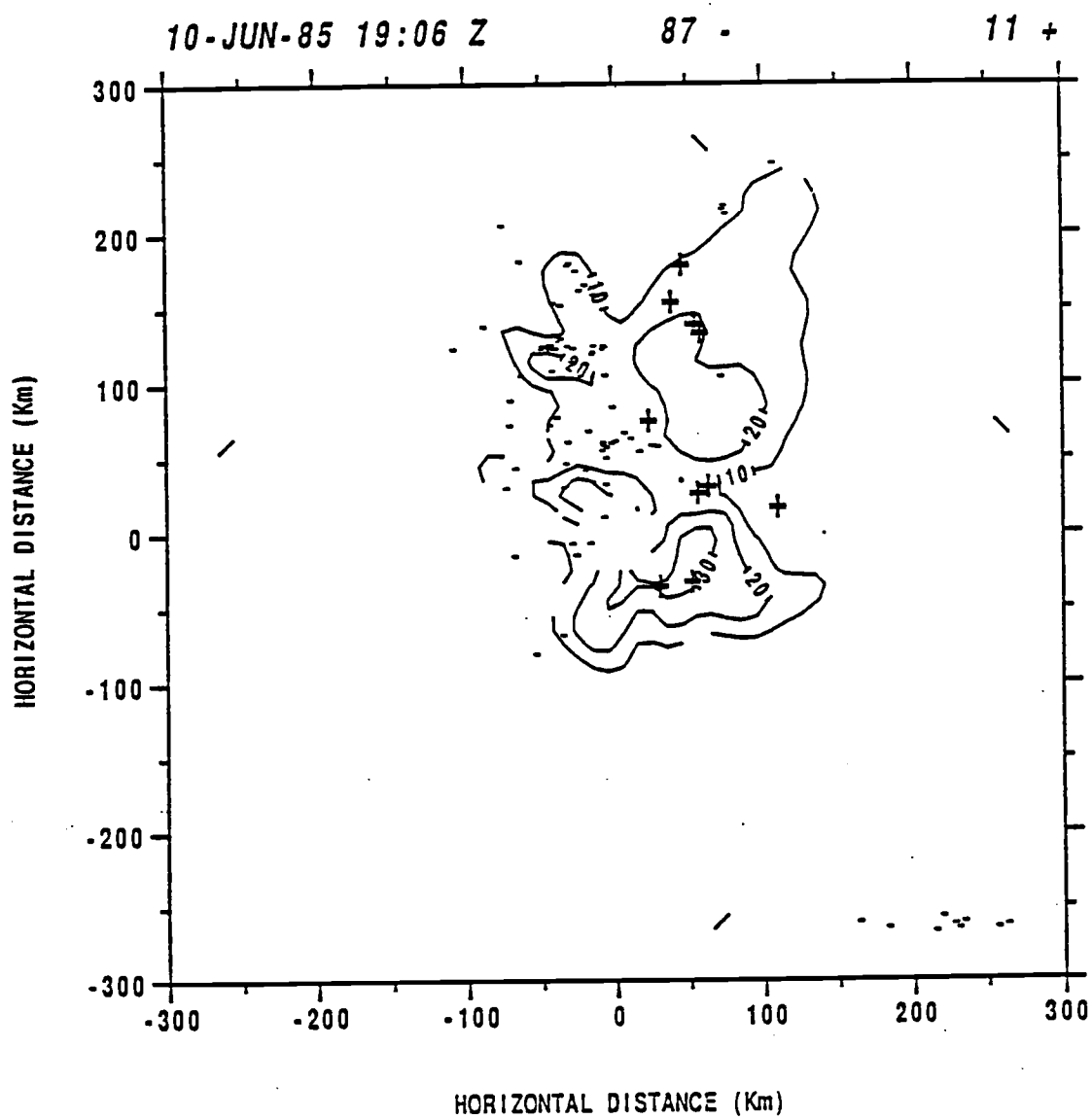


Fig. 3.68 Radar echo pattern and lightning map for 1906Z on 10 June.

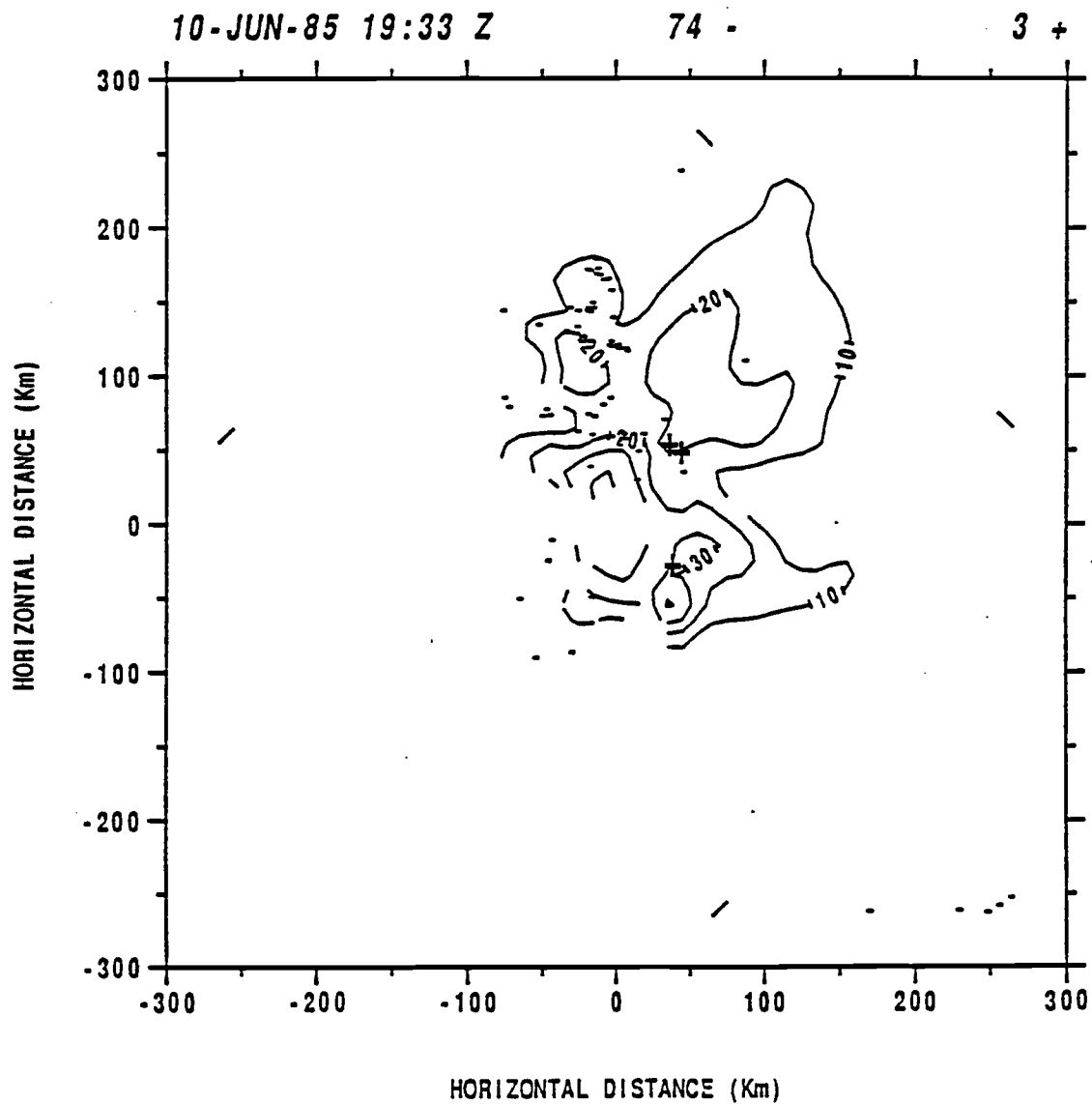


Fig. 3.69 Radar echo pattern and lightning map for 1933Z on 10 June.

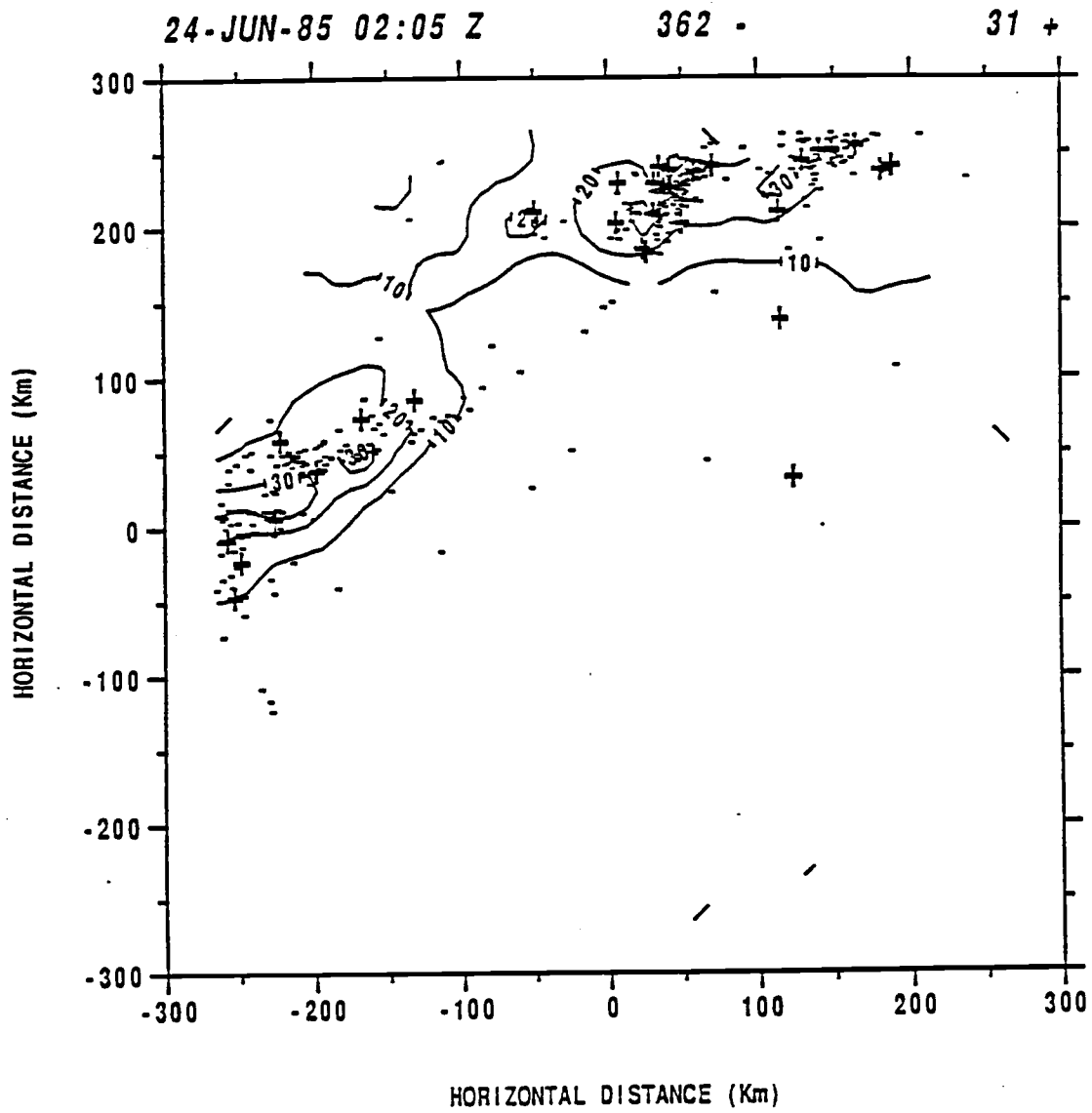


Fig. 3.70 Radar echo pattern and lightning map for 0205Z on 24 June.

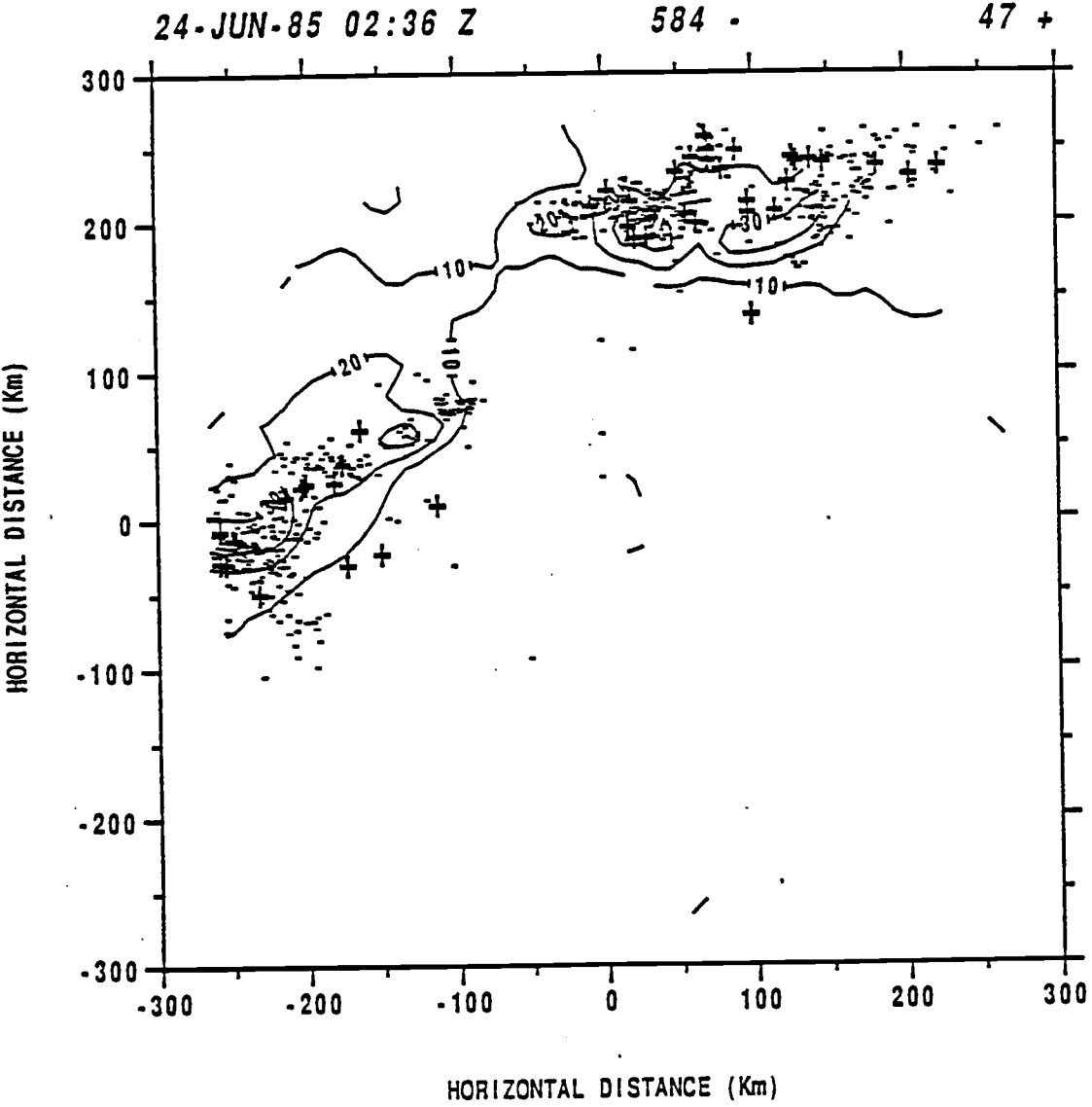


Fig. 3.71 Radar echo pattern and lightning map for 0236Z on 24 June.

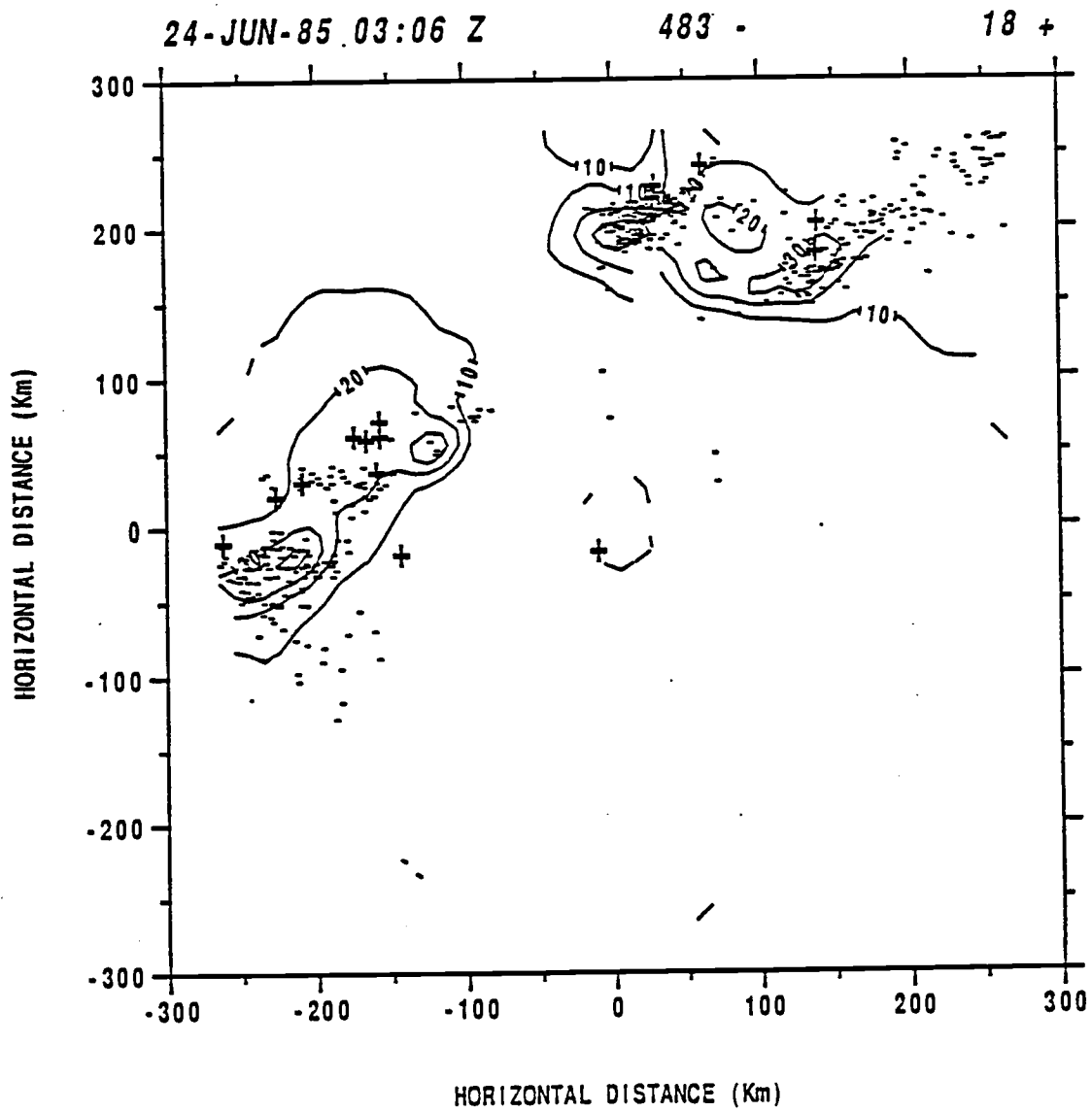


Fig. 3.72 Radar echo pattern and lightning map for 0306Z on 24 June.

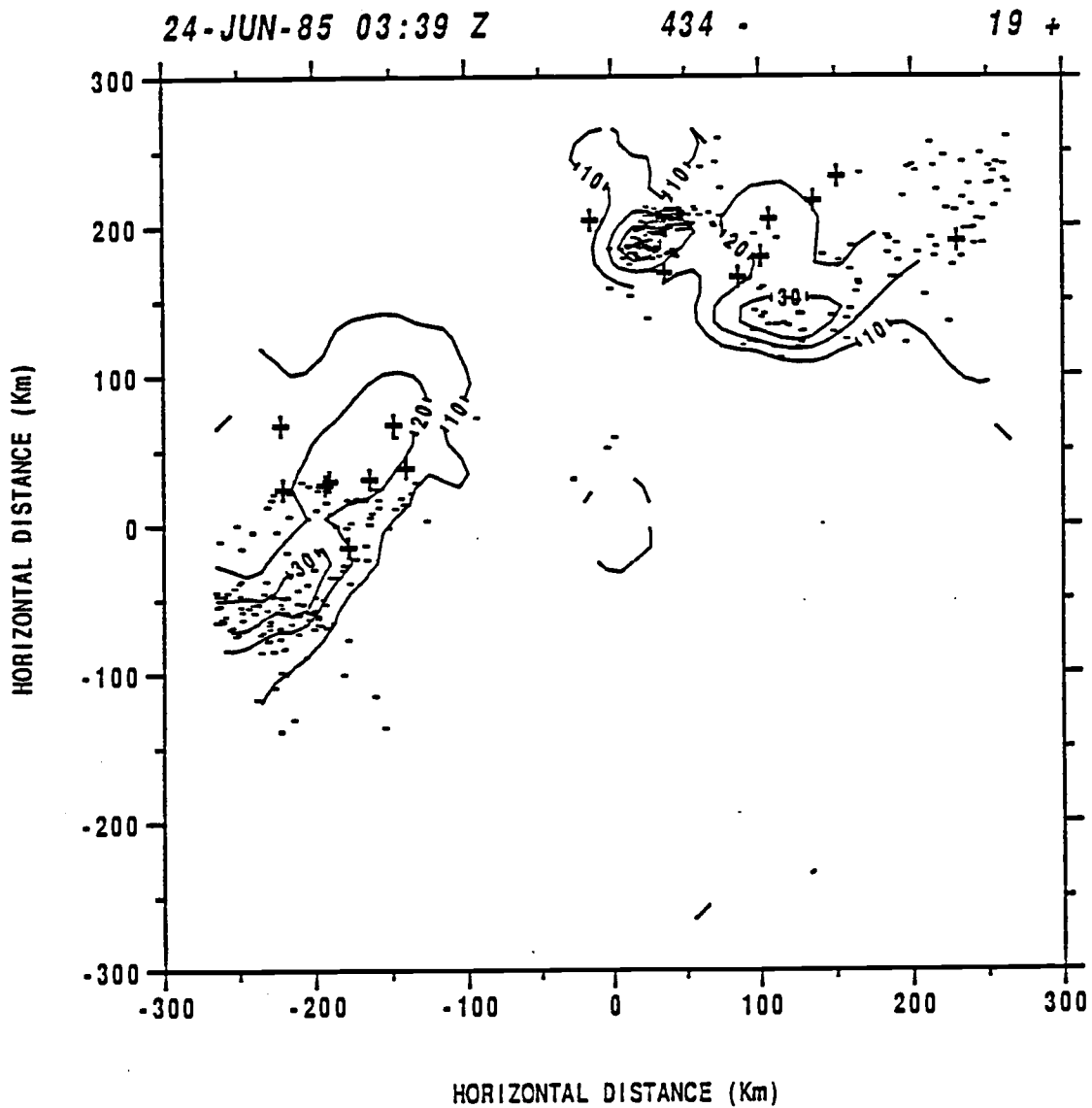


Fig. 3.73 Radar echo pattern and lightning map for 0339Z on 24 June.

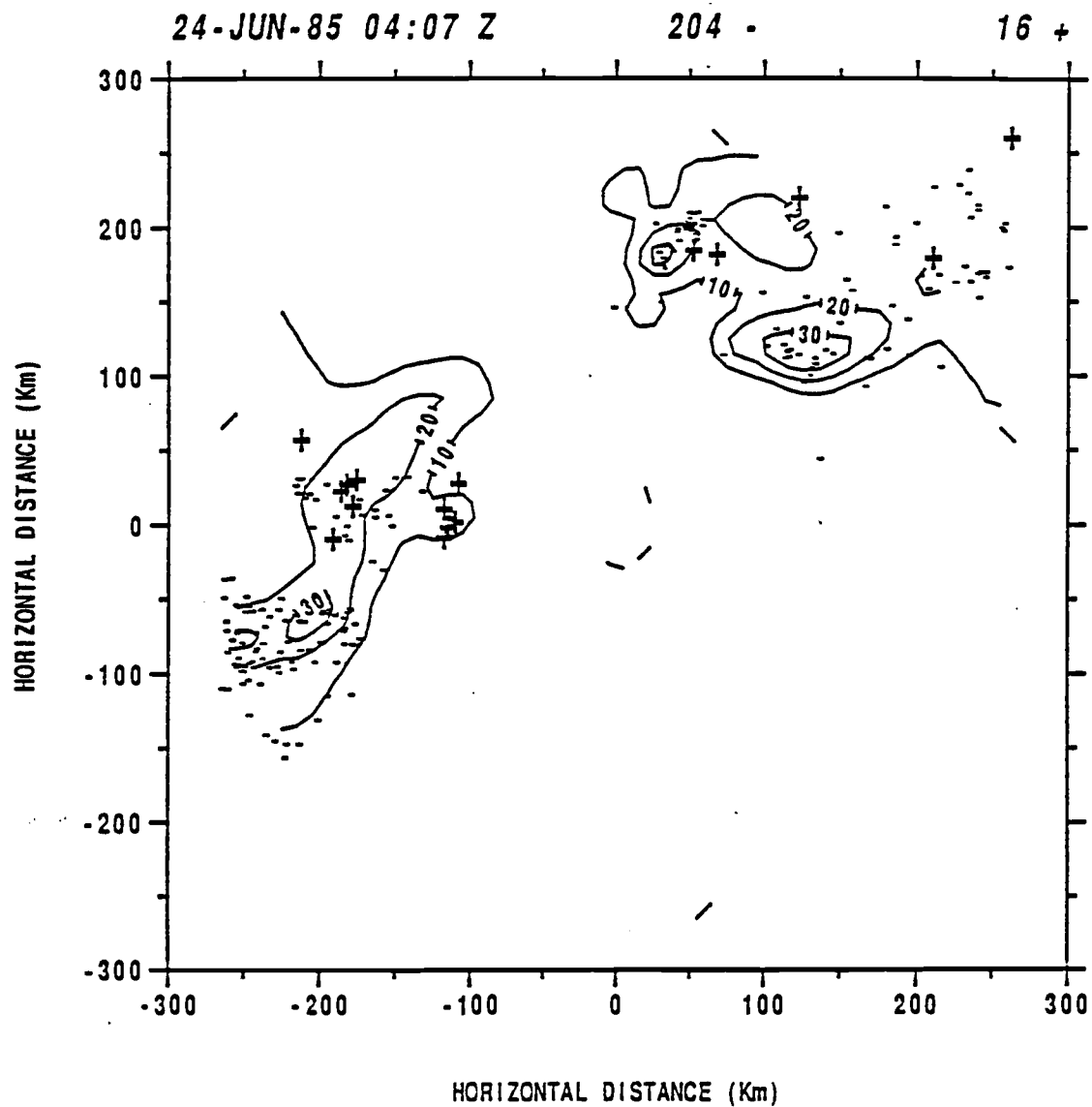


Fig. 3.74 Radar echo pattern and lightning map for 0407Z on 24 June.

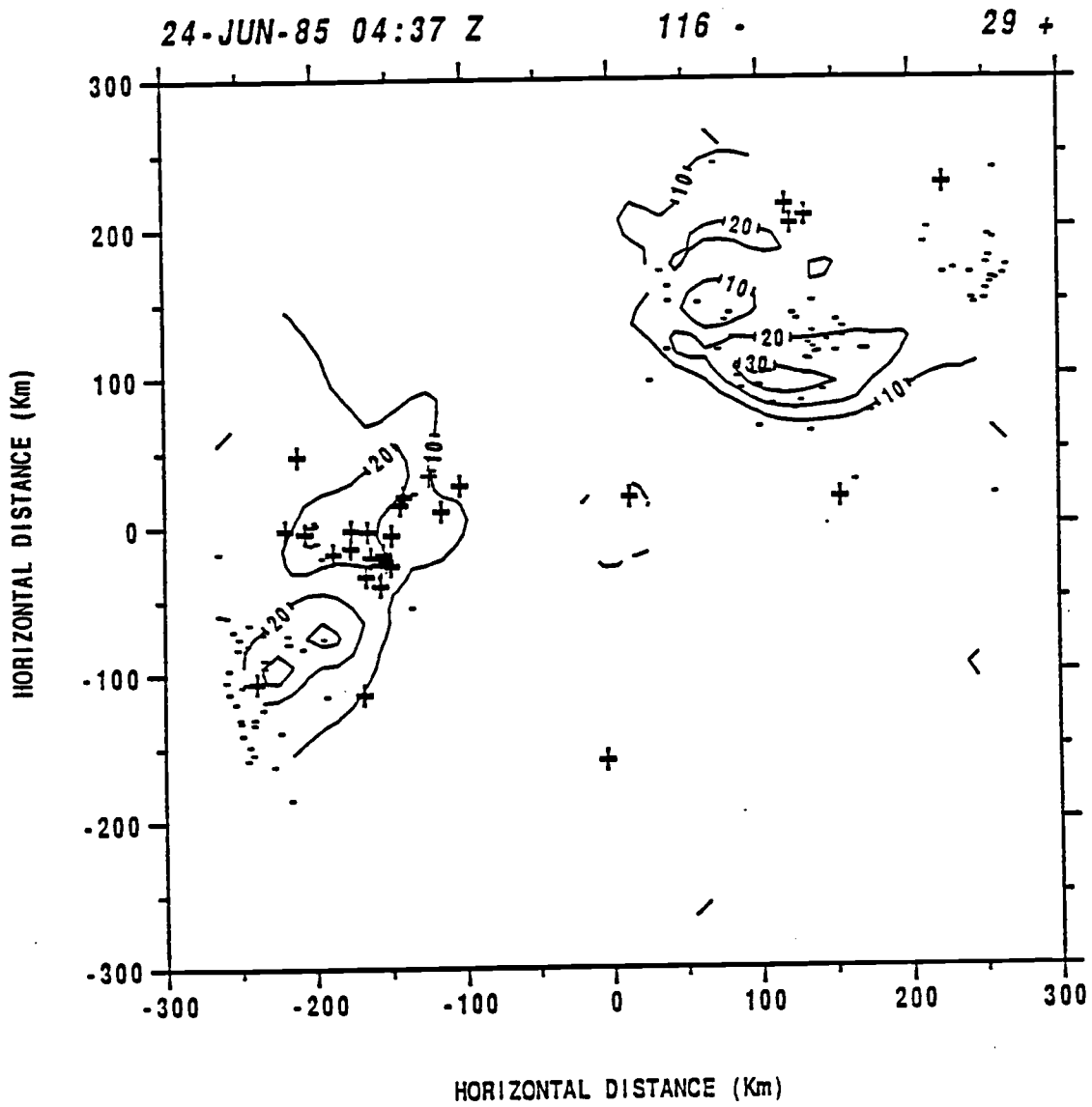


Fig. 3.75 Radar echo pattern and lightning map for 0437Z on 24 June.

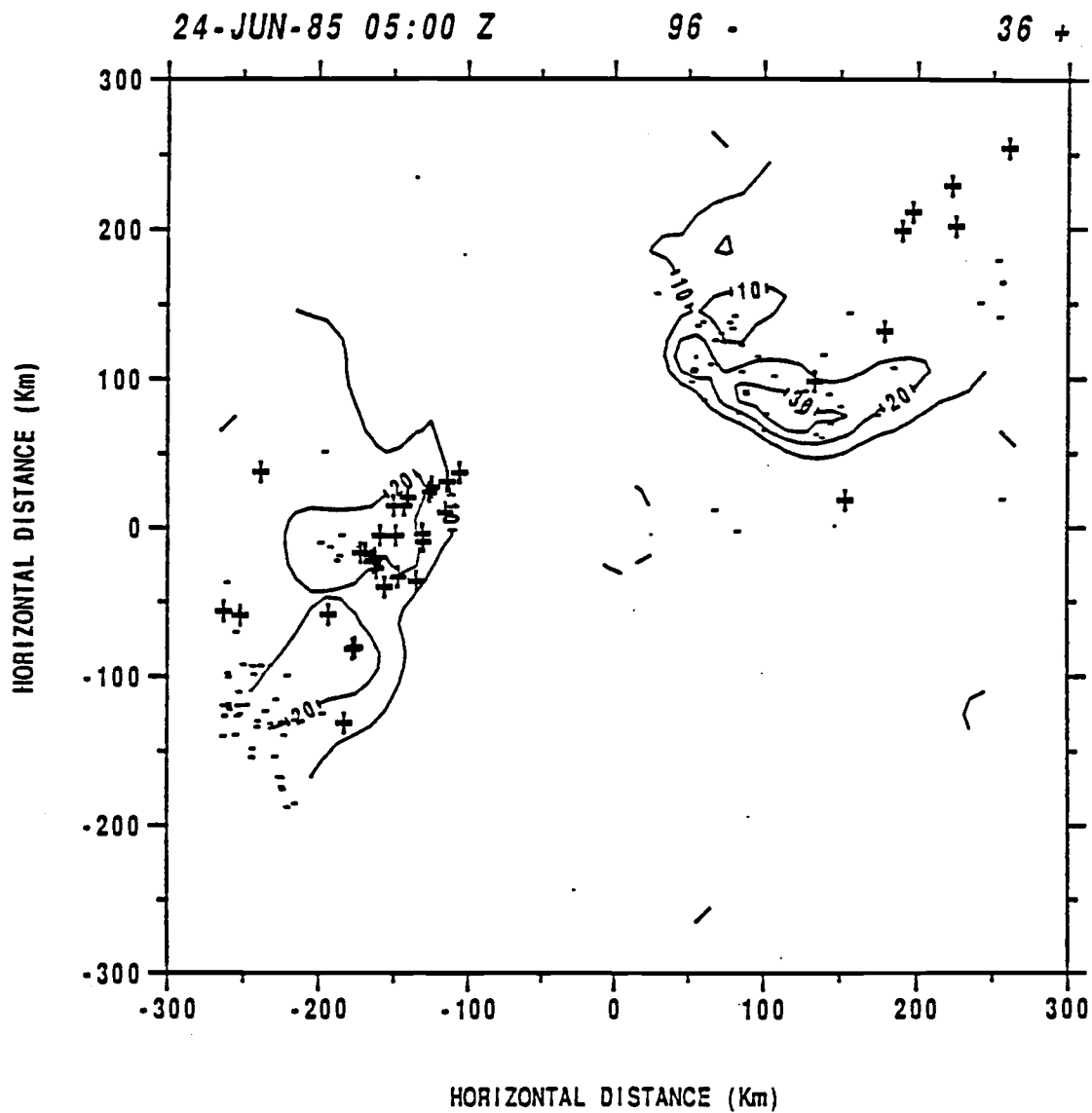


Fig. 3.76 Radar echo pattern and lightning map for 0500Z on 24 June.

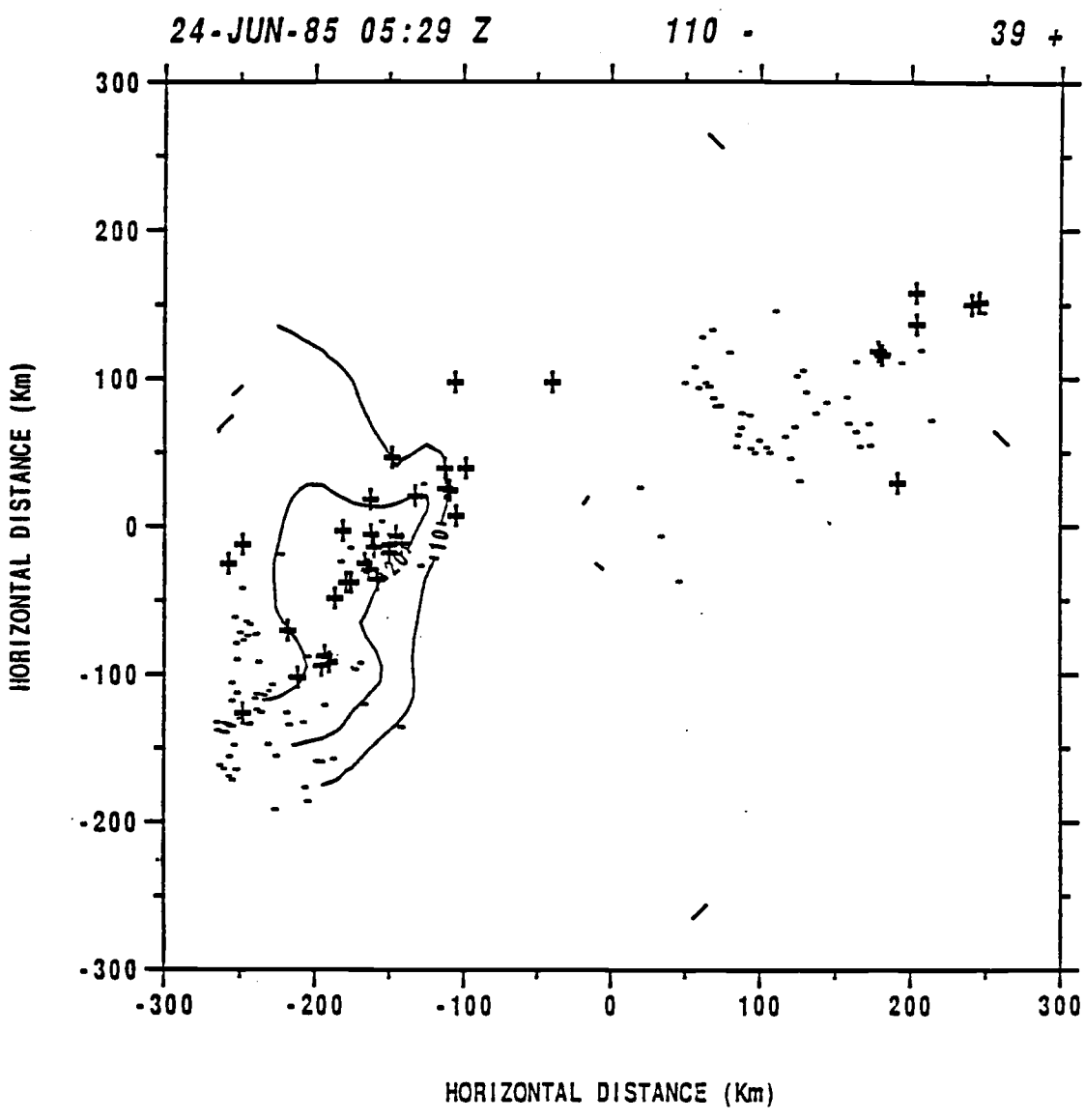


Fig. 3.77 Radar echo pattern and lightning map for 0529Z on 24 June.

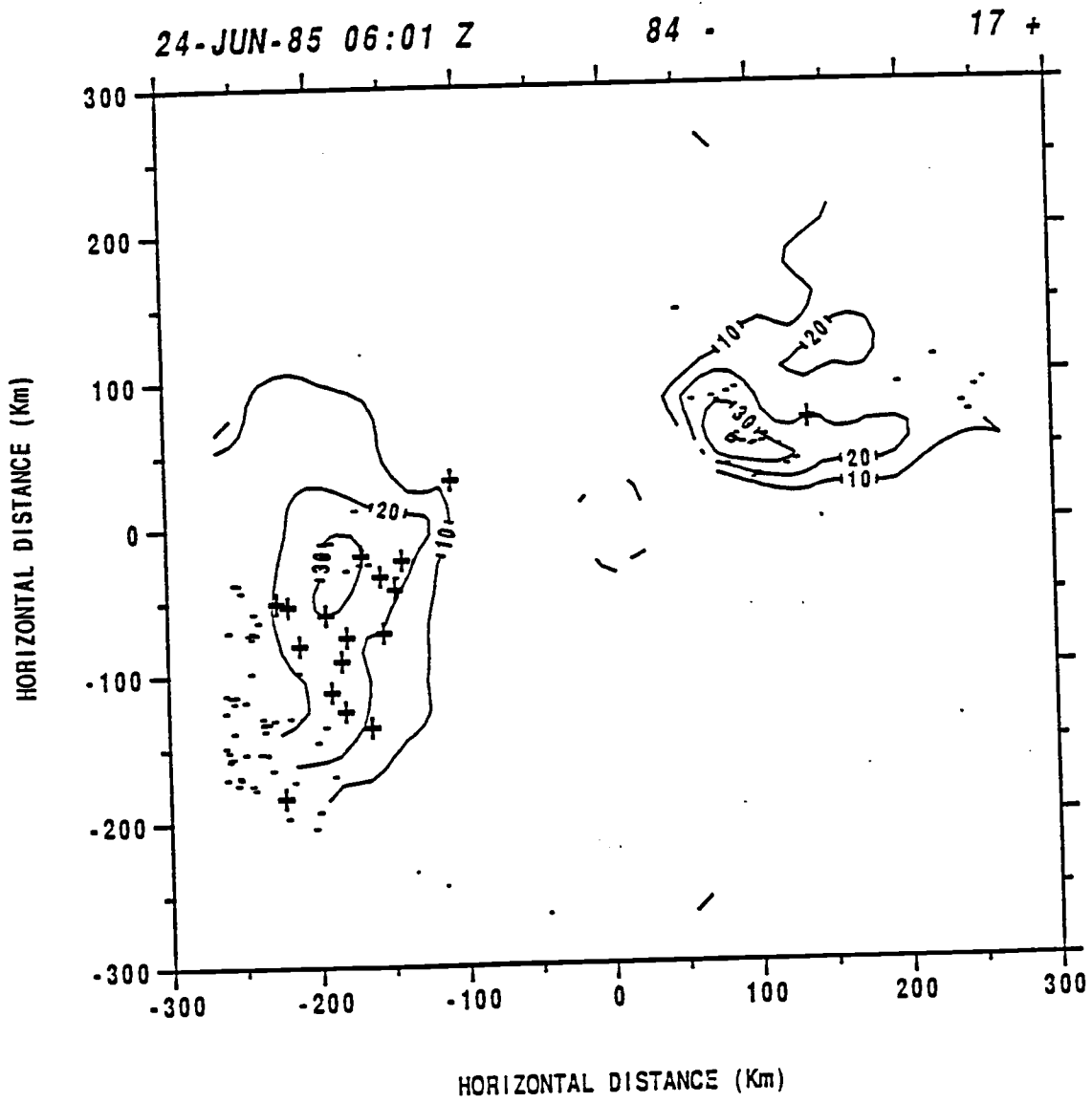


Fig. 3.78 Radar echo pattern and lightning map for 0601Z on 24 June.

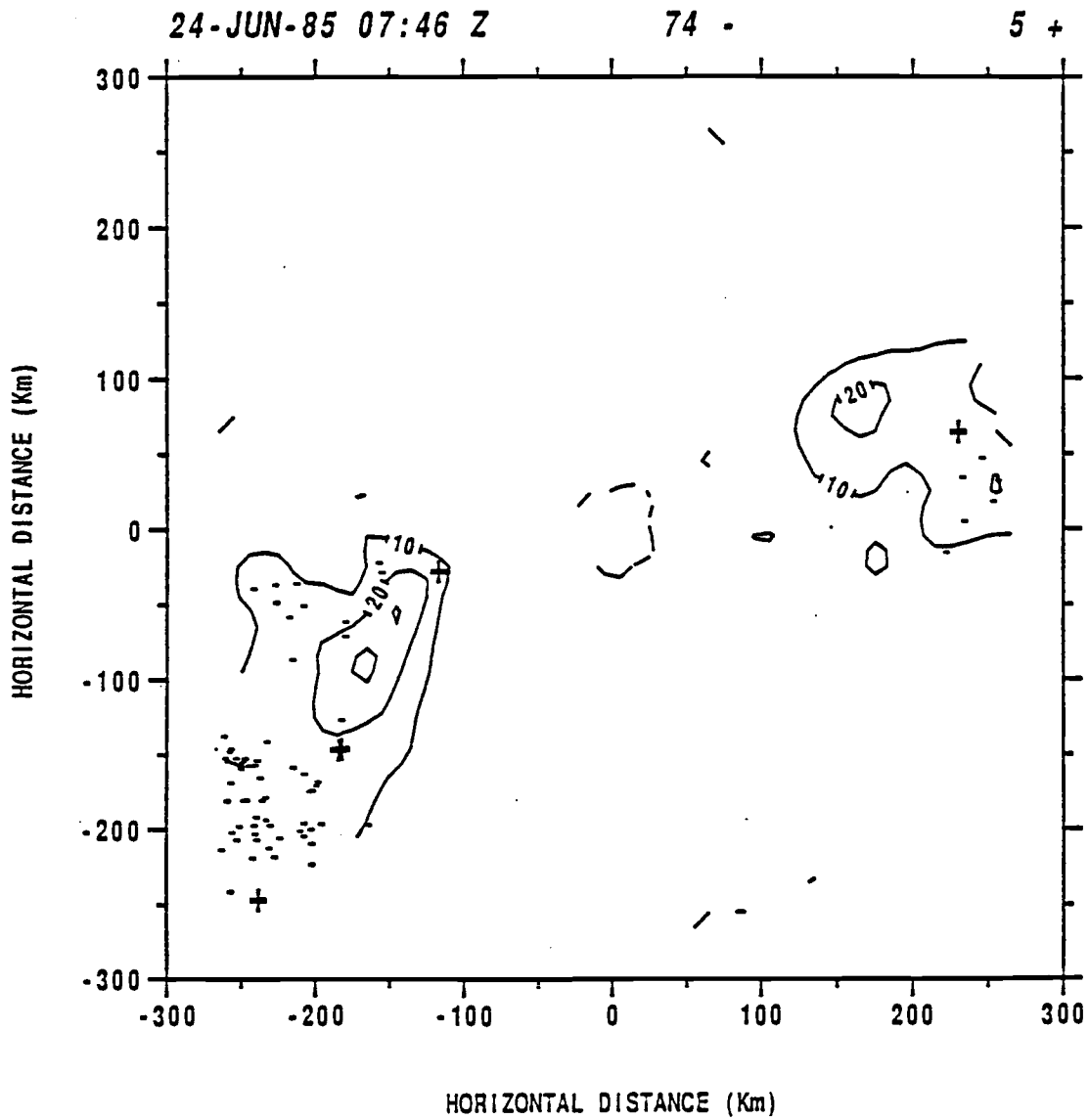


Fig. 3.79 Radar echo pattern and lightning map for 0746Z on 24 June.

4. Relationship of positive ground flashes to storm structure

In Chapter 3, we discussed the spatial and temporal characteristics of positive cloud-to-ground lightning flashes in conjunction with low level radar echo patterns. Two features of positive CG flashes were revealed from these discussions. First, positive cloud-to-ground flashes occurred more frequently in stratiform regions than in convective regions. Secondly, the frequency of positive CG flashes is highest during the later stages of the observed storm lifecycle. Based on these observations, a question will be asked: what physical processes are responsible for the achievement of these spatial and temporal characteristics of positive cloud-to-ground lightning flashes?

In general, there are two possibilities for the generation of positive cloud-to-ground flashes with regard to their location in the stratiform region. Considerable positive charge can either be transported from convective cells or possibly be generated locally in the stratiform region. To address this charge generation point more explicitly, we will use a continuity equation for charge generation to examine the potential for significant positive charge generation in the stratiform region. Our continuity equation model is of the form,

$$\frac{dQ}{dt} = S \quad (4.1)$$

where S represents the sources for charge generation in the stratiform region

through microphysical processes. We will neglect charge decay mechanisms (e.g. ion dissipation) since we are interested primarily in addressing the maximum rate of charge generation. By comparing derived charging rates with typical thunderstorm charge densities required for breakdown, we can assess the likelihood of positive charge generation leading to positive cloud-to-ground flashes in the stratiform region. Other minor processes, such as the fallout and eddy diffusion processes are also neglected. The only source term we consider is collisions between any ice particles in the presence of liquid water. Therefore, the continuity equation becomes,

$$\frac{\partial Q}{\partial t} = -\vec{v} \cdot \vec{\nabla} Q \pm \left(\frac{\partial Q}{\partial t} \right)_{in-situ} \quad (4.2)$$

The first term on the right-hand-side represents the charge advection from the domain outside the stratiform region. The second term is the source term in the stratiform region. The plus and minus signs indicate that charge generated by interaction between hydrometeors may be either positive or negative (i.e., the large hydrometeor may be charged either positively or negatively, depending upon the temperature and liquid water content following Saunders and Jayaratne, 1986). Hence, the charge advection mechanism and *in-situ* charge generation mechanism are proposed to explain positive charge generation in the stratiform region.

In this chapter, we will test these two mechanisms, and address the question being raised above. A 1-D charge generation model will be developed and a quantitative discussion will be given for the *in-situ* charge mechanism. The

evaluation of the charge advection mechanism will be based on knowledge of a vertical charge density profile and wind information from a dual-Doppler radar data analysis.

4.1 Discussion of *in-situ* charging mechanism

Mesoscale updrafts may play an important role in charge separation in the stratiform region. The mesoscale updraft is found throughout middle and upper levels in the stratiform region of MCSs, and the maximum updraft velocity may reach as large as 0.5 m s^{-1} or greater in some squall line type MCSs (Rutledge et al., 1988a). Vertical velocities of these magnitudes suggest that collisions between graupel (or rimed ice particles) and small ice particles will occur in the presence of supercooled water, consistent with the microphysical scenario modelled by Rutledge and Houze (1987). Hence, charge separation may be established through these interactions. This charge separation may form an inverted electric dipole with positive charge situated in the lower portion of the cloud, and negative charge aloft, following the charge reversal microphysics discussed by Saunders and Jayaratne (1986). This is opposite to that found in the convective region. If the density of positive charge with such a distribution exceeds the threshold value of 1 C km^{-3} (Krehbiel et al. 1979), positive cloud-to-ground flashes may occur in the stratiform region. As mesoscale updrafts intensify (and therefore liquid water contents and collision frequencies increase) during the mature and dissipating stages of MCSs (Rutledge et al., 1988a), positive CG flashes may occur more frequently. This *in-situ* charging mechanism has been proposed by Rutledge and MacGorman (1988), but confirmation of this hypothesis remains. Our work to test

this mechanism is primarily based on the experiment done by Saunders and Jayaratne (1986), as well as model output data from Rutledge and Houze (1987).

The charge generation in the stratiform region depends on interactions between two classes of hydrometeors (eq. 4.2.). In the presence of a strong mesoscale updraft, these interactions take place in the form of collisions mainly between graupel (or rimed aggregates) and small ice particles. Ice particles in the stratiform region of the 10-11 June MCS of this type have been confirmed by Rutledge et al. (1988b). The charge transferred when a graupel particle collides with a small ice particle has been discussed by Jayaratne et al. (1983) and more recently by Saunders and Jayaratne (1986). Fig. 4.1 is the laboratory result of this charge transfer variation with temperature and liquid water content when an ice crystals rebounded from a rimed ice particle (Saunders and Jayaratne, 1986).

In order to develop our 1-D charge generation model, we first developed a charge transfer (per collision) function based on the experimental results of Saunders and Jayaratne (1986). We choose a polynomial of order three to expand the charge transfer δq (in fC) as a function of temperature T ($^{\circ}$ C) of the form,

$$\delta q = a T^3 + b T^2 + c T + d \quad (4.3)$$

where a , b , c and d are expansion coefficients which were considered as the functions of liquid water content W (g m^{-3}).

For four different values of liquid water content, we identified a set of curves that best fit the laboratory results of Saunders and Jayaratne, given by the matrix equations,

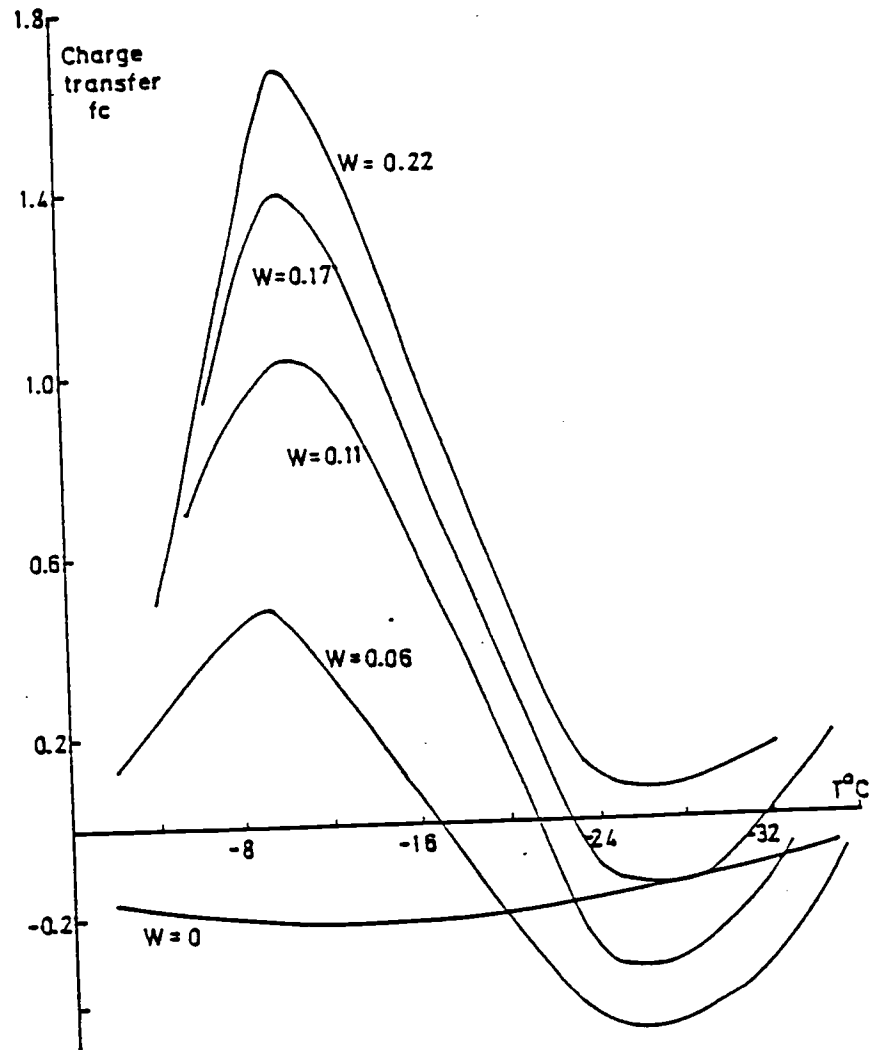


Fig. 4.1 The laboratory result of charge transfer per collision between graupel and small ice particles with temperature and liquid water content (Adapted from Saunders and Jayaratne, 1986). W denotes the liquid water content in g m^{-3} .

$$\begin{pmatrix} \delta q_1 \\ \delta q_2 \\ \delta q_3 \\ \delta q_4 \end{pmatrix} = \begin{pmatrix} a_1 & b_1 & c_1 & d_1 \\ a_2 & b_2 & c_2 & d_2 \\ a_3 & b_3 & c_3 & d_3 \\ a_4 & b_4 & c_4 & d_4 \end{pmatrix} \begin{pmatrix} T^3 \\ T^2 \\ T \\ 1 \end{pmatrix} \quad (4.4)$$

i.e.,

$$A = B \cdot C \quad (4.5)$$

Then we can further do a polynomial expansion of order two for a, b, c and d as a function of liquid water content,

$$\begin{aligned} a &= \alpha_1 W^2 + \beta_1 W + \gamma_1 \\ b &= \alpha_2 W^2 + \beta_2 W + \gamma_2 \\ c &= \alpha_3 W^2 + \beta_3 W + \gamma_3 \\ d &= \alpha_4 W^2 + \beta_4 W + \gamma_4 \end{aligned} \quad (4.6)$$

The expansion coefficient matrix

$$\begin{pmatrix} \alpha_1 & \beta_1 & \gamma_1 \\ \alpha_2 & \beta_2 & \gamma_2 \\ \alpha_3 & \beta_3 & \gamma_3 \\ \alpha_4 & \beta_4 & \gamma_4 \end{pmatrix} \quad (4.7)$$

can be determined by the known coefficient matrix B above.

In extrapolating the laboratory results to atmospheric condition, the charge transfer per collision as a function of temperature and liquid water content can be expressed as

$$\delta q = a(W) \tau^3 + b(W) \tau^2 + c(W) \tau + d(W) \quad (4.8)$$

where,

$$\begin{aligned} a(W) &= 3.37 \times 10^{-2} W^2 - 1.23 \times 10^{-2} W + 3.37 \times 10^{-4} \\ b(W) &= 2.02 W^2 - 0.68 W + 2.23 \times 10^{-3} \\ c(W) &= 34.51 W^2 - 11.51 W + 0.45 \\ d(W) &= 132 W^2 - 39.5 W + 2.05 \\ \tau &= T(z) - T_0 \\ T_0 &= 273.15 \text{ K} \end{aligned} \quad (4.9)$$

This function agrees well with the laboratory curves presented by Saunders and Jayaratne (1986). Fig. 4.2 shows the variation of this function (δq) with the temperature and liquid water content.

At this point we can begin to formulate our 1-D charge generation model. We assume that the collisions take place mainly between the graupel and snow. Because of sparse observational data for the cases analyzed in Chapter 3, we used the vertical profile of liquid water content, temperature, graupel mixing ratio and snow mixing ratio from Rutledge and Houze (1987) as our model input data. The particular case studied by Rutledge and Houze (1987) was the Oklahoma squall line of 22 May 1976, which is similar to the linearly organized storms in our studies, such as case of 27 May, 28 May, 10-11 June and 24 June. Rutledge and Houze used a 2-D diagnostic cloud model to predict the distribution of various hydrometeor fields

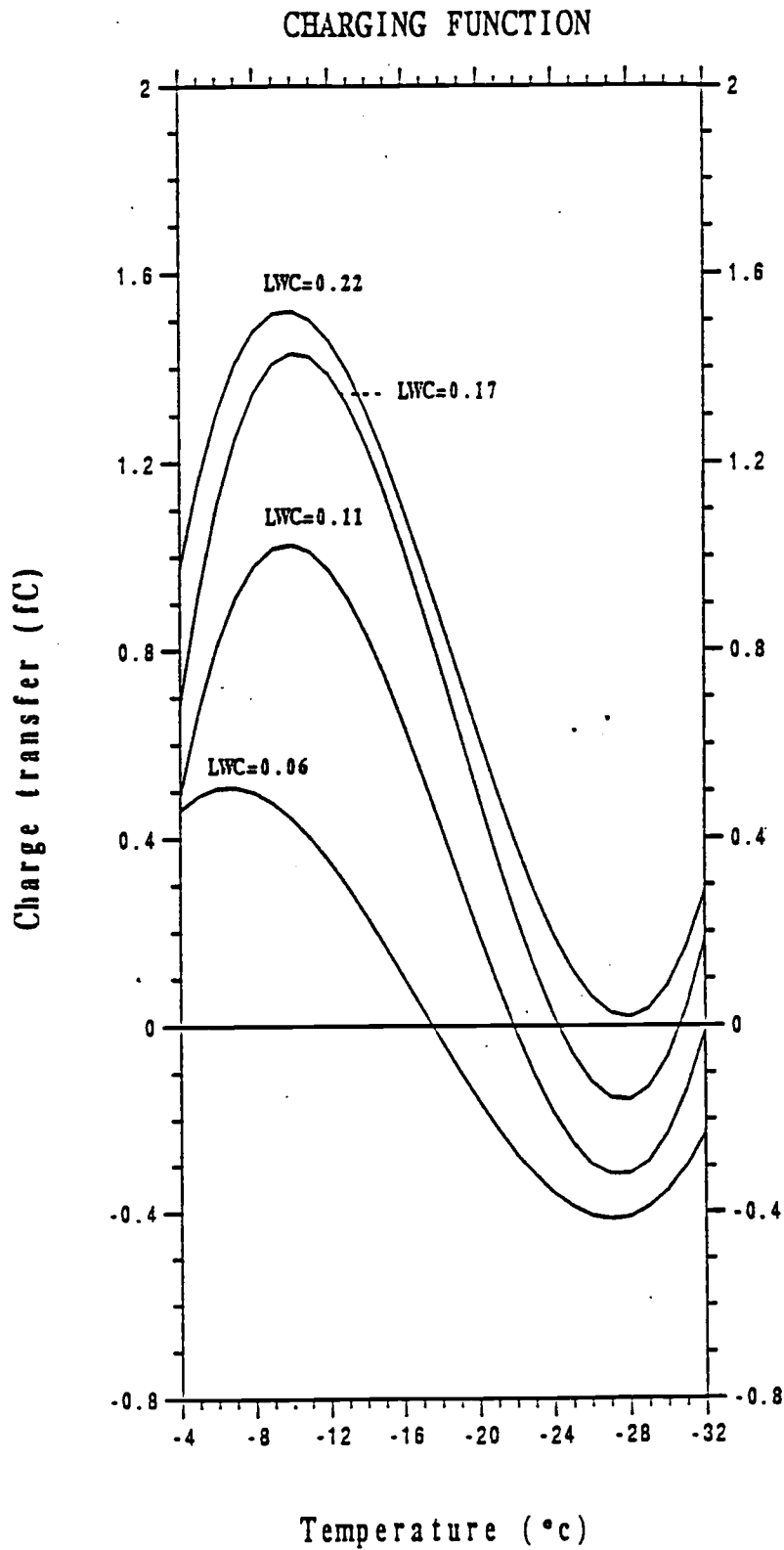


Fig. 4.2 Numerically derived function for δ_q for Saunders and Jayaratne experimental data.

in equilibrium with a specified mesoscale updraft field. From their results we obtained a representative vertical profile of liquid water content, temperature, graupel mixing ratio and snow mixing ratio in the center of the stratiform region. These profiles are shown in Fig. 4.3 a-d.

The charge generation rate for graupel with a size interval between $D_g + dD_g$ colliding with snow with size interval between $D_s + dD_s$ is (in $\text{fc sec}^{-1} \text{m}^{-3}$)

$$\left(\frac{\partial Q}{\partial t} \right)_{\text{colli}} = \frac{\pi}{4} (D_g + D_s)^2 \Delta V E_{gs} N_g N_s \delta q dD_g dD_s \quad (4.10)$$

where $\Delta V = |V_g - V_s|$ is the relative collision speed between graupel and snow. E_{gs} is the charge generation efficiency which equals the product of collision efficiency and charge transfer efficiency between graupel and snow. In this study we set $E_{gs} = 1$. Lack of experimental data for E_{gs} prevents the choice of any other value. The charge transfer per collision, as derived previously, is given by δq . N_g and N_s , the number concentrations for graupel and snow respectively, are functions of the diameter of graupel and snow and have the form of inverse exponential size distributions,

$$N_g(D_g) = N_{0g} e^{-\lambda_g D_g} \quad (4.11)$$

$$N_s(D_s) = N_{0s} e^{-\lambda_s D_s} \quad (4.12)$$

where λ_g and λ_s are the slopes of graupel and snow size distributions respectively, obtained from the genera relation,

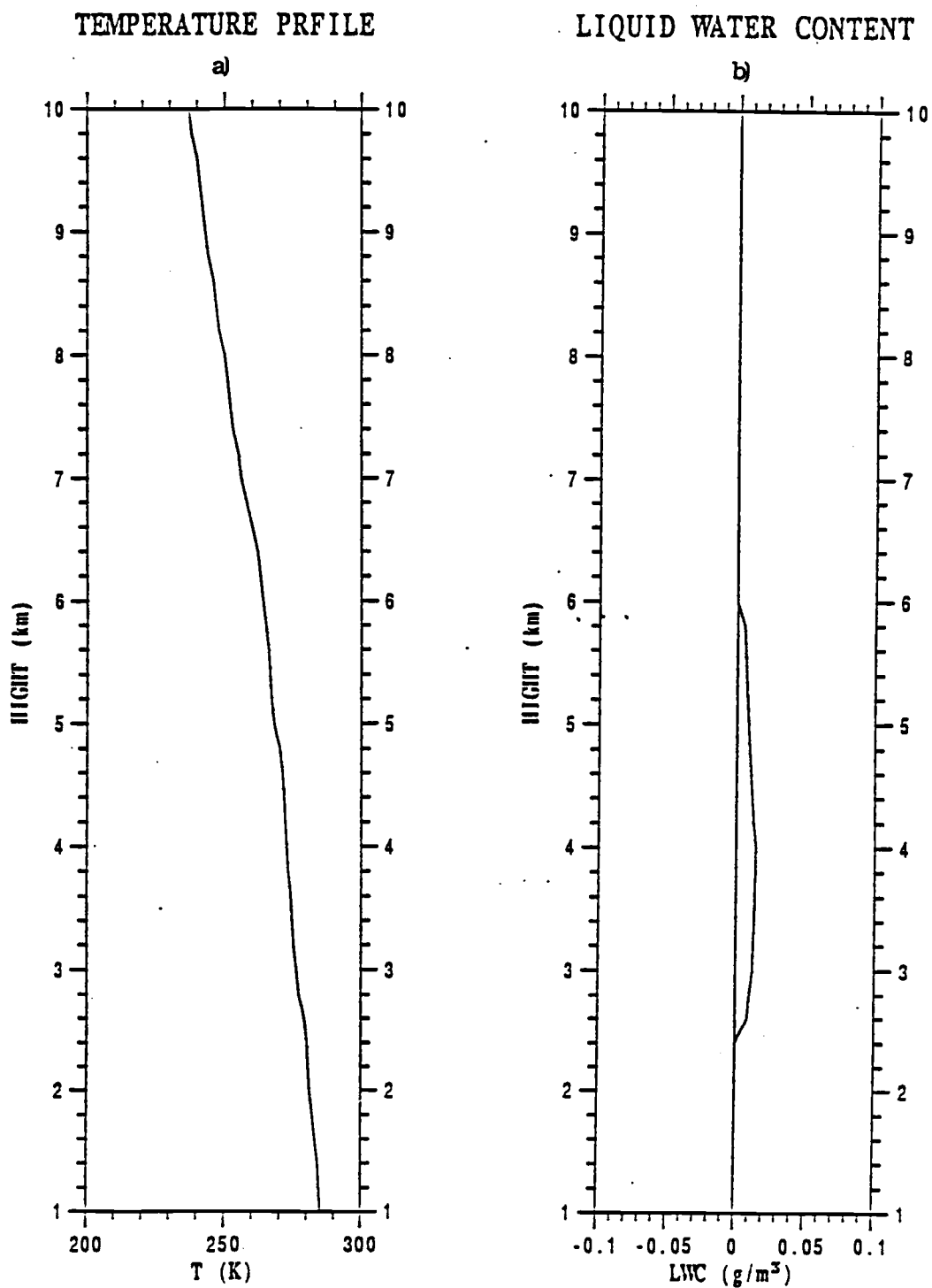
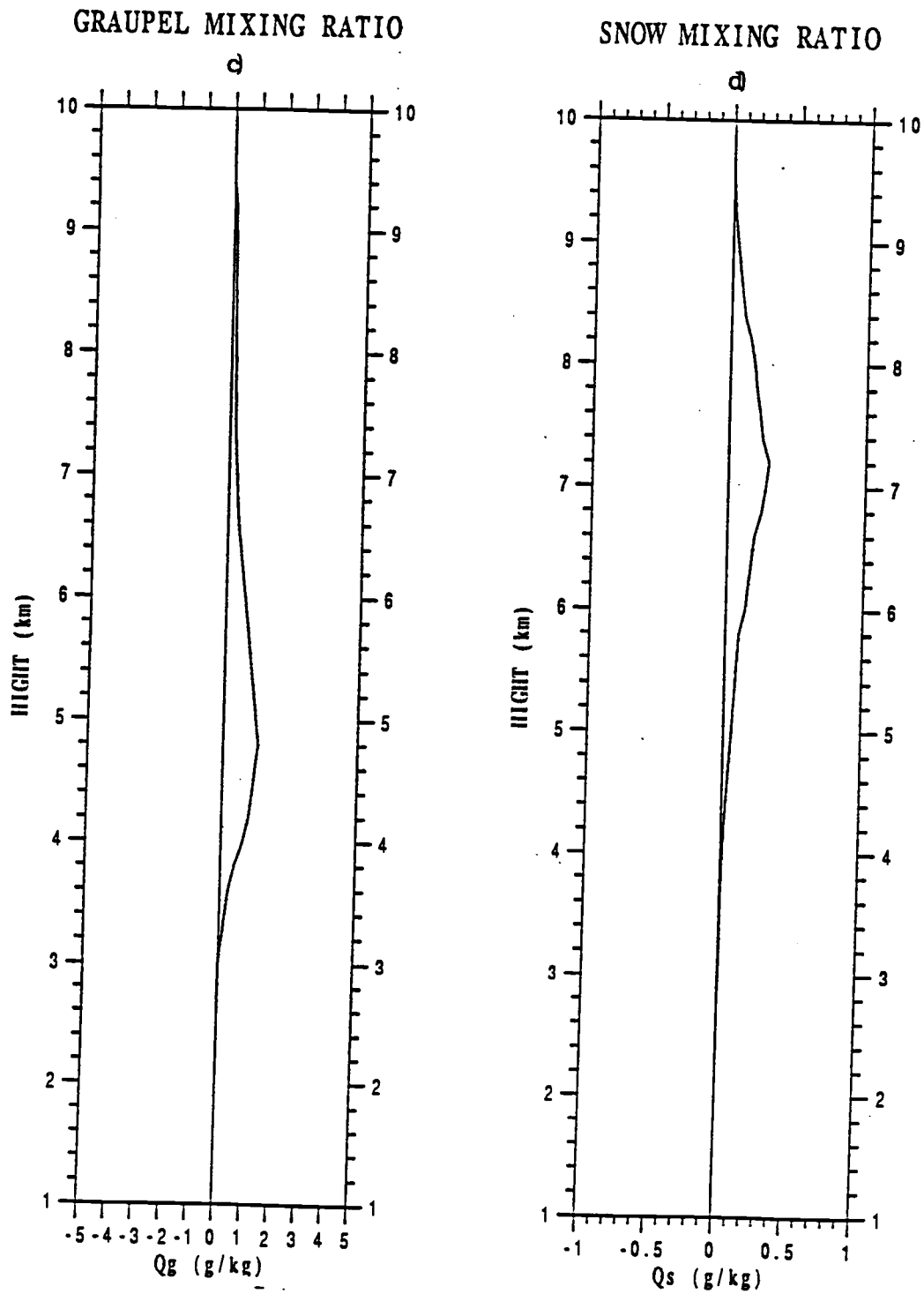


Fig. 4.3 Vertical profiles used in the 1-D model calculations, from Rutledge and Houze (1987). a) cloud water content; b) temperature;



c) graupel mixing ratio; d) snow mixing ratio.

$$M_i = \rho_a q_i = \int_0^{\infty} \frac{\pi}{6} \rho_i D_i^3 N_{0i} e^{-\lambda_i D_i} dD_i = \frac{\pi}{6} \rho_i N_{0i} \frac{\Gamma(4)}{\lambda_i^4} \quad (4.13)$$

$$\text{or,} \quad \lambda_i = \left(\frac{\pi \rho_i N_{0i}}{\rho_a q_i} \right)^{0.25} \quad (4.14)$$

Therefore, for λ_g and λ_s , we have

$$\lambda_g = \left(\frac{\pi \rho_g N_{0g}}{\rho_a q_g} \right)^{0.25} \quad (4.15)$$

$$\lambda_s = \left(\frac{\pi \rho_s N_{0s}}{\rho_a q_s} \right)^{0.25} \quad (4.16)$$

where ρ_g, ρ_s are the densities of graupel and snow, q_g, q_s are the mixing ratios of graupel and snow, ρ_a is the density of air, and $N_{0g} = N_{0s}$ are the slope intercept values in the graupel and snow size distributions. The charge generation rate can be found by computing the collision frequency between the graupel and snow distributions, of the form,

$$\frac{dn}{dt} = \frac{\pi}{4} (D_g + D_s)^2 |\bar{V}_g - \bar{V}_s| n_g n_s E_{gs} \quad (4.17)$$

Multiplying (4.16) by δq gives the desired charge generation rate.

For all graupel and snow sizes, the charge generation rate becomes,

$$\begin{aligned}
\left(\frac{\partial Q}{\partial t}\right)_{\text{colli}} &= \frac{\pi}{4} E_{g,s} |\bar{V}_g - \bar{V}_s| \delta q \int_0^\infty \int_0^\infty (D_g^2 + 2D_g D_s + D_s^2) N_{0g} e^{-\lambda_s D_s} N_{0s} e^{-\lambda_g D_g} dD_g dD_s \\
&= \frac{\pi}{4} N_{0g} N_{0s} E_{g,s} |\bar{V}_g - \bar{V}_s| \delta q \int_0^\infty \left(\frac{D_g^2 \Gamma(1)}{\lambda_s} + \frac{2 \Gamma(2) D_g}{\lambda_s^2} + \frac{\Gamma(3)}{\lambda_s^3} \right) dD_g \\
&= \frac{\pi}{4} N_{0g} N_{0s} E_{g,s} |\bar{V}_g - \bar{V}_s| \delta q \left(\frac{\Gamma(1) \Gamma(3)}{\lambda_s \lambda_g^3} + \frac{2 \Gamma(2) \Gamma(2)}{\lambda_s^2 \lambda_g^2} + \frac{\Gamma(3) \Gamma(1)}{\lambda_s^3 \lambda_g} \right) \quad (4.18)
\end{aligned}$$

In the derivation above we assumed that all graupel and snow particles fall at their mass-weighted fallspeeds, which depend on the graupel content (q_g) and snow content (q_s) respectively. These fallspeeds are defined as

$$\bar{V}_g = \frac{\int_0^\infty N_g(D_g) M(D_g) V_g(D_g) dD_g}{\int_0^\infty N_g(D_g) M(D_g) dD_g} \quad (4.19)$$

$$\bar{V}_s = \frac{\int_0^\infty N_s(D_s) M(D_s) V_s(D_s) dD_s}{\int_0^\infty N_s(D_s) M(D_s) dD_s} \quad (4.20)$$

where $M(D_g) = \frac{\pi}{6} \rho_g D_g^3$ and $M(D_s) = \frac{\pi}{6} \rho_s D_s^3$.

The fallspeed-diameter relation is given by Locatelli and Hobbs (1974) as

$$V_g(D_g) = a_g D_g^{b_g} \left(\frac{P_0}{P} \right)^{0.4} \quad (4.21)$$

$$V_s(D_s) = a_s D_s^{b_s} \left(\frac{P_0}{P} \right)^{0.4} \quad (4.22)$$

where the constants (in SI units) are,

$$a_g = 19.3, \quad b_g = 0.37, \quad a_s = 1.139, \quad b_s = 0.11.$$

From (4.11), (4.12), and (4.19 - 4.22):

$$\bar{V}_g = a_g \frac{\Gamma(4 + b_g)}{6} \lambda_g^{-b_g} \left(\frac{P_0}{P} \right)^{0.4} \quad (4.23)$$

$$\bar{V}_s = a_s \frac{\Gamma(4 + b_s)}{6} \lambda_s^{-b_s} \left(\frac{P_0}{P} \right)^{0.4} \quad (4.24)$$

Substituting all the results into (4.17), we obtain the charge generation rate as a function of height,

$$\left(\frac{\partial Q}{\partial t} \right) = \frac{\pi}{4} N_{0g} N_{0s} E_{gs} |\bar{V}_g - \bar{V}_s| \delta q \left(\frac{\Gamma(1)\Gamma(3)}{\lambda_s \lambda_g^3} + \frac{2\Gamma(2)\Gamma(2)}{\lambda_s^2 \lambda_g^2} + \frac{\Gamma(3)\Gamma(1)}{\lambda_s^3 \lambda_g} \right) \quad (4.25)$$

By inserting the vertical profiles of temperature, liquid water content, graupel and snow mixing ratio from the Rutledge and Houze calculation (Figs. 4.3 a-d), we arrive at the charge generation rate vertical profile shown in Fig. 4.4. This result shows that positive charge is generated in the lower portions of the cloud with maximum generation rate being located at about 4.5 km. Negative charging is situated in the upper portions of the cloud with maximum generation rate at about 6.8 km. Hence an inverted electric dipole is formed. The maximum positive charge generation rate is about $25 \text{ fC sec}^{-1} \text{ m}^{-3}$, or $2.5 \times 10^{-5} \text{ C sec}^{-1} \text{ km}^{-3}$. If we integrate this

VERTICAL PROFILE OF CHARGE GENERATION RATE

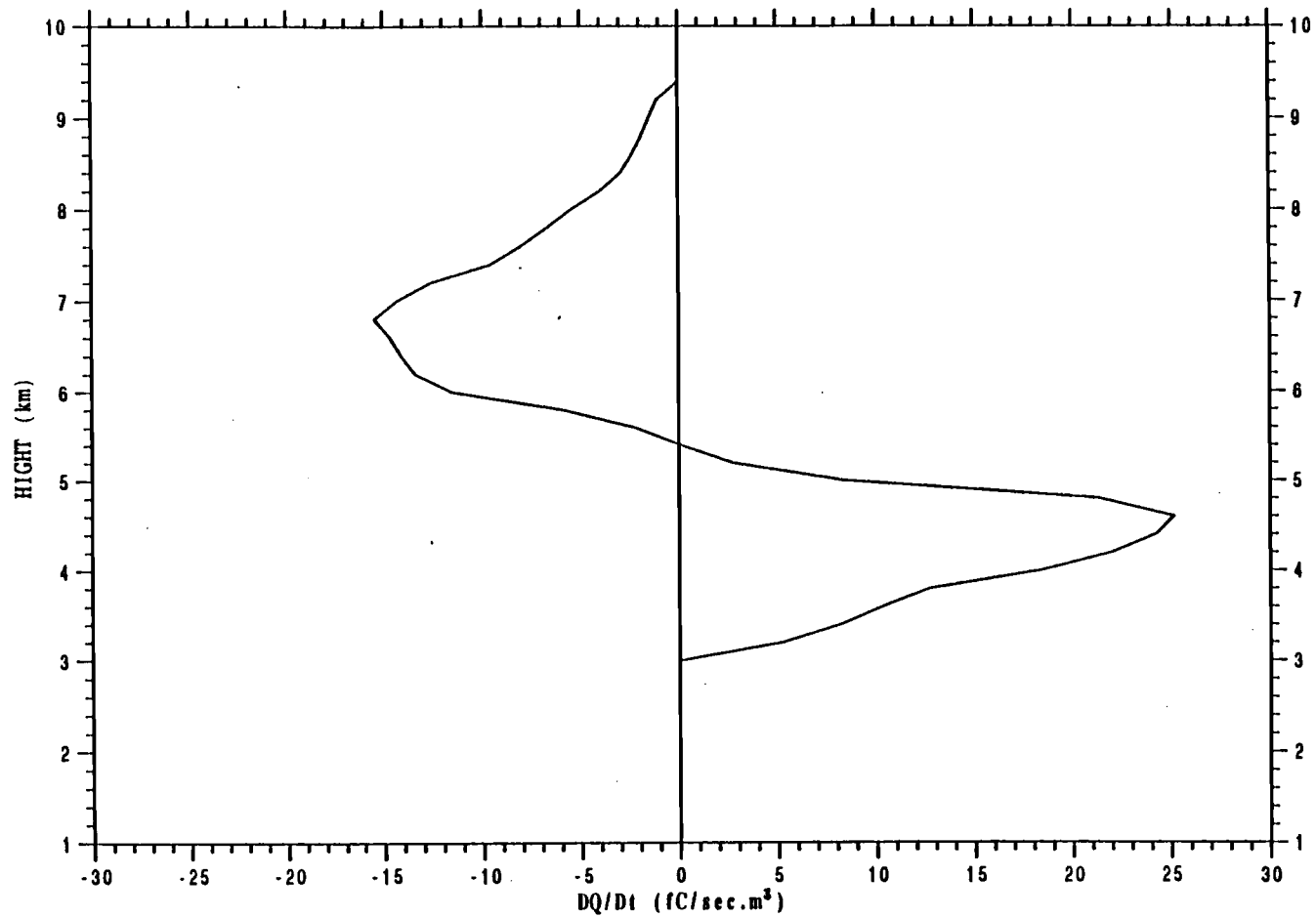


Fig. 4.4 Vertical distribution of charge generation rate produced by the 1-D model.

result with respect to time, over an hour for instance, this value would be approximately 0.1 C km^{-3} . Compared with the typical charge density just prior to a lightning stroke on the order of 1 C km^{-3} , this value appears to be substantially smaller than that necessary to trigger positive cloud-to-ground flashes. Therefore, this simple model suggests that *in-situ* charging process is unlikely to produce substantial volume charging rates required to produce breakdown and the occurrence of positive cloud-to-ground lightning flashes.

Because the model input data is provided by a squall line type MCS from Rutledge and Houze (1987), the argument above is most applicable to the linear MCSs (strong shear cases), such as 27 May, 28 May, 10-11 June and 24 June. For non-linear MCSs (cases of 3 June, 4 June and 10 June), the extension of the *in-situ* calculation is perhaps questionable, however we have no reason to believe that stratiform microphysics are any different in non-linear MCSs, suggesting that *in-situ* charging is also unimportant in those systems.

We can use the model to conduct sensitivity studies to determine under what atmospheric conditions *in-situ* charging may lead to significant charge generation in the stratiform region. There are two ways to enhance positive charge generation in the stratiform region. One way is to increase the liquid water content in the cloud. [The charge transfer per collision increases with liquid water content, according to the laboratory results of Saunders and Jayaratne, 1986]. Another way is to increase the collision frequency between graupel and snow. Various sensitivity studies conducted and their results are listed in Table 4.1. Increased amounts are considered to be upper-limit scenarios in stratiform region of MCSs. Results are presented graphically in Figs. 4.5 a-d.

Table 4.1. List of operations and results for five experiments.

Experiment	Original amount (max)	Increased amount (max)	New charge density(max)
1) Increase in LWC	0.014 g m^{-3}	0.28 g m^{-3}	0.108 C km^{-3}
2) Increase in Qs	0.3 g kg^{-1}	3.0 g kg^{-1}	0.23 C km^{-3}
3) Increase in Qg	1.3 g kg^{-1}	3.0 g kg^{-1}	0.171 C km^{-3}
4) Increase in both Qs and Qg	0.3 g kg^{-1} 1.3 g kg^{-1}	3.0 g kg^{-1} 3.0 g kg^{-1}	0.41 C km^{-3}
5) Increase in Qs, Qg and LWC	0.3 g kg^{-1} 1.3 g kg^{-1} 0.014 g m^{-3}	3.0 g kg^{-1} 3.0 g kg^{-1} 0.28 g m^{-3}	0.49 C km^{-3}

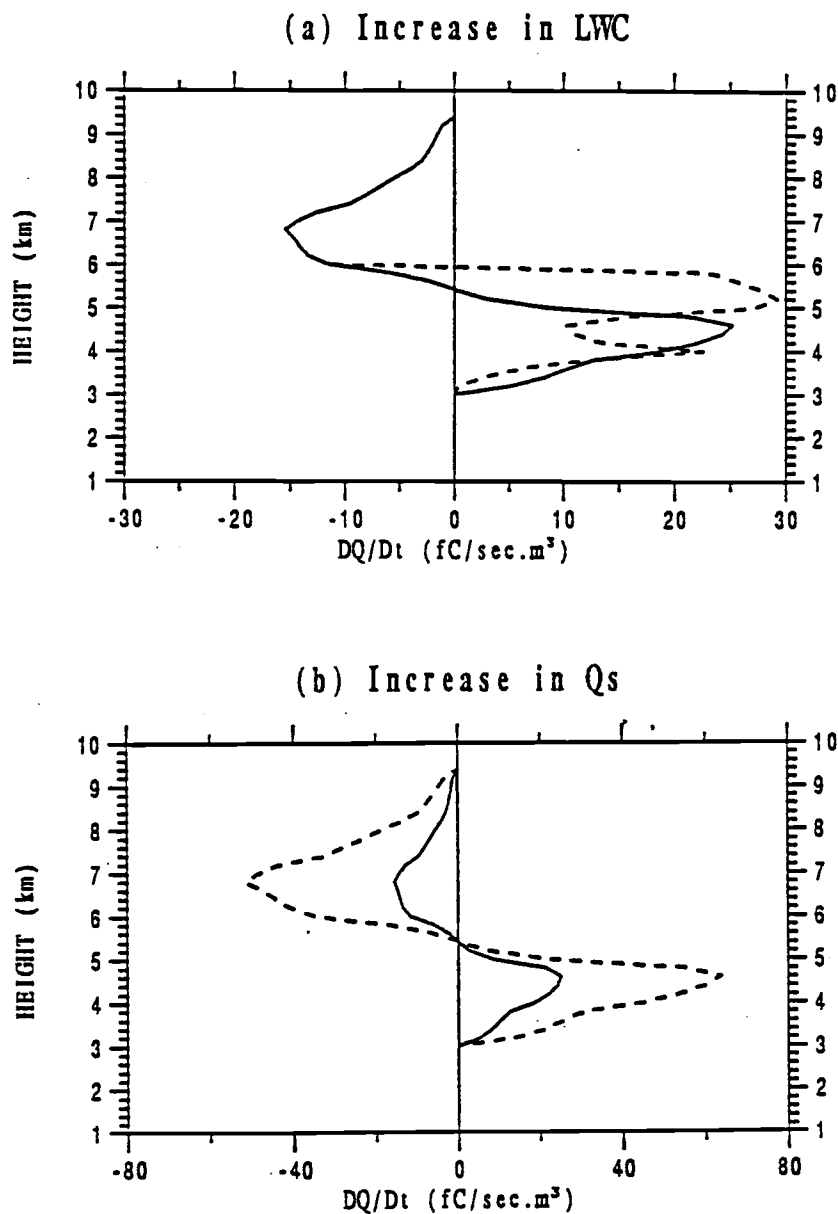


Fig. 4.5 Results of sensitivity studies discussed in text.

- a) Increase liquid water case.
- b) Increase in Q_s case.
- c) Increase in Q_g case.
- d) Increase in Q_s and Q_g .
- e) Increase in liquid water, Q_s and Q_g .

Note: scale changes on horizontal axis. Original charging profile indicated by (—). Sensitivity profile denoted by (---).

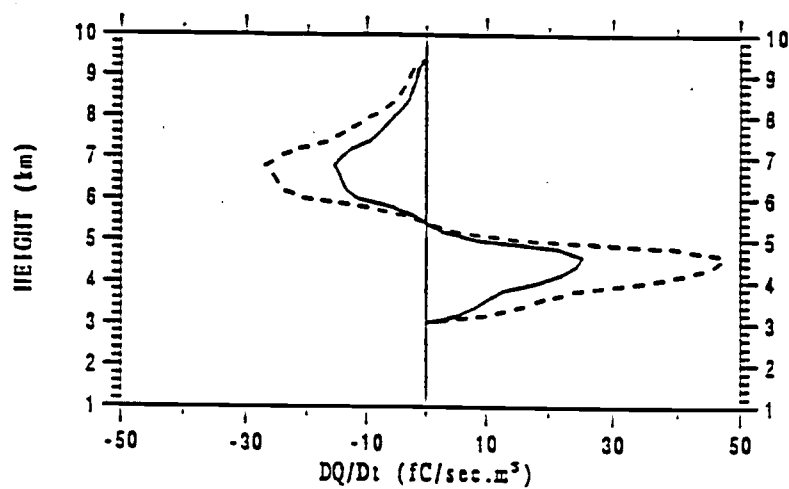
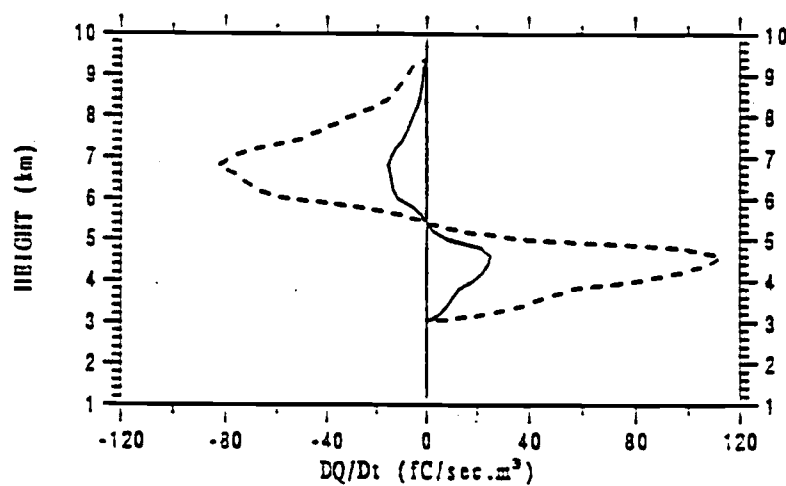
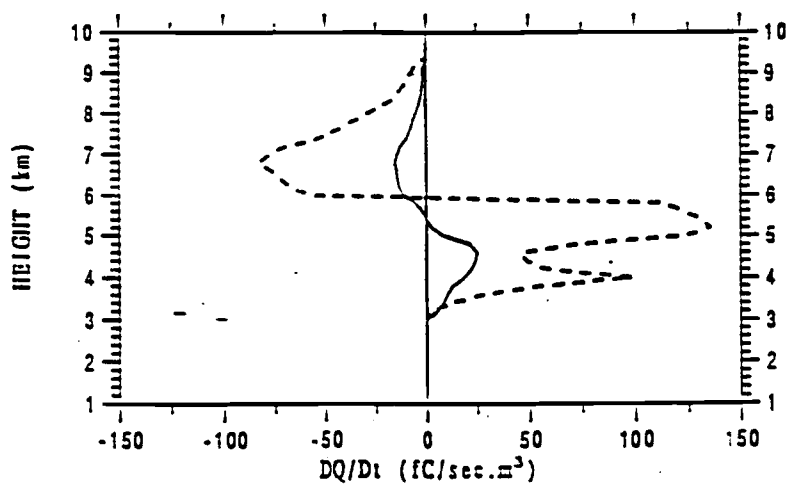
(c) Increase in Q_g (d) Increase in both Q_g and Q_s (e) Increase in Q_g , Q_s and LWC

Figure 4.5 Continued

In experiment 1), we increased the original amount of liquid water content by a factor of 20. The result showed that the maximum positive charge generation rate increased to $30 \text{ fC sec}^{-1} \text{ m}^{-3}$, i.e., the maximum positive charge density was increased to 0.108 C km^{-3} . Hence, increasing liquid water content is not an effective way to increase positive charge generation. In experiment 2) and 3), we individually increased the original amounts of snow and graupel to maximum reasonable values (3.0 g kg^{-1}). The maximum positive charge density reached 0.23 C km^{-3} and 0.17 C km^{-3} respectively. In experiment 4) the amount of snow and graupel were increased to 3.0 g kg^{-1} simultaneously. The charge density increased to 0.41 C km^{-3} (over a 1 hour period). Moreover, in experiment 5) we increased the liquid water content to 0.28 gm^{-3} , while at the same time increasing both the snow and graupel mixing ratios to 3.0 g kg^{-1} . The predicted charge density was 0.49 C km^{-3} (for 1 hour). This value, although it did not reach the value necessary to induce breakdown and therefore positive cloud-to-ground strokes, was nonetheless significant because if integrated over a period of two hours, the maximum charge density would be approximately 1 C km^{-3} , which is typical of thunderstorm charge density values.

From the sensitivity experiments we can see that the increase in number of collisions between graupel and snow particles is an effective way to produce substantial amount of positive charge in stratiform region of the cloud. This suggests that *in-situ* charging process strongly depends on the graupel and snow content in cloud. In general, *in-situ* charging process is not a dominant mechanism under normal atmosphere conditions. However it may become important if large snow and graupel contents are available. Hence, the *in-situ* charging mechanism cannot be completely dismissed as a potential mechanism for

the occurrence of positive cloud-to-ground lightning flashes.

4.2 Discussion of charge advection mechanism

In the continuity equation for charge generation (eq. 4.2), we see that the advection term (the first term on the right-hand-side) also contributes to the charge generation rate. The positive charge advection mechanism is described mathematically by this term. In the charge advection mechanism, it is assumed that the processes of charge attachment to the ice particles have been fulfilled, and therefore charge separation vertically in the convective region has been established by updraft of convective cells. Positive charge is advected from the convective cells to the cloud anvil or to surrounding stratiform regions by horizontal transport. Horizontal advection of positive charge (the tilted dipole model) has been suggested by MacGorman (1978), Lhermitte and Krehibiel (1979), Rust et al. (1981) and Brook et al. (1982), in explaining the presence of positive cloud-to-ground flashes near convective storms. More recent work was done by Rutledge and MacGorman (1988). The charge advection mechanism may also account for the observed temporal characteristic of positive CG flashes. The calculation of ice particle trajectories made by Rutledge and MacGorman has shown that the time required for ice particles to advect from the convective region to the stratiform region is equivalent to the time between the peak convective rainfall and the peak stratiform rainfall, thus implying that the most frequent occurrence of positive CG flashes during the later stages of storm lifetime is because positively charged ice particles need time to be transported from the convective region to the stratiform region.

Quantitative testing of the charge advection mechanism requires an explicit cloud model and complete set of dual-Doppler radar data. Furthermore, more complete microphysical processes are required. This is beyond the scope of the present study. Instead, we can attempt to address the charge advection mechanism by analyzing available electric field and dual-Doppler data.

Figs. 4.6 shows the reflectivity and wind field from a particular dual-Doppler radar data analysis for the 10-11 June storm. A convective region (Fig. 4.6a) was marked by strong reflectivities in the area between $x=30-60$ km. The area immediately behind the convective region ($x=0-15$ km) was defined as a transition zone, denoted by weak surface precipitation rates. A large area of stratiform precipitation was situated rearward of the transition zone. The relative horizontal wind field (Fig. 4.6b) indicates strong front-to-rear (right-to-left) flow from the convective region into the trailing stratiform region. This flow was identified by Rutledge and MacGorman (1988) as being potentially important to the rearward transport of positive charge into the stratiform region. The maximum front-to-rear flow was situated between the 5-8 km level, with maximum values exceeding 20 m s^{-1} immediately behind the convective line.

To address the topic of charge advection in more detail, we can examine the horizontal flow field together with a vertical profile of the electric field (or charge density) acquired in the transition zone of a similar squall line storm in Oklahoma (Marshall 1988, personal communication). The vertical profile of the electric field is shown in Fig. 4.7. By Guass's Law,

$$\nabla \cdot \vec{E} = \frac{\rho}{\epsilon} \quad (4.26)$$

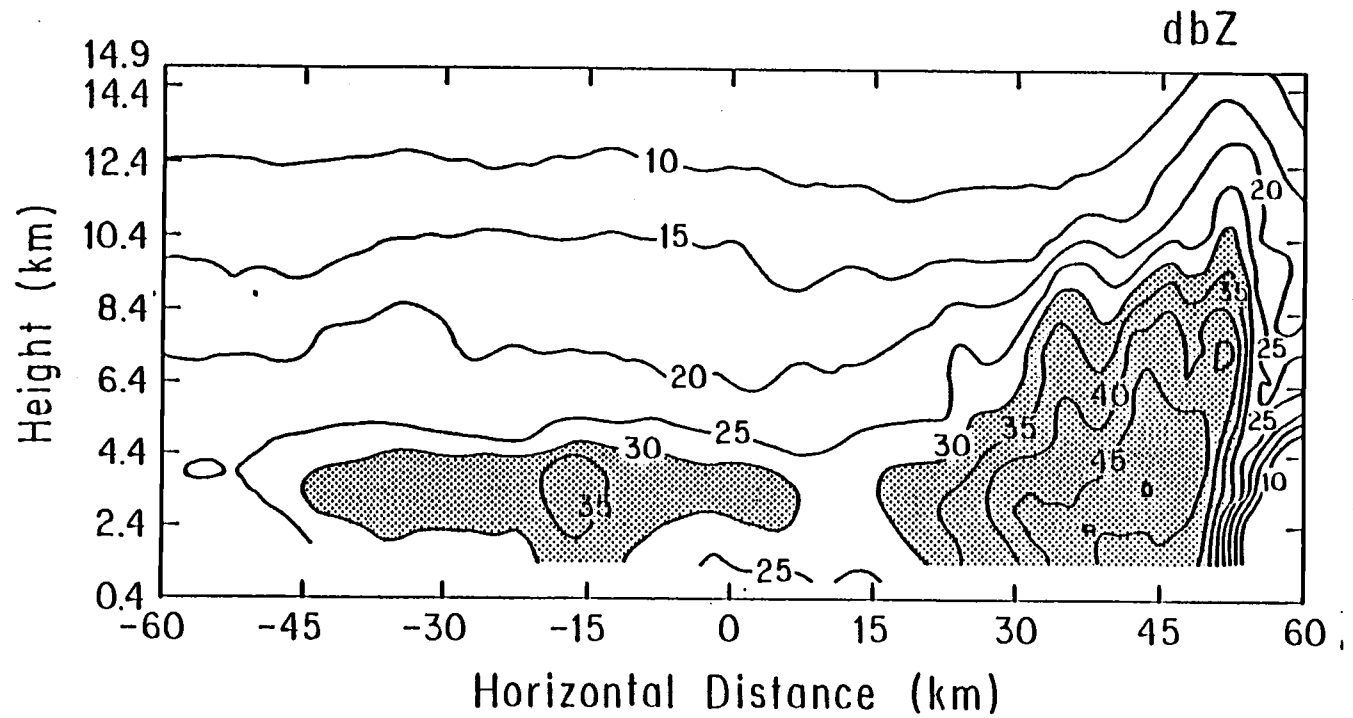


Fig. 4.6 Reflectivity and air motion fields for the 0202Z dual-Doppler analysis on 10-11 June 1985.

a) Reflectivity, shading for regions > 30 dBZ.

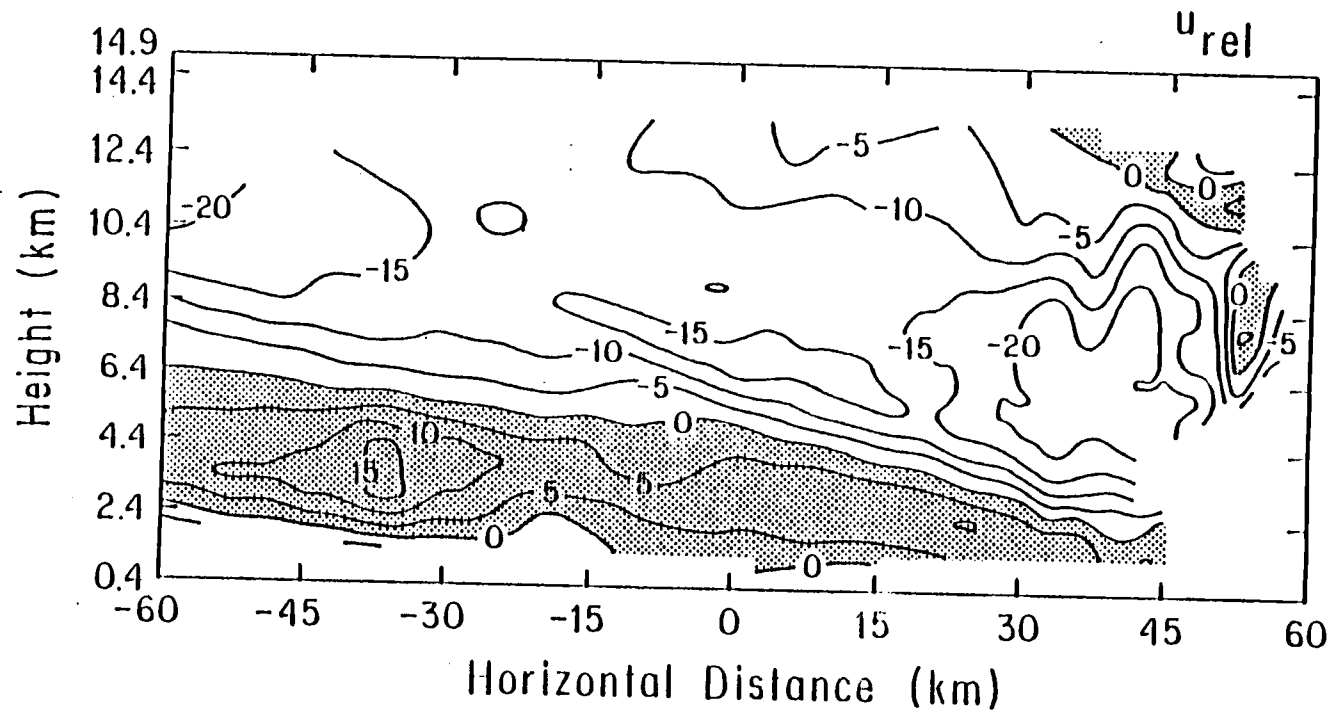


Figure 4.6 Continued

b) Horizontal relative flow perpendicular to squall line axis. Shading denotes flow from left to right, or towards the convective line.

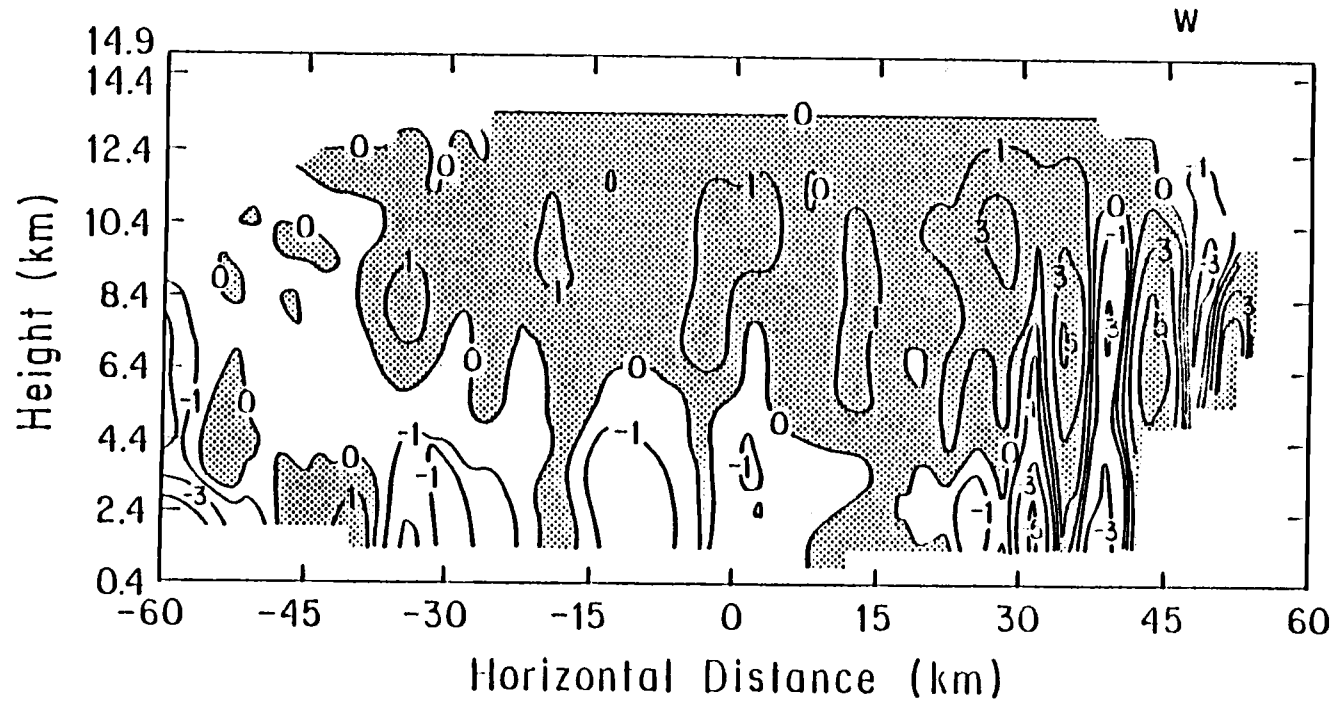


Figure 4.6 Continued

c) Diagnosed vertical velocity field. Shading denotes upward motion.

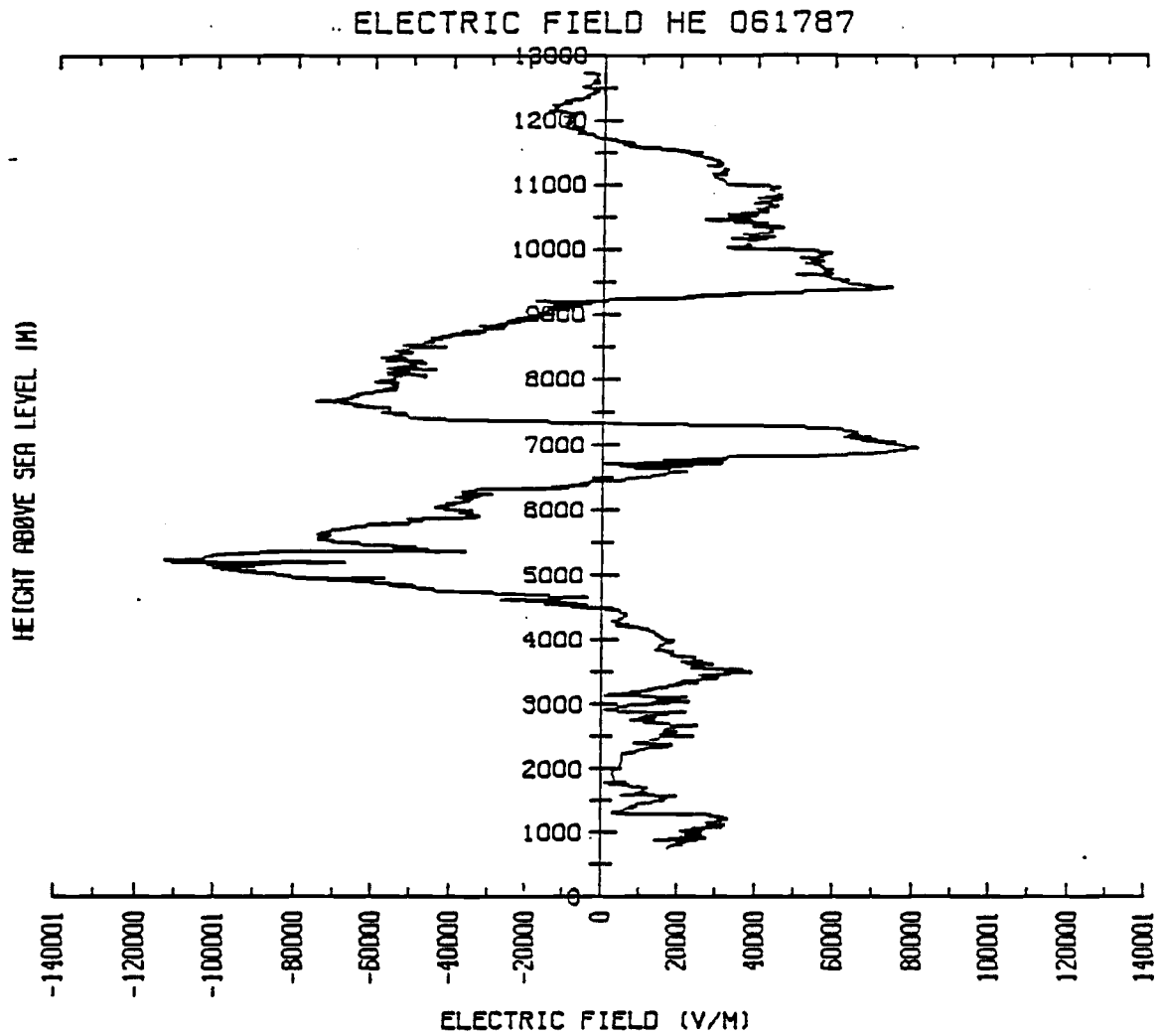


Fig. 4.7 Vertical profile of the electric field in the transition region of a squall-type MCS (from Marshall, 1988, personal communication).

where $\epsilon = 8.86 \times 10^{-12} \text{ F m}^{-1}$ is the permittivity of air, ρ is charge density (in C m^{-3}), and E is the electric field (in V m^{-1}), and assuming that electric field is horizontally homogeneous, we can arrive at an equation for the vertical profile of charge density as,

$$\frac{\partial E}{\partial Z} = \frac{\rho}{\epsilon} \quad (4.27)$$

Hence, vertical profile of charge density is calculated by the finite differential equation,

$$\rho(z) = \epsilon \frac{\Delta E}{\Delta z} \quad (4.28)$$

The vertical profile of charge density is shown in Fig. 4.8. The vertical distribution of charge indicates a pattern in fairly good agreement with the classical model (cf. Fig. 1.1). Positive charge exists near the -10°C and -40°C levels, with negative charge near the -20°C level. Negative screening layers exist at cloud base ($\approx 3.5 \text{ km}$) and cloud top. Volume charge densities are large, with peak values to $\pm 3 \text{ C km}^{-3}$.

By examining the dual-Doppler radar data for the 10-11 June case, we know that the strong front-to-rear air flow was found between the 5 and 8 km levels, with the maximum rearward flow around the 7 km height. A composite pattern of charge and horizontal wind (combining Figs. 4.6b and 4.8) suggests that the positive charge above the 8 km level is very likely to be transported into the stratiform region by this front-to-rear flow. It is possible that negative charge, situated in the layer of 7-

VERTICAL PROFILE OF CHARGE DENSITY

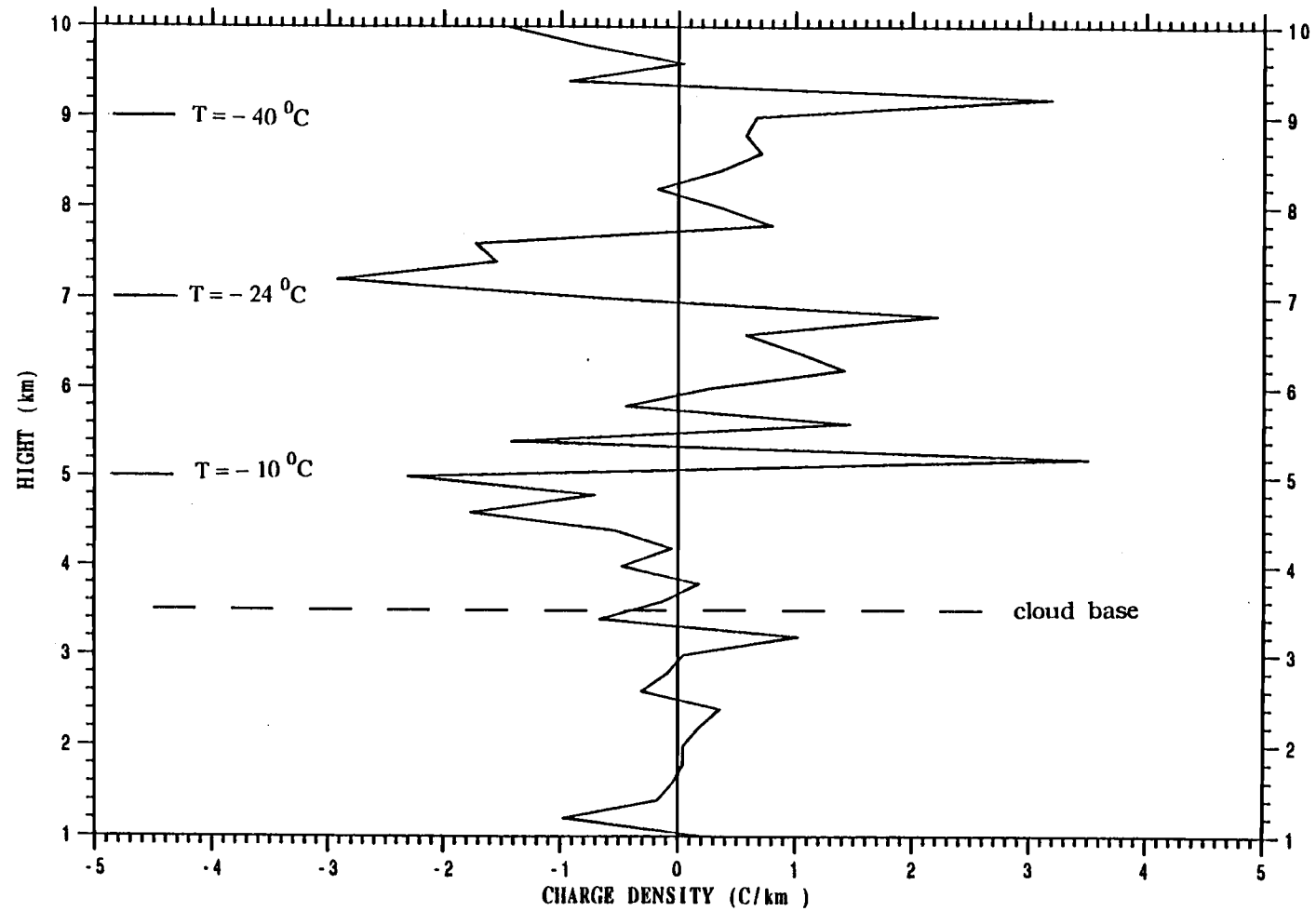


Fig. 4.8 Vertical profile of charge density derived from electric field profile.

7.8 km, may also be transported to the rear. The positive charge near the -10°C level likely resides on large hydrometeors with large fallspeeds, and hence are not likely to be advected rearward over any significant distance.

5. Conclusions

5.1 Conclusions

In this thesis, lightning data indicating the position and polarity of cloud-to-ground flashes, and low-level radar echo patterns from Wichita WAR-57 weather radar have been analyzed. Six MCS events experienced during the O.K. PER-STORM program (1985) were studied. Comparisons between these cases and the 10-11 June case studied by Rutledge and MacGorman (1988) were made.

From the data analyzed, two characteristics of positive cloud-to-ground flashes have been revealed. First, positive CG flashes occurred most frequently in the stratiform region associated with MCSs. A calculation of composite distribution for the seven cases (including the case of 10-11 June) showed that there was a range of preferential reflectivity (about 10-25 dBZ) where over 70% of total positive cloud-to-ground lightning flashes were situated. Echo domains extending to 30 dBZ enclosed 95% of all positive cloud-to-ground flashes. Secondly, the number of positive cloud-to-ground lightning flashes tended to peak during the later stages of the storm lifetime. This distinctive temporal feature of positive cloud-to-ground flashes existed in all seven cases. A calculation of evolution of convective and stratiform rainfall rate in conjunction with the frequencies of positive and negative CG flashes indicated that the maximum CG flash frequency was correlated in time with the rate of greatest stratiform rainfall intensification.

In order to examine what physical processes were responsible for the occurrence of positive cloud-to-ground lightning flashes, as well as for their spatial and temporal characteristics, two mechanisms were discussed. A 1-D charge generation model for a *in-situ* charging mechanism in the stratiform region was developed. This model showed that the vertical charge distribution in the stratiform region was characterized by an inverted electric dipole structure. The maximum positive charge density was about 0.1 C km^{-3} over an hour period, when typical vertical profiles of liquid water content, temperature, graupel and snow were used. This charge concentration is considered too low to lead to field breakdown. However, sensitivity studies showed that reasonable increases in the amount of liquid water (0.28 gm^{-3}), graupel (3.0 g kg^{-1}) and snow (3.0 g kg^{-1}) may lead to a significant production of positive charge (0.49 C km^{-3} over an hour) in stratiform regions. This implies that we may not dismiss the *in-situ* charge mechanism in some storms. A discussion of vertical and horizontal wind fields from the dual-Doppler data analysis in combination with vertical distribution of charge density indicates that the charge advection mechanism is a potential candidate responsible for the occurrence of positive cloud-to-ground lightning flashes.

5.2 Suggestions for further research

The test of a charge advection mechanism cannot be fulfilled unless a more complete quantitative study is conducted. This quantification requires a 2-D explicit cloud model along with observational data ideally from aircraft and dual-Doppler radar. It can be expected that this modeling study will involve more

complicated microphysical processes, and more sophisticated parameterizations. Hence, considerable work needs to be done in both the model development and data collection and analysis.

The 1-D charge generation model developed in this study should also be expanded. In this thesis, we neglected sink processes for positive charge, such as fallout and ion capture. Although these terms are likely comparatively small, neglecting them may possibly lead to an overestimate of the role of *in-situ* charge mechanism. Moreover, the comparison of the roles of charge advection and *in-situ* charging associated with different MCSs (both linear and non-linear system) needs more attention.

6. References

- Beasley, W., 1985: Positive cloud-to-ground lightning observations. *J. Geophys. Res.*, **90**, 6131-6138.
- Bluestein, H. B., and M. H. Jain, 1985: Formation of mesoscale lines of Precipitation: Severe squall lines in Oklahoma during the spring. *J. Atmos. Sci.*, **42**, 1711-1732.
- Brook, M., M. Nakano, and P. Krehbiel, 1982: The electrical structure of the Hokuriku winter thunderstorms. *J. Geophys. Res.*, **87**, 1207-1215.
- Cunning, J. B., 1986: The Oklahoma-Kansas Preliminary Regional Experiment for STORM-central. *Bull. Amer. Meteorol. Soc.*, **67**, 1478-1486.
- Fuquay, D. M., 1982: Positive cloud-to-ground lightning in summer thunderstorms. *J. Geophys. Res.* **87**, 7131-7140.
- Gamache, J. F., and R. A. Houze, Jr., 1982: Mesoscale air motions associated with a tropical squall line. *Mon. Wea. Rev.*, **110**, 118-135.
- Gardiner, B., D. Lamb, R. L. Pitter, J. Hattett and C.P.R Saunders, 1985: Measurements of initial potential gradient and particle charges in a Montana summer thunderstorm. *J. Geophys. Res.*, **90**, 6079-6086.
- Goodman, S. J., and D. R. MacGorman, 1986: Cloud-to-ground lightning activity in Mesoscale Convective Complexes. *Mon. Wea. Rev.*, **114**, 2320-2328.
- Hiscox, W. L., E. P. Krider, A. E. Pifer, and M. A. Uman, 1984: A systematic method for identifying and correcting "site errors" in a network of magnetic direction finders. *Proceedings, International Aerospace and Ground Conference on Lightning and Static Electricity*, Orlando, FL, available from NTIS, Springfield, VA, PP. 7/1-7/15.
- Holle, R. L., A. I. Watson, J. R. Daugherty, and R. E. Lopez, 1985: Cloud-to-ground lightning in the mesoscale convective system on May 20-21, 1979 during SESAME. *Preprints, 14th Conference on Severe Local Storms*, Indianapolis, Ind., Oct. 29-Nov. 1, *Amer. Meteor. Soc.*, Boston, 359-362.
- Holle, R. L., A. I. Watson, R. E. Lopez, and D. R. MacGorman, 1988: Lightning related

to echo type in four MCCs on 3-5, 1985 in the PRE-STORM area. *Preprints, 16th Conference on Severe Local Storms*. Baltimore, MD. *Amer. Meteor. Soc.*, Boston, MA.

Idone, V. P., R. E. Orville, and R. W. Henderson, 1984: Ground truth: A positive cloud-to-ground lightning flash. *J. Clim. and Appl. Meteor.*, **23**, 1149-1151.

Jayarathne, P. R., C. P. R. Saunders, and J. Hallet, 1983: Laboratory studies of the charging of soft hail during ice crystal interactions. *Quart. J. Roy. Meteor. Soc.*, **109**, 609-630.

Krehibel, P. R., M. Brook, and R. A. McCrory, 1979: An analysis of the charge structure of lightning discharges to ground. *J. Geophys. Res.* **84**, 2432-2456.

Lhermitte, R., and P. R. Krehbiel, 1979: Doppler radar and radio observations of thunderstorms. *IEEE. Trans. Geosci. Electron*, **GE17**, 162-171.

Locatelli, J. D., and P. V. Hobbs, 1974: Fallspeeds and masses of solid precipitation particles. *J. Geophys. Res.*, **79**, 2185-2197.

MacGorman, D. R., 1978: Lightning location in a storm with strong wind shear. Ph.D. dissertation, Rice University, Houston, Texas, 141 pp.

Mach, D. M., D. R. MacGorman, W. D. Rust, and R. T. Arnold, 1986: Site errors and detection efficiency in a lightning strike locating system. *J. Atmos. and Oceanic Tech.*, **3**, 67-74.

Marshall, J. S., and W. Palmer, 1948: The distribution of raindrops with size. *J. Meteor.*, **5**, 165-166.

Marshall, T. C., W. D. Rust, W. P. Winn, and K. E. Gilbert, 1988: The electrical structure in two thunderstorm anvil clouds. (Submitted to *J. Geophys. Res.*).

Rust, W. D., D. R. MacGorman, and R. T. Arnold, 1981: Positive cloud-to-ground lightning flashes in severe storms. *Geophys. Res. L.*, **8**, 791-794.

Rutledge, S. A., and R. A. Houze, Jr., 1987: A diagnostic modeling study of the trailing stratiform region of midlatitude squall line. *J. Atmos. Sci.*, **44**, 2640-2656.

Rutledge, S. A. and D. R. MacGorman, 1988: Cloud-to-ground lightning activity in the 10-11 June 1985 Mesoscale Convective System observed during O. K. PRE-

STORM. *Mon. Wea. Rev.*, **116**, 1393-1408.

Rutledge, S. A., and R. A. Houze, Jr., 1988a: The Kansas-Oklahoma squall line of 10-11 June 1985 observed in PRE-STORM: Precipitation structure and single-Doppler radar analysis. *Mon. Wea. Rev.*, **116**, 1409-1430.

Rutledge, S. A. and R. A. Houze, Jr., A. J. Heymsfield, and M. I. Biggerstaff, 1988b: Dual-Doppler and airborne observations in the stratiform region of the 10-11 June MCS over Kansas during PRE-STORM. *Extended Abstracts, 10th International Conf. on Cloud Physics*, 15-20 August, Bad Homburg, FRG.

Saunders, C. P. R., and E. R. Jayaratne, 1986: Thunderstorm charge transfer Values. *Preprint Volume, 23rd conference on cloud physics*, Snowmass, Co, American Meteorological Society, Boston, MA.

Sekhon, R. S., and R. C. Srivastava, 1971: Doppler radar observations of drop-size distributions in thunderstorms. *J. Atmos. Sci.*, **18**, 983-994

Smull, B. F. and R. A. Houze, Jr., 1985: A midlatitude squall line with a trailing region of stratiform rain: Radar and satellite observations. *Mon. wea. Rev.*, **113**, 117-133.

Smull, B. F. and R. A. Houze, Jr., 1987: Dual-Doppler radar analysis of a midlatitude squall line with a trailing region of stratiform rain. *J. Atmos. Sci.*, **44**, 2128-2148.

Takeuti, T., M. Nakano, M. Nagatani, and H. Nakada, 1973: On lightning discharges in winter thunderstorms. *J. Meteor. Soc. Japan*, **51**, 494-496.

Uman, M. A., 1969: *Lightning*, P. 3, McGraw-Hill, New York.